Torero T-16

An acrobatic racing aircraft designed to beat Red Bull at their own game at the Red Bull Air Race of 2018

K. Capiot	4160797	M. van Horssen	4134818
W.F. Datema	4155505	T.M. Hylkema	1312294
R.R. Duivenvoorden	4079604	J.H. Klingelhoefer	4116623
N.H.M. van den Dungen	4133420	L. Mengyang	4147952
J. Heijink	4141296	L. Verheij	4142306

Final Report

Design Synthesis Exercise

TU Delft Delft University of Technology

TORERO

Aerospace Engineering

June 24, 2014

Preface

For the 2014 Spring Design Synthesis Exercise, we, as a group of ten students working under the name *Torero*, were asked to design an aerobatic racing aircraft within ten weeks, fit to compete at the Red Bull Air Race© World Championship with its first flight in 2017. This report is the fourth report on the design progress, after the Project Plan, the Baseline Report and the Mid-term Report. It presents a preliminary design of the aircraft, the *Torero T-16*.

This report is targeted at fellow engineers. It is assumed the reader has fair knowledge on aerospace engineering related topics. Nonetheless, many aspects of the design of an aerobatic racing aircraft are slightly different from the general design methodology that is taught in aerospace engineering and these are explained as such.

Readers who are interested in the aircraft design are referred to Part II, Detailed Aircraft Design. The resulting final concept and its corresponding parameters are presented in Chapter 9 and Appendix B, respectively. For additional information, we would like to refer to the sources that can be found at the end of this report.

We would like to express our gratitude to our tutor Sonell Shroff for her guidance throughout this project. We would also like to thank our team coaches, Joost Ellerbroek and Etana Ferede for their input. Our appreciation goes to our core team coaches Professor Alan Rothwell and Darun Barazanchy.

We would also like to take this opportunity to acknowledge Loek Boermans, Koen Groot, Ricardo Pereira and Roelof Vos for their help on aerodynamic characteristics, Christos Kassapoglou for his input on the structural design, Professor Egbert Torenbeek for his help on Class I and Class II weight estimation methods, and finally Gianfranco La Rocca and Mark Voskuijl for their respective assistance on the control surface design and performance diagrams.

Lastly, we would like to express our thanks to Hendrik Jan van Overvest, for sharing his practical experience and knowledge and, above all, his hospitality.

Summary

The company *FlashCo.*, which has recently released a new energy drink, has invited *Torero* to design and develop an aerobatic racing aircraft fit to compete in the *Red Bull Air Race World Championship* in 2018. They wish to beat *Red Bull* at their own competition to make a mark in the energy drink market.

The aircraft shall be able to compete in the *Red Bull Air Race World Championship* complying with all relevant regulations, with its first flight in 2017 and within a budget of €275,000.-. *Torero* determined a development strategy for the project, containing a market analysis, operations and logistics and an interface analysis.

Starting with the system description and weight estimations, the aircraft design is consequently presented as a combination of subsystems, which are integrated into the full design. Detailed weight estimations are performed, which result in a maximum take-off weight equal to 698 kg. The wing and power loadings, which follow from the Class I weight estimation, are found to be 94.4 kg/m^2 and 3.66 kg/kW, respectively.

The aircraft is installed with the *Lycoming Thunderbolt AEIO-540-D* engine with *Hartzell 3-bladed 7690* propeller, as specified by the *Red Bull Air Race* regulations. The engine mounting is able to carry a weight of 29.43 kN, with a total propulsion system mass of 235 kg.

The load carrying structure of the fuselage is a truss, made of ASTM A514 Steel alloy. The fuselage skin consists of two different materials, namely jute-Biopol composites for the top part and synthetic fabric material for the aft and bottom skin. A titanium firewall is installed in order to protect the cockpit against possible engine fire.

In the design of the wing, first an airfoil is selected. The Eppler E479 airfoil is modified to meet the requirements of the aircraft. This results in an airfoil with a $C_{l_{max}}$ of 2.29, a stall angle of 23.1 ° and a C_{d_0} of 0.007. A slightly modified airfoil, which only has a smaller nose radius, is used in the root section of the airfoil, to ensure the root section stalls first. The wing has a root chord of 1.4 m, a tip chord of 0.7 m, a wing area of 7.3 m^2, a wing span of 7.6 m and a quarter chord sweep of −2.4 °. The taper of 0.5 is chosen for a lift distribution that approximates the ideal elliptical lift distribution. A wing box is designed to support the structure. At the tip, the top and bottom plate are 1.2 mm thick and the front and rear spar are 2 mm thick. At the root, the front beam is 8.4 mm, the rear beam is 7.2 mm and both the top and bottom plate are 2.8 mm. Four ribs are used with each a thickness of 5 mm and a composite skin of 2 mm thickness is applied. The total wing mass is 62 kg.

Subsequently, the empennage is designed. For the horizontal tailplane and vertical tailplane, the NACA 0012 and NACA 0009 airfoil are used, respectively. For the horizontal tailplane a taper ratio of 0.6 is used and the root and tip chord are 0.7 m and 0.4 m, respectively. For the horizontal tail structure, a beam of 2.4 mm thickness at the root and 1.6 mm at the tip is used. The vertical tail is tapered by a ratio of 0.3. The root and tip chord are 1.2 m and 0.3 m respectively. The structure consists of a beam with a thickness of 3.2 mm at the root and 1.6 mm at the tip. Also, three ribs are used in the tail to cope with skin buckling. The horizontal and vertical tailplane weigh 18.7 kg and 12 kg, respectively.

Thereafter the stability and control of the aircraft is determined. First the wing position and horizontal tail size are computed. The horizontal tail area is 11% of the area of the wing and the wing is positioned at 19% of the fuselage length, measured form the nose.

The aileron provides a roll rate 475 $°/s$, which is significantly higher than the reference aircraft. To achieve this, the ailerons take up 30% of the wing chord and 80% of the span. The elevator is designed in such a way that a pull-up manoeuvre can be performed at the maximum load factor of 10g at the manoeuvre speed of 91.7 m/s. This leads to an elevator with a chord ratio of 53% and a span of 1.62 m. The rudder is designed to recover from a spin of 240°$/s$ in no more than one turn. To achieve this, the rudder takes up 70% of the vertical tail chord and requires a span of 1.43 m. The position of the horizontal tailplane is determined to be 3.67 m from the wing aerodynamic centre. When looking at the control forces for maximum deflection, these result in 290 N for the aileron at a speed of 135 m/s, 743 N for the elevator at a speed of 139 m/s and 890 N for the rudder around the manoeuvre speed.

Finally the landing gear is designed. It is determined that it has to withstand a load of 31.4 kN and has a weight of 7.5 kg. The complete landing gear, including wheels, brakes and brake fairings, are off-the-shelf products, which are able to cope with the expected stresses. It is placed at a distance of 1.2 m from the nose.

For the final design the total cost adds up to €115,900.-. The remainder of the €275,000.- budget is allocated to further research and development. The electrical power required is estimated to be 1567 W, of which most goes to the starter for the engine.

The range and endurance of the aircraft are 404 km and 1.4 hr, respectively. The stall speed and maximum speed are determined to be 29.2 m/s and 134 m/s, respectively. The rate of climb at sea level is 24.5 m/s and the climb gradient 62%. The tightest turn is determined to be 28 m at a speed of 52 m/s. The fastest turn takes 3.3 s, also at a speed of 52 m/s.

A sustainable approach is of major importance to *Torero*. The use of recyclable materials is researched. Also for the post-mission phase, different approaches to sustainability are used. A modular design is developed, in which the wings and engine can be switched after the mission life of the aircraft to have a more sustainable aircraft. Furthermore, the option of converting the aircraft into an electrical aircraft is taken into consideration. However it is concluded that this is not a feasible option, because the right technology is not yet available.

Concluding, it is verified that all requirements are fulfilled and the reliability, availability, maintainability and safety characteristics are evaluated. Reliability of the aircraft is added to by the safety factors that are taken into account in the structural design. Also, the pilot's experience and the standard checks add to the reliability. The use of current technologies and off-the-shelf products in the aircraft increase the availability of the design and lower development cost, while not sacrificing performance. Besides that, there is still three years to go before the first test flight is scheduled, which gives enough time to take into account all delivery times of materials and parts. Maintenance is strictly scheduled and regulated, with a set amount of hours between required checks. The maintenance structure is based on the schedules of reference aircraft, to make sure it is complete. Finally safety is assessed. Safety is a strong desire of both the CS-23 regulation and the *Red Bull Air Race* regulations. Both are complied with, to ensure the safety of the system.

Contents

List of Abbreviations

Abbreviation	Description
CCT	Closed-Circuit Television
CFD	Computational Fluid Dynamics
CFRP	Carbon Fibre Reinforced Polymer
c.g.	Centre of Gravity
EASA	European Aviation Safety Agency
EFIS	Electronic Flight Instrument System
EW	Empty Weight
EOM	Equations Of Motion
FAA	Federal Aviation Agency
FARA	FlashCo. Aerobatic Racing Aircraft
FVM	Finite Volume Method
IAS	Indicated Airspeed
LE	Leading Edge
LLM	Lifting Line Method
MAC	Mean Aerodynamic Chord
MTOW	Maximum Take-Off Weight
RAMS	Reliability, Availability, Maintainability and Safety
Req.	Requirement(s)
Stk	Stakeholder Requirement
Ssys	Subsystem Requirement
Sys	System Requirements
TAS	True Airspeed
TE	Trailing Edge
TJBC	Treated Jute fibre-reinforced Biopol Composites
TSO	Technical Standard Order
VFR	Visual Flight Rules
VLM	Vortex Lattice Method

List of Symbols

Symbol	Description	Unit
A	Aspect ratio	$[-]$
A_h	Horizontal tail aspect ratio	$[-]$
a	Acceleration	$[m/s^2]$
b	Wing span	$[m]$
b_f	Fuselage width	$[m]$
b_v	Vertical tail span	$[m]$
C_D	Drag coefficient	$[-]$
C_{D_0}	Zero lift drag coefficient	$[-]$
C_L	Lift coefficient	$[-]$
$C_{L_{A-h}}$	Lift coefficient aircraft without tail	$[-]$
$C_{L_{max}}$	Maximum lift coefficient	$[-]$
C_{L_α}	Wing lift rate coefficient	$[rad^{-1}]$
$C_{L_{\alpha_h}}$	Horizontal tail lift rate coefficient	$[rad^{-1}]$
$C_{L_{\alpha_v}}$	Vertical tail lift rate coefficient	$[rad^{-1}]$
$C_{L_{\alpha_{wf}}}$	Wing - fuselage lift rate coefficient	$[rad^{-1}]$
C_l	Airfoil lift coefficient	$[-]$
$C_{l_{max}}$	Airfoil maximum lift coefficient	$[-]$
C_m	Pitching moment coefficient	$[-]$
$C_{m_{ac}}$	Pitching moment coefficient about aerodynamic centre	$[-]$
C_{m_q}	Variation in pitching moment due to a change in pitch rate	$[-]$
C_{m_u}	Variation in the pitching moment due to a change in airspeed	$[-]$
C_{m_α}	Change in pitching moment due to a change in angle of attack	$[-]$
$C_{m_{\delta_e}}$	Elevator effectiveness	$[-]$
$C_{m_{\dot{\alpha}}}$	Change in the pitching moment due to the acceleration along the top axis	$[-]$
$C_{N_{h_\alpha}}$	Change in horizontal tail normal force due to a change in angle of attack	$[-]$
C_{n_r}	Change in yawing moment by a change in roll rate	$[-]$
$C_{N_{w_\alpha}}$	Change in wing normal force due to a change in angle of attack	$[-]$
C_{X_0}	Component of the aerodynamic force in the nominal flight condition	$[-]$
C_{X_q}	Change in the aerodynamic force component due to a change in pitching velocity	$[-]$
C_{X_u}	Change in aerodynamic force component due to a change in airspeed	$[-]$
C_{X_α}	Variation in aerodynamic force component due to a change in angle of attack	$[-]$
$C_{X_{\dot{\alpha}}}$	Change in the aerodynamic force component due to an acceleration along the top axis	$[-]$
$C_{X_{\delta_e}}$	Change in aircraft drag with elevator deflection	$[-]$
C_{Y_p}	Variation in lateral aerodynamic force due to a change in roll rate	$[-]$
C_{Y_r}	Variation in lateral aerodynamic force due to a change in yaw rate	$[-]$
C_{Y_β}	Change in lateral aerodynamic force caused by a side-slip angle	$[-]$
$C_{Y_{\dot{\beta}}}$	Change in lateral aerodynamic force due to the acceleration along the top axis	$[-]$
$C_{Y_{\delta_a}}$	Change in lateral aerodynamic force due to a change in aileron deflection	$[-]$

$C_{Y_{\delta_r}}$	Change in lateral aerodynamic force due to a change in rudder deflection	$[-]$
C_{Z_0}	Component of the aerodynamic force in the nominal flight condition	$[-]$
C_{Z_q}	Change in the aerodynamic force component due to a change in pitch rate	$[-]$
C_{Z_u}	Change in the aerodynamic force component due to a change in airspeed	$[-]$
C_{Z_α}	Measure of the variation in the aerodynamic force component due to a change in angle of attack	$[-]$
$C_{Z_{\dot{\alpha}}}$	Change in the aerodynamic force component due to the acceleration along the top axis	$[-]$
$C_{Z_{\delta_e}}$	Change in the aerodynamic force component with elevator deflection	$[-]$
$\bar{c}$	MAC length	$[m]$
c_g	Geometric chord	$[m]$
c_r	Root chord of wing	$[m]$
c_{r_h}	Root chord of horizontal tail	$[m]$
c_t	Tip chord of wing	$[m]$
c_{t_h}	Tip chord of horizontal tail	$[m]$
D	Drag	$[N]$
$d\varepsilon/d\alpha$	Downwash	$[-]$
$d\sigma/d\beta$	Sidewash	$[-]$
E	Young's modulus	$[MPa]$
e	Oswald factor	$[-]$
F	Force	$[N]$
f	Fuel fraction	$[-]$
G	Shear modulus	$[MPa]$
h	Height	$[m]$
I	Moment of inertia	$[m^4]$
J	Polar moment of inertia	$[m^4]$
k	Reduced frequency	$[-]$
L	Lift	$[N]$
L/D	Lift-over-drag ratio	$[-]$
l_f	Fuselage length	$[m]$
l_h	Horizontal distance between wing quarter chord and horizontal tail quarter chord	$[m]$
l_v	Horizontal distance between wing quarter chord and vertical tail quarter chord	$[m]$
l/h	Canopy length-to-height ratio	$[-]$
M_y	Bending moment	$[Nm]$
m	Mass	$[kg]$
m_{tv}	Vertical scaling vector	$[-]$
n	Load factor	$[-]$
P	Power	$[W]$
P_a	Power available	$[W]$
P_{a_0}	Sea level power available	$[W]$
$P_{critical}$	Critical buckling load	$[N]$
P_r	Power required	$[W]$
p	Static pressure	$[Pa]$
p_0	Sea level pressure	$[Pa]$
q_0	Wing loading at the root	$[N/m]$
R_{air}	Gas constant of air	$[J/(kg \cdot K)]$
Re	Reynolds number	$[-]$
r	Horizontal scaling factor	$[-]$
rc	Rate of climb	$[m/s]$
rc_0	Sea level rate of climb	$[m/s]$
S	Wing surface area	$[m^2]$
S_h	Horizontal tail surface area	$[m^2]$
S_{net}	Net wing surface area	$[m^2]$
S_v	Vertical tail surface area	$[m^2]$
s_{land}	Landing distance	$[m]$
s_{TO}	Take-off distance	$[m]$
T	Torsion	$[Nm]$

T_a	Available thrust	$[N]$
T_{a_0}	Sea level available thrust	$[N]$
TOP	Take-Off parameter	$[-]$
t	Thickness	$[m]$
t	Time	$[s]$
t/c	Thickness ratio	$[-]$
V	Velocity	$[m/s]$
V_h	Horizontal tail velocity	$[m/s]$
V_s	Stall velocity	$[m/s]$
V_v	Vertical tail velocity	$[m/s]$
V_y	Shear force	$[N]$
W	Aircraft weight	$[kg]$
W_{min}	Minimum aircraft weight	$[kg]$
W/P	Power Loading	$[N/W]$
W/S	Wing Loading	$[N/m^2]$
w	Width	$[m]$
$\bar{x}_{ac}$	Aerodynamic centre with respect to MAC	$[-]$
$\bar{x}_{cg}$	C.g. location with respect to MAC	$[-]$
x_v	Tail length	$[m]$
z_h	Vertical distance between wing quarter chord and horizontal tail quarter chord	$[m]$
x_w	C.g. location of the wing	$[-]$

Symbol	**Description**	**Unit**
α	Angle of attack	$[rad]$
β	Prandtl-Glauert factor	$[-]$
γ	Climb gradient	$[-]$
γ_0	Nominal flight path angle	$[rad]$
δ	Deflection	$[m]$
η	Airfoil efficiency coefficient	$[-]$
η_p	Propeller efficiency	$[-]$
θ	Twist angle	$[rad]$
Λ	Sweep angle	$[rad]$
λ	Taper ratio	$[-]$
ρ	Density	$[kg/m^3]$
ρ_0	Sea level air density	$[kg/m^3]$
σ	$= \frac{\rho}{\rho_0}$	$[-]$
σ	Stress	$[Pa]$
σ_{yield}	Yield stress	$[Pa]$
τ_{yield}	Yield shear stress	$[Pa]$

Introduction

The *Red Bull Air Race World Championship* is a series of air races, where pilots need to manoeuvre their aircraft through an obstacle course as fast as possible. Being the fastest and most exhilarating motorsport series in the world, the race draws a great deal of attention. Several million spectators being on site each season and another half a billion following the event on TV makes it a significant event in terms of advertising for *FlashCo.* [1, 2]

Being in the middle of launching a new product, the energy drinks company *FlashCo.* sees this event as the perfect opportunity to be used for their marketing strategy. By beating *Red Bull* in their own competition, *FlashCo.* intents to accomplish that their new product, the *Flash Energy Drink*, gets established and makes a big mark in the energy drink market.

Within this context *FlashCo.* asked the company *Torero* - consisting of a team of ten engineering students - to design an aircraft that is capable of competing in the race. This aircraft, named *Torero T-16*, shall be ready for its first test flight in 2017 and have a unit cost below €275,000.- including development. Among other key requirements, the *T-16* shall comply with the CS-23 specifications as well as the *Red Bull Air Race* regulations. The *Torero* design team has to come up with a use for the aircraft after competing in the *Red Bull Air Race* and is required to plan the end-of-life disposal.

Torero's philosophy is that a sustainable approach should be taken for the design of any product. Therefore, even though aerobatic racing itself is not a sustainable sport, sustainability is taken into account in every possible aspect, such as the production process, the after race life and the disposal. Furthermore the design of the *T-16* is optimised for flight performance, based on the advice and inspiration of experienced people in the field of aerobatic air racing.

The purpose of this report is to present the detailed design of the *T-16*, and to inform *FlashCo.* on the current design progress. Based on extensive technical research in the field of aerobatic racing aircraft design, performance and optimisation analyses are performed to come up with a preliminary aircraft design, which complies with the requirements stated by *FlashCo.*

The report is divided into four parts - Development Strategy, Detailed Aircraft Design, Aircraft Characteristics, and Appendices. In Part I, development strategy, the market analysis is performed and the relevance of the project is explained. Thereafter operations and logistics is elaborated on. After the interfaces within *Torero* are presented, a brief project plan is made, lasting up to the end of life of the product.

In Part II, Detailed Aircraft Design, the system description is given. Based on reference aircraft, an initial weight estimation is given after which the aircraft is build up in different chapters. It starts off with propulsion and fuselage. The wing and empennage are explained in subsequent chapters. After the controls of the aircraft, the landing gear is presented. Lastly, the part concludes with the final design.

Part III, Aircraft Characteristics, starts off with the performance of the aircraft. After the sustainability approach, the requirements are verified. The risk is assessed in the subsequent chapter, and this part ends with reliability, availability, maintenance and safety characteristics.

Finally, a table of relevant data of reference aircraft is given and all parameters of the preliminary detailed design are presented.

Part I

Development Strategy

Chapter 1

Market Analysis

Before any new product is designed and produced, it should be analysed whether there is a market for it, thereby justifying the project. Aerobatic racing is a highly specialised market, making a proper analysis and justification even more critical due to the low number of potential buyers and thereby limited revenue. Appealing to multiple markets would be preferable, but is difficult for aerobatic racing aircraft. Even though many forms of aircraft racing exist and the sport is growing in popularity, each discipline is very specialised and the aircraft differ significantly between, for instance, F1 air racing and the *Red Bull Air Race* [3]. A design optimised for aerobatic racing in the *Red Bull Air Race* is not suited to compete in many of the other disciplines. Since the *Red Bull Air Race* is the only race of its kind, this severely restricts the market. This chapter identifies the markets that can be appealed to and the possibilities of opening new ones, all discussed in Section 1.1. Section 1.2 provides a cost estimate based on reference data and Section 1.3 expands on increasing product worth through end-of-mission applications and sustainable design.

1.1 Market Identification and Project Justification

Aircraft that participated in the *Red Bull Air Race* throughout the seasons from 2005 up to 2014 are listed in Table 1.1. The race was cancelled for the years 2011, 2012 and 2013. It is remarkable to see that over the years most pilots have switched to the *Zivko Edge 540*, even though only in 2014 a new version was introduced. It also should be noted that most aircraft, such as the *Extra 300 series*, the *MX2* and the *MXS-R*, were used for about three seasons before being replaced. [4]

Table 1.1: Aircraft participating in Red Bull Air Race 2005-2014

Red Bull Air Race Edition	Participating Aircraft		Red Bull Air Race Edition
2005	4x Extra 300S 2x Extra 300L 2x Zivko Edge 540 V2	9x Zivko Edge 540 V2 2x MX2 1x Extra 300SR	2008
2006	4x Zivko Edge 540 V2 4x Extra 300S 1x Extra 300L 1x MX2	10x Zivko Edge 540 V2 5x MXS-R	2009
		9x Zivko Edge 540 V2 6x MXS-R	2010
2007	10x Zivko Edge 540 V2 1x Extra 300S 1x MX2 1x CAP 232	4x Zivko Edge 540 V2 5x Zivko Edge 540 V3 2x MXS-R 1x Corvus Racer 540	2014

Based on the observations it is assumed that a new high performance aircraft should be able to compete with the current designs for at least three years. This has little consequence for the *T-16*, as it is a proprietary design. However, the gained experience from the design process could be used to create a new, commercially available design. The *Corvus Racer 540*, only designed for the purpose of competing in the *Red Bull Air Race*, debuted in 2010, which was an unfortunate moment considering that the race was cancelled for the subsequent three years. Incentive for further development has halted and its promotional website is still offline to this day [5–7]. The introduction of an aircraft specifically optimised for the *Red Bull Air Race* has raised interest in

aircraft of such kind.

Currently, the *Red Bull Air Race* is the only race of its kind, drawing a great deal of attention. However, the sport is growing. If this kind of air racing would have more events organised by other companies, such as *FlashCo.*, it would have the chance of expanding the market to include a wider range of competitors and teams. Having a commercially available, well performing design on the market would allow for increasing the grip on the new market. Therefore *FlashCo.* could take advantage by creating own events, for example, events where only *T-16s* are permitted to compete.

A commercially available aircraft offers additional economical benefits compared to a proprietary design. Assuming that more than one unit is sold, development costs can be distributed over a certain number of sold products. A better estimation of this number would be based on further analysis of available markets, the number of potential buyers and the age and technological level of current products in the market. Being able to distribute the one-time expenses of development, such as wing and fuselage mould costs, over multiple units gives the possibility to reduce the unit cost compared to proprietary designs. This means a commercially available aircraft could also have a financial edge over other designs.

One has to realise, that aerobatic racing is still a young sport. It is a legit assumption that as the sport ages, more customised designs follow the *Corvus Racer 540* and appear on the market. This limits the chances of a new aircraft being as successful as the *Zivko Edge 540*.

As mentioned before, the aerobatic racing market is a very small one, which currently does not expand much further than the twelve pilots that fly in the Master Class. As of 2014, the new Challenger Class is added, where newcomers fly in a pre-determined aircraft supplied by the organisation [8]. This could be seen as an addition to the market. However, the chances of a new version of the *T-16* being adopted as the standard are rather slim while it is a young aircraft. It is therefore not assumed that the new Challenger Class immediately adds to the opportunities a new design could take advantage of.

When the *Red Bull Air Race* was first introduced in 2003, most of the competing aircraft were already favourites in the aerobatics world. Aircraft like the *Zivko Edge 540*, which is still the aircraft of choice for the majority of racers, were well known as being incredibly agile aerobatic aircraft. In other words, an aircraft designed for aerobatic racing might also find a spot in the aerobatics market. Whereas the design for the *Red Bull Air Race* needs to be updated constantly to stand a chance in the evolving events, the primary design of a purely aerobatic aircraft lasts much longer. By emerging in a bigger market than the *Red Bull Air Race* itself, development costs can be distributed over a bigger range of products. Most of the *Red Bull Air Race* competitors are renowned aerobatics pilots [9], which strengthens the assumption that an aerobatic racer will also get the attention of purely aerobatic performers.

1.2 Cost Estimate

Since the design of the aircraft is currently still in a preliminary phase and is not ready for production yet, it is difficult to determine the unit cost including production. An estimation of the unit cost is made using the standard prices of reference aircraft. Table 1.2 shows the cost per unit in both US dollars and Euros for a number of popular aircraft that are or have been used in the *Red Bull Air Race*. Also the average of all reference aircraft is shown.

Before the average in Table 1.2 is directly used as an estimate of cost per unit, attention has to be paid to the number of units produced. The *Zivko Edge 540 V2*, for instance, is and has been a favourite in both aerobatic racing and aerobatics for many years. By the end of 2011, 40 *Zivko Edge 540* aircraft were built [7], while the *MXS-R* and *MX2* respectively only had 14 and 13 units

produced by 2013. Moreover, the development of the *Corvus Racer 540* only resulted in two builds by 2011 [7]. Depending on the strategy of the company, development costs can be spread over an expected number of units sold, which has strong effects on price, as mentioned previously in Section 1.1.

Therefore, to determine a cost estimate, not only the average cost has to be taken into account, but also the number of units produced of each aircraft. Since the *FlashCo.* design is proprietary, only a single (or at most a few) unit(s) are built, similar to the *Corvus Racer* project. A *Corvus Racer 540* could be specially ordered ready-to-fly for € 250,000.- in 2011 [7], which is below the average found in table 1.2. Given the similarity of the project, it is therefore expected that the cost of the *T-16* aircraft is in the same range, making the customer requirement of € 275,000.- strict, but reasonable.

Table 1.2: Cost per unit of reference aerobatic racing aircraft [5, 7]

Aircraft	**Price** *US $*	**Price** *€*
Zivko Edge 540 V3	500,000.-	361,000.-
Corvus Racer 540	347,000.-	250,000.-
Extra EA-330LX	07,500.-	293,990.-
MXS-R	385,000.-	277,758.-
MX2	390,000.-	281,365.-
Zivko Edge 540 V2	95,000.-	212,827.-
Average	**387,417.-**	**279,490.-**

To justify the estimated unit cost above, a little more attention is given to the actual expenses that are made. For this particular project, development costs remain very low, as all members of the development team work on a pro bono basis and no external development is included in the project. Most costs, including big one-time expenses, such as wing and fuselage moulds, are considered production costs. It has already been reasoned that development costs are normally a large additional cost to proprietary design projects, as all costs are directed to one customer. This is less so for the *T-16* project. Furthermore, large parts of the aircraft body of aerobatic aircraft are made of carbon fibre [6, 7], which is an expensive material and represents a major part of production and manufacturing costs. Since 2010, the cost of carbon fibre has dropped significantly [10–12], meaning production and manufacturing of such parts has become less expensive. This justifies the assumption that the project can be finished within the budget stated by the customer.

1.3 Post-Mission and Sustainability

In Section 1.1 it is determined that an aerobatic racing aircraft design has an expected mission life of three years within the *Red Bull Air Race*. However, the lifespan of the product itself is much larger than that: the team has identified this to be approximately twenty years. With an eye on sustainability and improving product worth, a post-mission analysis is performed to identify possible further applications of a dedicated aerobatic racing aircraft, such as the *T-16*. The use of sustainable materials is also considered separately.

1.3.1 Post-Mission Phase

After its rather short mission life as a competitor in the *Red Bull Air Race*, the aircraft could still be used for several decades before disposal. However, finding an application for a heavily specialised product may prove difficult.

One of the simplest solutions is to keep it close to its original purpose: aerobatics. As mentioned in Section 1.1, aerobatic racing is strongly linked to aerobatics. An aircraft such as the *T-16* may be too 'aged' as a *Red Bull Air Race* competitor after three years, but can still be used as an aerobatic aircraft for many more years. It can be used as a high performance single-seater, or it can be converted to a twin-seater to be used as an aerobatics trainer. Whether the latter is an option depends on the chosen configuration and materials, since a metal tubular frame, for example, is

easier to convert or strengthen than a complete carbon fibre monocoque. Parties such as private aerobatic enthusiasts or aerobatic training centres may be interested in the aircraft.

Furthermore, the *T-16* could be used for further testing, research and development of high performance aerobatic aircraft. Interested parties may include universities, aircraft developers or even the *Torero* company itself.

FlashCo. could also opt to keep the aircraft, to be used in commercial appearances in the future. Having a company aircraft that is often seen in public during airshows and other events can provide additional revenue for a company, especially when having made a name for itself during an event like the *Red Bull Air Race*.

1.3.2 Sustainability

Most of the post-mission applications of the *T-16* require less performance than is desired during the *Red Bull Air Race*. This means the engine can be downsized, reducing emissions. The engine that is mandatory for the *Red Bull Air Race* as of 2014, is an engine that has been used for many years and possibly for many years to come. Assuming *Red Bull* sticks to the same engine for the years to come, it could be resold to *Red Bull Air Race* competitors. Since championship races only take little over a minute [4], wear of the engine is relatively small in the short lifespan of the *T-16* as an aerobatic racer.

Other options to make the design more sustainable, apart from the post-mission application, which already increases sustainability, regards the use of materials. First of all the production processes can be considered. Depending on the design, materials can be chosen that are produced with sustainable methods compared to other production processes.

Furthermore, after the post-mission application, the aircraft has to be disposed of. Using as many recyclable materials as possible helps making the design more sustainable. Carbon fibre polymers can be ground down and reused in, for instance, short fibre reinforced concrete [13]. Metal frames can be molten down and recycled and as many of the instruments in the cockpit are determined by CS-23 regulations [14], these can be recycled as spare parts for other aircraft.

In Chapter 2 in Part III the approach to sustainable design and the post-mission aspects are elaborated upon.

Chapter 2

Operations and Logistics

Having identified the market, it is necessary to investigate the logistical aspect. This chapter investigates the logistics of getting the aircraft to and from the *Red Bull Air Race* and the operations and logistics at the event.

To provide an overview of the operations and logistics associated with the aerobatic racing aircraft, a functional flow diagram is presented in Figure 2.1. The top level is split up into pre-flight and post-flight activities. A number of these activities is discussed in more detail.

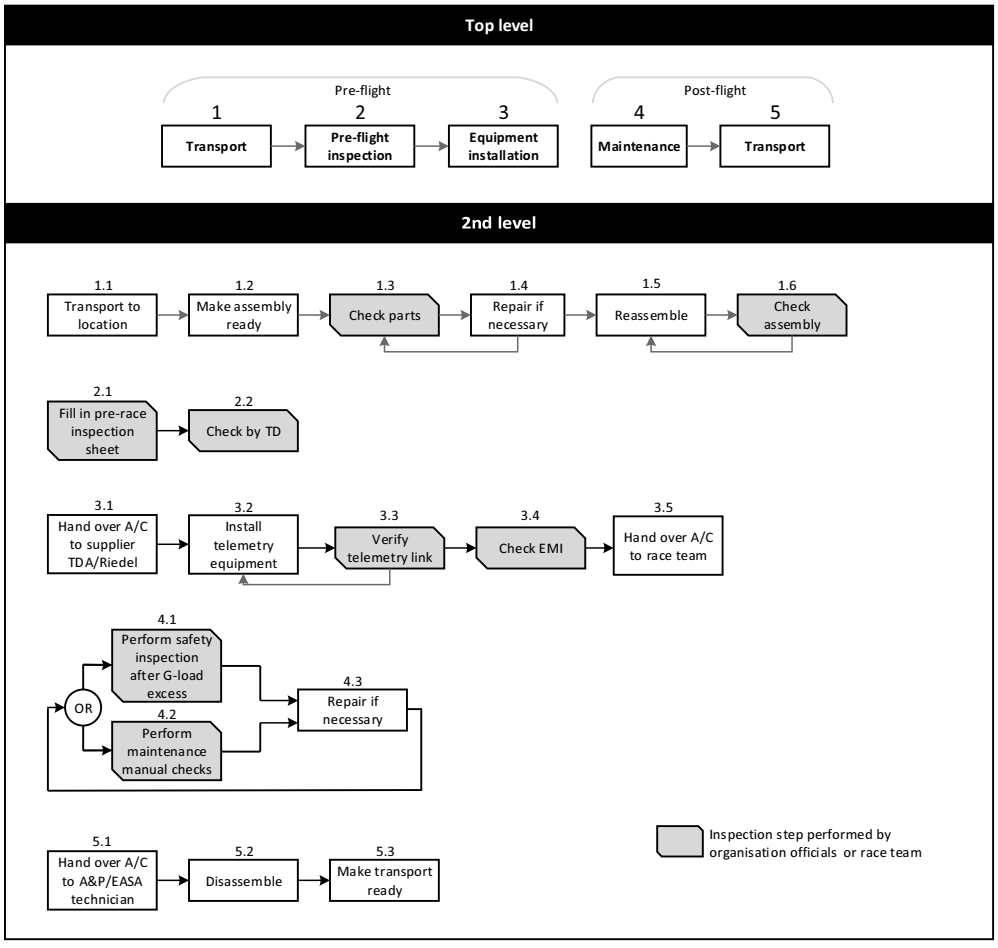

Figure 2.1: Top level and second level of the operations and logistics functional flow diagram.

The transportation of the aircraft to and from the *Red Bull Air Race* location is done with the help of the *Red Bull Air Race World Championship* official logistics partner, *DHL*. The aircraft are shipped via container ship or cargo aircraft for large distances and by truck for smaller distances. For these journeys, the current aircraft are disassembled into three main parts: the wing, the fuselage and the tail. Disassembly typically takes six hours, while reassembly takes up to eighteen hours. [15]

Red Bull Air Race events have a strict flow of procedures regarding competing aircraft. Different areas are designated to different functions and all competitors have to comply with the flow of procedures. Figure 2.2 gives an overview of these areas and the sequence in which pilots pass these areas.

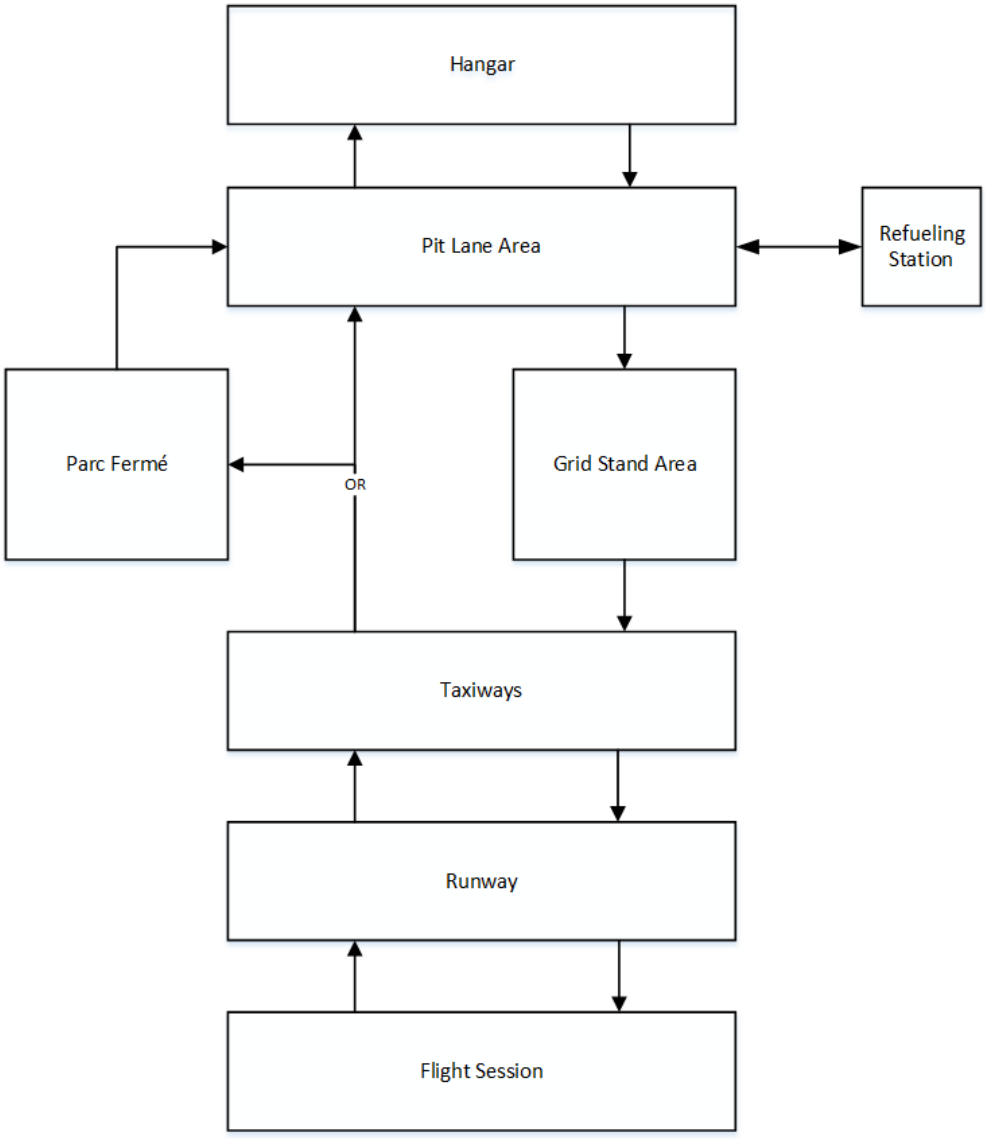

Figure 2.2: Flow Diagram of Operations on Location

At each event, hangars are set up for each team, with enough room to work on the aircraft when needed. The pit lane area is the area in front of the hangars and connects to the refuelling station and grid stand area. The grid stand area consists of two strips next to the tower, or Grid Stand, as it is called. All competitors assemble here before taking off to perform their flight session. From the grid stand area, aircraft proceed to the runway using the taxiways. The flight session includes all operations in the air, such as loiter and race. After landing and taxiing, the aircraft and the pilot return to the hangars or to the Parc Fermé, if required, where press and media gather to talk to the pilots. [16]

Chapter 3

Interface Analysis

In this chapter the interfaces between the departments within *Torero* are presented and the technical interfaces between the subsystems of the *T-16* are discussed. Section 3.1 elaborates on the structure of the technical departments within the company and the flow of information in the design process of the *T-16*. Subsequently, the data flow between the subsystems of the *T-16* itself is presented in Section 3.2.

3.1 Technical Structure Torero

Torero is divided in multiple technical departments that each work on a separate subsystem of the *T-16*, while constantly updating the other departments. The flow of information between the departments is graphically represented by an N^2-chart, as shown in Figure 3.1.

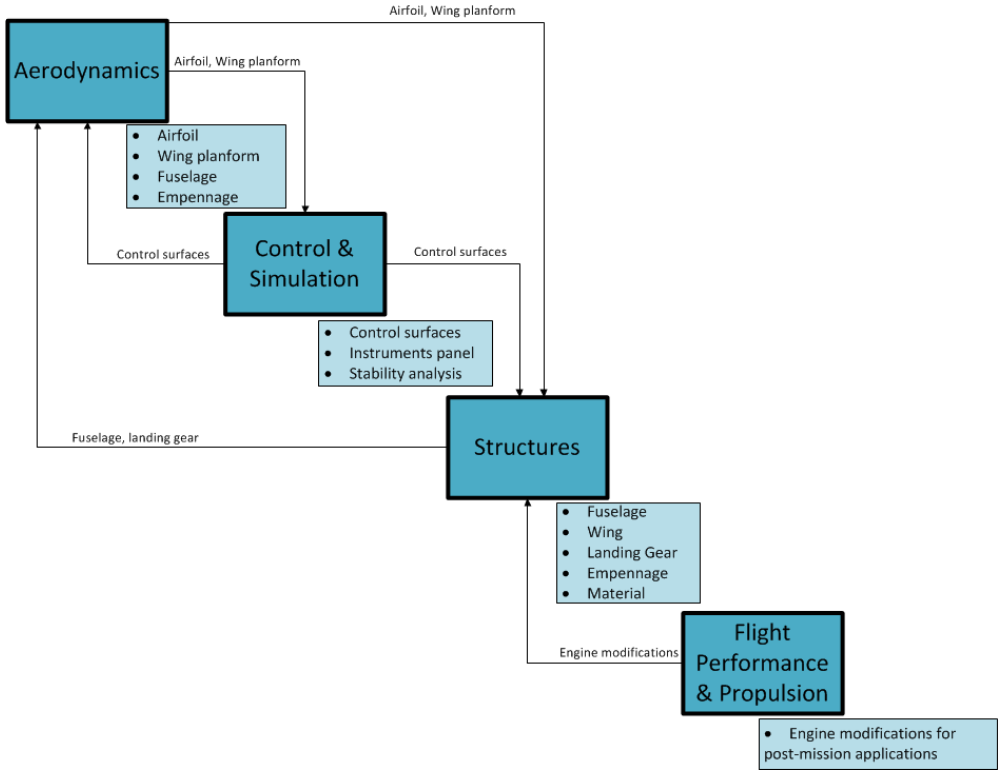

Figure 3.1: N^2-chart representation of technical departments within Torero

The following sections describe the N^2-chart in more detail with respect to the inputs and outputs (i.e. feedback and feedforward) of information between the departments.

3.1.1 Aerodynamics

The Aerodynamics department is leading the design process of the *T-16*, because the aerodynamics of the aircraft determine to a great extent the performance of the aircraft and could give an extra advantage during the race. The main tasks of this department are choosing the airfoils and wing

layout, since these are required inputs for the Control & Simulation department and the Structures department. The key elements that are fed back to the Aerodynamics department are:

- Wing and airfoil
- Fuselage layout
- Landing gear layout

The Aerodynamics department gets feedback from the Structures department on potential structural constraints. Furthermore, in cooperation with the Control & Simulation department, the control surfaces and ampennage are designed.

3.1.2 Structures

The Structures department is tasked with making the aerodynamic aircraft design as light as possible, while still being able to withstand the high load factors up to 15g. The main inputs for this department are:

- Airfoil type
- Wing planform layout
- Control surfaces

The Structures department also needs to account for potential airframe modifications to allow the use of a different or modified engine for sustainable post-mission applications. Another task for the Structures department is the implementation of the designed control surfaces of the Control & Simulation department.

3.1.3 Control and Simulation

In cooperation with the Aerodynamics department, the Control & Simulation department is responsible for designing the control surfaces to obtain high manoeuvrability without unacceptably compromising the stability of the aircraft. Inputs for the Control & Simulation departments include:

- Centre of gravity (c.g.) ranges
- Desired control characteristics
- Aircraft lay-out

The outputs of the Control & Simulation department go to the Aerodynamics and Structures department. The Aerodynamics department gives feedback on the changes in aerodynamic forces due to control deflections and the Structures department implements the control surfaces in the airframe.

3.1.4 Flight Performance & Propulsion

The Flight Performance and Propulsion department is the smallest department of *Torero*. Since the engine type and maximum load factors are determined, there is less research required in this field. The main focus of this department lies in finding sustainable solutions for the aircraft regarding post-mission applications.

3.2 Interface Identification

In this section the data flows for the system are discussed. The data flow is illustrated in a communication flow diagram, where all elements that are part of the communication chain are indicated in blocks and the data and command flows are represented by arrows [17]. Two

communication flow diagrams are presented: one indicating the data flow during the race and one for the data flow after the race.

The communication flow diagram during the race flight is shown in Figure 3.2. The flow of data consists of flight data, video data and radio communication. There are four main elements in the diagram: aircraft, radio station, control tower and media. The aircraft itself contains all the instruments to collect the data, that apart from being sent also need to be stored on board. The control tower continuously receives information about the aircraft, such as velocity, altitude and g-forces. To allow the media to broadcast live feeds from cameras attached to the aircraft and inside the aircraft, a video downlink is required. The radio station plays a role as an intermediary between the pilot and ground operations.

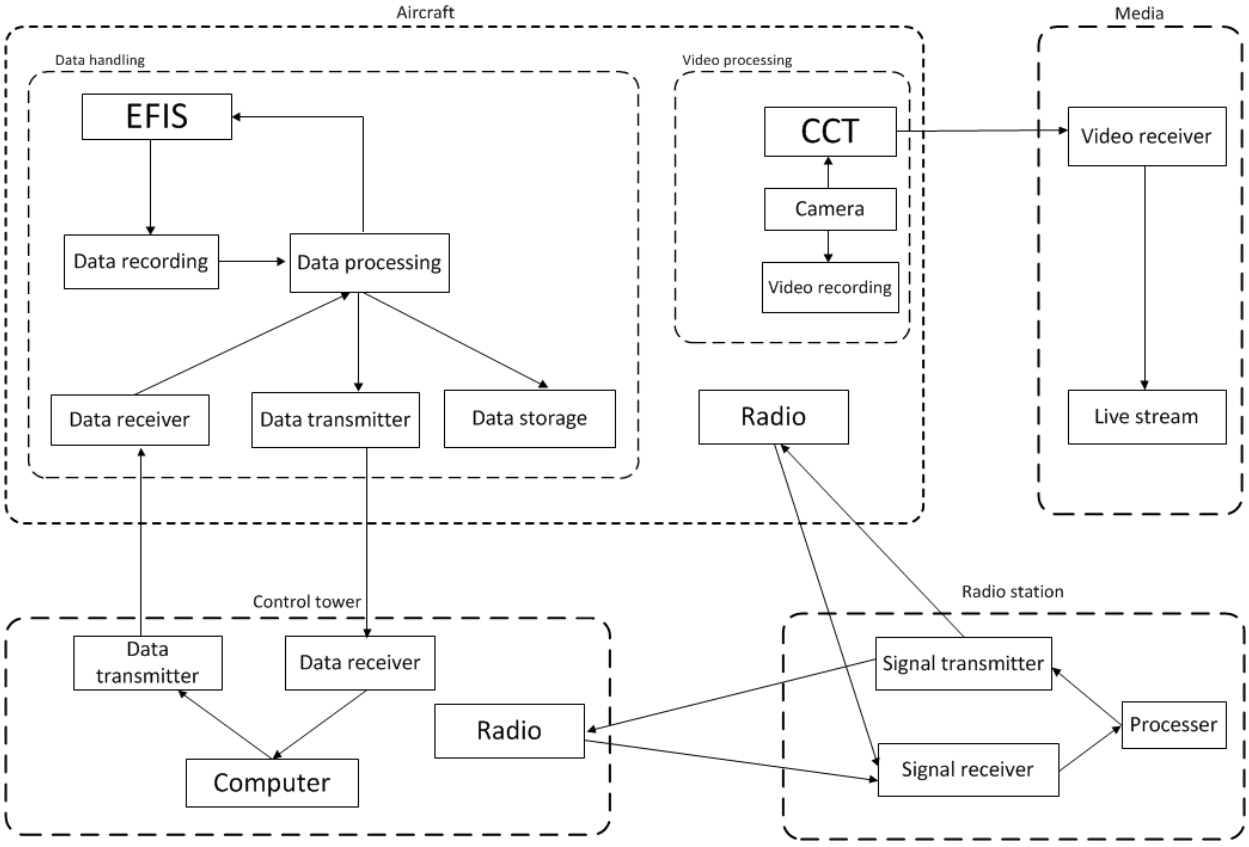

Figure 3.2: Communication Flow Diagram during flight

After the race, the data need to be processed and further engineering work is performed to prepare for the next race. Therefore, another communication flow diagram for the post-flight phase is shown in Figure 3.3. In this diagram it can be seen that both the data stored on board of the aircraft and the data stored on the ground are analysed. The results are reported to all stakeholders. Meanwhile, the analysed data serve as a guideline for planning the maintenance activities. Based on these data, the technical team modifies the aircraft for the next race.

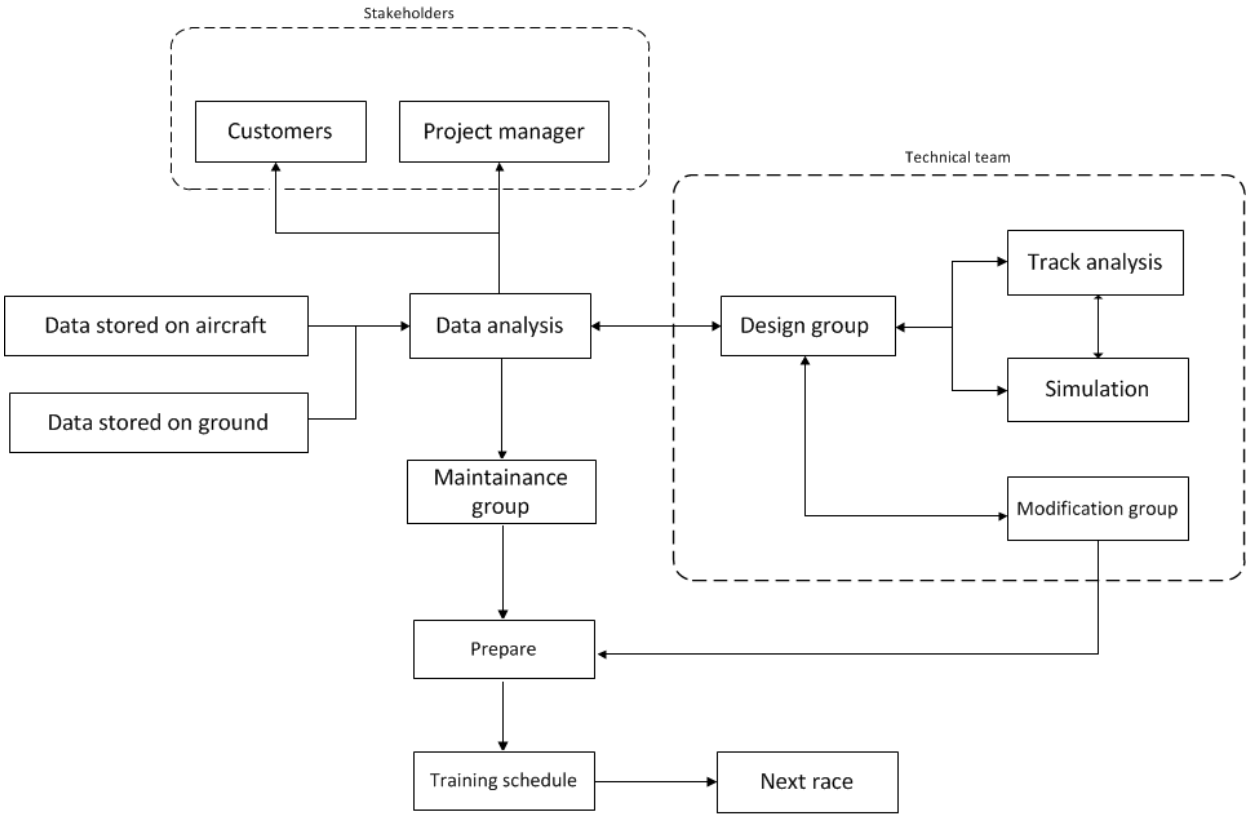

Figure 3.3: Communication Flow Diagram after flight

Chapter 4

Further Development and Production Outline

This report concludes with the preliminary design phase. However, a lot still has to be done before the aircraft is ready to race in the *Red Bull Air Race* in 2018. This chapter includes a Gantt chart to visualise both the process for further development and the production plan. The production plan is actually part of the process for further development, but is presented separately for the sake of legibility.

4.1 Further Development

Figure 4.1 shows the Gantt chart for further development. It can be seen that this consists of a detailed design phase, a production and testing phase, a mission phase, a post-mission phase and the end-of-life disposal. The post-mission phase and end-of-life disposal are not fully shown in the visual representation of the Gantt chart, again for the sake of legibility.

The detailed design phase includes further research and design based on the recommendations that are given in this report regarding each department. The production phase is elaborated in Section 4.2. Testing needs to be performed after the aircraft is completely designed in detail. The testing includes both wind tunnel tests and flight tests with the actual aircraft. The first flight is performed in 2017, as per the requirements presented in Chapter 3 in Part III. Further flight testing is done before certification is started, which is estimated to take about half a year.

After certification, the aircraft can be handed over to *FlashCo.* as a finalised product. It can then be used for training before the 2018 season of the *Red Bull Air Race* starts in February. The mission life of the aircraft is estimated to be three seasons, as found from the market analysis 1. The subsequent post-mission phase is expected to last at least twenty years, before the aircraft is disposed of.

4.2 Production Plan

Figure 4.2 shows the production plan for the aircraft. It is important that manufacturing and assembly are done in a logical order. The complete production process, including the manufacturing of moulds and other required tools, is estimated to be completed in about 160 days. The assembly and disassembly, as has to be performed for transportation of the aircraft, should be completed in about 24 hours.

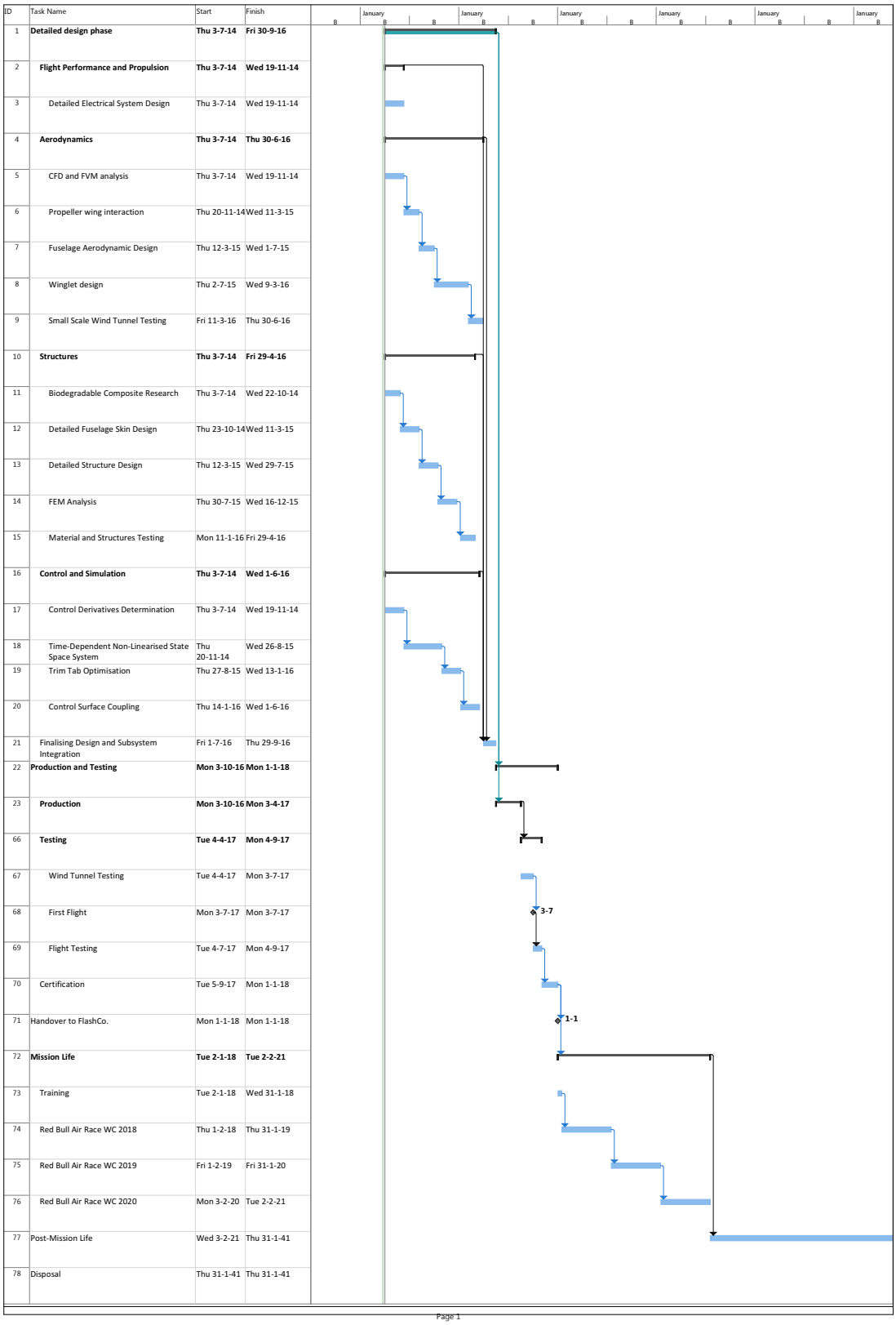

ID	Task Name	Start	Finish
1	**Detailed design phase**	**Thu 3-7-14**	**Fri 30-9-16**
2	**Flight Performance and Propulsion**	**Thu 3-7-14**	**Wed 19-11-14**
3	Detailed Electrical System Design	Thu 3-7-14	Wed 19-11-14
4	**Aerodynamics**	**Thu 3-7-14**	**Thu 30-6-16**
5	CFD and FVM analysis	Thu 3-7-14	Wed 19-11-14
6	Propeller wing interaction	Thu 20-11-14	Wed 11-3-15
7	Fuselage Aerodynamic Design	Thu 12-3-15	Wed 1-7-15
8	Winglet design	Thu 2-7-15	Wed 9-3-16
9	Small Scale Wind Tunnel Testing	Fri 11-3-16	Thu 30-6-16
10	**Structures**	**Thu 3-7-14**	**Fri 29-4-16**
11	Biodegradable Composite Research	Thu 3-7-14	Wed 22-10-14
12	Detailed Fuselage Skin Design	Thu 23-10-14	Wed 11-3-15
13	Detailed Structure Design	Thu 12-3-15	Wed 29-7-15
14	FEM Analysis	Thu 30-7-15	Wed 16-12-15
15	Material and Structures Testing	Mon 11-1-16	Fri 29-4-16
16	**Control and Simulation**	**Thu 3-7-14**	**Wed 1-6-16**
17	Control Derivatives Determination	Thu 3-7-14	Wed 19-11-14
18	Time-Dependent Non-Linearised State Space System	Thu 20-11-14	Wed 26-8-15
19	Trim Tab Optimisation	Thu 27-8-15	Wed 13-1-16
20	Control Surface Coupling	Thu 14-1-16	Wed 1-6-16
21	Finalising Design and Subsystem Integration	Fri 1-7-16	Thu 29-9-16
22	**Production and Testing**	**Mon 3-10-16**	**Mon 1-1-18**
23	**Production**	**Mon 3-10-16**	**Mon 3-4-17**
66	**Testing**	**Tue 4-4-17**	**Mon 4-9-17**
67	Wind Tunnel Testing	Tue 4-4-17	Mon 3-7-17
68	First Flight	Mon 3-7-17	Mon 3-7-17
69	Flight Testing	Tue 4-4-17	Mon 4-9-17
70	Certification	Tue 5-9-17	Mon 1-1-18
71	Handover to FlashCo.	Mon 1-1-18	Mon 1-1-18
72	**Mission Life**	**Tue 2-1-18**	**Tue 2-2-21**
73	Training	Tue 2-1-18	Wed 31-1-18
74	Red Bull Air Race WC 2018	Thu 1-2-18	Thu 31-1-19
75	Red Bull Air Race WC 2019	Fri 1-2-19	Fri 31-1-20
76	Red Bull Air Race WC 2020	Mon 3-2-20	Tue 2-2-21
77	Post-Mission Life	Wed 3-2-21	Thu 31-1-41
78	Disposal	Thu 31-1-41	Thu 31-1-41

Figure 4.1: Further development and mission Gantt chart

ID	Task Name	Duration
1	**Production**	**160 days**
2	**Manufacturing**	**135 days**
3	Manufacture Skin Molds	20 days
4	Manufacture Truss	10 days
5	Manufacture Wing Structure	20 days
6	Manufacture Second Wing Structure	20 days
7	Manufacture Empennage Structure	15 days
8	Manufacture Skins	30 days
9	Manufacture Control Surfaces	15 days
10	Manufacture Wiring Harnesses	5 days
11	Manufacture Landing Gear	5 days
12	**Assemble Landing Gear**	**2 days**
13	Install Wheels and Brakes	1 day
14	Attach Brake Fairings	1 day
15	**Assemble Fuselage**	**7 days**
16	Attach Landing Gear to Truss	1 day
17	Install Fuel Tank	1 day
18	Install Wiring Harness	1 day
19	Install Control Rods and Wires	2 days
20	Install Control Panel	2 days
21	Install Seat and Equipment	2 days
22	Install Engine	1 day
23	Attach Skin	2 days
24	Install Cockpit Instruments	2 days
25	Attach Engine Cover	1 day
26	Install Canopy	1 day
27	**Assemble Wing**	**4 days**
28	Install Wiring Harness	4 days
29	Install Control Surfaces	4 days
30	Install Control Rods	4 days
31	Attach Skin	4 days
32	**Assemble Second Wing**	**4 days**
33	Install Wiring Harness	4 days
34	Install Control Surfaces	4 days
35	Install Control Rods	4 days
36	Attach Skin	4 days
37	**Assemble Empennage**	**4 days**
38	Install Control Surfaces	4 days
39	Install Control Rods	4 days
40	Attach Skin	4 days
41	Attach Wing and Empennage	4 days
42	Integrate Controls and Wiring	4 days
43	Attach Propeller	4 days

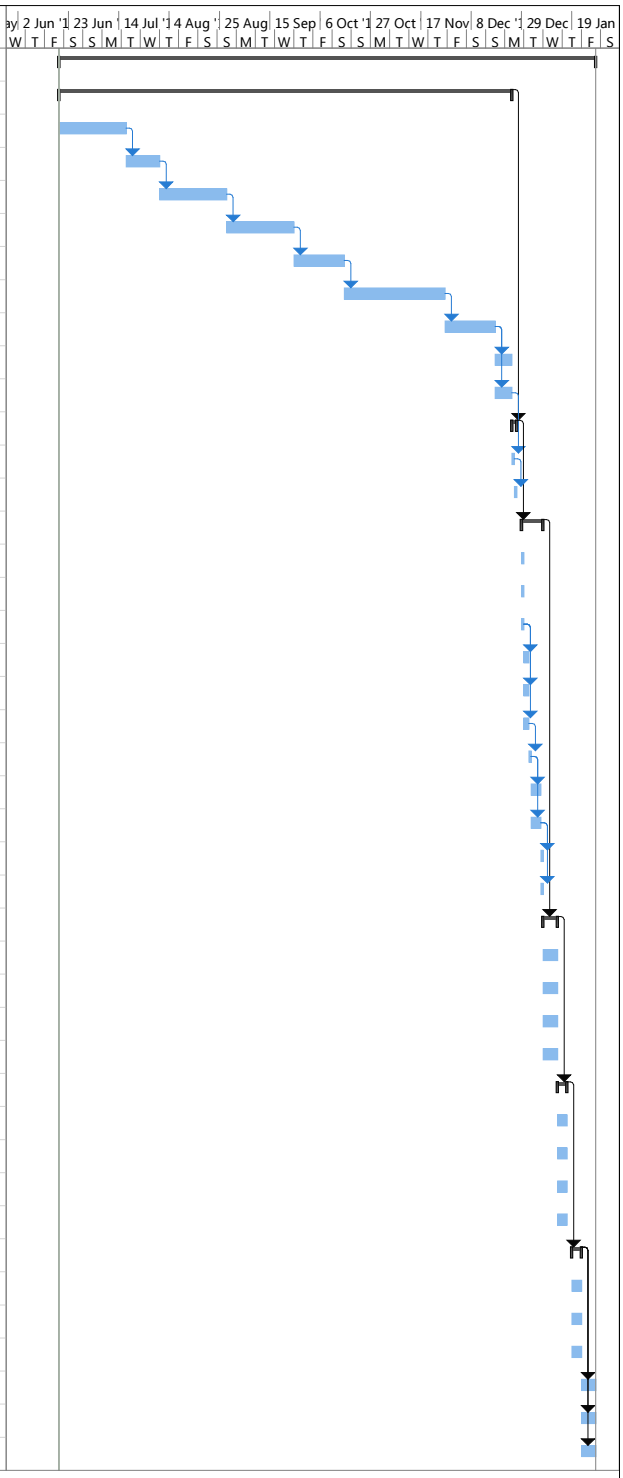

Page 1

Figure 4.2: Torero T-16 production plan

Part II

Detailed Aircraft Design

Chapter 1

System Description

In this chapter, a clear definition is provided of what the mission is and what the system has to do. This starts with the system definition in Section 1.1, followed by a discussion of the mission profile in Section 1.2. Finally, Section 1.4 gives the functional flow diagram of the aircraft as well as its functional breakdown structure.

1.1 System Definition

The system is presented in Figure 1.1 together with its relations to external factors, identified as the 'environment'. Maintenance and the pilot are not within the system boundaries. The reason for this is that maintenance is merely supporting the aircraft system, but is not part of the system itself, and the pilot controls the aircraft, but is not part of the design objective either. Both elements are external factors interacting with the aircraft system and should be considered part of the 'environment'.

It can be seen that maintenance is mutually related to the system. This means that the system determines the required maintenance activities, while the maintenance resources may play a roll in certain design choices. The same is true for transport of the aircraft to and from the race location. The other relations work only one way and are considered self-explanatory. It should be noted that for clarity the internal system relations (between subsystems) and the relations between environmental factors are not shown in Figure 1.1.

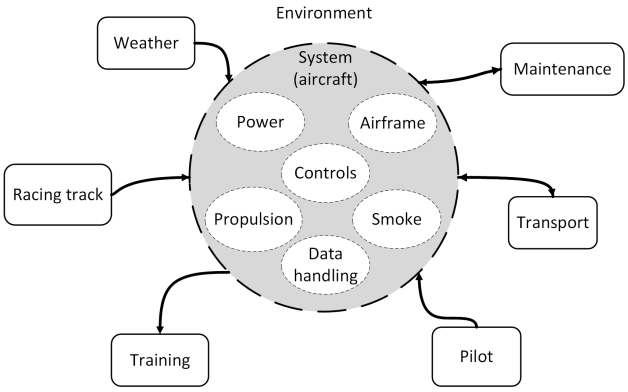

Figure 1.1: Visualisation of the system with its subsystems and relations to the environment

1.2 Mission Profile

The mission profile diagram given in Figure 1.2 presents the mission phases of a typical mission on a race day. The sequence of these phases is given by the *Red Bull Air Race* regulations [16]. A missed approach is not included in this diagram, for two reasons. First of all, this contingency is unlikely to happen. Secondly, the consequence of this event is far from critical. In case of a missed approach, the pilot performs a go around returning in the aerodrome traffic circuit. Then flying one round and if approved by the tower, start another landing approach. However this is not considered because first of all a missed approach is unlikely, and because a go-around takes only an inconsiderable amount of time. The race itself takes no longer than two minutes. Furthermore, including the total flight time to the race track and back to the airport, and the ground operations at the airport, the entire mission takes no longer than approximately half an hour.

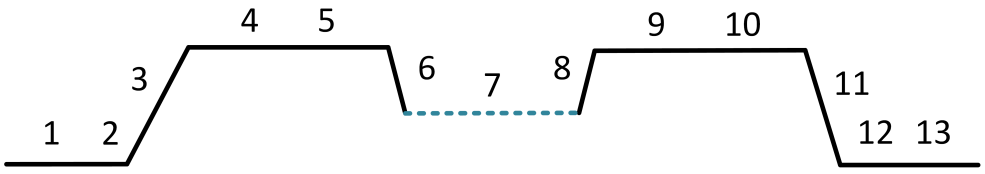

Figure 1.2: Mission profile diagram of a typical mission of the T-16

1. Taxi
2. Take-off
3. Climb
4. Fly to holding number 1 and loiter while performing last equipment check
5. Fly to holding number 2 and loiter while awaiting race track clearance
6. Fly to start gate
7. Fly race (indicated with dashed line)
8. Fly to holding number 3
9. Loiter at holding number 3 while awaiting landing clearance
10. Fly back to airport
11. Descend
12. Land
13. Taxi

1.3 Load Factor Definition

During the race, the pilot pushes the aircraft and his own body to the limits by flying at maximum load factor in most of the manoeuvres. To avoid confusion on the load factor limits applying for the design during the race, a summary is provided in this section.

The maximum load factor pilots are allowed to fly at during the race is 10g. The aircraft structure is designed to withstand a load factor of 15g, which equals the limit load factor times a safety factor of 1.5. Stakeholder requirement FARA-Stk-09 3.1 and *Red Bull Air Race* regulations [16] stating the design should be able to withstand a maximum load factor of 12g is therefore met.

1.4 System Functionality

This section outlines the functions that the system has. These functions can be described in multiple ways. First the functional flow diagram is given after which different functions are defined in more detail in the functional breakdown structure.

1.4.1 Time Sequence of Functions

The sequence in time of functions that the system is executing can be indicated by a functional flow diagram. Within this diagram multiple levels can be identified. The functional flow diagram is shown in Figure 1.3.

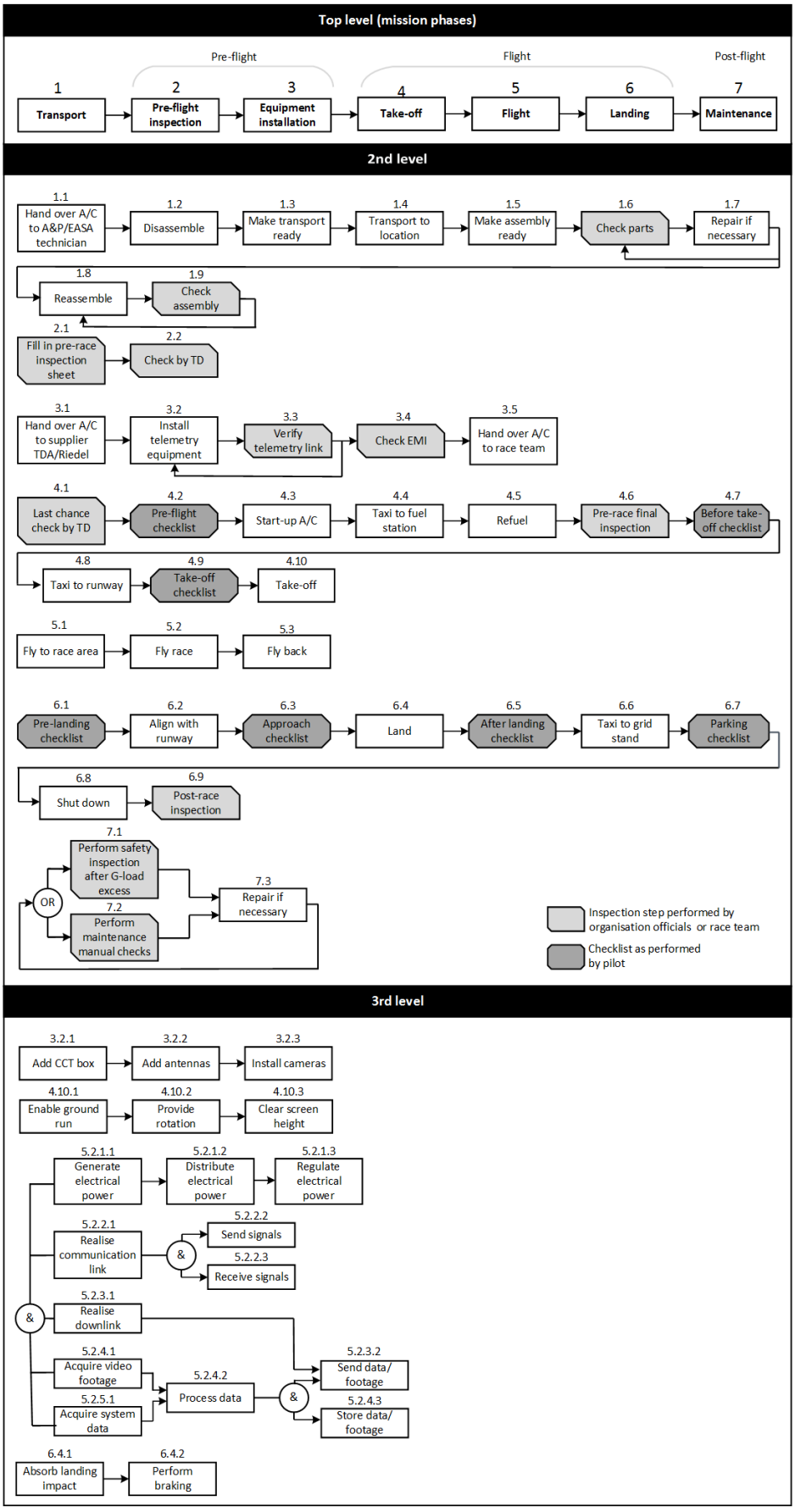

Figure 1.3: Functional flow diagram

1.4.2 Breakdown of System Functionality

In the functional breakdown structure an overview is given of the functions that the systems executes in a hierarchical way. The tree is an AND tree, which means that all functions below the main functions are part of the block above. The functional breakdown structure is shown in Figure 1.4.

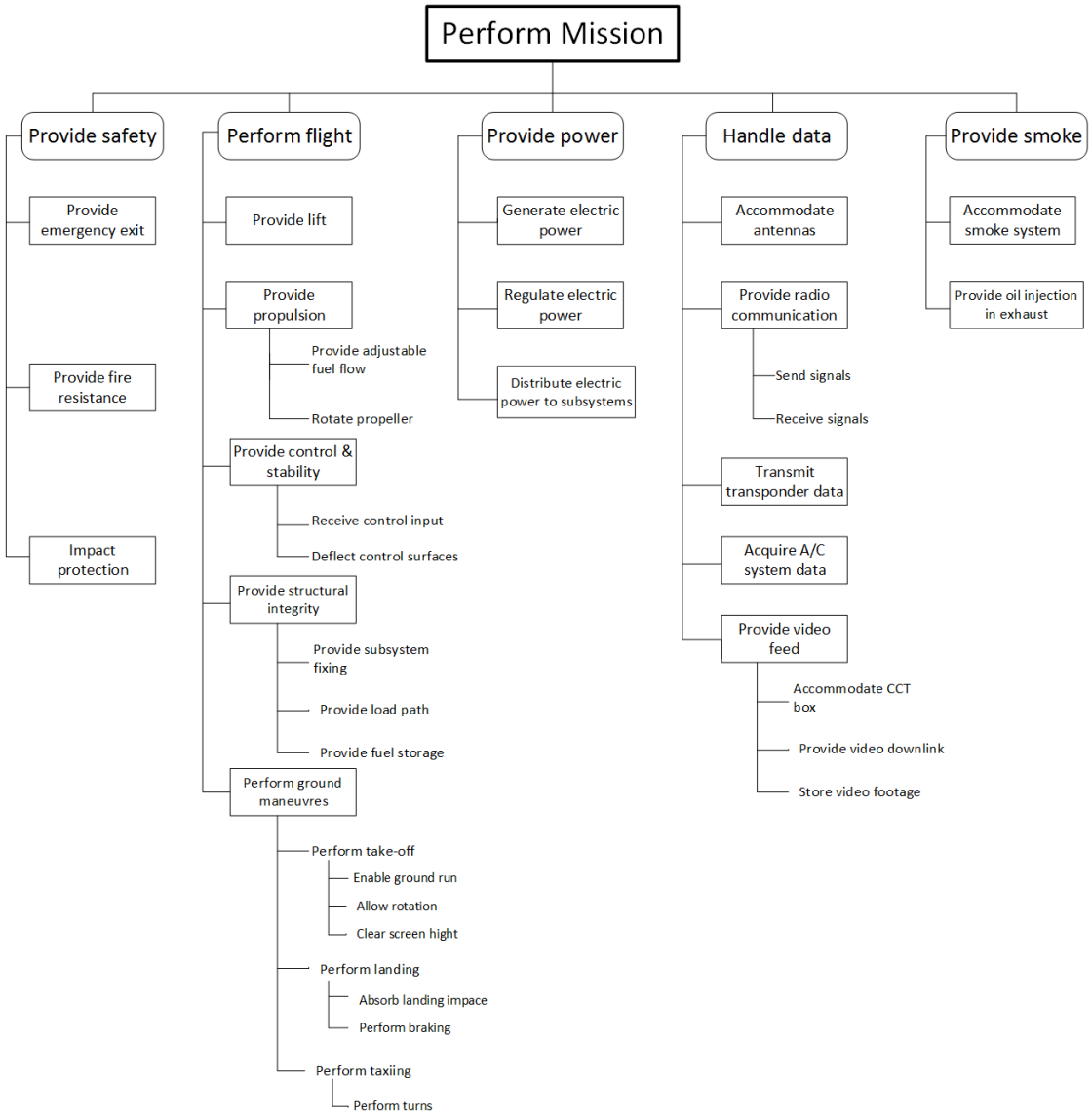

Figure 1.4: Functional breakdown structure

Chapter 2

Weight Estimation

In this chapter the weight estimation method is explained. This method is used to estimate the aircraft weights by using statistical computations based on the parameters of existing aircraft. By making these first weight estimations, it is possible to create a preliminary aircraft design, which is used for further detailed calculations. These detailed calculations are performed throughout Part II, analysing the aerodynamic, structural and flight performance. An aircraft consists of different subsystems, such as the fuselage, wing, tail and landing gear. All subsystems are interrelated, meaning that a change in wing size for example affects the size of the tail. Therefore an iterated design approach is necessary, repeating the design cycle until each subsystem is in harmony with the other subsystems. [18]

The general explanation of the weight estimation method is explained in Section 2.1, where the different classes of weight estimations are introduced. Sections 2.2 and 2.3 go into more detail on the Class I and Class II weight estimations respectively.

2.1 Weight Estimation Method Classes

The weight estimation of an aircraft is a statistical method used to estimate the aircraft weights at different phases of the design process. In general the weight estimation method can be divided into the following classes: [18]

- Class I
- Class II
- Class III
- Class IV

Figure 2.1 shows where each weight estimation class is located on the design time-line, according to basic Systems Engineering [18]. The process starts at early conceptual methods and concludes with the final design. The Class IV weight estimation lies outside of the design scope of the *T-16*, which is further enlightened in Section 2.1.

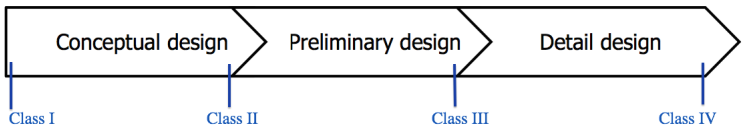

Figure 2.1: Weight estimation procedures indicated on design time line as defined by Torero.

The weight estimation method is furthermore graphically depicted in Figure 2.2, to indicate the relations between the different classes. It can be seen that after each class of weight estimations, the Empty Weight (EW) and Maximum Take-Off Weight (MTOW) are refined. The next sections explain Figure 2.2 in more detail, with respect to the inputs and outputs of the classes. The Class I, II, III and IV weight estimations are explained in Sections 2.1-2.1, respectively.

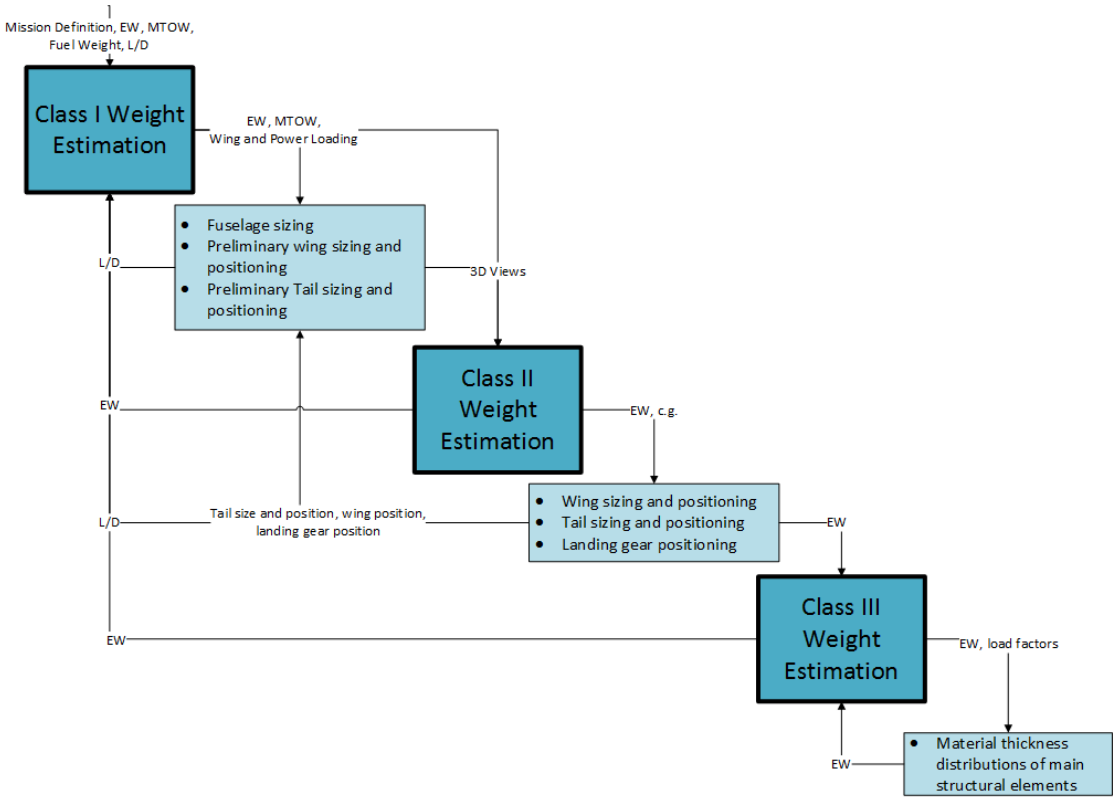

Figure 2.2: N^2-chart representation of the weight estimation method

Class I

The Class I weight estimation method serves as starting point in the conceptual design phase. At the beginning only the requirements are known. When designing an airliner, the method of fuel fractions is applied in the first weight estimation [18]. However, the purpose of the aerobatic racing aircraft does not lie in transporting as much payload as possible over a great distance. Its mission is to fly under high loads for a short period of time, meaning that the weight barely changes while completing the mission. Therefore the approach needs to be changed slightly. The inputs for the Class I weight estimation are:

- Mission description
- EW (minimum value as defined by *Red Bull Air Race*)
- Lift over drag ratio L/D (first assumption)
- Fuel weight (minimum value as defined by *Red Bull Air Race*)
- MTOW (assumed to be the minimum race weight as stated by *Red Bull Air Race*)
- Power (results in thrust)

The outputs are EW, MTOW, and the wing and power loading. These outputs are used to perform initial sizing of fuselage, wing and tail as well as the initial positioning of wing and tail.

Class II

The Class II weight estimation method concludes the conceptual design phase. The approach estimates the weight of each component group, still based on statistical data. Apart from an initial three-view drawing, the following criteria, outputs by Class I, serve as input:

- EW
- MTOW
- Wing loading
- Power loading
- Ultimate load factors (from requirements)
- Geometric parameters (span, sweep, chord, t/c, taper, surface area)

This class computes a new value for EW and gives a first estimate of the c.g. The wing and tail sizing and positioning is iterated. Additionally, an initial position for the landing gear is obtained.

Wing and tail size and position, as well as landing gear position, L/D ratio and EW are fed back to the Class I estimation to allow for iteration.

Class III

The Class III weight estimation stretches over the entire preliminary design phase. A fairly detailed model of the aircraft baseline is required at this stage, to compute the final material thickness distributions of the aircraft main components such as skin and stringers. The following items serve as input for the estimation:

- Fairly detailed model
- (Aerodynamic) load cases
- Material data and allowable
- Preliminary models of outer surfaces
- Preliminary thickness distributions
- Masses of non-structural items

The approach that is taken is based on analytical methods. The loads analyses and preliminary structural sizing yields a detailed and well-defined breakdown of the weight components including their c.g. locations at subsystem level. The outputs of this method are thickness distributions and the weight of the main structural elements, such as skin panels, spars, ribs and frames.

Class IV

The Class IV weight estimation is related to the detailed aircraft design phase. However, the design of the *T-16* developed by *Torero* ends with the preliminary design phase or Class III weight estimation, see Figure 2.1. Once the detailed design phase or Class IV method has is done, the aircraft is ready to be produced. This means that every part of the aircraft is fully analysed up until the rivets.

At this moment, the design team of *Torero* has finished the Class III weight estimation. This means that the *T-16* is about to be designed in full detail, however *FlashCo.* only requests a preliminary design of the *T-16*. Already some detailed structural calculations are made, but this is not iterated in the design yet.

2.2 Class I Weight Estimation

In the previous section the weight estimation methods used throughout the *T-16* design are described. This section goes into more detail on the methodology of the Class I weight estimation.

Normally the Class I weight estimation starts with computing the fuel mass fraction during cruise, which depends on the range of the aircraft [18]. However, since this is not applicable for aerobatic racing aircraft, the Class I weight estimation is slightly modified. The following procedure is executed:

1. Estimate EW and MTOW based on reference aircraft and *Red Bull Air Race* regulations, see Section 2.2.1
2. Determine wing and power loadings based on performance requirements, which can be found in Chapter 3, see Section 2.2.2 and 2.2.3.

2.2.1 Initial Aircraft Weights

To start initialising the aircraft weights, the requirements defined by *Red Bull* are analysed, since these already define the minimum EW and MTOW. The restrictions on the aircraft weights imposed by *Red Bull Air Race* regulations are given in Table 2.1 [16].
To come up with an optimum design that performs the best in the *Red Bull Air Race*, *Torero* designs the *T-16* as light as possible. Therefore, it is decided to design the *T-16* as close to the minimum race weights defined by *Red Bull Air Race* Regulations [16]:

- EW = 540 kg
- MTOW = 698 kg

If the aircraft design of *Torero* is lighter than the minimum required weight defined by *Red Bull*, additional ballast weights should be added. This can be beneficial since this makes a shift of the c.g. of the aircraft possible, increasing the manoeuvrability.

Table 2.1: Regulations on aircraft weights according to Red Bull Air Race

Item	**Mass** *[kg]*
Aircraft empty weight	540.0
50 litres of fuel	36.0
Pilot	82.0
Telemetry	15.3
Cameras and camera control system / EFIS	1.5
G-Race Suit or G-Race-Suit Penalty Weight	6.5
Helmet and parachute	15.7
Total	698.0

2.2.2 Wing and Power Loadings

The next step in the Class I weight estimation is the determination of the wing and power loadings. These are the ratios between the aircraft weight W, wing surface area S and propulsion power P. If the wing and power loadings are computed, an estimation of S is determined. This is done by using the MTOW, which is already determined by the regulations. Defining the design wing and power loading is done using a wing and power loading diagram.

The wing and power diagram is a graph which contains the limitations on the wing and power loading W/S and W/P, based on performance requirements defined by CS-23 and the *Red Bull Air Race* regulations, see Chapter 3. The optimum design point of the wing and power loading diagram is determined by the limitations based on the following methods:

Sizing for:

- Stall Speed
- Take-Off
- Landing
- Climb Rate
- Climb Gradient
- Maximum Load Factor
- Optimum power loading

It is desirable to have a high W/S as possible. For a given aircraft weight the wing surface area S should be at a minimum, because a small wing is lighter than a large wing. This saves wing weight, cost and drag. The power-to-weight ratio for aerobatic racing aircraft should be as high as possible, which corresponds to a minimum W/P. This follows from the aircraft weight that should always be minimised, while the available power should be maximised. This results in maximum power to weight ratio which corresponds to a minimum W/P-ratio. The detailed explanation of the construction of the wing and power loading diagram, based on the different sizing limitations, can be found in the Mid-Term Report of *Torero* [19]. [18]

2.2.3 Wing and Power Loading Diagram

By combining all calculations and restrictions, the final wing and power loading diagram is constructed, see Figure 2.3. The variables in this graph are the maximum lift coefficient $C_{L_{max}}$ and the aspect ratio A. The lift coefficient is optimised by the Aerodynamics department of *Torero*, which is explained in Section 5.3. The aspect ratio is optimised by first assuming a value for A, which results in a value of S. With this value of S and the wingspan limitation of $b = 7.6\,m$ defined by *Red Bull* [16] a new value for A is computed, which is iterated in the wing and power loading diagram, until the inputs and output aspect ratios for the diagram are within 5% difference. The optimum power loading is based on the available engine power of the *Lycoming Thunderbolt AEIO-540 D*, which has an engine power of $P_e = 315\,hp = 235\,kW$. According to *Red Bull Air Race* regulations, this engine should be used. [16] This is further elaborated in Section 3.

The iterated values of the wing and power loading diagram are:

- $\left(\frac{W}{S}\right)_{max} = 926\,N/m^2 = 94.4\,kg/m^2$
- $\left(\frac{W}{P}\right)_{opt} = 0.036\,N/W = 3.66\,kg/kW$

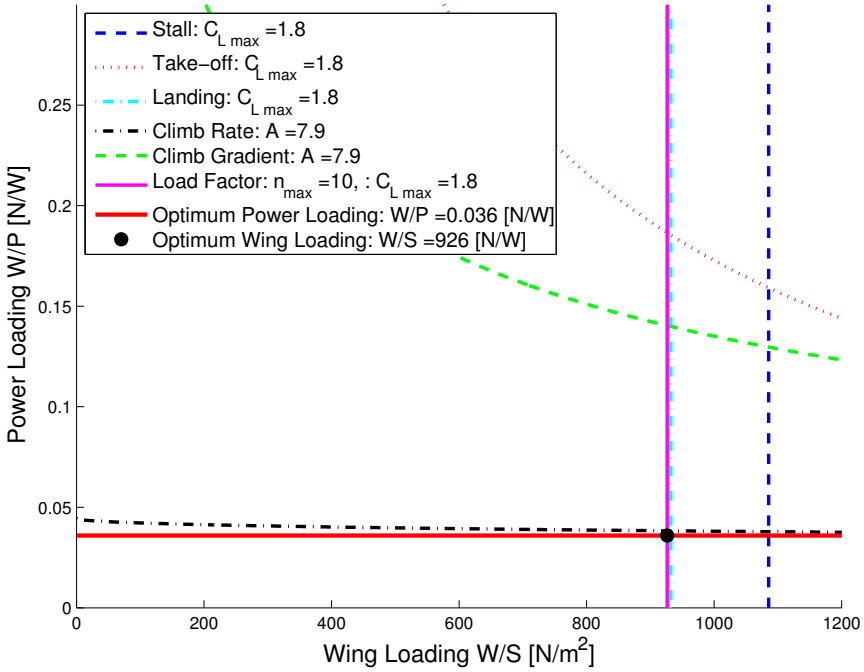

Figure 2.3: Wing and Power Loading Diagram

Comparing these results with the reference aircraft, see Appendix A, it is concluded that the wing loading of the *T-16* is higher and therefore better than the wing loadings of the reference aircraft. The power loading can not further be optimised, since this value is computed with the minimum race weight and propulsion system defined by *Red Bull*.

2.3 Class II Weight Estimation

The previous section concludes the Class I weight estimation by giving EW, MTOW, W/S and W/P of the aircraft. The Class II weight estimation continues with a more detailed weight estimation, based on the weights and c.g. locations of the main aircraft components. The main aircraft components are:

- Wing
- Empennage
- Fuselage
- Engine
- Landing Gear
- Control Surfaces
- Instruments

The following procedure is executed for the Class II weight estimation:

1. Determine main aircraft component weights, see Section 2.3.1
2. Determine c.g. position of each component, see Section 2.3.2

The procedure behind finding the weights is based on the statistical method described by Torenbeek [20]. This method uses statistical equations based on the geometrical parameters and locations of the aircraft main components, to compute the corresponding weights and c.g. locations. This section gives the result of the Class II weight estimation. The full explanation of this method can be found in the Mid-Term report of *Torero* [19].

2.3.1 Aircraft Component Weights

At first, the component weights are estimated with the Torenbeek weight estimation method [20]. However, during the preliminary design phase certain systems such as the wing, empennage and fuselage, are designed in great detail which made it possible to directly compute the subsystem weight with the dimensions and material properties. These detailed weight estimations are compared to the Torenbeek estimations, to check if the new values differ significantly. Table 2.3.1 presents the component weights and how these progress through the many iterations of the aircraft weight estimation method. Corresponding pie charts of these component weights are found in Figures 2.4 to 2.5b.

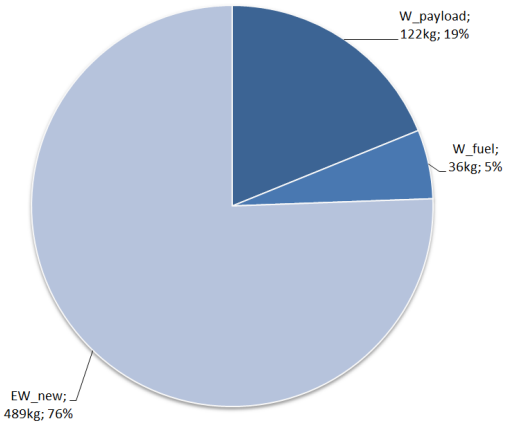

Figure 2.4: Representation of main aircraft weights as fractions of the MTOW, based on the Class I weight estimation [kg]

Weight group	**Class I** *[kg]*	**Class II** *[kg]*	**Detailed** *[kg]*
W_{wing}		53	95
$W_{empennage}$		12	20
$W_{fuselage}$		280	97
W_{engine}		200	235
$W_{landing\ gear}$		24	24
$W_{control\ surfaces}$		14	14
$W_{instruments}$		4	4
EW_{zero} *ballast*			*489*
$W_{ballast}$		0	51
EW	**540**	**588**	**540**
$W_{payload}$	122	122	122
W_{fuel}	36	36	36
MTOW	**698**	**746**	**698**

Table 2.2: Component Weights

The final weight computation results in EW = 489 kg and MTOW = 647 kg. Since these values are below the minimum race weights defined by *Red Bull*, additional ballast weight must be positioned in the aircraft to participate in the race. With $W_{ballast} = 51\ kg$ the empty race weight of the *T-16* is 540 kg, which allows the aircraft to race the *Red Bull Air Race*.

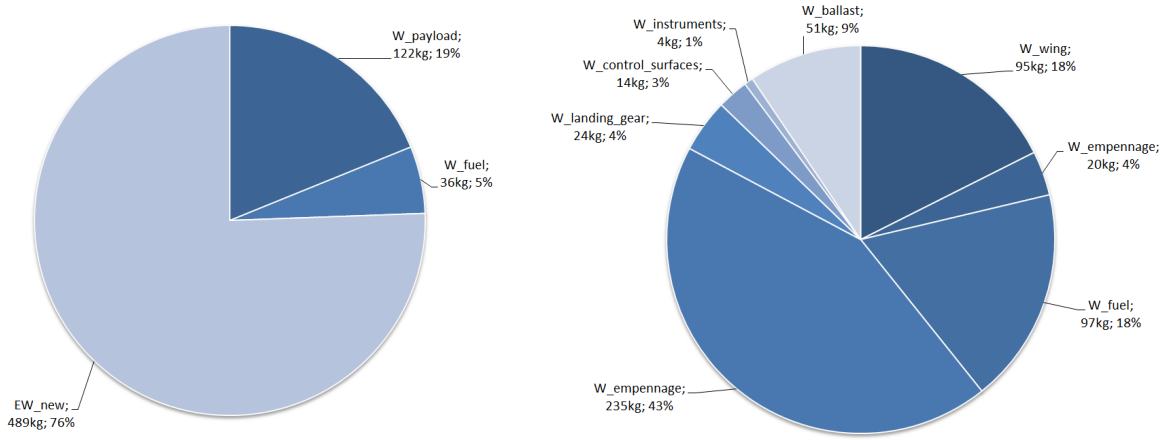

(a) Aircraft weights as fractions of MTOW [kg] *(b) Component weights as fractions of EW [kg]*

Figure 2.5: Pie chart representations of the aircraft weights, based on the class II weight estimation

The significant decrease in weight for the fuselage, see Table 2.3.1, is due to the material choice and the fact that Torenbeek does not estimate the fuselage weight for aerobatic racing aircraft, but for general aviation. The light truss structure in combination with the carbon fibre skin results in a very light fuselage. Furthermore, the weight of the propulsion system increases, since it includes the engine mounting and propeller weight. The engine itself weighs 200 kg, to which the weight of three carbon fibre propeller blades, variable pitching system and an engine mounting truss is added. The total propulsion weight therefore, is $W_e = 235\ kg$.

2.3.2 Centres of Gravity

Torenbeek also describes a statistical procedure to estimate the c.g. locations of the main aircraft components. The longitudinal center of gravity locations, measured from the nose of the aircraft, are: [20]

- $x_{cg_{wing}}$ is located at 40% from the root chord length, measured from the Leading Edge (LE) of the wing.
- $x_{cg_{tail}}$ is located at 42% from the root chord length of the horizontal stabiliser, measured from the LE.
- $x_{cg_{fuselage}}$ is located at 35% of the fuselage length.
- $x_{cg_{engine}}$ is located at 5% of the fuselage length. A factor of 0.05 is assumed, since the engine is in front of the aircraft a small value for the c.g. of the engine is valid.
- $x_{cg_{control\ surfaces}}$ is located at Trailing Edge (TE) of Mean Aerodynamic Chord (MAC).
- $x_{cg_{landinggear}}$ is located at the center of gravity of the zero ballast Empty Weight $EW_{zero\ ballast}$.
- $x_{cg_{ballast}}$ is located at 80% of the fuselage length. Ballast should be in the back of the aircraft to increase manoeuvrability, see explanation in Chapter 7.

The resulting c.g. location of the EW of the aircraft is computed using Equation (2.1), which corresponds to the summation of the main aircraft component weights multiplied by that corresponding c.g. locations, divided by the sum of the aircraft main component weights, which is equal to EW.

$$x_{cg_{EW}} = \frac{\sum_{i=1}^{n} W_i \cdot x_{cg_i}}{EW} \tag{2.1}$$

The c.g. locations of the payload and fuel, assumed by *Torero* based on reference aircraft, are:

- $x_{cg_{pl}}$ is at TE of wing
- $x_{cg_{fuel}} = 0.2 \cdot l_f$ Fuel lies between engine and cockpit

By dividing the c.g. locations of the components either by fuselage length l_f or MAC, the c.g. shift can be graphically represented in a c.g. shift diagram, presented in Figures 2.6a and 2.6b, respectively. Figures 2.6b is later used for the scissor plot of the Control & Simulation department, see Section 7.1.

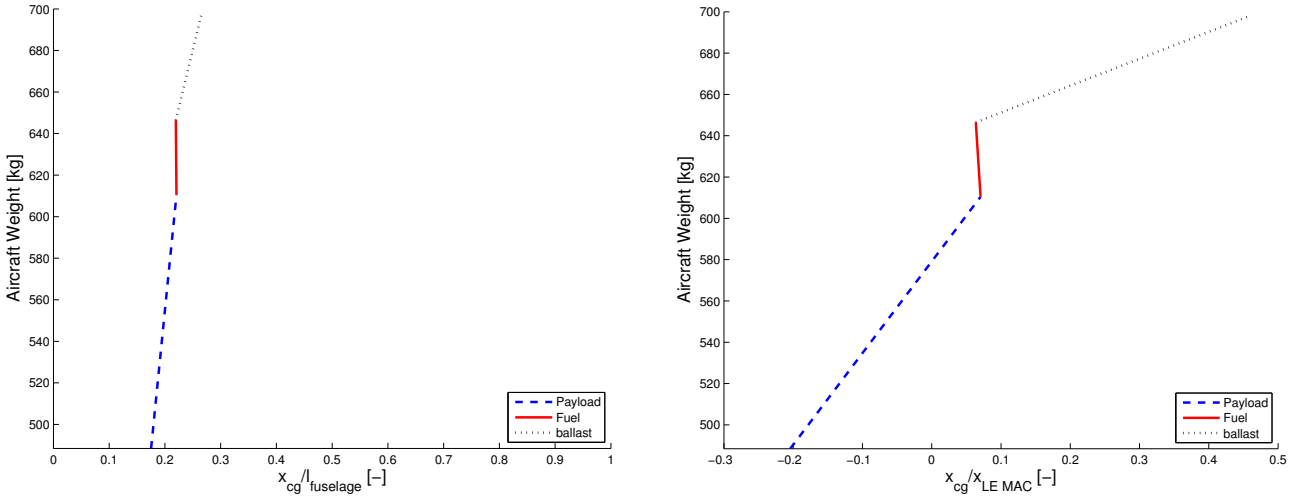

(a) C.g. shift w.r.t fuselage

(b) C.g. shift w.r.t. MAC

Figure 2.6: C.g. range diagrams

In the figures it can be seen how the additional ballast weight affects the c.g. of the aircraft. In Chapter 7 it is explained why it is beneficial to have the c.g. located more to the back of the aircraft.

Chapter 3

Propulsion

This chapter presents the propulsion system of the *T-16*. The propulsion system consists of the engine, propeller blades, variable pitch mechanism, smoke system and engine mounting. The entire propulsion system except for the engine mounting is completely fixed by *Red Bull Air Race* regulations [16]. An overview of these defined subsystems is given in Section 3.1. Since this propulsion system is not completely optimised for the post-mission phase, possible modifications of the propulsion system are given in Section 3.2. Finally in Section 3.3 the engine mounting design is presented.

3.1 Propulsion System

The engine, propeller and fuel type are determined by the *Red Bull Air Race* regulations. Teams are not allowed to modify the system to improve engine performance. This means that all aircraft flying in the *Red Bull Air Race* have the same available power.

The engine which is used during the race, is the *Lycoming Thunderbolt AEIO-540-D*. This engine has an engine power of $P_e = 315\,hp = 235\,kW$, a rotational rate of 2700 rpm, and a weight of 200 kg [16]. The propeller is a *Hartzell 3-bladed 7690* structural composite propeller, which is supplied by *Red Bull*. Based on the technical specifications provided by *Hartzell*, it is assumed that the propeller has an maximum efficiency of $\eta_p = 0.8$ [21]. The fuel used during the race is *Aviation Gasoline 100LL* in accordance with standards of ASTM D 910 [16]

The available power of the propulsion system is computed by Equation (3.1), which gives $P_a = 188\,kW$.

$$P_a = P_e \cdot \eta_p \tag{3.1}$$

While in flight, the power of the aircraft is regulated by means of a variable propeller pitch system. By controlling the pitch angle of the propeller blades with respect to the airflow, the total available propulsion power can be adjusted. At maximum power available, the pitch angle is optimal so the propeller efficiency is assumed to be $\eta_p = 0.8$. Research should be performed to investigate the relation between propeller efficiency and the propeller pitch angle. Additionally extensive Computational Fluid Dynamics (CFD) analysis could be performed during the post DSE phase to validate this relation.

During the race, the aircraft should be equipped with a *Sky Dynamics* 6 to 1 standard exhaust system [16]. All participating racing aircraft should have a system installed to produce a trail of smoke behind the aircraft at every moment during the race. This system can only be based on injecting oil into the exhaust. To fulfil requirement FARA-Sys-Smo-01 from Section 3.2 in Part III, an option is to install the *SA-100 series* 3.5 gallons kit that injects three litres of oil per minute into the exhaust and can produce smoke for a duration of five minutes [22].

3.2 Post-Mission Engine Modifications

An opportunity to increase sustainability of the aircraft after the *Red Bull Air Race*, is to modify the engine to better suit the intended purpose during the post-mission phase. Potential modifications

to the propulsion system are:

- Switch to engine with less horsepower that is sufficient for commercial use to decrease fuel consumption. This is elaborated on in Part III Section 2.1
- Use fuel with less lead content, to decrease environmental pollution. This is discussed in Part III Section 2.1.
- Add diffuser or muffler to decrease noise produced by engine
- Use different propeller to reduce noise

Multiple recommendations can be given to optimise the performance of the *Lycoming Thunderbolt AEIO-540 D*. Additionally, efficiency can be improved which benefits sustainability. Several options are [23–25]:

- Add ram air valve to increase pressure of the air before it enters the engine (to increase engine efficiency)
- Implement electronic fuel injection system (to increase efficiency and the engine power)
- Increase piston size (to increase compression ratio)
- Use an electronically timed ignition system (to improve ignition timing and therefore engine power)
- Integrate the exhaust system with engine cooling air (to reduce air intake size and therefore aircraft drag)

3.3 Engine Mounting

The structure that attaches the piston engine to the fuselage section is referred to as the engine mounting. This structure consists multiple members that carry the engine weight even at high loads that occur during manoeuvres. The design of the engine mount structure is discussed in this section.

For ease of manufacturing and for reasons that have been stated in the fuselage material selection in Section 4.1, the material selected for the tubes is ASTM A514 steel alloy. For designing the engine mount, an approach similar to the fuselage frame design is taken that is described in Section 4.1. First of all the constraints on the structure implied by the fuselage frame and the engine suspension structure are determined. The engine mount structure is given in Figure 3.1a where every member is given a number to identify it. After fixing the geometrical parameters, the load acting on the structure is considered. The engine weight is estimated to be 200 kg in Section 2.3.1. The maximum load factor the engine mount is designed for is 15g which includes a safety factor of 1.5. This is equal to the load factor the fuselage structure is designed for. Additionally a safety factor of 1.3 is applied to account for variations in welding quality such that $\sigma = 450\ MPa$. The resulting load acting on the engine mount is determined by Equation (3.2) and acts in either positive or negative direction depending on the direction of the turn. Now using *MatrixFrame* that is used to design the fuselage structure, the compressive or tensile loads acting on the members are analysed. These loads are consequently converted to stresses using Equation (4.2). Also the buckling load each member is limited to is calculated using Equation (4.4). The diameter and thickness of each member is adjusted to the critical failure case being either buckling or material deformation. Finally the iteration is brought to a stop if the margin of safety is in between 0 and 0.10. An impression of the assembly of the engine, engine mount and fuselage is presented in Figure 3.1b, where the engine mount is highlighted.

$$P_{engine} = W_e \cdot g \cdot 15 = 29.43\ kN \tag{3.2}$$

Table 3.1: Design of steel tubes for engine mount structure

Member #	Force [kN]	Length [mm]	Diameter [mm]	Thickness [mm]	Mass [kg]	Margin of safety [-]
1,2	39.1	469	25	2	0.53	0.06
3,4	7.28	551	16.5	1.5	0.31	0.01
5,6	26.0	368	22	1.5	0.28	0.08
7,8	4.69	410	13.5	1.5	0.18	0.09
9,10	13.0	360	17.5	1.5	0.21	0.05
Total mass					**3.02**	

The entire engine mount consists of the tubular frame structure and assembly elements, such as attachment surfaces to bolt the engine mount to the fuselage frame, shock absorbing elements and weld material. With the tubular frame weighing approximately 3.0 kg and a margin of 3 kg for assembly elements, the total weight is 6 kg.

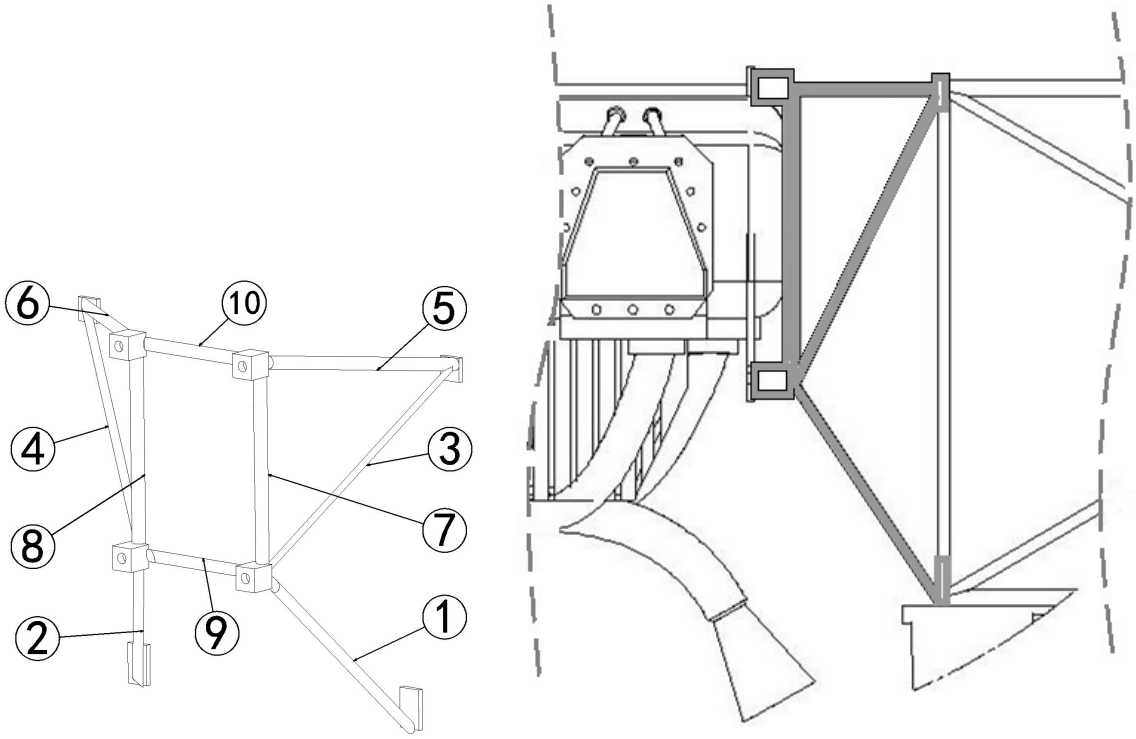

(a) Engine mount isometric drawing *(b) Installation of engine mount*

Figure 3.1: Engine Mounting

From the previously presented sections, the complete propulsion system is estimated to weigh $W_e = 235\,kg$, corresponding to the Class II weight estimation in Section 2.3.1. From this total weight, the engine is 200 kg, the truss mounting including shock absorbers is 6 kg and the remaining 29 kg is reserved for the exhaust system and propeller system.

Chapter 4

Fuselage

After the selection of the propulsion system, the next step is to design the subsystem into which this propulsion system is integrated, namely the fuselage. Besides accommodating the other subsystems and thereby serving as a central link, it shall also be designed in a way to keep the pilot safe in case of an emergency situation. In the Mid-Term Report of *Torero* [19] trade-off leads to the decision to use a truss structure covered by a fuselage skin. In the following sections the truss structure is developed that takes up all structural loads that act on the aircraft. Integration of the landing gear and the main wing are determined. Subsequently, the optimal shape of the outer surface is elaborated on. Also taking the aerodynamic aspects into account, the fuselage skin is designed and implemented. To finalise the fuselage subsystem, a preliminary design of the firewall is presented. This chapter ends with recommendations to design the fuselage structure in greater detail.

4.1 Truss Structure

Just as any other subsystem the fuselage needs to be designed to withstand a loading of 15g including the safety factor of 1.5, as explained in 1.3 in Part I. To come up with an optimum truss structure, it is crucial to identify the critical loads and their locations.

4.1.1 Load Determination

In the very first instant of a manoeuvre the aircraft is still assumed to be in equilibrium. The challenge is to idealise and rearrange the applied forces in a way such that all sums of forces and moments are zero. This is also crucial for modelling the truss structure into a program, since a structure always needs to be constrained by supports to prevent it from 'floating around in space'. For this it is necessary that these supports are imaginary and do not have any reaction forces to keep the structure in equilibrium. Three different load cases need to be considered, for which slightly simplified models are created:

1. Bending about pitch axis
2. Bending about yaw axis
3. Torsion about roll axis

Load Case 1 - Bending about pitch axis

The bending about the pitch axis is approached by splitting up the aircraft into different sections. Figure 4.1 illustrates the forces that act on the fuselage in the vertical plane, whereas Table 4.1 indicates at what exact location they act and what magnitude they are of. Each part is stated, including its mass and the distance from the c.g., which is for simplicity assumed to be at the quarter chord location of the wing. By assuming so, the lift due to main wing has no impact on the moment. The force stated is computed by multiplying the mass by 15 times the gravitational acceleration. This value is then divided by two, since each side of the truss takes up an equal share of the loads. Bending around the pitch axis has the biggest affect on the design of the side segments of the truss.

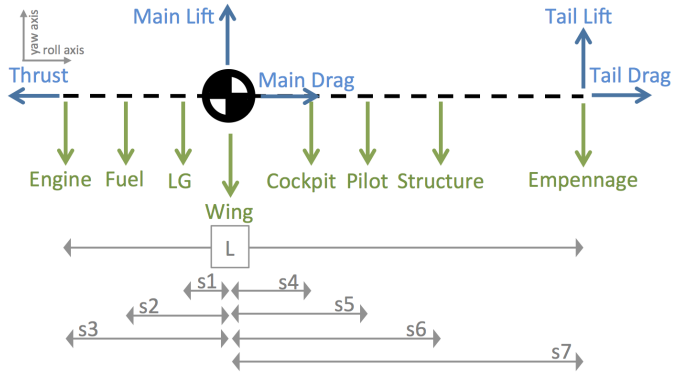

Figure 4.1: Forces acting on aircraft leading to a bending around the pitch axis

Part	Mass [kg]	Distance [m]	Force [kN]
Engine	234	-0.6 (s3)	-17.5
Fuel	40	0 (s2)	-3
Landing Gear	30	0 (s1)	-2.25
Wing	144	0	-10.8
Cockpit	100	1.4 (s5)	-7.5
Pilot	77	2.18 (s6)	-5.8
Structural	40	2.96 (s7)	-3
Empennage	35	4.4 (s8)	-2.6
Tail Lift	100	4.4 (s8)	7.5
Wing Lift	600	0	45

Table 4.1: Idealised forces with distance acting on aircraft (Load factor 15)

Load Case 2 - Bending about yaw axis

For the second load case a sketch is created in Figure 4.2, showing the forces that act on the structure that lead to bending about the yaw axis. In this particular case, it is assumed that the fuselage is clamped all the way in the front. The only force acting on the structure is due to the rudder. The magnitude of the maximum rudder force is assumed to be $F_{Rudder} = 2\ kN$ at a distance of 6 m. Note that this value is slightly higher than in reality. Bending around the yaw axis determines the thickness of the four main tubes upper and lower truss structure in the horizontal plane.

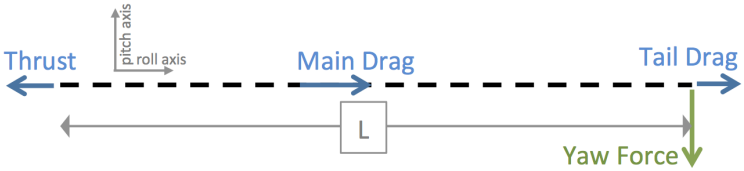

Figure 4.2: Rudder acting on aircraft leading to a bending around the yaw axis

Load Case 3 - Torsion about roll axis

The third load case deals with torsion induced by the engine torque as well as the rudder force, due to the offset between the c.c. and the point of application of the rudder force. Figure 4.3 illustrates where the torsion is introduced. This simplified model considers the truss to be supported at the location of the wing, since the wing always stays level by counteracting the moment. Hence M_{Engine} and M_{Rudder} are only dealt with by the truss over distance $s1$ and $s2$, respectively. Some members in the upper and lower horizontal plane are necessary to shape the fuselage as required and to serve as points for attachment. To fulfil the torsion criteria these segments need to be sized properly and more segments might need to be added. To calculate the torque that the engine is able to produce, Equation 4.1 [26] is used. This equation represents the relation between the engine torque T_e, engine horse power P_4 and rotational velocity in rounds per minute rpm.

$$T_e[ft \cdot lb] = \frac{P_e[hp]}{rpm} \cdot 5252 = \frac{315}{2700} \cdot 5252 = 613[ft \cdot lb] \approx 831[Nm] \tag{4.1}$$

This yields a maximum torque of $M_{Engine} = 831\ Nm$ for the first section. In section 2 the rudder exerts a force of 2 kN at a distance of 1 m, yielding yielding a rudder moment of $M_{Rudder} = 2\ kNm$.

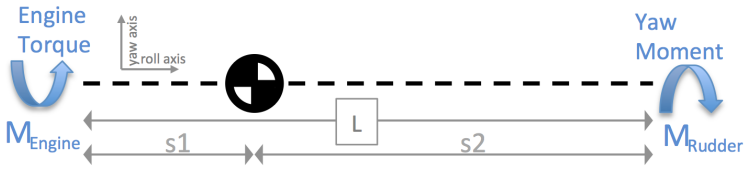

Figure 4.3: Torsion in truss induced by engine torque and rudder force

4.1.2 Sizing Methodology

Now that the loads are known, the main structure that holds the whole aircraft in place can be developed. The fuselage already has minimum width, height and length constraints. The engine and therefore, the required minimum width and height up front are known. The cabin needs to offer sufficient room to accommodate the pilot, constraining the minimum width and height at cockpit location. At the locations where subsystems such as wing, landing gear and empennage are attached, structural reinforcements are required to be able to withstand the loads acting at the certain locations. Other truss members are added based on trial and error and reference aircraft. The structure is modelled into *MatrixFrame* [27] a program calculating the resulting tension or compression forces in each member of a 2D structure. By inserting additional truss members and changing the location of others, the internal forces are decreased.

Based on the force F in each segment at the highest load case of 15g, the size of each segment can be computed. Two conditions must be fulfilled; neither shall the normal yield stress in any member be exceeded, nor shall any member buckle.

Normal Stress

The normal stress σ is determined using the basic relation stated in Equation (4.2). Where F is the applied force on a certain surface area A.

$$\sigma = \frac{F}{A} \tag{4.2}$$

As already determined in the Mid-Term Report [19], the material is chosen to be *ASTM A514 Steel*, which has a yield stress of $\sigma_{yield} = 600\ MPa$. Applying a safety factor of 1.3 the assumed yield stress is $\sigma_{yield} = 450\ MPa$. This safety factor takes into account that the material may not have uniform properties at every point in the structure due to variations in welding quality. Therefore, the required area A_{req} for each segment can be computed. Taking a general wall thickness of $t = 2\ mm$ the diameter d of each tube can be calculated, using the following simple, geometric relations:

$$d = \frac{A_{req}}{t \cdot \pi} + t \tag{4.3}$$

Buckling criterion

The critical load P_{cr} that a beam can handle without a buckling failure is determined using Equation (4.4)

$$P_{cr} = \frac{\pi^2 E \cdot I}{L^2} \tag{4.4}$$

where E is the Young's Modulus, I is the Moment of Inertia and L the length of the certain segment.

Truss Side Segments

First *Load Case 1* is considered. Thereafter it is evaluated whether the sizing is also sufficient to withstand *Load Case 2*. The normal stress calculation defines the required values for diameter and thickness, with which the moment of inertia of each segment can be calculated. Then length, Young's Modulus and moment of inertia are known, leading to to a value of the critical load, P_{cr}, at which each segment starts to buckle. Subsequently, P_{cr} of each segment is compared to the load F, that each segment is experiencing, to find out if all segments fulfil both the normal stress as well as the buckling criteria, which might not be the case for any segment.

Since sizing for the normal stress criteria does not fulfil the buckling criteria, the diameter of each segment needs to be increased, such that it can withstand the force without buckling. This is done manually by increasing the diameter and keeping the thickness unchanged, so that for each segment P_{cr} is higher or equal to the applied force F.

After the required diameter and thickness for *Load Case 1* are determined, it needs to be confirmed that this is also true for *Load Case 2*. The moment, along the length L of the fuselage truss, can be determined with Equation 4.5.

$$M_x = F_{Rudder} \cdot (L - x) \tag{4.5}$$

Where M_x is the moment at an arbitrary point along the fuselage length and x is the distance from the beginning of the truss at the side of the engine. By slightly simplifying the model, it is assumed that bending only transforms into a compression and tension force in the four outer tubes. Since in reality the bending is partially also compensated by a few other members, this approach may lead to an over design. The normal stress in the four outer members due to the bending about the yaw axis can be determined using Equation 4.6,

$$\sigma = \frac{M_x y}{I} \tag{4.6}$$

where y is the distance from the neutral axis, hence half the fuselage width at location x and I the moment of inertia of the truss at location x. The moment M_x has the highest value at $x = 0$, however, since the y and I change along x three locations are investigated; $x = 0$, $x = L/3$ and $x = 2L/3$. The normal stress values at the certain locations do not exceed the normal yield stress of the material. Therefore both bending criteria about the pitch axis and yaw axis are fulfilled.

Table 4.2: Normal stress in outer tubes due to bending about yaw axis

Location	$\mathbf{M_x}$ *[kNm]*	$\mathbf{\bar{y}_{max}}$ *[m]*	**I** *[m^4]*	σ *[MPa]*
x=0	12	0.45	5E-5	106
x=L/3	8	0.35	3E-5	90
x=2L/3	4	0.15	6E-6	106

Figure 4.4 illustrates the layout of each truss segment. Note that the wing reinforcement is not elaborated on at this point, but rather in Section 4.1.3. Table 4.3 shows the corresponding length and maximum force it has to handle. In addition it shows the diameter and thickness required to fulfil both the normal stress and buckling criterion, which are the design parameters. The critical buckling load P_{cr} is also presented.

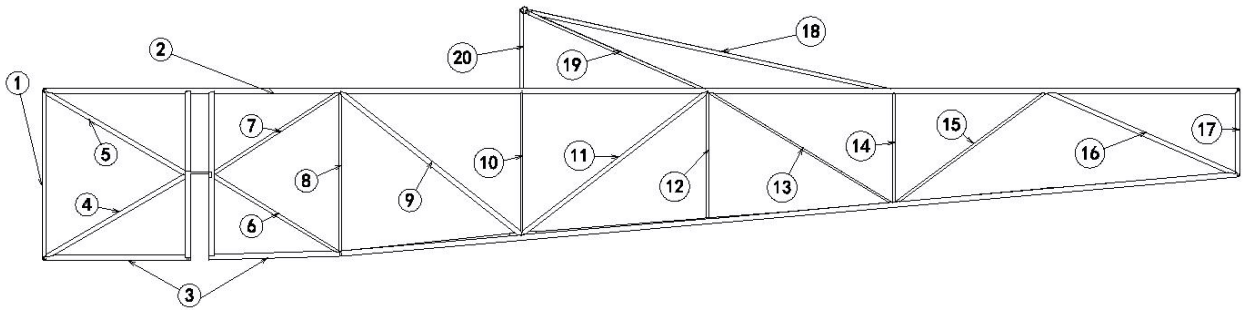

Figure 4.4: Side view of the fuselage truss structure

Table 4.3: Truss member properties, including force, length, critical buckling load and final diameter and thickness

#	Length *[m]*	Force *[kN]*	P_{cr} *[kN]*	Diameter *[mm]*	Thickness *[mm]*	#	Length *[m]*	Force *[kN]*	P_{cr} *[kN]*	Diameter *[mm]*	Thickness *[mm]*
1	0.7	8.33	9.08	16	2	10	0.6	0	1.63	10	1
2	5	18.6	20.6	22	2	11	0.98	10.9	13.3	22	2
3	5	18	18.4	22	2	12	0.48	6.27	7.17	12	2
4	0.69	18.3	19.4	20	2	13	0.91	0.93	1.04	10	2
5	0.69	16.5	19.4	20	2	14	0.38	0	4.05	10	1
6	0.72	11.6	12.7	18	2	15	0.74	6.42	8.12	16	2
7	0.72	11.6	12.7	18	2	16	0.82	13.4	13.9	20	2
8	0.67	5.34	6.29	14	2	17	0.2	4.88	14.6	10	1
9	1	17.61	2.12	26	2						

Note that truss segments 10 and 14 are identified as zero force members when considering only loads in the vertical plane and therefore bending around the pitch axis. However, they are necessary for structural integrity when considering torsion, to serve as a point of connection for other subsystems and to guarantee the pilot's safety during an unfortunate event. This is also the purpose of tubes 18, 19 and 20, which keep the pilot from being harmed in a tip over situation. These members are of minimum diameter and thickness. It is decided to make no tube smaller than 10 mm in diameter and 1 mm in thickness, for ease of manufacturing, as well as considering different types of loads the structure could suffer from. One should also consider that welding can be performed much better if the thicknesses are in a similar range of diameter. Also, the four corner tubes are of the same diameter and thickness throughout the whole length of the fuselage. This adds around 2 kg of mass, but further increases the strength and safety by having less welding spots and simplifies the manufacturing process. Herewith, the truss side part design is concluded and attention is shifted to the top and bottom of the truss.

Top and bottom segments

The purpose of segments in the horizontal plane at top and bottom is to withstand the torsion introduced by *Load Case 3*. Additional points of consideration are guaranteeing the safety of the pilot during an unforeseen event and the necessity for attachment at some points, such as the landing gear, the cockpit, partially for the wing integration, and the empennage. Therefore many segments need to be integrated, even though they might not event be required to support the structure. Figure 4.5 illustrates the segments in the horizontal top and bottom plane that are required.

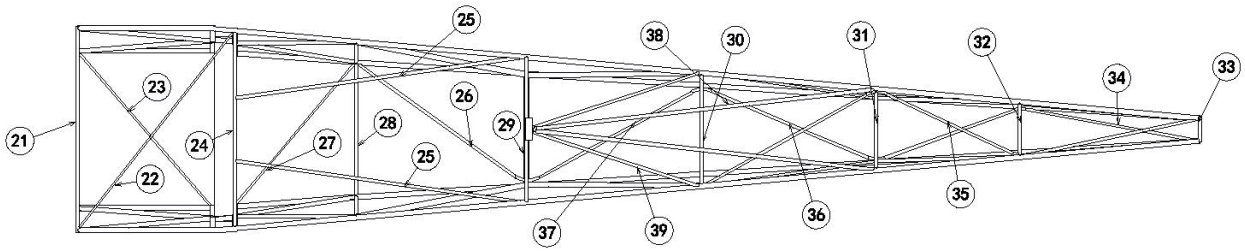

Figure 4.5: Top view of the fuselage truss structure

Again, similar to the simplification of the model for *Load Case 1*, assumptions are made. Instead of calculating the torsional properties of a truss, a thin-walled rectangular box is used, which has the same volume of material as the truss has. To validate the torsional rigidity, the same method that is developed to do the wing box calculations in Section 5.6 is used. The main wing is assumed to act in the way a fixed support would act, since it counteracts the induced torques. Therefore, two sections need to be considered, from the front to the wing connection and from the wing connection all the way to the end. Since tubes are decided to not have a diameter and thickness smaller than 10 mm and 1 mm, respectively, it needs to be evaluated whether this already fulfils the torsion criteria.

For stability purposes and to prevent the fuselage skin from buckling, the front section shall not twist more than 0.5° and the aft section shall not exceed a twist angle of 1°. Calculation shows that the first section twists no more than 0.2°, whereas the back section does not exceed a twist of 0.8°. Therefore it is not necessary to further strengthen neither the top, nor the bottom segments.

4.1.3 Fuselage to Wing Connection

The following Section elaborates on how the wing is connected to the fuselage. Note that a connection system is designed that fulfils the requirement of being able to detach the wing on a regular basis for means of transport. As determined in Chapter 5 the wing is a coherent part, hence both wing sides cannot be disconnected from each other. However, only the main spar is continuous. The wing is attached to the fuselage by sliding it in from the bottom. Figure 4.6 illustrates how the mounting structure.

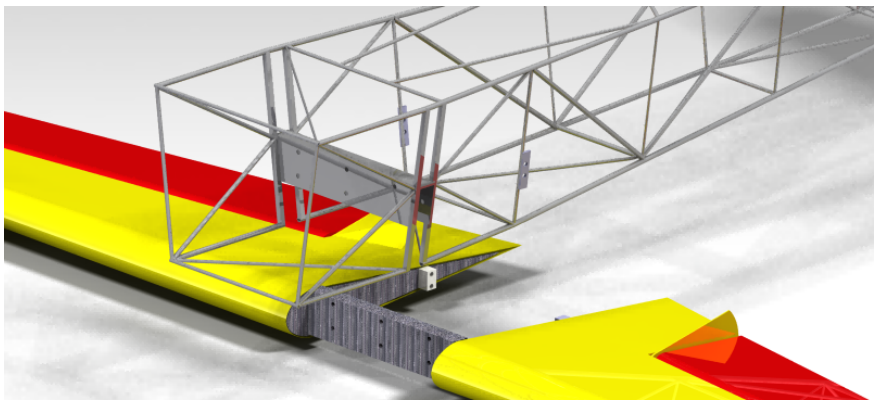

Figure 4.6: Illustration of wing mounting strucutre. The wing slides into the fuselage and is connected with bolds. The back spar is also connected to the fuselage with bolts.

The structure is strengthened to guarantee that the loads are transferred from the wing to the fuselage seamlessly. Two aluminium plates are integrated into the fuselage. The way that the wing main spar slides in between these plates. This serves the purpose that the the wing spar can easily be bolted to the fuselage. In addition to the wing main spar, also the more aft wing spar is bolted to the fuselage truss. Figure 4.6 illustrates how this connection is realised.

4.1.4 Fuselage to Landing Gear Connection

The landing gear connection is rather simple and discussed in great detail in Chapter 8.6. This section only deals with preparing the fuselage structure in a way that the landing gear can be connected to it. For this purpose it is sufficient to mount a rectangular member at the location where the landing gear is connected. This location is determined in Section 2.3. An illustration is given in Figure 8.3b.

4.1.5 Firewall

It is crucial that the safety of the pilot during flight is guaranteed and all safety requirements are met. Because the probability exists the engine catches fire as long as it is running, measures shall be taken to make sure that the fire does not spread to the fuselage, harming the pilot or affecting the primary controls.

CS-23 regulations [14] state that a firewall shall be implemented that is able to resist a flame of $1093°C$ for a duration of 15 minutes. Several material are allowed by EASA to be used without testing, which are stated in Table 4.4 with the corresponding required minimum thickness of each material.

Table 4.4: Required firewall thickness of approved materials

Material	**Thickness** *[mm]*	**Density** *[kg/m^3]*
Stainless Steel	0.38	8050
Mild Steel	0.45	7850
Monel Metal	0.45	8800
Titanium	0.41	4430

To select the firewall material a trade-off is performed, taking into account the criteria cost and weight. First of the plate area is determined to compare the weight of the plate of different materials afterwards. The top and bottom sections are 0.9 m and 0.7 m, respectively. The height is 0.7 m, yielding an area of $A = 0.56\ m^2$. Applying the different thicknesses corresponding to the different materials yields the volume of the plate and thereby the different weights and costs. By considering the cost per weight of each material, the cost of a plates for a certain material can be computed. Table 4.5 presents the material and the corresponding weight and cost of each plate.

Since the weight of the plates of the approved materials are relatively low, it is decided to use an already approved material and not spend more resources researching other materials. It can be seen that the costs of the plates are negligible for the trade-off. Therefore the lightest material, Titanium, is selected. This results in a total plate weight of 1.02 kg. The plate is connected in between the engine mounting and the fuselage truss structure.

Table 4.5: Weight and Cost of each approved Firewall Option

Material	**Weight** *[kg]*	**Price** *[€ / kg]*	**Cost** *[€]*
Stainless Steel	1.7	1.1	1.87
Mild Steel	1.97	0.37	0.73
Monel Metal	2.21	6.6	14.62
Titanium	1.02	6	6.12

4.2 Fuselage Skin

The two main parts of the fuselage structure are chosen to be an internal tubular frame structure carrying the high-g loads and a fuselage skin that only covers the truss to increase the aerodynamic performance of the fuselage without carrying loads. The goal of the present section is to select appropriate skin materials. To determine the which materials are suitable, first preferable characteristics of the skin materials are listed. The following aspects are of interest in selecting the fuselage skin:

- Low cost
- Low structural weight
- Low flammability
- High impact safety
- High availability
- Ease of maintenance and repair
- Optimal surface finish and smoothness
- Good recyclability

4.2.1 Straight Skin Sections

Following from the fact that the fuselage skin does not carry loads, a cloth or fabric material would suffice to cover the truss structure and give the aircraft its aerodynamic shape. The weight of the fuselage skin can be minimised by using fabric as skin material wherever possible. In practice fabric can only be used for straight skin sections, because for curved fuselage sections too much weight is added by longitudinal elements required to maintain a smooth outer surface. Therefore fabric can only be implemented for the side and lower aft fuselage sections. Taking for instance the *Extra 300 LX*, a fabric called *Ceconite 102* covers the tubular frames forming the lower fuselage section [28]. The Federal Aviation Administration (FAA) has issued Technical Standard Order (TSO) C15d to prescribe performance requirements aircraft fabric materials must meet. Only a limited number of material types have received approval, from which the oldest is Grade-A cotton, and later approved synthetic fabric types are *Ceconite*, *Stits*, *Superflite* and *Air-Tech* among others. To use new types of fabric, compliance with TSO requirements must be demonstrated. [29]

Although Grade A cotton itself is organic, coatings and dopes required for maintaining the fabric are not easily recyclable. The cotton is less durable than synthetic fabrics and needs to be replaced more frequently over its life time. Therefore this organic fabric can be regarded as less sustainable. Because cotton is not commonly used on the latest generation of aircraft, is it less available compared to synthetic fabrics. In a test properties of the four previously stated synthetic fibres have been measured under influence of environmental conditions over a certain time span. From this it is concluded the *Stits Poly-Fiber* fabric performed best on degradation criteria. After a more extensive study on the other performance requirements a definitive choice can be made.

4.2.2 Curved Skin Sections

The previous section has concluded that fabrics cannot be used for curved parts of the fuselage skin. Therefore more rigid lightweight materials are considered. Because the cockpit is not pressurised and the truss structure takes all the loads, strong materials such as steel or aluminium or a fatigue resistant composite material such as *Glare*^{TM} are not suitable for the fuselage skin. Thin aluminium sheets dent easily if too thin and become too heavy when thickness is increased. Carbon fibre, glass fibre and aramid fibre reinforced polymer materials are easier to shape and can provide a very smooth surface finish while being very lightweight. Therefore all three are good candidates for curved sections of the fuselage skin. A fourth material class is considered, being natural composites. Consisting of natural fibres supported by a biologically degradable matrix, this material class is fully biodegradable and therefore greatly reduces the environmental footprint. The great recyclability of this material class increases aircraft sustainability. The advantages and disadvantages of natural composites compared to synthetic composites are given in Table 4.6.

Table 4.6: Advantages and disadvantages of natural composites compared to synthetic composites

Advantages	Disadvantages
Lower price	Higher moisture sensitivity
Better recyclability	Higher flammability
Availability	Less durability
Health aspects during production	Less overall strength
	Limited compatible epoxy materials
	Slightly higher density

Three major complications biodegradable composite materials face are moisture sensitivity, flammability and a short life span due to degrading. The degrading process is different for every material type, but it mostly depends on operational conditions. Research has shown that ramie, jute and kopak fibres are more resistant to environmental conditions than other natural fibres. Out of these three, jute has the lowest density and cost price. In case jute is chosen as fibre material, the number of suitable thermoplastics available for matrix material is limited due to low fibre thermal stability of only 230°. Selecting a biodegradable matrices such as Biopol, PHB-HV copolymer or Bioceta makes the composite fully biodegradable [30]. Because of this advantage, jute reinforced Biopol composites were already a material of interest in the past, also having a density of only 1.30 g/cm^3. Research has shown that infusing this type of composites with 4% nanoclay reduces the moisture and water absorption and delays the degrading process [31]. Whether this additive is sufficient to prolong the life time of the part up to twenty years as stated in Section 1.3 must still be proven. After its life time, the composite can be fully reground and composted [32]. To quantify the characteristics of this natural composte, Table 4.7 gives the properties of Treated Jute fibre-reinforced Biopol Composites (TJBC) with 4% nanoclay and those of Carbon Fibre Reinforced Polymer (CFRP) material.

Table 4.7: Biodegradable TJBC versus synthetic CFRP

Material	**Strength** $[MPa]$	**Density** $[g/cm^3]$	Price $[\cdot 10^3$ \$ $/tonne]$	Manufacturing energy [GJ]
CFRP	600	1.60	12.5	130
TJBC	40	1.25	0.2 - 1.0	4

Besides additives, also coatings can solve previously stated problems of natural composites to a large extent. Coatings offer UV protection and protection from other environmental hazards and keep the temperature the material is subjected to within certain limits. However, they mostly consist of chemical compounds that harm the environment when being composted. Whether the same level of recyclability of the coated natural composite can be acchieved must be further investigated.

As for the reason that *FlashCo.* plans to draw attention by advertising the *T-16*, a great message can be sent by choosing a unique structural material like natural composites. In case this market strategy is chosen, additional research is required to refine the matrix and fibre types to make the material serve the purpose. After future research a more founded decision can be taken on durability and recyclability. This is elaborated upon in Section 2.1.1 in Part III. A third aspect that affects the material choice is availability. Although the natural composite can be available for implementation on time judging on the research that has been performed in the past, certification might slow down the process. This is discussed in Section 5.2, Part III. In case the advantages of recyclability do not balance the durability and availability aspects, a synthetic composite material should be selected.

4.2.3 Additional Skin Sections

This small section shortly discusses additional design features of the fuselage skin: the canopy and secondary cockpit windows. The canopy allows most of the visibility for the pilot and also contributes to the aircraft's aerodynamic shape. Hinging the canopy to one side of the aircraft provides easy accessibility for the pilot. The component itself is assumed to take any structural loads, but aerodynamic loads and can therefore be constructed of lightweight material. During this design phase, only an initial draft of the outer shape is made and this design is further refined in the next design phase [33]. The main requirement of the material is to provide sufficient transparency, which makes Plexiglas a good candidate. This material can also be used for floor and side windows in the cockpit section of the fuselage, to give the pilot more insight to his attitude when performing manoeuvres such that he can consequently adjust his flying strategy. The sizes of these panels are

primarily based on reference aircraft and component weights are not calculated in detail in this design phase.

4.3 Aerodynamic Shape

Having determined the fuselage dimensions and the fuselage skin material, it is necessary to design the fuselage shape to make it aerodynamically as efficient as possible. The main requirement is that the fuselage produces little drag. The aerodynamic moments C_l, C_m and C_n induced by the fuselage should be as small as possible too. The lift force induced by the fuselage shall be larger than zero.

4.3.1 Fuselage Design

Since the propeller is located at the front of the aircraft, the airflow over the fuselage is turbulent and the flow velocity is larger than the free stream velocity. The propeller also induces a vortex going around the fuselage, which is known to cause a rolling and yawing moment as an upwash is experienced by the wing and vertical fin respectively, swirl effects [34]. For the fuselage design, the swirl effects can be minimised by making the fuselage circular: the vortex swirls around the fuselage with minimum resistance and the induced moments are minimised. [34, 35]

For the analysis of the fuselage, Computational Fluid Dynamics (CFD) tools are considered. However, this type of analysis is paired with uncertainty: the drag and moment coefficient values computed by CFD tools such as Fluent are prone to errors. Furthermore, the swirl effect and turbulence are difficult to model, which again increases the level of uncertainty [36]. Also considering the inexperience of the team, it is decided not to design the fuselage using CFD computations in the current design phase.

The drag coefficient of the aircraft depends linearly on the aircraft's frontal area [37]. Hence it is important to design the fuselage with a minimal frontal area. However, a trade-off needs to be made between frontal area and making the fuselage circular. Since no CFD computations are done, this balance is decided by literature [38] and by studying reference aircraft, see Appendix A. In general, the fuselage shapes of reference aircraft are square, indicating that reducing the frontal area has priority.

The skin shall be easy to manipulate, to ensure the option of applying a complex shape, except the side and bottom panels behind the canopy. The natural fibre cannot be formed easily, which means that the natural fibre panels are shaped around the truss structure. Since these straight panels are far behind the propeller, the impact of the straight panels on the aerodynamic characteristics of the fuselage is estimated to be small. The restrictions for the fuselage design are the truss structure and the engine. Obviously these components need to lie inside the fuselage skin, with the skin as closely around these components as possible to minimise frontal area.

Figure 4.7: Impression of the fuselage shape.

An impression of the fuselage is shown in Figure 4.7 (for more detailed drawings, see Figure 9.1 in Chapter 9, Part II. The engine cover, highlighted in Figure 4.7, encloses the engine as tight as possible, while the rest of the fuselage encloses the truss structure as tight as possible. To account for swirl effects, the edges around the engine and the truss structure have been made smooth.

4.3.2 Canopy Design

To ensure that the pilot has good visibility, a canopy encloses the cockpit. Studies on canopy design have been made: a NACA report describing wind tunnel experiments mentions that the drag of canopy may account for as little as 1 % of the total fuselage drag, and suggest that a rounded canopy with length-to-height ratio l/h of 10 has lower drag than canopies with a lower l/h [39]. Hoerner suggests an ideal l/h of 12 [40].

In Figure 4.7, one can see the canopy design. Its value of l/h is 11.6, which approximates the l/h of 12 as suggested by Hoerner [40]. The frontal surface area is 0.75 m^2. One can see that the cross-section of the canopy at its point of maximum height is triangular. The reason for this is to minimise frontal area, which reduces canopy drag.

4.4 Recommendations

This chapter deals with the design of the subsystem that establishes the link between all other subsystems. First the truss is designed to withstand the different loads and be able to integrate the wing and the landing gear. Thereafter the aerodynamic shape of the fuselage is optimised. The skin is selected to put an emphasise on biodegradable materials. Finally the firewall, guaranteeing safety, finishes the fuselage design.

The methods used to design the fuselage subsystem described in the previous sections include certain assumptions. To finalise the fuselage design recommendations are given to refine the design and increase the level of detail.

The truss analysis is conducted on the basis of simplified models. The weights and location of subsystems and items are altered to make an analysis even possible. For the torsional load case of the truss it is assumed that one deals with a thin walled rectangular box with constant thickness throughout the two sections. As the design goes into further detail, more resources shall be allocated into validating and optimising the truss even further. In regards to the skin material selection it is concluded that fully biodegradable composite materials are optional for implementation. To ascertain the mission life of the composites, research is required on degradation and loss of strength and the effects of coatings. Bio-based coatings can be considered to keep the same level of recyclability of the composite according to the department of *Novel Aerospace Materials of the Faculty of Aerospace Engineering, TU Delft*. The fabric used to cover straight fuselage sections is determined to be of synthetic type. To choose the exact type, an extensive investigation on degradation aspects and the loading conditions of the fabric material is required to make a correct trade-off.

Having designed the fuselage and the propulsion system integrated, attention can be shifted to the subsystem that provides the lift, the main wing.

Chapter 5

Wing

With the fuselage design being done, it is time to design the wings. The sizing of the wing depends mostly on the stability and controllability of the aircraft, while the aerodynamics department optimises the wing to achieve its characteristics with maximum efficiency. The structures department optimises the wing structure to make it as light as possible, while still being able to withstand a load factor of 10g.

In Chapter 5.1, the aerodynamic tools that are used to analyse the wing's performance are described. The airfoil design is reported in Chapter 5.2. The design of the wing geometry is described in Sections 5.3 and 5.4. The use of wingtip devices is elaborated upon in Section 5.5. Finally, the wing structure is described Section 5.6.

5.1 Aerodynamic Analysis Tools

For the analysis of both airfoil and wing planform designs, a tool called *XFLR5* is used. This tool is a coding translation of the airfoil analysis tool *XFoil*, from the original language *Fortran* to *C++*. Furthermore, it is been put into a more user friendly interface and expanded with 3D analysis capabilities. The tool is verified with *XFoil* data extensively, always with consistent results [41]. *XFoil* in turn is verified with many NACA airfoils [42] and is a standard in aerodynamics departments, often modified to increase reliability of results.

5.1.1 Design tools

XFLR5 has an implemented airfoil design tool, which can also refine the distribution of measurement points on an existing surface and scale geometrical properties such as maximum thickness over chord t/c ratio, maximum thickness location and leading edge radius. Furthermore it includes a wing design tool which allows the user to input the geometrical properties of the wing and analyse its performance. The tool is used for both airfoil and wing design, taking into account all limitations, as explained further in section 5.1.2.

For the airfoil design, a combination of *XFLR5* and *Matlab* is used. The original airfoil chosen in Mid-Term Report of *Torero* [19], the E479, is modified using *Matlab* mainly on the geometry of its tail section and maximum t/c ratio. *XFLR5* is used to modify maximum thickness location and leading edge radius, using the scaling functions implemented in the airfoil design tool. Analyses are run at $Re = 6.5 \cdot 10^6$, the approximate Reynolds number at the Mean Aerodynamic Chord MAC of the wing. For the determination of candidates for variable airfoil, see Section 5.2.4, Reynolds numbers of $Re = 5 \cdot 10^6$ and $Re = 12 \cdot 10^6$ are used, representing tip and root respectively.

Wing design is fully done with *XFLR5*, as it includes a Lifting Line Method (LLM), horseshoe and ring Vortex Lattice Methods (VLM) and a 3D panel method, saving the trouble of creating, verifying and validating such a tool from scratch. The ring VLM is mostly used, as this has the most capabilities of all methods [41]. Analysis is run at velocities between 60 and 100 m/s.

5.1.2 Limitations

XFoil, and therefore *XFLR5*, has some important limitations, that have to be taken into account when analysing airfoil performance. First of all, its prediction of the maximum lift coefficient of the airfoil $C_{l_{max}}$ is usually optimistic and everything after the stall angle is a very crude approximation that cannot be relied on. However, it is very capable at calculating the first and second linear slopes of the $C_l, \alpha-$ curve and at predicting the point where it starts deviating from the linear slope. This means that up to this transition point, results can be assumed to be reliable and the prediction of $C_{l_{max}}$ can be used as a simple approximation.

XFLR5 includes a fairly accurate boundary layer growth model, which also predicts drag on the airfoil (C_d). It usually underestimates the drag however, and not too much trust should be put in the absolute values of C_d. Nonetheless, it can be used to show the drag increases and reductions at certain ranges of C_l relative to other airfoils. From wind tunnel tests on the airfoil of the *Extra 300*, it is found that a boundary layer transition criterion of $N_{crit} = 7$ gives the best approximation of results in *XFLR5* for this kind of airfoil. This value is an input for *XFLR5*, which determines at what point the boundary layer transitions from laminar to turbulent. This is an important parameter to obtain reliable results and changes per type of airfoil. For an even better approximation, this value should be set differently for top and bottom of the airfoil. However, *XFLR5* does not allow this.

The 3D wing design analysis of XFLR5 provides some good looking results, but are not very reliable when it comes to full scale aircraft. It uses the data of the chosen airfoil at a large range of Reynolds numbers for interpolation and adds the 3D effects by use of a horseshoe or ring vortex model. Since there is no real viscous calculation other than the model applied to the airfoil data, drag and downwash results provided by the tool cannot be used with any certainty. The lift distribution can still be used as an approximation of the span efficiency of one wing compared to another, as tip vortices are simulated, albeit idealised.

5.2 Airfoil

During the preliminary design phase, the Eppler E479 airfoil was chosen for the wing of the *T-16* aircraft. This airfoil was to serve as a baseline, from which changes could be implemented to optimise the airfoil for the *T-16*. This section elaborates on this optimisation process.

5.2.1 Design Criteria

Before optimisation can be initiated, the desired airfoil characteristics have to be identified, which are derived from the airfoil design criteria. One of the main criteria is a high $C_{l_{max}}$, such that sufficient lift can be produced for high-g turns and low speed landings, without requiring very large wings, which would increase drag. Many aerobatics aircraft are designed to have a high C_d for low values of C_l, to keep the engine from overturning during high speed dives [43]. However, such manoeuvres are not performed during the *Red Bull Air Race*. A lower C_d at low C_l allows for a higher velocity on the straight sections of a course, creating an advantage compared to regular aerobatic aircraft. A low C_d at high C_l is also important, as this allows the aircraft to take high-g turns faster. As most turns are made at between load factors of 6g and 10g, the required C_L range for these turns is between 0.9 and 1.4, as calculated with Equation 5.1. This is the standard definition of C_L with the lift L multiplied by load factor n [37]. Applying a 2D to 3D lift correction factor $C_{L,max}/C_{l,max}$ of 0.818 based on *XFLR5* results, see Section 5.4, yields a range of C_l between 1.1 and 1.7. Thus an airfoil is needed with a low drag in that region of C_l.

$$C_L = \frac{L \cdot n}{0.5\rho V^2 S} \tag{5.1}$$

Stall and after-stall behaviour is also an aspect that requires attention. For most aerobatic aircraft, stall is designed to be very sharp and sudden, often by use of a leading edge stalling airfoil. This mean that the airflow suddenly separates from the leading edge, completely stalling the airfoil. This stall behaviour enables the pilot to perform manoeuvres such as snap rolls. However, during the *Red Bull Air Race*, no such manoeuvres are performed. A somewhat softer stall is much more desirable, as it is much safer, especially since the aircraft is flying low to the ground. A trailing edge stalling airfoil will stall less sudden than the previously mentioned leading edge stalling airfoil, as the flow separates from the trailing edge and the separation point moves forward with increasing angle of attack. An added benefit of trailing edge stall is that the hysteresis effect, where separated flow reattaches at a lower angle of attack than it separates at, is less significant. This increases safety, as it is easier to recover from stall at low altitude. [43–45]

5.2.2 Airfoil Design

To be able to optimise the airfoil for the design criteria identified in section 5.2.1, it should be known which parameters are controlled by which geometrical properties. For this purpose, a large number of analyses are run in *XFLR5*, where systematically different geometrical properties of the original E479 airfoil are varied, to identify their contribution to the airfoil characteristics. The results, along with knowledge gained from [43, 45–47], are used for the development of a final series of airfoils, from which the best performing one is chosen. Properties that are varied include maximum thickness location, maximum t/c ratio, tail curvature of different orders and leading edge radius.

5.2.3 Airfoil Optimisation Results

The optimal airfoil performance is found in a heavily modified version of the E479. The location of maximum thickness is moved forward by 11% of the chord. The forward and aft sections are scaled accordingly. The thickness is modified to only 70% of the original t/c ratio and the leading edge radius is increased by a factor 2.2 to enable a higher $C_{l_{max}}$. This last modification moves the location of maximum thickness forward even more, towards 10% of the chord length. It also smooths out the pressure distribution peak over the airfoil at high angles of attack, which reduces undesired viscous effects [43]. Figure 5.1 shows the original E479 and the new E479Mod. One more airfoil is designed, nearly equal to the E479Mod, but with a leading edge radius that is only increased by a factor 2. This E479Mod-2 airfoil is presented in Section 5.2.4.

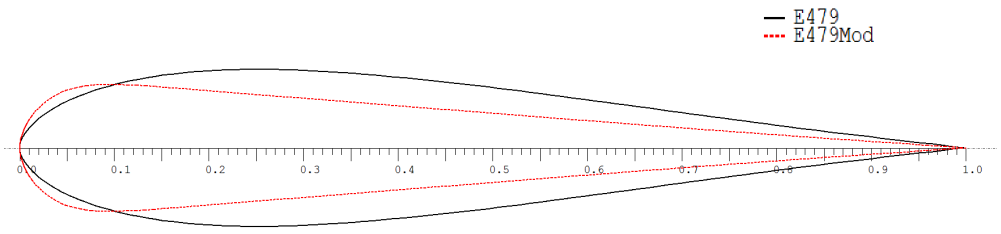

Figure 5.1: Airfoil lay-out of the E479 and E479Mod

Figures 5.2a and 5.2b show the C_l, C_d- and C_l, α-curves of the original and modified airfoil. The increase in $C_{l_{max}}$ and also the more reliable $C_{l_{max_{lin}}}$, the maximum C_l of the linear trend, is very

high, up to values above $C_l = 2.0$. This is required to have a C_L to fly high-g turns, taking into account the 3-dimensional losses. It can be seen that a = higher C_d at low C_l is a consequence of this increase in lift coefficient. This increase in drag is minimised, but cannot be avoided.

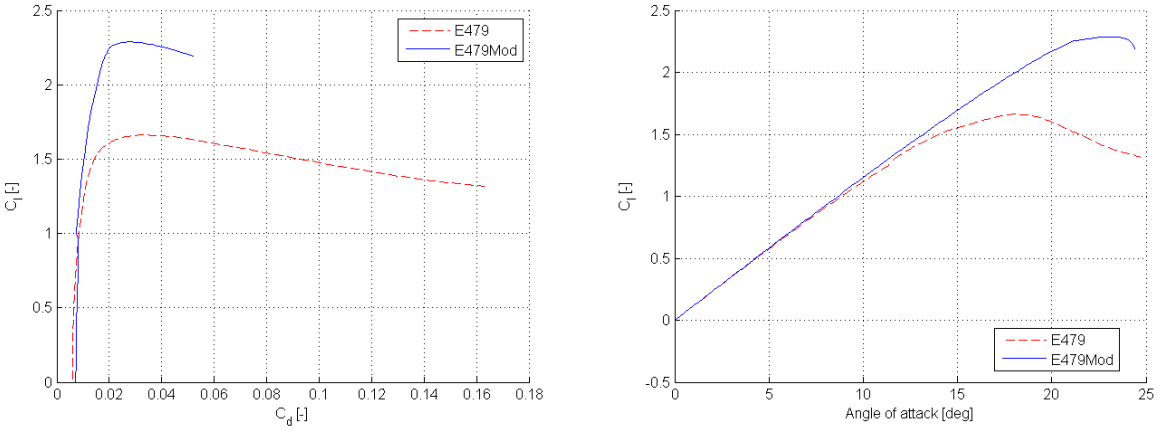

(a) Lift versus drag curve of E479 and E479Mod

(b) Lift curve of E479 and E470Mod

Figure 5.2: Lift and drag curves of E479 and E479mod airfoils

Table 5.1 summarises data of both airfoils obtained from *XFLR5*. It includes a value for $(\frac{t}{c})_{0.0125c}$, which is an indication of the stall behaviour of the airfoil. Using the method described in [44], it is determined that both airfoils have trailing edge stall behaviour. The modified airfoil performs better than the original airfoil with respect to all parameters, except the zero-lift drag and moment coefficient. However, from figure 5.2a it is found that the drag at high C_l is definitely improved. This is also represented in the maximum $(\frac{C_l}{C_d})_{max}$. The maximum moment coefficient has more than doubled, however the values are still relatively small and are assumed negligible.

Table 5.1: Comparison of airfoil data

Parameter	E479	E479Mod
$C_{l_{max}}$	1.66	2.29
$C_{l_{max_{lin}}}$	1.36	2.13
α_{stall}	18.1	23.1
C_{d_0}	0.0059	0.0072
$C_{m_{max}}$	0.0314	0.06651
$(\frac{C_l}{C_d})_{max}$	121	146
$(\frac{t}{c})_{0.0125c}$	3.44%	4.66%

5.2.4 Variable Airfoil

As mentioned in section 5.2.3, another airfoil is designed which is slightly different from the E479Mod. The E479Mod-2 has a slightly smaller nose radius, as can be seen in figure 5.3a, where only the nose of the airfoils is shown. The rest of the airfoils is exactly the same.

Though these airfoils are very similar, the smaller nose radius of the E479Mod-2 causes a different performance in the $C_{l_{max}}$ region. It stalls at a slightly lower angle of attack, without losing too much lift. The $C_{l_{max_{lin}}}$ is actually the same value. Their performance at different Reynolds numbers is also different, which makes the E479Mod-2 a perfect candidate to be used in a variable airfoil wing. Figure 5.3b shows the stall region of the E479Mod at Re $= 5 \cdot 10^6$ and the E479Mod-2 at Re $= 1.2 \cdot 10^7$. These Reynolds numbers represent outboard and inboard flow conditions, respectively. It can be seen that both airfoils reach nearly the same values of C_l for a given angle of attack, but the E479Mod-2 has a lower stall angle. Variable airfoil is further treated in section 5.4.3.

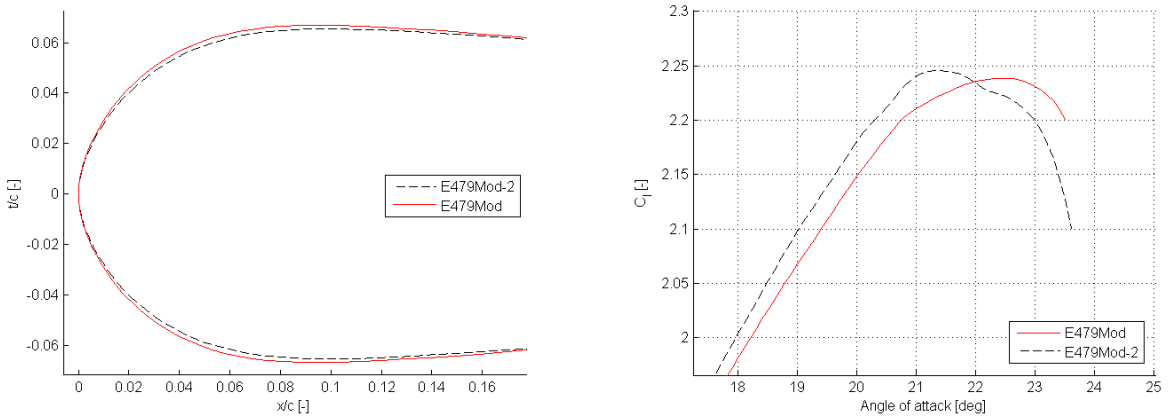

(a) Nose of the E479Mod and E479Mod-2 airfoils

(b) Lift curve for the E479Mod and E479Mod-2 airfoils

Figure 5.3: Sketch and lift curves of E479Mod and E479Mod-2 airfoils

5.2.5 Recommendations

The airfoil design can be improved by the use of more reliable measurement tools, based on, for instance, Finite Volume Method (FVM) software. This kind of software is more accurate in predicting drag and stall region airfoil behaviour. Attention should also be paid to the unsteady aerodynamics (Theodorsen theory), along with dynamic stall and piston effect characteristics of the airfoil, as these are very important for an aerobatic aircraft design [48]. The final airfoil, or a series of well performing airfoils, should also be tested in a wind tunnel, to verify the results obtained from the software. Also, phenomena such as hysteresis are very difficult to predict other than by performing experiments and are of vital importance.

5.3 3D Wing Theory

Now that the airfoil design is concluded, the wing geometry is addressed. In this section the theory behind 3D wing analysis is elaborated on. This theory is applied to the design of the wing and horizontal tail, which is addressed in Section 5.4 and 6.1, respectively.

In 3D wing analysis, induced drag needs to be taken into account. The angle of attack of the tail consists of the induced angle of attack and the effective angle of attack, as shown in Figure 5.4 [49].

In this figure the effect of the downwash is shown. The downwash causes the local angle of attack to decrease. Because the induced angle of attack is always lower than the geometric angle of attack the lift curve slope of a 3D finite wing is lower than that of its 2D projection. Furthermore, due to the induced angle of attack a horizontal drag component arises as can be noticed in Figure 5.4. The induced drag component causes the total drag of the wing to increase. The angle of attack can be described by Equation (5.2).

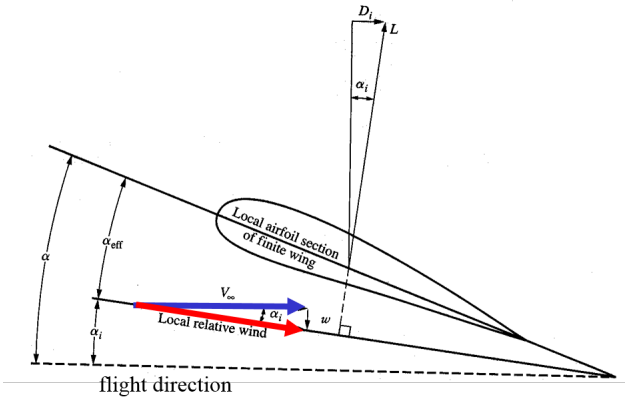

Figure 5.4: Finite wing induced drag due to downwash

$$\alpha = \alpha_{eff} + \alpha_i \tag{5.2}$$

To quantify the effect of changing the wing geometry on the lift, an equation that relates the vorticity to the spanwise location needs to be

obtained. This can be done by first establishing a relation between angle of attack and lift coefficient. Using these equations together with the expression for downwash leads to a final relation between local angle of attack and spanwise location. The effective angle of attack is defined in Equation (5.3), where c_l is the lift coefficient, a_0 is the lift slope and $\alpha_{L=0}$ is the zero lift angle of attack. All equations are based on incompressible aerodynamics theory. [49]

$$\alpha_{eff} = \frac{c_l}{a_0} + \alpha_{L=0} \tag{5.3}$$

The 2D lift coefficient of the wing is defined by Equation (5.4), where L' is the lift per unit length, ρ the density, V_∞ the freestream velocity and c the chord length .

$$c_l = \frac{L'}{\frac{1}{2}\rho {V_\infty}^2 c} = \frac{\rho V_\infty \Gamma}{\frac{1}{2}\rho {V_\infty}^2 c} = \frac{2\Gamma(y_0)}{V_\infty c(y_0)} \tag{5.4}$$

The induced angle of attack (α_i) is defined by Equation (5.5).

$$\alpha_i(y_0) = -\frac{w(y_0)}{V_\infty} \tag{5.5}$$

The downwash, $w(y_0)$, as function of the span wise location is defined in Equation (5.6), where Γ is the circulation and y_0 is the spanwise location.

$$w(y_0) = -\frac{1}{4\pi}\int_{-b/2}^{b/2} \frac{(d\Gamma/dy)}{(y_0 - y)} dy \tag{5.6}$$

Substitute Equation (5.6) into (5.5) and (5.4) into (5.3) and subsequently (5.5) and (5.3) into (5.2), leads to Prandtl's lifting line theory which is given by Equation (5.7).

$$\alpha(y_0) = \frac{2\Gamma(y_0)}{a_0 V_\infty c(y_0)} + \alpha_{L=0}(y_0) + \frac{1}{4\pi V_\infty}\int_{-b/2}^{b/2} \frac{(d\Gamma/dy)}{y_0 - y} dy \tag{5.7}$$

To calculate the actual value of lift a relation needs to be found between circulation and lift. This relation is described by the Kutta-Joukowski equation, Equation (5.8).

$$L' = \rho V_\infty \Gamma \tag{5.8}$$

Prandtl's lifting line theory gives a relation between the lift and geometry of the wing. Therefore it forms the basis of the Vortex Lattice Method (VLM). The horseshoe model is based on Prandtl's theory, which is shown in Figure 5.5 [49].

The trailing vortices that are curling around the sides of the horseshoe are shown in Figure 5.5. The sides of the horseshoe run to infinity. The middle side of the horseshoe, the bound vortex, has constant circulation Γ . Since the circulation is constant in spanwise direction, the model is not very accurate to determine a lift distribution. In order to solve this, the wing surface is divided into several horseshoe vortex models and by means of superposition the accuracy of the lift distribution is much improved. So for each spanwise position of the

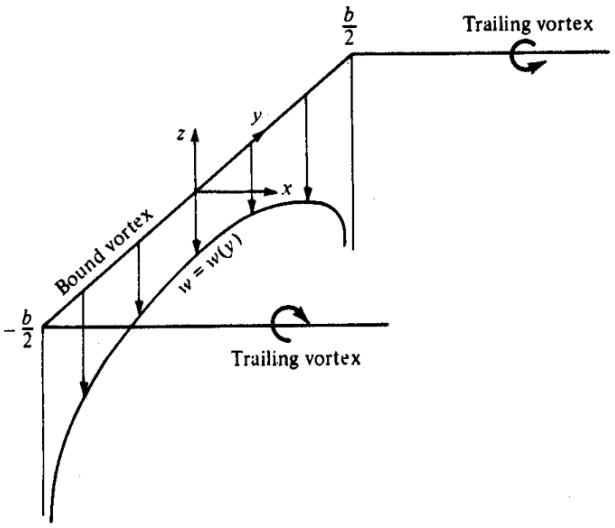

Figure 5.5: Horseshoe vortex model

wing the induced angle of attack is calculated. Having determined the induced angle of attack the actual lift at that section can be determined.

In order to execute the VLM within XFLR5, three built in subroutines are used. The first routine consists of determining the amount of horseshoe vortices in chordwise and spanwise direction. Next the circulations are calculated that satisfy the tangent flow boundary condition. This is done by solving a matrix with all values found in different control points. The final step is to calculate the lift by applying the Kutta-Joukowski relation. The VLM that is implemented in XFLR5 assumes incompressible, inviscid and irrotational flow. [50]

5.4 Wing Planform

Having optimised the airfoil and understood the 3D wing theory, the next step is to design and optimise the wing planform. This optimisation is closely related with other departments, such as Control & Simulation. The wing planform design is based on preliminary sizing values of aspect ratio A and wing surface area S obtained from the weight estimation methods described in Chapter 2. This means that the wing planform design is an iterative process. The design goal is to minimise the induced drag C_{D_i} of the wing, mainly by designing the wing planform such that the lift distribution is as close to the ideal elliptical lift distribution as possible.

5.4.1 Sweep Angle

During the preliminary design phase, it is found that a sweep angle between 0 and -10 ° should be used. For this range of sweep, phenomena such as inboard boundary layer thickening and inboard spanwise flow are negligible [51]. This range of sweep mainly effects certain stability derivatives, which is explained further in Section 7.9. It is for that reason that the Control & Simulation department of *Torero* has the most influence on the choice of sweep angle. As discussed in Section 7.9, the leading edge cannot be swept forward past 0°, as the aircraft would become too unstable. As the aircraft needs to be as close to neutral stability as possible, a 0° leading edge is chosen for the wing design. This corresponds to a quarter chord sweep angle of $\Lambda_{0.25c} = -2.4$ °.

5.4.2 Lift distribution

The optimal lift distribution can be obtained by varying two parameters, namely taper ratio λ and wing span b. The wing is constrained by the surface area calculated from the weight estimation, see Chapter 2. The final iteration is done for a surface area of $S = 7.3\,m^2$. It is known that for sweep angles of 0 to -10 ° of sweep, the optimal taper ratio is in the range of $\lambda = 0.4 - 0.5$ [47]. The wing span is limited by the requirements [19] to a range of $7.0 < b < 7.6\,m$. As the wing planform is being designed for minimum induced drag, aspect ratio is as important as span efficiency, as per Equation (5.9) and (5.10).

$$C_{D_i} = \frac{C_L^2}{\pi \cdot A \cdot e} \qquad (5.9) \qquad\qquad A = \frac{b^2}{S} \qquad (5.10)$$

It is found that a shorter wing span slightly improves the lift distribution, but this improvement is offset by the strong negative contribution of the smaller aspect ratio. For that reason, maximum span is chosen to maintain an aspect ratio as large as possible, as found from Equation 5.10. With this additional constraint, taper ratio is varied between 0.4 and 0.5 to find the optimal taper ratio. This is found to be $\lambda = 0.5$ for a straight leading edge wing, which corresponds to what is found in [47] for a wing with this sweep angle. Figure 5.6 shows the resulting lift distribution, which is close to the ideal elliptical lift distribution.

5.4.3 Variable Airfoil Wing

Stall behaviour is a parameter that should be taken into account in the wing design. To maintain lateral control in the stall region as long as possible, wings are modified to stall at the root first. Because the root section stalls before the tip section, aileron effectiveness is maintained for as long as possible, since the ailerons are most effective towards the tips. Normally, this is done by introducing a certain amount of geometrical twist in the wing, which changes the relative angle of attack of root and tip sections. However, this effect would reverse during inverted flight, which is undesirable for the *T-16*. Varying the airfoil along the span is therefore a better option. Using different airfoils along the span with different stall angles, the wing can be modified to stall at the root first. Section 5.2.4 has introduced a second airfoil which is very slightly modified from the standard airfoil for the *T-16*. This airfoil is used at the root of the wing, which will therefore stall before the tips.

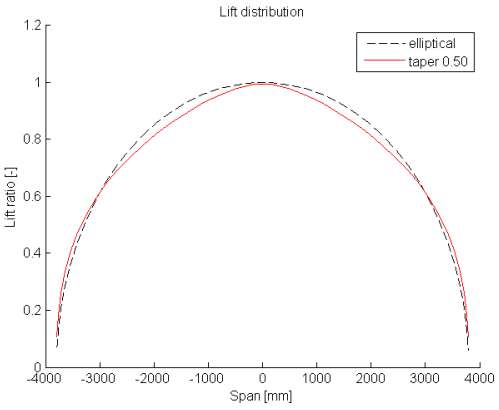

Figure 5.6: Lift distribution of wing vs elliptical lift distribution

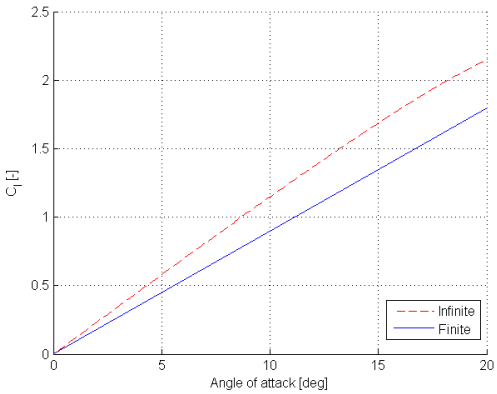

Figure 5.7: Infinite wing vs. Finite wing lift curve

A difficult aspect of using multiple airfoils is the wing integration. A varying thickness across the span due to different maximum thickness ratios of the airfoils complicates the structural integration. However, these airfoils only have a slightly different nose radius, which means that the integration of the main spars is not an issue. It should be noted that small differences in nose radius have large influence on the performance of the airfoil, hence the manufacturing of the wing should be of high quality to make sure these slight changes are implemented properly.

5.4.4 Final Results

The wing planform design leads to a wing with a root chord of $c_r = 1.3\,m$, a tip chord of $c_t = 0.64\,m$ and a wing surface area of $S = 7.3\,m^2$. The wing span is chosen to be the maximum allowed $b = 7.6\,m$, because the effect on aspect ratio dominates the effect on spanwise efficiency factor. The wing has a straight leading edge, meaning a quarterchord sweep of $\Lambda = -2.4\,^\circ$. The corresponding optimal taper ratio is found to be $\lambda = 0.5$, giving the wing the best possible approximation to an elliptical lift distribution. The airfoils E479Mod and E479Mod-2, discussed in Section 5.2, are used at tip and root respectively, with a linear interpolation in between. This is done to have the root section stall before the tip section.

Figure 5.7 shows the lift curve for the infinite and finite wing, up to approximately $C_{l,max_{lin}}$ of the infinite slope. C_{l_α} is approximately 6.16 rad^{-1}, while C_{L_α} is approximately 5.16 rad^{-1}. Assuming the same stall for both cases, it is approximated that $C_{L_{max}} = 1.8$.

5.4.5 Recommendations

For further analysis of the wing planform, several recommendations can be made. First and foremost, a CFD analysis tool should be used, to obtain more reliable values of the aerodynamic characteristics which include viscous effects. A proper analysis tool can then also be used to determine wing-fuselage interactions, from which wing blending sections can be designed to reduce drag on the aircraft. An investigation into unstable aerodynamic effects such as flutter and divergence should also be started. Experimental values are also vital to the success of the design, so wind tunnel tests should be performed at a later stage. The detailed design phase should also include investigation of the need for and possible benefits of stall strips, stall fences, vortex generators, boundary layer trip strips and similar devices.

5.5 Wingtip Devices

The use of wingtip devices is a very interesting design option for the *T-16*. Currently, only one competitor in the *Red Bull Air Race* uses winglets on his aircraft, which are retrofitted on the *MXS-R*. These allegedly increase roll rate [52].

5.5.1 Advantages and Disadvantages

Wingtip devices come in many different shapes and sizes, but all are designed to restrict the wingtip vortices due to the pressure differential between top and bottom of the wing. These vortices are the main contributors to induced drag, which is therefore decreased by the use of winglets. Furthermore, because the tips have less tip vortex effects, the lift generated by the tips increases, changing lift distribution and increasing effective aspect ratio and again thereby decreasing induced drag. Also, the effectiveness of the ailerons towards the tips increases, which improves roll rate. Properly designed wingtip devices can even introduce a forward pointed aerodynamic force, which adds to the total thrust of the aircraft. [53, 54]

However, the use of wingtip devices comes at a cost, quite literally. The design of wingtip devices is a complex process and they are often expensive to manufacture due to their shape, especially when they are 'blended' with the wing structure. They are prone to flutter, often suffer from parasitic drag due to the integration with the wing and can increase the adverse pressure gradient towards the tip, causing tip stall. Furthermore, larger wingtip devices suffer additional drag due to a larger frontal area which will have to be offset by the induced drag reduction they offer. The same applies to retrofitted wingtip devices, which will change the lift distribution of the wing, often making it less elliptical and thereby increasing induced drag. Large wingtips will also experience more disturbance due to sideslip. [53, 54]

5.5.2 Wingtip Design

Based on [53] and [54], it is found that the disadvantages can quickly catch up with advantages, mainly due to the relation to speed and size. Induced drag is inversely related to the square of the velocity, while parasitic drag is directly related to the square of the velocity. This means that as speed increases, parasitic drag of the winglet can rapidly exceed the induced drag reduction it offers. Proper winglet design requires a lot of time, which is not available in the current design stage.

A smaller wingtip device could still be used to increase the aileron effectiveness, as suggested by [45]. A small wingtip plate does not have the advantages or disadvantages of larger winglets, but can still improve aileron effectiveness, by moving the tip vortices away from the ailerons. The improved flow over the aileron in turn improves roll rate. This kind of wingtip device requires hardly any designing, as it is simply constrained by the airfoil thickness and the maximum aileron deflection. A similar plate at the inboard section can also be added, for the same purpose. The drag increase

is negligible as the plate only has to be very thin, and the same goes for weight increase. Figure 5.8 gives an impression of what the plate would look like, both inboard and outboard.

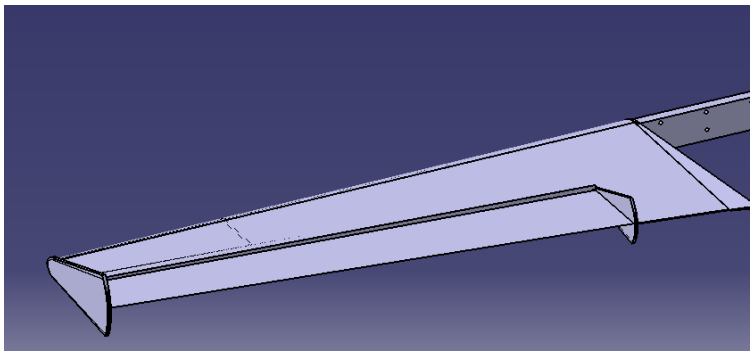

Figure 5.8: Wingtip device to improve aileron effectiveness

5.5.3 Recommendations

As stated in [53], it is possible to improve any wing by specifically designing winglets for it. Hence, this is also a possibility for the *T-16*, provided that enough time is allotted for it. The main subject of interest would be the increasing profile/parasitic drag and the deterioration of span efficiency factor due to additional tip loading. This should be offset by the reduction in induced drag the addition of the winglet offers.

Also, close attention should be paid to the orientation of the winglet in all three planes, along with the airfoil used. By properly orienting the winglet and using the appropriate airfoil a resulting aerodynamic force in the x-direction of the aircraft can be obtained, effectively increasing thrust without modifying the propulsion system. The airfoil also should chosen such that it diffuses the tip vortices and effectively reduces spanwise flow [53]. [54]

5.6 Wing Structure

Now that the layout of the wing planform is determined, as discussed in Section 5.4, this section elaborates on how the wing is structured. First, the wing box layout is presented in Section 5.6.1. Secondly, the numerical approach to compute the stresses in the wing box is described in Section 5.6.2.

5.6.1 Wing Box Layout

The layout of the wing cross-section, that is presented in the Mid-Term Report of *Torero* [19], is changed from a two spar configuration of equal size carrying all the loads, to a full wing box structure where the top and bottom skins also carry loads to increase torsional rigidity of the wing. This new cross sectional configuration consisting of four wing box elements is presented in Figure 5.9a.

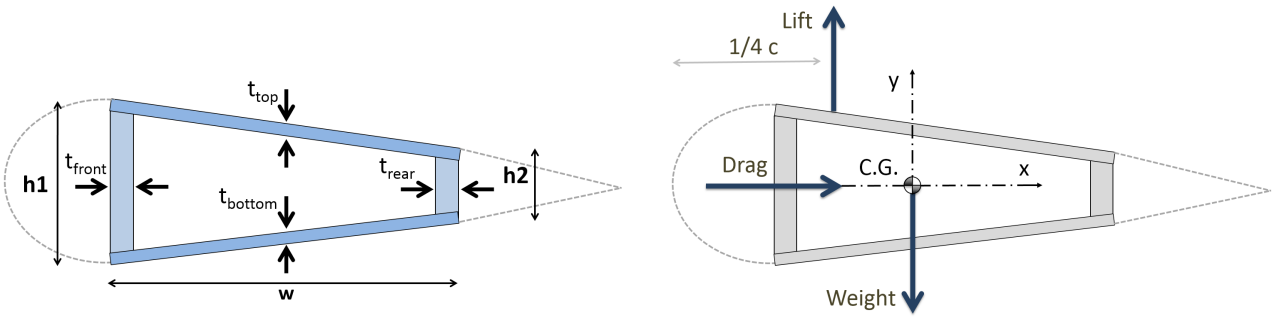

(a) Dimensions and thicknesses of wing box elements *(b) Loads acting and axis system location of wing box*

Figure 5.9: Visualisation of wing box

5.6.2 Numerical Approach

The numerical approach to compute the stresses in the wing box is depicted in a flow diagram in Figure 5.10. After every step in the process only the outputs required for further steps in the process are shown. The approach involves using two programs: *Matlab* and *Kolibri*. The role of each of the two is discussed in the following sections.

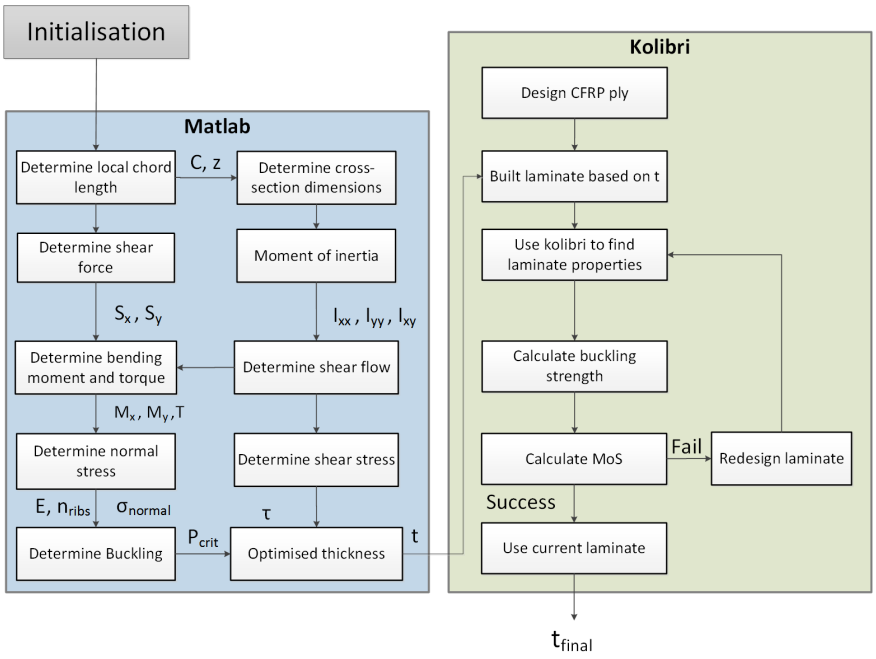

Figure 5.10: Flow diagram for wing structure analysis

Isotropic Wing Box Analysis in Matlab

After initialising the wing parameters, the procedure starts by optimising a fully metal wing. This procedure only allows analysing a wing box comprising isotropic materials. As a first step, the wing is discretised into n segments from tip to root and the local chord length for each section is determined using the taper ratio and the root chord length. Then after calculating the centroid location $\bar{x}$ using Equation (5.11), the moment of inertia I is computed using Equation (5.12) with respect to the c.g. depicted in Figure 5.9b. The wing is analysed from tip to root and the loads on each wing segment are calculated. A linear lift distribution increasing from $L = 0\,kN$ at the tip to $L = 26.4\,kN$ at the root is assumed that adds up to the total lift force acting upwards in a turn at maximal structural load factor of 15g as is determined in Section 1.3 Part I. The drag experienced by the wing is calculated using a zero lift drag coefficient of $C_{D_0} = 0.017$ and the total drag is also

distributed linearly from tip to root. As a third loading, a linear distribution of the wing weight is applied where the total weight equals $W_w = 95\,kg$ according to the Class II weight estimation discussed in Section 2.3.

$$\bar{x} = \frac{\Sigma x_i A_i}{\Sigma A_i} \quad , \quad \bar{y} = \frac{\Sigma y_i A_i}{\Sigma A_i} \tag{5.11}$$

$$I_{xx} = \int\int y^2 dydx \quad , \quad I_{yy} = \int\int x^2 dxdy \quad , \quad I_{xy} = \int\int xydxdy \tag{5.12}$$

These loads introduce bending moment and shear force distributions throughout the wing box. The shear forces in both x- and y-directions S_x and S_y respectively are found by integrating the loads along the wing span. Multiplying this by the arm, which is the distance between two wing elements, the bending moment M is calculated. This moment serves as input for Equation (5.13) resulting in the normal stress acting on the wing box element. The shear forces also induce a shear flow q throughout the cross section. Since the wing structure is a closed section, there is a cut shown in Figure 5.11. Shear flows due to two shear forces are analysed separately. The shear forces and having an offset from the shear centre can be replaced by a shear force that goes through the shear centre and a torque T . The shear flow for an open section can be found by Equation (5.14), to close the section, a constant shear flow due to torque q_0 is added up to each part of the section. The direction of this shear flow is based on the position of the shear force that is acting. The magnitude of the shear flow can be determined by Equation (5.15). Dividing the shear flow by through one element by the corresponding thickness, the shear stress for this element is determined in Equation (5.16). Besides the torque by the offset of lift, also a torque by the aileron deflection is considered. This torque is calculated by the Aerodynamics department by simulating the difference in moment coefficient of the airfoil due to a full aileron deflection upwards. The airfoil profile is discussed in Section 5.2. Then the resulting torque $T_{aileron}$ is calculated using Equation (5.17) with $C_M = 0.10$, $rho = 1.225 kg/m^3$, $V = 100 m/s$ and $S = 7.3$ and this torque is added to the torque due to lift.

$$\sigma_z = \frac{M \cdot y}{I} \tag{5.13}$$

$$q_s = \frac{I_{xx} \cdot S_x - I_{xy} \cdot S_y}{I_{xx} I_{yy} - I_{xy}^2} \int_0^s tx \cdot ds - \frac{I_{yy} \cdot S_y - I_{xy} \cdot S_x}{I_{xx} I_{yy} - I_{xy}^2} \int_0^s ty \cdot ds \tag{5.14}$$

$$q_0 = \frac{T}{2A} \tag{5.15}$$

$$\tau = \frac{q}{t} \tag{5.16}$$

$$T_{aileron} = C_M \frac{1}{2} \rho V^2 S c_{wing} \tag{5.17}$$

The thicknesses of structural elements are optimised to keep the wing weight as low as possible while still meeting the Von Mises stress criteria and buckling strength criteria. The Von Mises stress σ_{VM} is calculated using Equation (5.18) and the critical buckling stress of a wing box element is determined by using Equation (5.19). For the latter, compressive buckling coefficient k_c is used for k to determine the critical compressive buckling stress. Shear buckling coefficient k_s is substituted for k to determine the critical shear buckling stress. Both coefficients are a function of the plate aspect ratio and the support types as presented in Figures D.1a and D.1b, Appendix D. The resulting thickness from every wing segment is used as input for the next program.

$$\sigma_{VM} = \sqrt{\frac{{\sigma_z}^2}{2} + 3{\tau_{xy}}^2} \tag{5.18}$$

$$\sigma_{critical} = \frac{k\pi E}{12(1-v^2)(b/t)^2} \tag{5.19}$$

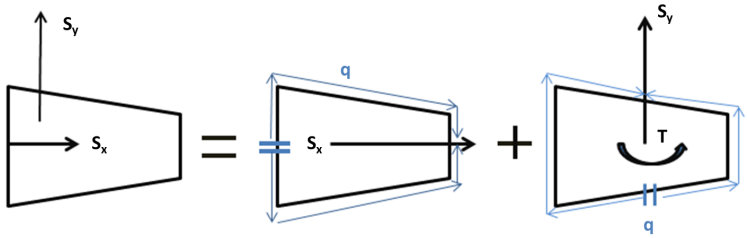

Figure 5.11: Shear flow through wing box cross section due to the vertical and horizontal shear forces

Laminate Analysis using Kolibri

A second program called *Kolibri* is used to analyse the strength of carbon fibre reinforced polymer laminates. This material is chosen as a result from the material selection for the wing structure that is reported in the Mid-Term Report of *Torero* [19]. The laminates are given the thickness that is obtained with *Matlab*. Then different ply lay-ups and orientations are considered to increase the laminate strength such that it can cope with the stresses resulting from the isotropic analysis. Ply properties for this approach are given in Table 5.4. To ensure robustness of the laminate, specific design rules are applied that result in quasi-isotropic properties [55]:

- Laminates are symmetric and balanced to maximise buckling strength
- Laminates should have at least 10 % of their plies in 0 °, ±45 ° and 90 °
- Maximum layer thickness is limited to 4 plies
- Maximum percentage of plies in any direction is 60 %
- Tapering in between segments is performed by adding or removing only the outer plies

After calculating the buckling strength of the laminate, the limiting failure case is determined which is either buckling or exceeding the yield stress. For the limiting case the margin of safety is calculated and it is kept as low as possible, close to zero.

5.6.3 Verification

Before the results from the numerical approach are discussed, first the code is verified by means of a unit test for the root section of the wing. Equations (5.11) to (5.16) are solved analytically to find all intermediate results. A comparison between the analytical and numerical solutions is given in Table 5.2. Parameters y_c and I_{xy} are not included in this table because both results give a zero value. The reason for this value is the skin thickness being equal for top and bottom skins to fly both positive and negative g-turns, resulting in a cross section that is symmetrical around the x-axis. Also it can be seen that the shear force in horizontal direction S_x and the corresponding bending moment M_y due to drag are not included because these two are only 0.60 % of the shear force S_y and bending moment M_x respectively caused by the lift distribution.

Table 5.2: Numerical approach unit test

Parameter	Numerical Result	Analytical Result	Error *[%]*
x_c $[m]$	-0.0537	-0.0502	6.5
I_{xx} $[m^4]$	$0.819 \cdot 10^{-4}$	$0.84909 \cdot 10^{-4}$	3.37
I_{yy} $[m^4]$	$0.99 \cdot 10^{-3}$	$1.01 \cdot 10^{-3}$	1.9
S_y $[kN]$	54.0	54.0	0
M_x $[kNm]$	64.1	64.0	0.16

Table 5.3: Numerical approach system test

Parameter	Numerical Result	Analytical Result	Error *[%]*
σ_z $[Pa]$	$-1.1513 \cdot 10^8$	$-1.1455 \cdot 10^8$	0.5
τ_{xy} $[Pa]$	$-2.3020 \cdot 10^7$	$-2.4256 \cdot 10^7$	5.4

Besides the unit test, a system test is performed particularly for the front spar at the root section of the wing, at maximum y value. The normal stress and shear stress are calculated and the error between both solutions is presented in Table 5.3. The error in normal stress is small because a simple equation is used from which the shear force and moment of inertia are already verified. The error for shear stress is more significant because the numerical solution uses discretisation to evaluate the shear stress at different points along the spar, while the analytical solution uses integration.

5.6.4 Numerical solution

The previously described numerical approach is applied to four wing segments. With four elements per segments, 16 elements are considered in total. To avoid stress concentrations, the thickness is assumed to reduce linearly from root to tip as depicted in Figure 5.14a. A layout of the connection of spars to the skin is shown in Figure 5.14b. The load distributions from tip to root are shown in Figure 5.12. The presented loads are averaged per section. Therefore the shear force and torque are not equal to zero at segment one. The maximum vertical shear force is 54 kN, with a corresponding maximum bending moment of 64 kNm at the root section. The torque is also maximum at the root with a value of 32 kNm.

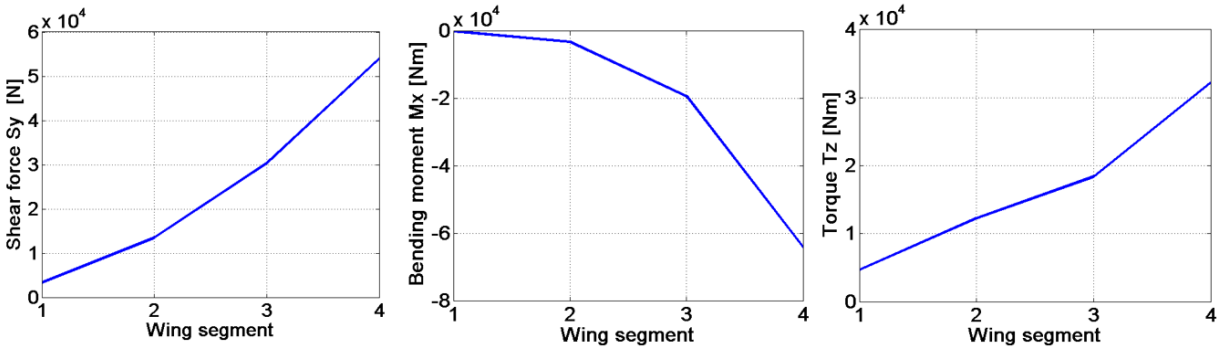

Figure 5.12: Load distribution. Wing segments go from tip to root.

For all laminates that have been designed, the margins of safety for both normal and shear stress are shown in Figure 5.13. Laminates 1, 2 and 5 are rejected because the negative margin of safety indicates failure under applied loads. Table 5.5 presents the selected laminate L and thickness of every element for each wing segment and Table 5.6 gives the lay-up sequence of the laminates. In the latter, the subscript s indicates a symmetric lay-up is applied. It can be observed that the laminates of top and bottom skins of every wing segment are similar, to provide the same structural integrity in both positive and negative g-turns.

Table 5.5: Laminates types and thicknesses of wing box elements

Segment #		Wing box element			
		Front	**Rear**	**Top**	**Bottom**
1	Laminate	L3	L3	L8	L8
	Thickness $[mm]$	1.6	1.6	0.8	0.8
2	Laminate	L4	L11	L8	L8
	Thickness $[mm]$	2.4	3.2	0.8	0.8
3	Laminate	L6	L12	L9	L9
	Thickness $[mm]$	4.8	4	1.6	1.6
4	Laminate	L7	L13	L10	L10
	Thickness $[mm]$	8.4	7.2	2.8	2.8

Table 5.4: Ply Description

E_1	$143.4\,GPa$	σ_{c1}	$1723\,MPa$	t	$0.2\,mm$
E_2	$11.37\,GPa$	σ_{c2}	$306.1\,MPa$	ρ	$1580 kg/m^3$
G_{12}	$5.17\,GPa$	σ_{t1}	$2592\,MPa$	μ	$0.316 kg/m^2$
v	0.32	σ_{t2}	$115.8\,MPa$	τ	$120\,MPa$

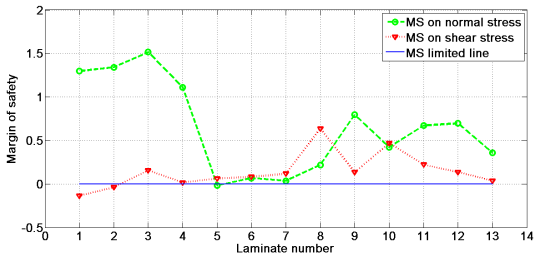

Figure 5.13: Margin of Safety of Laminates

Table 5.6: Laminate lay-up

Laminate #	lay-up $[^\circ]$	Laminate #	Lay-up $[^\circ]$
L3	$[90/\pm 45/0]_s$	L12	$[90/\pm 45/0/(\pm 45)_3]_s$
L4	$[90/\pm 45/0/\pm 45]_s$	L13	$[90/\pm 45/0/(\pm 45)_6/(90/0)]_s$
L6	$[90/\pm 45/0/(\pm 45)_3/(90/0)]_s$	L8	$[90/0]_s$
L7	$[90/\pm 45/0/(\pm 45)_4/(90/0)_4/0]_s$	L9	$[90/0/\pm 45]_s$
L11	$[90/\pm 45/0/(\pm 45)_2]_s$	L10	$[90/0/\pm 45/0/\pm 45]_s$

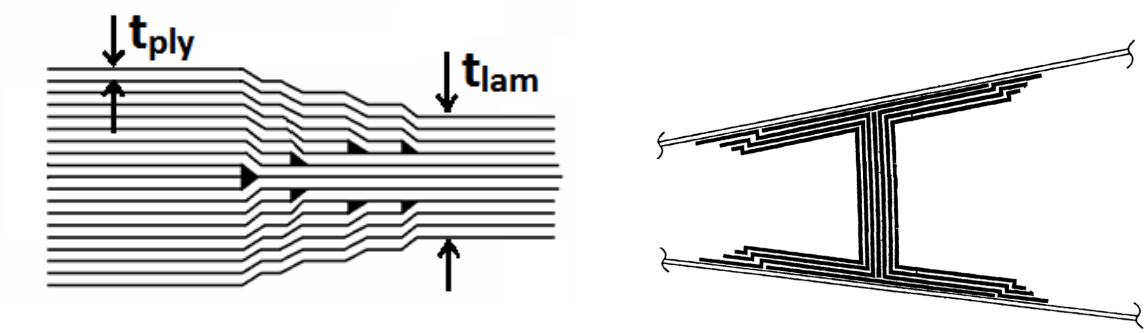

(a) Visualisation of laminate tapering *(b) Spar and skin interconnection*

Figure 5.14: Properties of laminates used for wing structural design

Concluding from the results, the composite wing structure is designed to withstand 15g for positive and negative turns, under the assumption that quasi-isotropic composite material can be treated as fully isotropic material. The two spars take most of the bending load, and two skins take most of the torsion. The maximum loads on the structure are 54 kN vertical shear load and a 64 kNm bending moment. The front spar has a thickness of $t_{front} = 8.4\,mm$ at the wing root, while the rear spar thickness is $t_{rear} = 7.2\,mm$. The skin thickness for both top and bottom panel is $t_{top} = t_{bottom} = 2.8\,mm$ at the root. Five ribs are used to lower the plate aspect ratios of wing elements to increase the value of buckling coefficients as shown in Figures D.1a and D.1b, Appendix D. This approach is taken to sufficiently increase the critical buckling stress. The leading and trailing edge skins that are not part of the wing box are also constructed from carbon fibre reinforced polymer with a thickness of 1 mm. It is assumed this thickness is sufficient to keep the wing shape uniform along the wing span and minimise wing deflection, while providing pylon impact protection. Additional research, simulations and tests are required to justify this assumption.

The total wing box weight is 62 kg by taking a material density of Carbon Fibre Reinforced Plastic (CFRP) of $\rho_{CFRP} = 1580\,kg/m^3$. Additional leading edge and trailing edge skins add 6.30 kg to the total wing weight, resulting in $W_w = 62 + 6.30 = 68.30\,kg$. An impression of the wing structure is provided in Figure 5.15 showing both the outer skin and internal structural elements.

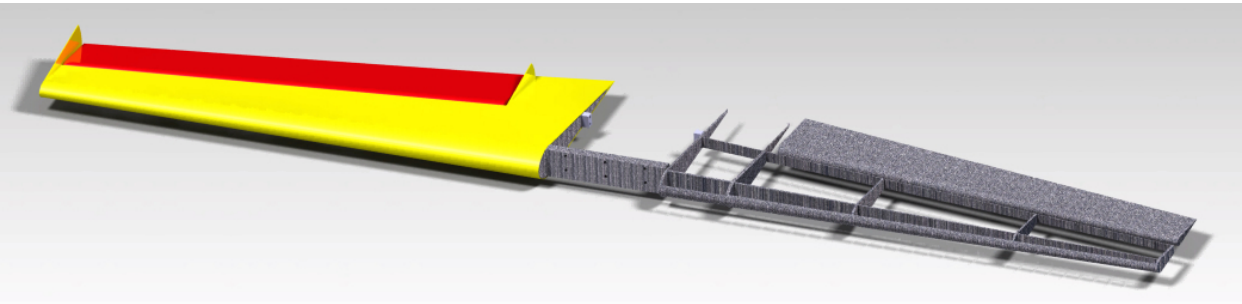

Figure 5.15: Impression of the wing structure and outer skin

5.6.5 Recommendations

The following recommendations for the wing structural design are considered. The code to analyse the isotropic wing structure is not validated by any experimental test data, neither data reference aircraft could be used. On the contrary, *Kolibri* is a professional analysis tool which should be validated.

Due to separate analysis of each single laminate, the number of laminates is limited to only four. If the accuracy of the approach is to increase, a more efficient analysis procedure should be considered

to design composite laminates. It is recommended to analyse the maximum deflection and rotation the wing has when subjected to the loads in turns at maximum load factor. An accurate analysis tool that is capable of accounting for non-isotropic materials and wing box sweep.

In designing the composite material, only symmetric laminates are used to approximate quasi-isotropic performance. This approach leads to overdesign of the wing elements. It is demonstrated that the margin of safety of a number of laminates is slightly more than one. If the wing structural design approach is adapted to only composite materials from the start, the laminates can be asymmetric to further optimise the design.

The new computed total wing weight is 68.30 kg, however the last iteration of the Class II weight estimation contains a total wing weight of 95 kg. Due to the fact that *Kolibri* could not be integrated into the preceding code it is not possible to automatically iterate the entire wing design. Further iterations should be performed to decrease the offset between these values.

Chapter 6

Empennage

The next step in the design process is sizing the empennage. Based on an extensive design option analysis that is executed in the Baseline Report [56] and in the Mid-Term Report [19] it is decided to use a conventional tail configuration. Furthermore, the horizontal tail and vertical tail are sized based on optimisation of the span and taper ratio.

XFLR5 is used to analyse different empennage designs. In order to aerodynamically optimise the performance of the horizontal and vertical tail, drag has to be minimised. The empennage consists of the horizontal and vertical tail plane, which have a NACA 0012 and a NACA 0009 airfoil, respectively. These airfoils have a low t/c and already have a low profile drag compared to other airfoils [57]. Therefore, the main drag contribution that has to be minimised is the induced drag. Induced drag can be minimised by adapting geometrical parameters such as taper and span. This optimisation process is executed for the horizontal tail. For the vertical tail different aspects are considered, such as the position of the aerodynamic centre and the wake interference from the horizontal tail.

6.1 Horizontal Tail

The tail has to generate sufficient lift to provide good controllability and stability characteristics to the aircraft. The control and stability analysis is performed by the Control & Simulation department that determines the required horizontal tail area. To size the empennage for minimum induced drag, the taper and span are modified.

Concerning the actual simulations of the horizontal tail in *XFLR5*, a similar procedure is used as for the planform design of the main wing. Both taper ratio and span are varied. For each configuration a run in *XFLR5* is executed. The resulting lift distribution is evaluated, as this provides the basis for quantifying the induced drag. The lift distribution is compared to the ideal elliptical lift distribution. The circulation for an elliptical lift distribution is defined in Equation (6.1), where Γ_0 is the circulation at half span, y is the spanwise location and b is the wing span.

$$\Gamma(y) = \Gamma_0 \sqrt{1 - \left(\frac{y}{b/2}\right)^2} \tag{6.1}$$

Several runs are executed in *XFLR5*, for different taper ratios. First a batch is created for the NACA 0012 profile, the 2D airfoil profile consists of 98 data points, in which all individual elements are then interpolated in order to run a 3D analysis for the main wing. The batch runs from $Re = 5 \cdot 10^5$ up to $Re = 9 \cdot 10^6$, which is a representative range of Reynolds numbers encountered during flight. The angles of attack for which the model is evaluated ranges from zero to ten degrees. For higher angles of attack the software becomes less reliable [41]. Now that the batch is refined, a 3D analysis of the horizontal tail is performed. The 3D analysis is performed using the Vortex Lattice Method, which is a numerical implementation of horseshoe vortex models.

To minimise the surface area of the horizontal tail the taper ratio of the wing is varied, while keeping the area that is found from the Class II weight estimation and the wing and power loading analysis the same, see Chapter 2. In Figure 6.1 - 6.4 the results of the *XFLR5* simulations for different taper ratios can be found.

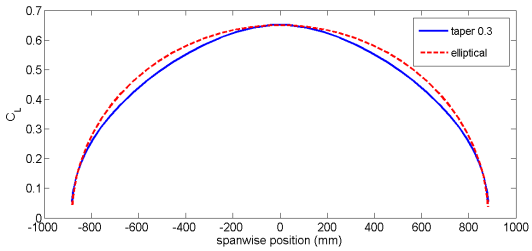

Figure 6.1: Tail lift distribution for a taper ratio of 0.3

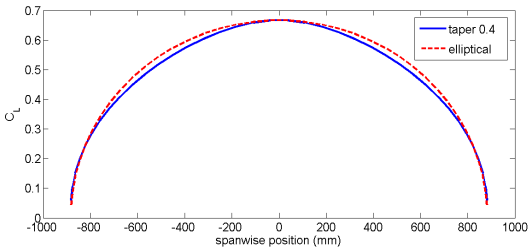

Figure 6.2: Tail lift distribution for a taper ratio of 0.4

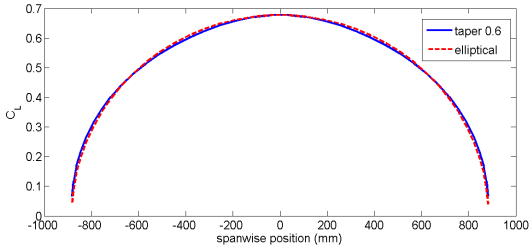

Figure 6.3: Tail lift distribution for a taper ratio of 0.6

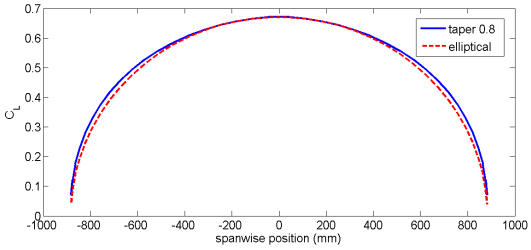

Figure 6.4: Tail lift distribution for a taper ratio of 0.8

The difference between values obtained from an elliptical lift distribution and the actual values of C_L, is determined. So the closer the difference is to zero, the better the elliptical distribution is approximated. The deviations from the elliptical lift distribution for different taper ratios can be found in Table 6.1.

Table 6.1: Deviation from elliptical lift distribution for different taper ratios of the horizontal tail

Taper ratio	Deviation from elliptical lift distribution
0.3	0.0206
0.4	0.0148
0.6	0.0106
0.8	0.0177

Based on Figures 6.1 - 6.4 and Table 6.1 it is concluded that a taper ratio of 0.6 gives a lift distribution that is closest to an elliptical lift distribution and therefore generates the lowest amount of induced drag for a given wing loading. Since the wing area and span are fixed so that the tail does not experience too much disruptions from the aileron wake the root chord of the horizontal tail is 0.7 m and the tip chord is 0.4 m.

A downside of the use of VLM in *XFLR5* is that it does not take viscosity into account. Therefore, the results for drag simulation could be more accurate. Especially for higher angles of attack viscous drag becomes more important, because the size of the boundary layers increases. A recommendation for future analysis is to use a more advanced program that has visous terms implemented in the code. Such a program would give more reliable results for higher angles of attack. [58]

6.2 Vertical Tail

The size of the vertical tail is largely dictated by the Control & Simulation department. An important criterion that determines the position of the vertical tail with respect to the horizontal tail is the wake interference from the horizontal tail. To limit wake interference, sufficient sweep needs to be implemented. The size of the vertical tail should also have a minimum size such that sufficient effective rudder area remains. Wake interference is further elaborated on in Section 7.4. The airfoil that is used for the vertical tail is the NACA 0009 airfoil as is sated in the Mid-Term Report [19]. The vertical tail does not have a large angle of attack during flight, therefore the

induced drag is limited. The shape of the vertical tail is designed to meet the controllability and stability requirements of the aircraft. Taking into account the previous considerations leads to the final vertical tail dimensions that can be found in Table B.1. The stability and controllability calculations on which these values are based on are described in Chapter 7.

6.3 Structure of Empennage

Taking into account the required aerodynamic characteristics of the empennage and considerations from the Control & Simulation department, the next step in designing the empennage is realising a load carrying structure. The entire empennage structure including the skins and internal structural elements, is made of carbon fibre reinforced polymer composite for the same reasons as stated for the main wing. Because the horizontal and vertical tail surfaces are smaller and produce less lift compared to the main wing, the load carrying structure is a single beam. Skins are added to provide the aerodynamic shape, which determined discussed in Sections 6.1 and 6.2.

The number of segments considered for the analysis procedure depicted in Figure 5.10 is two. Now an approach similar to the methodology described in 5.6 is taken. Neglecting the drag forces and weight of the structure itself, it is assumed that the maximum lift force acting on the horizontal tail $L_{hortail} = 10.1\,kN$ which is 11% of the maximum lift acting on the main wing which follows from Section 7.1. In Tabel 6.2 the laminates and the corresponding thicknesses are shown for the horizontal and vertical tails. Again the skin thickness is assumed to be $1\,mm$ to account for aerodynamic loads and to provide impact safety. The laminates used to construct the main spars of the empennage are listed in Table 6.2 and their corresponding the plie lay-up is given in Table 5.6. The total weights of horizontal tail and vertical tail are $18.7\,kg$ and $12\,kg$ respectively. Three ribs are used to prevent skins on the horizontal and vertical tail wings from buckling and to maintain the airfoil shapes. Figure 6.5 presents the internal structure and outside skins of the empennage subsystem.

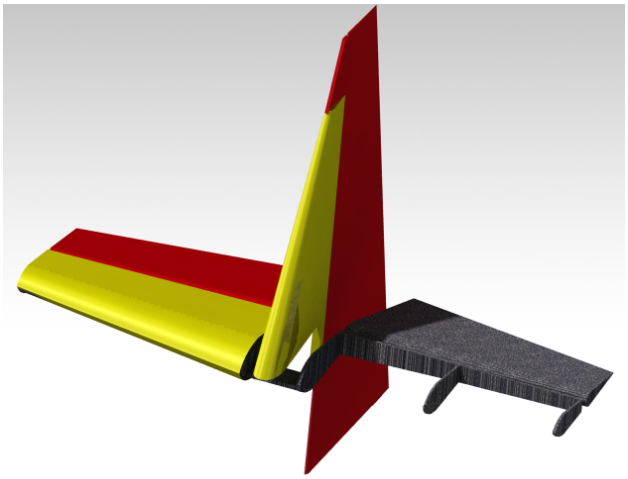

Figure 6.5: Impression of the empennage structure and outer skin

Table 6.2: Laminates and thicknesses for empennage structure.

Segment #		Horizontal tail	Vertical tail
1	Laminate number	L3	L3
	Thickness [mm]	1.6	1.6
2	Laminate number	L4	L11
	Thickness [mm]	2.4	3.2

6.4 Recommendations

The empennage preliminary design presented in the Sections 6.1 to 6.3 gives both the aerodynamic characteristics of the empennage and control aspects of the elevator and rudder. For the current approach, the main limitation in determining aerodynamic characteristics of the empennage design is that downwash of the main wing cannot be simulated using *XFLR5* reliably. A recommendation would be to use more advanced CFD software that can simulate this effect. Furthermore CFD offers an opportunity to analyse the effects of the propeller wake on the tail.

From the structural point of view, the empennage structure is simplified by assuming all loads are carried by one main spar, running from root to tip. In this preliminary analysis, only the lift acting on the horizontal tail surface is considered, acting at the main spar. Future analysis should include the torsion caused by deflections of the elevator and rudder. The magnitude of these torsions needs to be found by simulations or testing.

Chapter 7

Controls

Now most of the aircraft is designed, it is time to consider the controls. This chapter starts with the positioning of the wing and the tail sizing. The chapter continues with the design of the control surfaces: the ailerons, the elevator and the rudder. Next, aerodynamic balancing and mass balancing of these control surfaces are discussed. The control forces are discussed after which the cockpit configuration and the lights installed on the aircraft are elaborated on. Finally, the control and stability characteristics and eigenmotions of the aircraft are analysed.

7.1 Wing Position and Horizontal Tail Size

The position of the wing is determined based on a scissor plot combined with a c.g. range plot. A scissor plot shows the control and stability and stability limits of the aircraft and a c.g. range plot shows the minimum and maximum c.g. positions encountered during operation of the aircraft. Depending on the maximum allowed c.g. range, the position of the wing, measured from the nose, and the minimum horizontal tail size are calculated. The methodology behind constructing a scissor plot is explained in the Mid-Term Report [19].

Figure 7.1 shows the matching of the scissor plot and the c.g. range plot. The stability limit is plotted without any stability margin, which means the most aft allowed c.g. position corresponds to the condition in which the aircraft is neutrally stable.

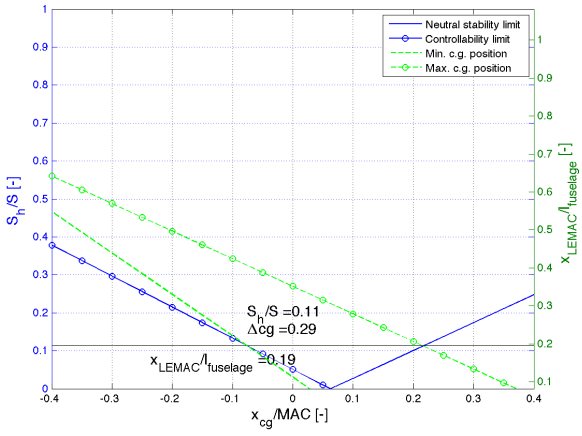

Figure 7.1: Scissor plot and c.g. range match

With a c.g. range of $\Delta c.g. = 0.29\bar{c}$, expressed in terms of the MAC, a horizontal tail surface area ratio of $S_h/S = 0.11$ and a wing position with respect to the fuselage length of $x_{LEMAC}/l_{fuselage} = 0.19$ are found. This is the minimum possible horizontal tail surface area to be able to cope with the shift in c.g. during operation of the aircraft. Any increase in tail surface area will lead to a larger tail than required, which yields an increase in weight. Since the aircraft needs to be lightweight, it is decided to design for the minimum horizontal tail surface area.

Since the empty weight of the aircraft is lower than the minimum empty weight required by *Red Bull*, a penalty weight has to be carried on board. This penalty weight can be used to shift the c.g. to improve the controllability of the aircraft. For better controllability the penalty weight should be positioned such that the c.g. lies as far to the back as possible, without compromising the longitudinal stability of the aircraft. In other words, for high controllability the c.g. should be as close to the neutral stability limit as possible.

7.2 Ailerons

Now that the wing positioning is determined, it is important to look at the control surfaces. First the aileron is considered.
Reference aircraft can achieve roll-rates of about 400 to 420 $°/s$. For reference aircraft presented in Appendix A ailerons generally take up about 80 to 90% of the span.
First the size of the ailerons is determined and afterwards the control system for these ailerons is designed.

7.2.1 Aileron Sizing

To design the aileron the inputs listed in Table 7.1 are used.

Table 7.1: inputs for aileron sizing

Input	Symbol	Value	Unit	Obtained from
Wing Surface	S	7.29	m^2	Wing design
Aspect Ratio	A	7.86	-	Wing design
Taper Ratio	λ	0.5	-	Wing design
Wing Lift Curve Slope	$C_{L_{\alpha_w}}$	4.69	rad^{-1}	Wing design
Wing Span	b	7.6	m	Wing design
Inboard Aileron span	b_{ai}	0.76	m	Iterative process on aileron design
Outboard Aileron span	b_{ao}	3.8	m	Iterative process on aileron design
Mean Aerodynamic Chord	$\bar{C}$	0.99	m	Wing design
Wing root chord	C_r	1.28	m	Wing design
Chord ratio aileron	$\frac{C_a}{C}$	0.3	m	Iterative process on aileron design
Manoeuvre Speed	V_m	97.2	$m \cdot s^{-1}$	Reference aircraft
Zero-Lift Drag coefficient	C_{D0}	0.017	-	Wing design
Maximum Aileron Deflection	$\delta_{a_{max}}$	25	°	Iterative process on aileron design

The expected output values are roll rate, roll authority and roll damping. These values are needed because they determine the roll behaviour and lateral stability of the aircraft. The first values that are calculated are the inboard and outboard span location of the aileron, y_i and y_o respectively, see Equations (7.1a) and (7.1b). The higher y_o and the smaller y_i the higher the roll rate is, since the aileron has a larger surface in that case.

$$y_i = \frac{b_{ai}}{b} \cdot \frac{b}{2} \tag{7.1a}$$

$$y_o = \frac{b_{ao}}{b} \cdot \frac{b}{2} \tag{7.1b}$$

Another parameter is determined is the aileron effectiveness C_{δ_a}. This is a function of the ratio between the aileron chord $\frac{C_a}{C}$ and the mean aerodynamic chord $\bar{C}$ and can be found from Figure 7.2 [59]. The higher the aileron efficiency, the higher the roll authority and thus the higher the roll rate.

From Figure 7.2 it is found that for a chord ratio $\frac{C_a}{C} = 0.3$ the efficiency $\tau_a = 0.52$.

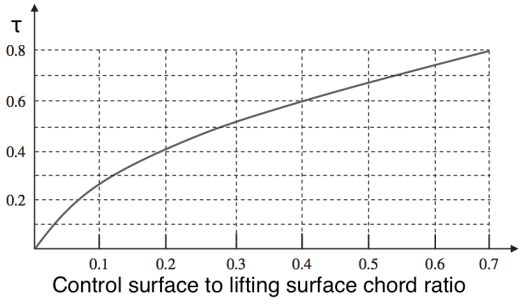

Figure 7.2: Control surface efficiency versus chord percentage

With these parameters are known, the roll authority, $C_{l_{\delta_a}}$, can be calculated using Equation (7.2). A higher roll authority will result in a higher roll rate.

$$C_{l_{\delta_a}} = \frac{2C_{L_{\alpha_w}} C_r}{Sb} \cdot \left(\frac{y_o^2 - y_i^2}{2} + \frac{2}{3} \frac{\lambda - 1}{b} \left(y_o^3 - y_i^3 \right) \right) \tag{7.2}$$

One more parameter has to be known before the roll rate can be calculated, which is the roll damping C_{l_p}. This can be calculated using Equation (7.3). The roll damping counteracts the roll, so the higher the roll damping, the lower the roll rate.

$$C_{l_p} = -\left(C_{L_{a_w}} + C_{D_0}\right) \frac{c_{root} \cdot b}{24S} \left(1 + 3\lambda\right) \tag{7.3}$$

Subsequently the roll rate can be computed using Equation (7.4)

$$p = -\frac{C_{l_{\delta_a}}}{C_{l_p}} \delta_{a_{max}} \frac{2V_m}{b} \tag{7.4}$$

The resulting outputs are shown in Table 7.2

Table 7.2: Outputs aileron design

Output	Symbol	Value	Unit
Roll rate	p	475	$^\circ/s$
Roll authority	$C_{l_{\delta_a}}$	-0.51	-
Roll damping	C_{l_p}	-0.65	-

7.2.2 Aileron Control System

As recommended by [45], one trick to increase the chances of winning the *Red Bull Air Race* is to use non-linear aileron deflection, where the rate of deflection is increased over time, rather than applying a maximum deflection instantly. This will cause the roll rate to develop slightly slower, but the drag during the roll maybe decreases. In the current racing aircraft this is only done by the pilot himself, but in the design of the *T-16* a system is integrated which provides a non-linear aileron deflection for constant rate of stick deflection. The challenge for such a system is that no electronic systems are allowed for the primary controls, thus a mechanical solution is required.

The system, that is integrated in the *T-16*, is a simple, fully mechanical system. Figure 7.3 shows an schematic impression of the system. The transfer mechanism mentioned in figure 7.3 is shown in more detail in figure 7.5. It shows two rods, connected by a flat hinge, attached to a slider and a plate with a curved slot. This slider is attached to a spring, which is not shown in the render, to keep it at its neutral position — represented by the dashed circle — when no stick deflection is applied. The rods represent the connection to the stick on one end and the connection to the aileron on the other. Figure 7.4 gives an impression of where the mechanism would be positioned and finally figure 7.6 shows the slider hinge that is required at the aileron connection.

As can be seen in figure 7.3, subsequent equal amounts of stick deflection in x-direction, will yield two unequal amounts of deflection in y-direction, which governs aileron deflection. This requires however, that the connection to the aileron also shifts in x-direction, which is why a slider hinge as depicted in figure 7.6 is necessary. The dimensions of this hinge and the transfer mechanism are dependent on the maximum stick deflection and any transmissions which may be added to any of both rods.

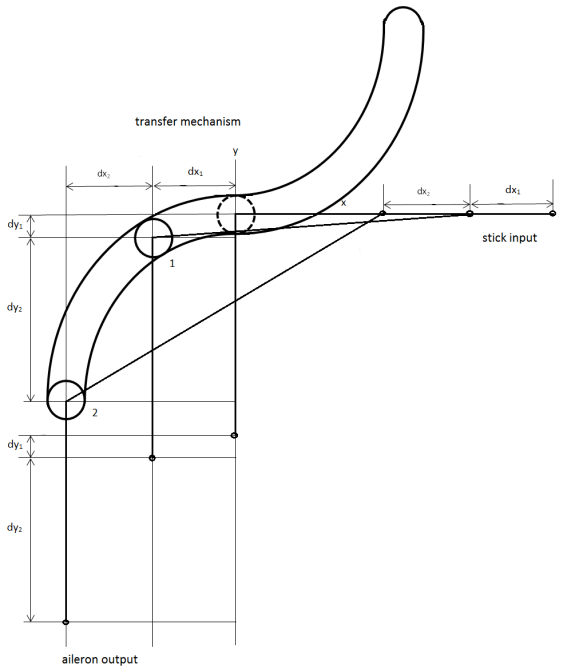

Figure 7.3: System schematic

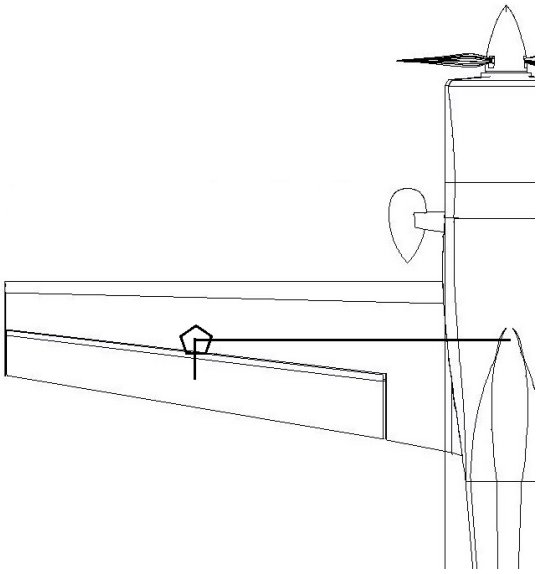

Figure 7.4: Mechanism location

The effect of the whole system is that a constant rate of deflection of the stick will yield an increasing rate of deflection of the aileron. The spring in the transfer mechanism limits the speed at which deflection can be applied. All together, it still enables fast roll, but more controlled and with less drag compared to a more instantly applied aileron deflection.

Figure 7.5: Render or transfer mechanism

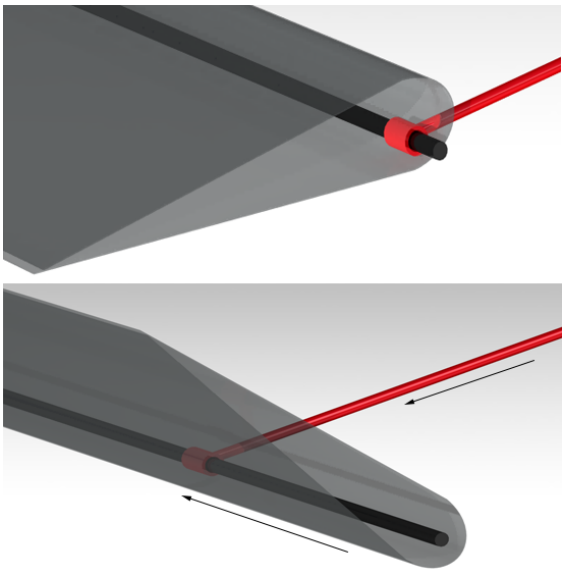

Figure 7.6: Aileron slider hinge

7.3 Elevator

The preliminary aileron design is established. Therefore the design can continue by considering the control surface that is located on the horizontal tail plane. First the size of elevator is determined after which the control system is designed.

7.3.1 Elevator Sizing

The elevator is the movable surface at the trailing edge of the horizontal tail that provides pitch control for the aircraft. A deflection of the elevator effectively changes the camber of the horizontal tail. The air is deflected either upward or downward, which generates a force in vertical direction and a corresponding pitching moment about the c.g. of the aircraft. For aircraft in general, the take-off run is usually the most critical phase for which the elevator should be designed. The elevator must be able to provide a moment that is large enough to facilitate rotation about the main landing gear, otherwise the aircraft cannot take off. However, for aerobatic (racing) aircraft pull-up manoeuvres are most crucial for the elevator design. Since the *T-16* is a taildragger aircraft, no rotation is required during take-off [60]. Taildraggers are usually designed to have an angle of attack near the stall angle when standing on the ground, which is convenient for landing. However, for take-off the angle of attack should be smaller. During take-off in a taildragger, the pilot should push the stick slightly forward to lower the nose to climb attitude (i.e. lift the tail) and simply let the aircraft lift off [60].

The inputs for the elevator design are listed in Table 7.3.

Table 7.3: Input parameters for the elevator design.

Input	Symbol	Value	Unit
Maximum load factor	n_{max}	10	$[-]$
Gravitational acceleration	g	9.81	$[m \cdot s^{-1}]$
Manoeuvre speed	V_m	91.7	$[m \cdot s^{-1}]$
Horizontal tail efficiency	$\frac{V_h}{V}$	0.95	$[-]$
Air density	ρ	1.225	$[kg \cdot m^{-3}]$
Wing reference area	S	7.29	$[m^2]$
Mean aerodynamic chord	$\bar{c}$	0.99	$[m]$
Pitch damping	C_{m_q}	-5.97	$[rad^{-1}]$
Gearing ratio	$\frac{d\delta_e}{ds_e}$	1	$[-]$

7.3.2 Pull-Up Manoeuvre

During the race the pilot is not allowed to exceed the maximum load factor of 10g, as was stated in Section 1.3. For a pull-up manoeuvre at a load factor n, the required pitch rate at manoeuvre speed V_m is given by Equation (7.5) [61].

$$q_{req} = \frac{(n_{max} - 1)g}{V_m} \tag{7.5}$$

The moment required to achieve this pitch rate is given by Equation (7.6).

$$M_q = \tfrac{1}{2}\rho V_m^2 S\bar{c} C_{m_q} \frac{q\bar{c}}{2V_m} \tag{7.6}$$

Dividing this moment by the tail arm l_h yields the force that should be provided by the tail, as shown in Equation (7.7).

$$F_e = \frac{1}{l_h}\tfrac{1}{2}\rho V_m^2 S\bar{c} C_{m_q} \frac{q\bar{c}}{2V_m} \tag{7.7}$$

This force is generated by deflecting the elevator. Equation (7.8) is an expression for the elevator force in terms of the hinge moment. This expression is valid under the assumption that the gearing ratio is equal to one, i.e. the control system is designed such that the stick force is exactly equal to the elevator force. Equation (7.8) can be used to relate the elevator force to the required elevator deflection.

$$F_e = -\tfrac{1}{2}\rho V_{m_h}^2 S_e \bar{c}_e C_{h_e} \tag{7.8}$$

The hinge moment C_{h_e} can be split up into a hinge moment due to the angle of attack of the horizontal tail, a hinge moment due to the elevator deflection and a hinge moment due to the trim tab deflection. Substituting these separate contributions for C_{h_e} into Equation (7.8) yields Equation (7.9), from which the required maximum elevator deflection can be obtained.

$$F_e = -\tfrac{1}{2}\rho V_{m_h}^2 S_e \bar{c}_e \left(C_{h_\alpha}\alpha_h + C_{h_{\delta_e}}\delta_e + C_{h_{\delta_{t_e}}}\right) \tag{7.9}$$
$$\delta_e = \left[-\frac{F_e}{\frac{1}{2}\rho V_{m_h}^2 S_e \bar{c}_e} - \left(C_{h_\alpha}\alpha_h + C_{h_{\delta_{t_e}}}\right)\right]\frac{1}{C_{h_{\delta_e}}}$$

In the expression for the elevator deflection, α_h is defined as in Equation (7.10), where the zero lift angle of attack α_0 and the horizontal tail incidence angle i_h are assumed to be equal to zero.

$$\alpha_h = (\alpha - \alpha_{L=0})\left(1 - \frac{\mathrm{d}\varepsilon}{\mathrm{d}\alpha}\right) + (\alpha_{L=0} + i_h) \tag{7.10}$$

Substituting Equation (7.10) into Equation (7.9), equating Equation (7.7) to Equation (7.9) and rewriting gives the final expression for the required maximum elevator deflection, Equation (7.11).

$$\delta_e = \frac{1}{C_{h_\delta}}\left\{-\left(\frac{V_m}{V_{m_h}}\right)^2 \frac{S}{S_e}\frac{\bar{c}^2}{\bar{c}_e}\frac{C_{m_q}}{l_h}\frac{q_{req}}{2V_m} - \left[C_{h_\alpha}\alpha\left(1 - \frac{\mathrm{d}\varepsilon}{\mathrm{d}\alpha}\right) + C_{h_{\delta_{t_e}}}\delta_{t_e}\right]\right\} \tag{7.11}$$

If the elevator deflection exceeds the maximum allowed deflection, the elevator should be resized. To decrease the required deflection, the elevator size should be increased. This process is iterated until a feasible elevator design is obtained with a size as low as possible. It is of key importance to limit the size of the elevator, since the control forces increase with increasing elevator size. If the elevator is too large, the control forces may become too high and the pilot would be unable to control the aircraft. The elevator control force is elaborated on in Section 7.6.3.

The output parameters for the elevator design are presented in Table 7.4

Table 7.4: Output parameters for the elevator design.

Output	Symbol	Value	Unit
Elevator chord ratio	$\frac{c_e}{c_h}$	0.53	[−]
Elevator span	b_e	1.62	[m]
Max. elevator deflection	$\delta_{e_{max}}$	29	[°]

7.3.3 Elevator Control System

After the elevator is sized, the control system of the elevator is designed. For the elevator push-pull rods are used. This option is chosen over cables, simply because cables are not a feasible option for the elevator, as they need two points of attachments with a certain vertical distance between them. This would be hard to implement in the fuslage structure. An example of this elevator control system is shown in Figure 7.7 [62]. Figure 7.7 is taken from the maintenance manual of the *Extra 330LX* [33], which is a two-seater and therefore has two control sticks.

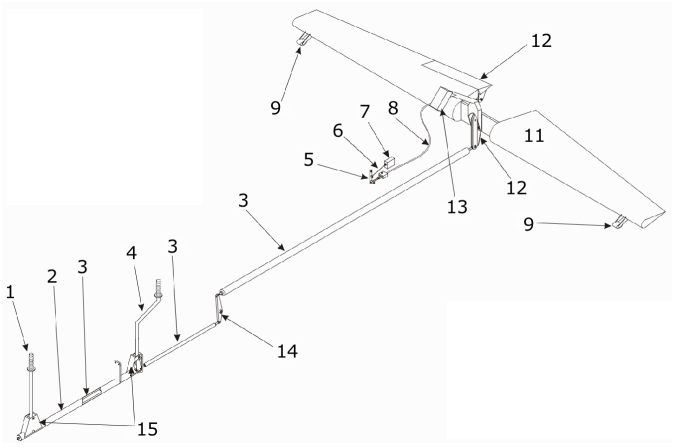

1. Front seat stick
2. Torque tube
3. Push–pull rod
4. Rear seat stick
5. Trim lever
6. Trim servo rod
7. Trim servo
8. Trim control bowden cable mechanism
9. Mass balance weights
10. Trim tab
11. Elevator
12. Elevator actuator arm
13. Mass balance weights
14. Rocker type bellcrank
15. Travel stops

Figure 7.7: Elevator control system

When the pilot pulls the stick towards him, the rod in the front moves forward, which causes the second rod after the hinge to move backward. Hence, the elevator deflects up and generates a downward tail force, causing the aircraft to pitch up. When the pilot pushes the stick away from him, the elevator deflects down and generates an upward tail force, causing the aircraft to pitch down.

7.4 Rudder

The last control surface that has to be designed is the rudder, which is located on the vertical tail.

7.4.1 Rudder Sizing

First the rudder control surface has to be sized before the design of the rudder control system. The rudder is the movable surface located at trailing edge of the vertical tail that provides directional control for the aircraft. By deflecting the rudder the camber of the vertical tail is changed. Therefore, a side-force is generated, which causes a yawing moment about the c.g. of the aircraft. In addition, a rolling moment is generated, as the vertical tail is usually located above the c.g. of the aircraft. In general, the main functions of the rudder are providing directional control and directional trim. The rudder plays different roles depending on the type of aircraft and the flight condition. For the design of the rudder the most critical control function must be considered. Three control functions that apply to all aircraft are the following:

- *Cross-wind landing*: The rudder should provide directional control to keep the aircraft aligned with the runway heading during cross-wind landings
- *Coordinated turn*: The rudder must allow the aircraft to perform a coordinated turn, i.e. without side-slip and lateral acceleration
- *Adverse yaw*: The rudder should be able to overcome the adverse yaw generated by the ailerons when performing a turn

However, for single engine aerobatic racing aircraft these are not the most important functions of the rudder. For this type of aircraft the most crucial function of the rudder is *spin recovery* [59]. When performing aerobatic manoeuvres the aircraft can get into a spin, either intentionally or unintentionally. Spin is generally characterised by fast rotation about the vertical axis and a fully stalled wing. The spin is a combination of stall, roll, yaw and dive. If the aircraft cannot recover from such spin, it will inevitably crash.

The inputs for the rudder design are listed in Table 7.5.

Table 7.5: Input parameters for the rudder design.

Input	Symbol	Value	Unit
Number of turns to recover	n_{turns}	1	$[-]$
Initial spin rate	ω_{start}	0	$[rad \cdot s^{-1}]$
Final spin rate	ω_{end}	4.19	$[rad \cdot s^{-1}]$
Moment of inertia about X_b	I_{xx}	355	$[kg \cdot m^2]$
Moment of inertia about Z_b	I_{zz}	2065	$[kg \cdot m^2]$
Product of inertia	I_{xz}	100	$[kg \cdot m^2]$
Angle of attack during spin	α	60	$[°]$
Air density	ρ	1.225	$[kg \cdot m^{-3}]$
Stall speed	V_{stall}	29.2	$[m \cdot s^{-1}]$
Wing reference area	S	7.29	$[m^2]$
Wing span	b	7.6	$[m]$
Vertical tail lift curve slope	$C_{L_{\alpha_v}}$	2.41	$[rad^{-1}]$
Vertical tail arm	l_v	4.0	$[m]$
Vertical tail efficiency	$\frac{V_v}{V}$	0.95	$[-]$
Vertical tail aspect ratio	A_v	1.9	$[-]$
Vertical tail half chord sweep	$\Lambda_{0.5\bar{c}_v}$	0.395	$[rad]$
Compressibility correction	β	1	$[-]$
Vertical tail airfoil efficiency	η	0.95	$[-]$

7.4.2 Spin Recovery

If the aircraft gets into a spin, the rudder should be able to provide enough control power to oppose the spin rotation and recover from the spin. Typical angles of attack during spin are 30 to 60 degrees and a rate of spin of 120 to 240 $°/s$ (20 to 40 rpm). The larger the angle of attack, the larger the rate of spin [59]. Due to the high angles of attack encountered during spin, the vertical tail may be partially in the wake of the horizontal tail. This reduces the effectiveness of the rudder and the vertical tail as a whole. Therefore, it is important to make sure that the rudder is never completely in the wake of the horizontal tail and that the effective rudder area is large enough to recover from spin. According to [63], as a guideline, at least one third of the rudder and vertical tail should be outside the wake. However, if the horizontal tail can be positioned such that a larger effective rudder area can be guaranteed during spin, the rudder can be sized smaller.

CS-23 and FAR-23 specifications have specific requirements for spin recovery. CS-23 specifications require the aircraft to recover from spin in "not more than 1.5 turns after applying recovery controls" [14]. FAR-23 specifications, on the other hand, require recovery from spin in "not more than one additional turn after initiation of the first control action for recovery" [64]. Hence, FAR-23 poses a more stringent requirement on spin recovery. Since the *Red Bull Air Race* is an international event and may be held in the USA, the more stringent FAR-23 spin recovery requirement is considered for the rudder design.

With an assumed rate of spin of 240 $°/s$, the required spin recovery yaw acceleration $\dot{r}_{SR}$ can be determined based on the FAR-23 spin recovery requirement. The number of turns n_{turns} after time t is simply the average spin rate multiplied by t, divided by 360 °, as in Equation (7.12).

$$n_{turns} = \frac{1}{360} \frac{\omega_{start} + \omega_{end}}{2} t \tag{7.12}$$

The rate of spin is initially zero ($\omega_{start} = 0$) and increases to the assumed value of 240 $°/s$ ($\omega_{end} = 240$ $°/s$). Furthermore, the aircraft should recover from spin in one turn ($n_{turns} = 1$). Equation (7.12) can be rewritten by substituting $\omega_{end} = \dot{\omega} t$ and $\omega_{start} = 0$, which yields Equation (7.13).

$$n_{turns} = \frac{1}{360}\frac{1}{2}\dot{\omega}t^2 \tag{7.13}$$

The required rate of spin recovery yaw rate is then obtained from Equation (7.14).

$$\dot{r}_{SR} = 2(360)\frac{n_{turns}}{t^2} \tag{7.14}$$

The required spin recovery yawing moment N_{SR} that should be generated by deflecting the rudder can be computed using Equation (7.15) [59].

$$N_{SR} = \left(\frac{I_{xx}I_{zz} - I_{xz}^2}{I_{xx}}\right)_w \dot{r}_{SR} \tag{7.15}$$

The moments and product of inertia in Equation (7.15) are expressed in the wind-axis system (indicated by the subscript w). The aircraft moments and product of inertia, which are expressed in the body-fixed reference frame, should therefore be transformed to this wind-axis system using the transformation given in Equation (7.16) [59].

$$\begin{bmatrix} I_{xx_w} \\ I_{zz_w} \\ I_{xz_w} \end{bmatrix} = \begin{bmatrix} \cos^2\alpha & \sin^2\alpha & -\sin 2\alpha \\ \sin^2\alpha & \cos^2\alpha & \sin 2\alpha \\ \frac{1}{2}\sin 2\alpha & -\frac{1}{2}\sin 2\alpha & \cos 2\alpha \end{bmatrix} \begin{bmatrix} I_{xx_b} \\ I_{zz_b} \\ I_{xz_b} \end{bmatrix} \tag{7.16}$$

The required spin recovery yawing moment N_{SR}, computed with Equation (7.15), can also be expressed as in Equation (7.17) [59]. In this equation the stall speed is considered, because during spin the aircraft stalls. At low speed the rudder generates the smallest side force and is therefore the least effective.

$$N_{SR} = \tfrac{1}{2}\rho V_{stall}^2 SbC_{n_{\delta_r}}\delta_r \tag{7.17}$$

Rewriting Equation (7.17) yields an expression for the required rudder deflection δ_r, Equation (7.18). This is the rudder deflection needed to generate the required spin recovery yawing moment.

$$\delta_r = \frac{2N_{SR}}{\rho V_{stall}^2 SbC_{n_{\delta_r}}} \tag{7.18}$$

Subsequently, the rudder control derivative during spin $C_{n_{\delta r}}$ follows from Equation (7.19).

$$C_{n_{\delta_r}} = -C_{L_{\alpha_v}}\frac{S_{v_e}l_v}{Sb}\left(\frac{V_v}{V}\right)^2 \tau_r \frac{b_{r_e}}{b_v} \tag{7.19}$$

Where:

- $C_{L_{\alpha_v}}$ is the lift curve slope of the vertical tail, estimated using the DATCOM method [65] presented in Equation (7.20)
- S_{v_e} is the effective vertical tail surface area
- b_{r_e} is the effective rudder span
- τ_r is the control surface efficiency, obtained from Figure 7.2

$$C_{L_{\alpha_v}} = \frac{2\pi A_v}{2 + \sqrt{4 + \left(\frac{A_v\beta}{\eta}\right)^2\left(1 + \frac{\tan\Lambda_{0.5\bar{c}_v}{}^2}{\beta^2}\right)}} \tag{7.20}$$

The required rudder deflection is then obtained from Equation (7.21).

$$\delta_r = \frac{2N_{SR}}{\rho V_{stall}^2 SbC_{n_{\delta_r}}} \tag{7.21}$$

This rudder deflection may not exceed the maximum allowed deflection. Maximum deflections are typically between 25 and 30 ° [59]. Deflections larger than that may cause the vertical tail to stall. The required rudder deflection can be influenced among others by changing the vertical tail size and the dimensions of the rudder (i.e. chord ratio and span), but it also depends on the effective rudder span and effective vertical tail area. The final rudder design output parameters are listed in Table 7.6.

Table 7.6: Output parameters for the rudder design.

Output	Symbol	Value	Unit
Rudder chord ratio	$\frac{c_r}{c_v}$	0.7	$[-]$
Rudder span	b_r	1.43	$[m]$
Spin recovery time	t_{SR}	3	$[s]$
Rate of spin recovery yaw rate	$\dot{r}_{SR}$	1.40	$[rad \cdot s^{-2}]$
Spin recovery yawing moment	N_{SR}	651	$[Nm]$
Rudder control derivative	$C_{n_{\delta_r}}$	-0.079	$[rad^{-1}]$
Required max. rudder deflection	δ_r	-0.52	$[rad]$

The maximum rudder deflection of $-0.52\ rad$ is equivalent to an angle of 29.8°, which is smaller than the maximum allowed deflection of 30 °.

7.4.3 Horizontal Tail Positioning

The required rudder deflection to recover from spin can be lowered if the effective rudder and vertical tail area can be increased. This can be achieved by changing the position of the horizontal tail with respect to the vertical tail. To ensure that the effect of the horizontal tail wake on the vertical tail is limited during spin, the horizontal tail can either be shifted forward and up or it can be shifted aft. Figure 7.8 [63] shows how the position of the horizontal tail changes the area of the vertical tail and rudder affected by the wake.

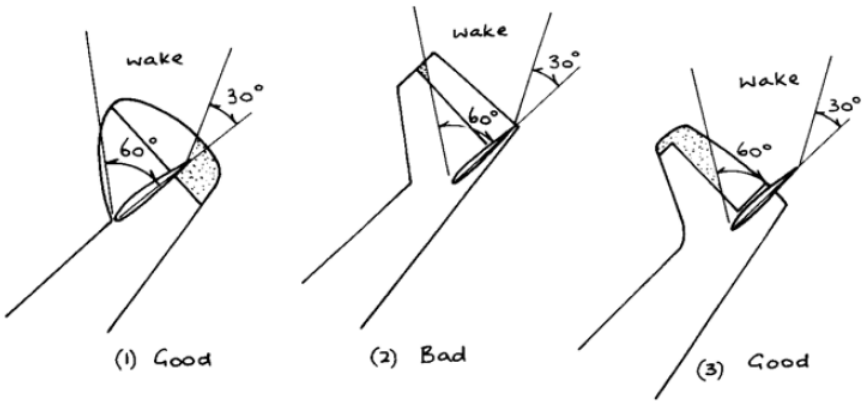

Figure 7.8: Rudder shielding by the wake of the horizontal tail for different horizontal tail positions.

The wake of the horizontal tail can be estimated as the area between a line originating from the leading edge at an angle of 60 ° with respect to the chord of the horizontal tail and a line under an angle of 30 ° from the trailing edge, as shown in Figure 7.8 [63]. Positioning the horizontal tail more aft increases the tail moment arm, which improves stability. However, this also increases the pitch damping and therefore the controllability in pitch. Hence, for high manoeuvrability it is better to shift the horizontal tail forward. Positioning the horizontal tail higher ensures that the area of the vertical tail and the rudder below the horizontal tail is always effective.

For given vertical tail and rudder dimensions, the required effective rudder area is dependent on the maximum allowed rudder deflection. A larger effective rudder area results in a lower required

rudder deflection to recover from spin. Thus, if the maximum deflection is exceeded, the horizontal tail can be shifted such that the effective rudder area is increased. If the resulting required rudder deflection is much larger than the maximum allowed deflection and the effective area cannot be increased enough, then the dimensions of the vertical tail and rudder can be changed. This is iterated until a feasible rudder design and corresponding horizontal tail position are found.

The effective rudder and vertical tail area are simply computed as the total rudder and vertical tail are minus the wake area, as defined in Figure 7.8. The resulting effective rudder and vertical tail area ratios and the horizontal tail position with respect to the vertical tail are given in Table 7.7. The horizontal tail position with respect to the vertical tail is negative, which means that the horizontal tail is slightly in front of the vertical tail.

Table 7.7: Effective rudder and vertical tail area ratios and horizontal tail position.

Output	Symbol	Value	Unit
Effective rudder area ratio	$\frac{S_{r_e}}{S_r}$	0.58	[−]
Effective vertical tail area ratio	$\frac{S_{v_e}}{S_v}$	0.50	[−]
Horizontal tail position	$\Delta x_{LE_{vh}}$	-0.33	[m]

The elevator deflection also has an influence on the size of the wake that shields the rudder, as shown in Figure 7.9 [63]. If the elevator is deflected upward, the wake becomes smaller and the effective rudder area is larger. On the other hand, if the elevator is deflected downward, the wake becomes larger and the rudder area shielded by the wake also increases. Thus, to recover from spin, pilots should first apply a corrective rudder deflection before deflecting the elevator down.

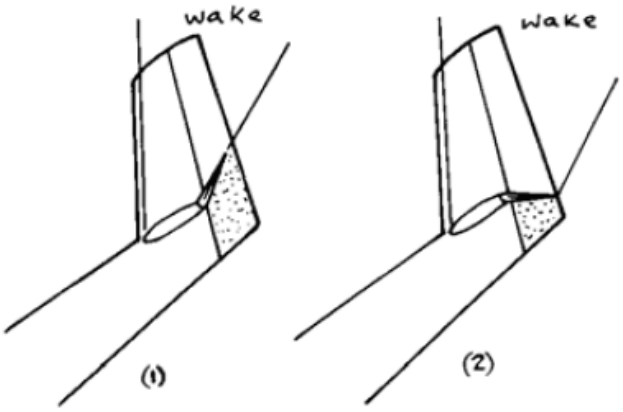

Figure 7.9: Effect of the elevator deflection on the wake of the horizontal tail

7.4.4 Rudder Control System

The next step in the design process is to design the control system for the rudder.
For the control of the rudder, control cables are the best option. A cable system for the rudder is easily implemented in the fuselage and weighs less than a control system consisting of rods. An example layout of the rudder control system is shown in Figure 7.10 [62]. This figure is taken from the maintenance manual of the *Extra 330LX* [33], which is a two-seater and therefore has two rudder pedals.

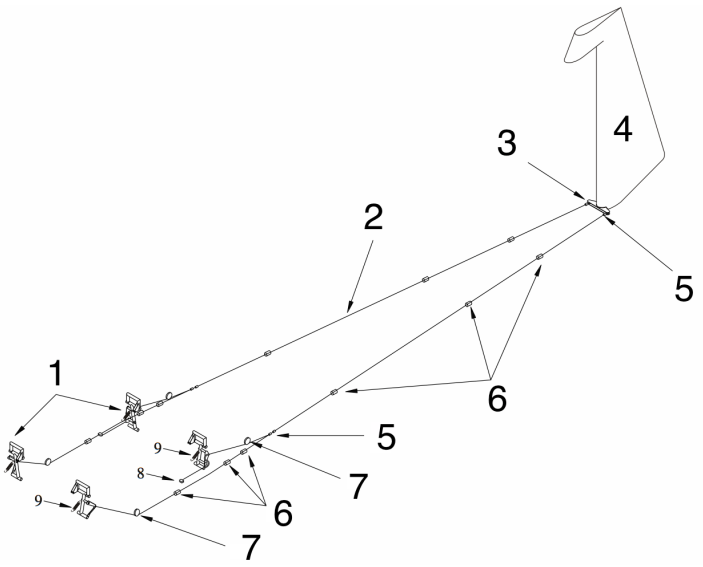

1. Rudder pedals
2. Rudder control cable
3. Bottom hinge bellcrank
4. Rudder
5. Sleeves
6. Fairleads
7. Pulley
8. Cable fastening
9. Spring

Figure 7.10: Rudder control system

7.5 Control Surface Balancing

Balancing of the control surfaces is very important for the handling qualities of the aircraft, especially for an aerobatic racing aircraft. There are two types of balancing for the control surfaces: aerodynamic balancing and mass balancing. The purpose of aerodynamic balancing is to keep the stick force the pilot has to exert within a reasonable range. Mass balancing is required to prevent undesirable aeroelastic phenomena such as flutter [59, 63].

7.5.1 Aerodynamic Balancing

The *aerodynamic balance* is defined as the ratio of area moments forward and aft of the hinge line [63]. If a control surface is unbalanced, the hinge moment derivatives C_{h_α} (due to angle of attack) and C_{h_δ} (due to control surface deflection) are too large in magnitude, resulting in a control force that is unacceptable [59]. The control surfaces can be balanced aerodynamically by changing the distribution of surface area about the hinge line to balance the aerodynamic moments about the hinge line. There are different ways to aerodynamically balance the control surfaces.

One way is to use so-called *horns*. Horns are simply balancing surfaces added in front of the control surface hinge line, as shown in Figure 7.11a [63]. In general, when a control surface is deflected, a force is generated behind the hinge line that tends to reduce the desired deflection. If the control surface is equipped with a horn, the moment generated by the horn opposes the moment behind the hinge line that tends to reduce the deflection [59]. In other words, horns generate a force and a corresponding moment that helps deflecting the control surface. There are two types of horns: *shielded* and *unshielded* horns. Unshielded horns extend to the leading edge of the control surface, whereas shielded horns are 'shielded' by a fixed part of wing or stabiliser surface area in front of them. The latter are less susceptible to ice accumulation on the leading edge [66]. Ice accumulation could lead to control problems, but does not occur on an aerobatic racing aircraft flying at low altitude. Thus, for the *T-16* unshielded horns can be used.

Another way to apply aerodynamic balancing is by using nose overhang, shown in Figure 7.11b [63]. By moving the hinge line more aft, towards the centre of pressure of the control surface, the nose can deflect into the air stream. Similarly to the horn balance, a force is generated that counteracts

the force behind the hinge line. Additionally, the moment arm of the aerodynamic force behind the hinge line is reduced.

For balancing the ailerons often *spades* are used. Spades are shovel-shaped balancing surfaces mounted on arms forward of the ailerons, which reduce the effort to roll the aircraft [67]. An example of an aileron spade is given in Figure 7.12 [68]. In neutral position the spades are aligned with the flow and have no effect. When the ailerons are deflected, the spades have an angle of attack and generate a force that helps deflecting the ailerons. Aileron spades for aerobatic (racing) aircraft are often 'designed' empirically. Pilots are always tweaking them, based on experience, to obtain the desired control feel [67].

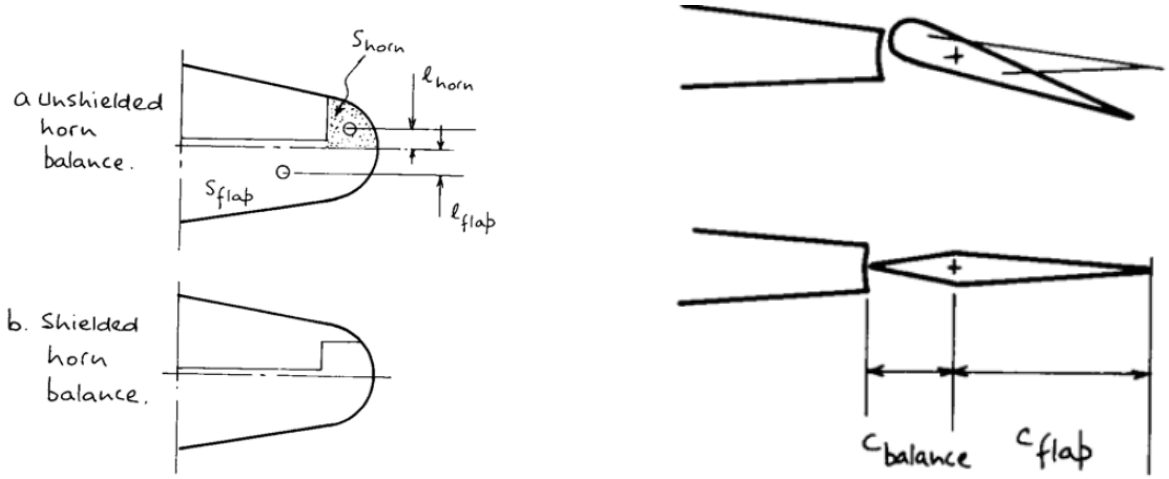

(a) Example of a shielded and unshielded horn balance. *(b) Example of a nose-overhang balance.*

Figure 7.11: Two types of aerodynamic balancing

The options described are the most common and simple ways to balance the control surfaces. More ways to influence the hinge moments are described by [59, 63], such as internal balancing and contouring. For the *T-16* aerodynamic balancing is required to reduce the control force of the rudder, since this force is too high, as discussed in Section 7.6.4. This can be done by applying one of these aerodynamic balancing surfaces or a combination of them. The actual design and sizing of such balancing surfaces, however, would require wind tunnel testing or actual flight testing, which is beyond the scope of this project. Although the balancing surfaces have not been sized, they are included in the CATIA model of the aircraft to illustrate the concepts. Aerodynamic balancing should be done very accurately and care should be taken not to overbalance the control surfaces. Overbalanced control surfaces do not go back to the neutral position after a disturbance, but deflect even further, resulting in control instability.

Figure 7.12: Example of an aileron spade.

7.5.2 Mass Balancing

Mass balancing of the control surfaces is an effective way to prevent flutter. Flutter is a high frequency oscillation caused by an interaction of the aerodynamic force and the stiffness and weight of the control surface, which could lead to dynamic instability [59, 63]. The hinge line of control surfaces is typically located at 5-10% of the chord (measured from the leading edge), while the c.g.

is located more aft, at 20-40% of the chord [59]. Hence, the c.g. of the control surfaces generally lies behind the hinge line. When a disturbance causes the control surface to deflect, the resulting aerodynamic force opposes this deflection and brings the control surface back to the neutral position. However, due to the momentum the control surface tends to overshoot the neutral position, which results in undesirable oscillations and may lead to flutter [69]. Therefore, the control surfaces should be balanced about their c.g. in the absence of any airflow, i.e. they should be *statically balanced*.

Static balance is achieved by adding a counterweight that creates a moment about the hinge line that is equal in magnitude and opposite in sign to the moment generated by the control surface weight. In other words, the counterbalancing mass should shift the c.g. of the complete control surface (including counterweight) to coincide with the hinge line. This simple static equilibrium of moments is expressed in Equation (7.22), where m_b and l_b are the mass and moment arm of the counterweight, respectively, and m_{cs} and l_{cs} are the mass and moment arm of the control surface.

$$m_b l_b = m_{cs} l_{cs} \tag{7.22}$$

For very low-speed aircraft mass balancing is not necessary, but for aircraft with mechanical controls and a maximum speed above 100 knots, such as the *T-16*, it is required [59]. The weight distribution needs to be very precise for mass balancing. When a control surface is repaired or even only repainted, it is essential to check the balance again [69].

The counterbalancing mass can be either attached to an arm (see Figure 7.13 [63]), similarly to the aileron spades, or implemented in the leading edge of the control surface as a distributed mass along the span. Often, the counterweights are aerodynamically shaped to reduce drag, which makes them quite similar to aileron spades. Therefore, the function of aerodynamic balance and mass balance could also be combined. A spade could function as a counterweight, while having the right aerodynamic shape to generate a force and corresponding moment that balances the aerodynamic hinge moment.

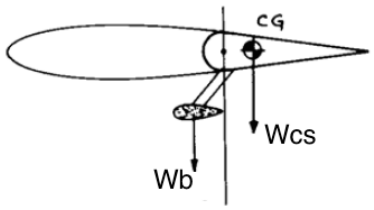

Figure 7.13: Example of a mass balance attached to an arm forward of the hinge line.

7.6 Control Forces

After having designed the control surfaces, it is possible to find the control forces on the stick and pedals. In general, the control force can be calculated using $F = -\frac{d\delta}{ds}\frac{1}{2}\rho V^2 S\bar{c}C_h$, where $C_h = C_{h_\alpha}\alpha + C_{h_\delta}\delta + C_{h_{\delta_t}}\delta_t$. Three coefficients need to be determined: control surface hinge moment with respect to angle of attach C_{h_α}, control surface hinge moment with respect to control surface deflection C_{h_δ} and control surface hinge moment due to tab deflection $C_{h_{\delta_t}}$. The first section explains the method of obtaining the control force coefficients, after which the aileron, elevator and rudder control force are given, respectively.

7.6.1 Control Force Coefficients

As stated in the introduction of this section, three coefficients need to be determined: hinge moment with respect to angle of attack C_{h_α}, hinge moment with respect to control surface deflection C_{h_δ} and hinge moment with respect to tab deflection $C_{h_{\delta_t}}$. To calculate these hinge moment coefficients, a method described by Roskam is used [70]. The methodology is explained in Appendix C.

The control forces required to deflect each of the control surfaces are presented in Sections 7.6.2-7.6.4.

7.6.2 Aileron Control Force

The aileron control force is the force on the stick due to an aileron deflection, which is a function of airspeed. Equation (7.23) shows this relationship,

$$F_a = -\left(\frac{\mathrm{d}\delta_a}{\mathrm{d}s_a}\right)\tfrac{1}{2}\rho V^2 S_a c_a C_{h_a} \tag{7.23}$$

where

- $\frac{\mathrm{d}\delta_a}{\mathrm{d}s_a}$ is the gearing ratio
- $\frac{1}{2}\rho V^2$ is the dynamic pressure
- S_a and c_a are the surface area and chord of the aileron, respectively
- C_{h_a} is the aileron hinge moment coefficient

C_{h_a} is a function of change in angle of attack due to aileron deflection, aileron deflection itself and aileron trim tab deflection. Since the aileron does not have a trim tab, this contribution is discarded. The result is shown in Figure 7.14. For an increasing airspeed, the aileron stick force becomes more negative, which corresponds to a stick displacement to the right. At zero airspeed, there is no control force and the absolute magnitude of the force increases quadratically with airspeed.

With a maximum allowed control force of 290 N for the aileron [14], it is possible to fly up to a speed of approximately 135 $m \cdot s^{-1}$. This speed is above the manoeuvre speed, so the aileron control force does not need to be reduced by aerodynamically balancing the aileron or applying a spring in the control system.

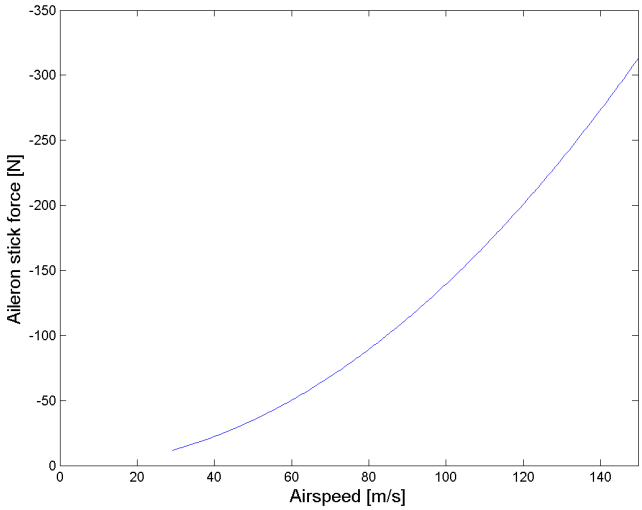

Figure 7.14: Aileron control force as a function of airspeed at a maximum deflection of $\delta_a = 25\,^\circ$

7.6.3 Elevator Control Force

The elevator control force depends on the gearing ratio, the airspeed, the elevator size and the hinge moment, as follows from Equation (7.24),

$$F_e = -\left(\frac{\mathrm{d}\delta_e}{\mathrm{d}s_e}\right)\tfrac{1}{2}\rho V_h^2 S_e c_e C_{h_e} \tag{7.24}$$

where

- $\frac{\mathrm{d}\delta_e}{\mathrm{d}s_e}$ is the gearing ratio
- $\frac{1}{2}\rho V_h^2$ is the dynamic pressure at the horizontal tail
- S_e and c_e are the surface area and chord of the elevator, respectively
- C_{h_e} is the elevator hinge moment coefficient

However, it is assumed that the control system is designed such that the stick needs to be deflected over the same angle as the elevator itself. That means that the gearing ratio is equal to one, hence the stick force is equal to the elevator force given by Equation (7.9). Figure 7.15 shows the plot of the elevator control force as a function of airspeed for the maximum elevator deflection $\delta_e = 29\ ^\circ$ and an elevator trim tab deflection $\delta_{t_e} = 1\ ^\circ$. This trim tab deflection is required to trim the aircraft at the manoeuvre speed $V_m = 91.7\ m \cdot s^{-1}$.

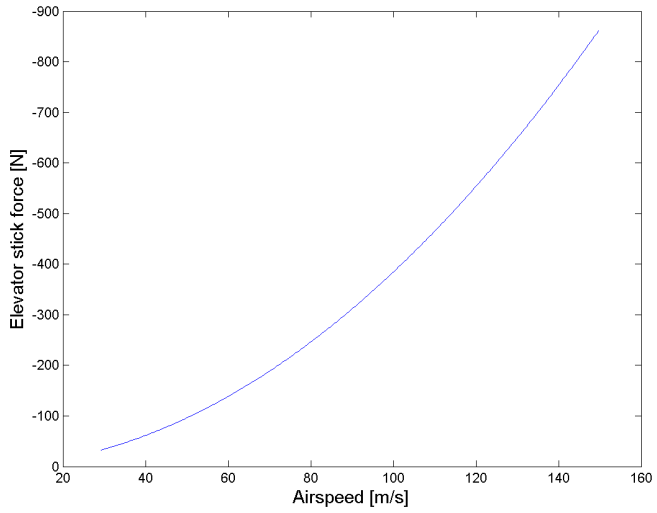

Figure 7.15: Elevator control force as a function of airspeed at a maximum deflection of $\delta_e = 29\ ^\circ$ and a trim tab deflection of $\delta_{t_e} = 1\ ^\circ$.

The elevator stick force is negative, thus the pilot needs to pull the stick to perform a pull-up manoeuvre, which is not surprising. At zero airspeed the control force is zero and the absolute magnitude increases quadratically with airspeed. Hence, the pilot needs to pull harder with increasing airspeed due to the increased force exerted on the elevator by the airflow. According to the CS-23 specifications, the maximum elevator stick force may not exceed 743 N [14]. That maximum force is reached at an airspeed of approximately 139 $m \cdot s^{-1}$, which is well above the manoeuvre speed of 91.7 $m \cdot s^{-1}$. Therefore, no aerodynamic balancing is required.

More important for aerobatic (racing) aircraft is the stick force per g. This stick force per g should be constant and not too large. According to [71], a good value for the stick force per g is 50 N at most. The elevator stick force per g is computed using Equation (7.25),

$$\left(\frac{\mathrm{d}F_e}{\mathrm{d}n}\right)_{pull} = -\left(\frac{\mathrm{d}\delta_e}{\mathrm{d}n}\right)_{pull} \frac{W}{S}\left(\frac{V_h}{V}\right)^2 S_e c_e \frac{C_{h_{\delta_e}}}{C_{m_{\delta_e}}}\left(\frac{C_{m_\alpha}}{C_{N_\alpha}} + \frac{C_{m_q}}{2\mu_c}\right) \tag{7.25}$$

where

- $\frac{\mathrm{d}\delta_e}{\mathrm{d}n}$ is the elevator deflection per g
- S_e and c_e are the surface area and chord length of the elevator, respectively
- $\frac{W}{S}$ is the wing loading
- $\frac{V_h}{V}$ is the speed ratio of horizontal tail to main wing

- $C_{h_{\delta_e}}$ is the change of hinge moment coefficient with respect to elevator deflection
- $C_{m_{\delta_e}}$ is the change of moment coefficient with respect to elevator deflection
- C_{m_α} is the change of moment coefficient with respect to angle of attack
- C_{N_α} is the change of normal force with respect to angle of attack
- C_{m_q} is the pitch damping
- μ_c is the non-dimensional mass

Substituting the correct values yields a stick force per g of $-17.6\ N$. Therefore, the stick force at 10g is roughly 160 N, which is a reasonable value. It should be noted that the stick force at 1g (i.e. during normal flight) is zero. Thus, the elevator stick force as a function of load factor n is obtained by multiplying the stick force per g by a factor $(n-1)$. Figure 7.16 shows a plot of the stick force as a function of the load factor n.

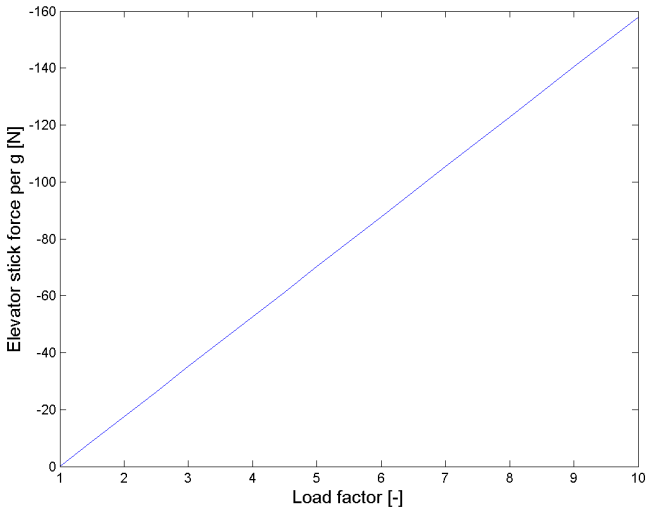

Figure 7.16: Elevator control force as a function of the load factor n

7.6.4 Rudder Control Force

The rudder control force is the force on the stick due to a rudder deflection, which is a function of airspeed. Equation (7.26) shows this relationship.

$$F_r = -\left(\frac{\mathrm{d}\delta_r}{\mathrm{d}s_r}\right)\tfrac{1}{2}\rho V_v^2 S_r c_r C_{h_r} \tag{7.26}$$

Where:

- $\frac{\mathrm{d}\delta_r}{\mathrm{d}s_r}$ is the gearing ratio
- $\frac{1}{2}\rho V_v^2$ is the dynamic pressure at the vertical tail
- S_r and c_r are the surface area and chord of the rudder, respectively
- C_{h_r} is the rudder hinge moment coefficient

C_{h_r} is a function of change in angle of attack due to rudder deflection, rudder deflection itself and rudder trim tab deflection. Since the rudder does not have a trim tab, this contribution is discarded. The result is shown in Figure 7.17. For an increasing airspeed, the rudder pedal force becomes more negative, which corresponds to a push force on the right pedal. At zero airspeed, there is no control force and the absolute magnitude of the force increases quadratically with airspeed.

The maximum allowed stick force for rudder is 890 N [14], which is obtained around the manoeuvre speed of 91.7 $m \cdot s^{-1}$. To decrease the stick force, the rudder can be aerodynamically balanced. Control surface balancing is explained in Section 7.5.

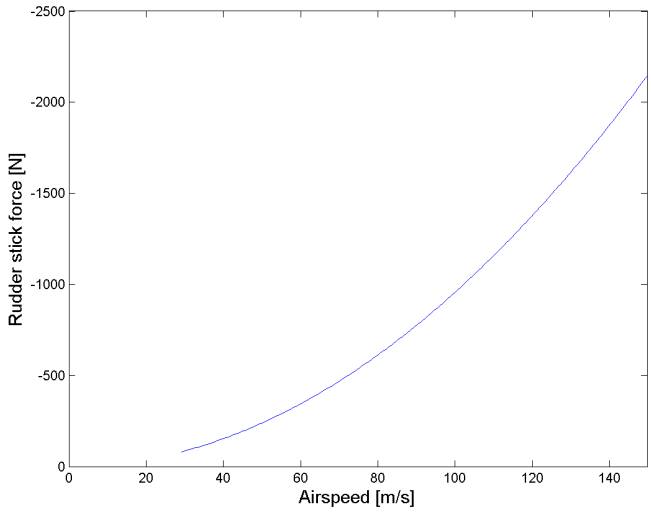

Figure 7.17: Rudder control force as a function of airspeed at a maximum deflection of $\delta_r = 29.8$ °

7.7 Cockpit

Table 7.8 gives an overview of the chosen avionics and instruments. The mass budget available for the avionics and instruments is set to 3 kg [56]. The total mass in Table 7.8 is below that value, but does not yet include the mass of the fuel indicators and oil gauges. The mass of these instruments is around 0.3 kg each, which results in an extra 1.5 kg added to the total mass. Since most of the instruments are already the lowest mass options, choosing alternative instruments will not reduce the total mass much. Therefore, the budget is adjusted slightly.

The cost of the instruments is much higher than anticipated. It can be concluded that the cost budget set in [56] is too optimistic. Therefore, it is updated to more realistic values. The required power, on the other hand, is much lower than the power budget available for avionics and instruments. Hence, the power budget for avionics and instruments is reduced.

Table 7.8: Overview of chosen avionics and instruments.

Instrument	**Type**	**Mass** *kg*	**Cost** *[€]*	**Power** *[W]*
Airspeed indicator	Mid-Continent 8140-B.457	0.27	752.-	-
Altimeter	United Instruments 5934P	0.36	1,770.-	-
Fuel quantity indicator (x3)	U.M.A T1821251	N/A	127.-	-
Compass	Precision PAI-700	0.27	222.-	-
Oil temperature gauge	U.M.A. oil temperature	N/A	150.-	-
Oil pressure gauge	U.M.A. oil pressure	N/A	150.-	-
Transponder	Trig Avionics TT22	0.44	1,475.-	4.8
Radio	VAL Avionics COM2KR	1.30	682.-	14.5
	Total	**2.64**	**5,582.-**	**19.3**

7.7.1 Instrument Panel Layout

Based on the selected avionics and instruments, the design of the instrument panel layout presented in [56] is updated. First of all, a different layout is used. The top part is smaller, and the pilot has

a set of indicators just behind the stick. This reduces the total width and space needed for the instruments. Furthermore, instead of a round transponder and radio, rectangular ones are selected. Figure 7.18 shows the instrument panel layout.

Figure 7.18: T-16 instrument panel layout.

Number	Instrument
1	starter
2	trim indicator
3	airspeed indicator
4	EFIS
5	altimeter
6	radio
7	transponder
8	g-meter
9	oil temperature
10	heading indicator
11	fuel indicators
12	oil pressure
13	switches

Table 7.9: Instrument panel explanation

The numbers in Figure 7.18 indicate the different instruments and avionics. Table 7.9 states the names of the instruments with the corresponding number.

7.7.2 Pitot Tubes and Static Ports

Some instruments require pitot tubes and static ports to function properly. To be precise, there are three instruments: airspeed indicator, vertical speed indicator and altimeter. Figure 7.19 [72] shows a pitot-static system and the instruments that need these tubes and ports.

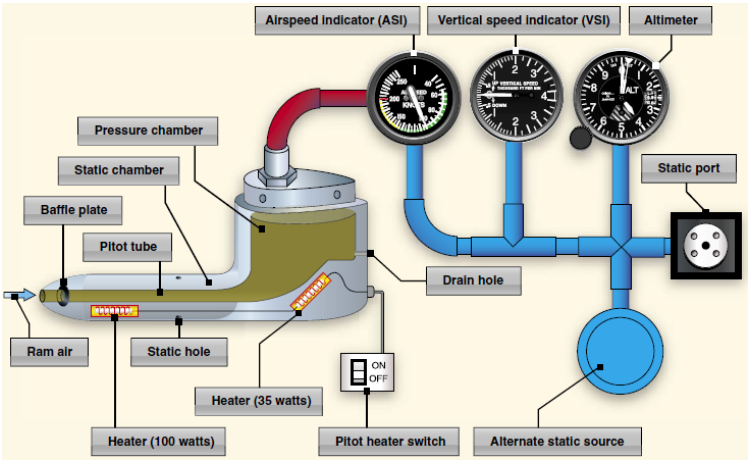

Figure 7.19: Pitot-static system with instruments.

7.8 Aircraft Lights

Besides the equipment inside the cockpit, also the lights on the outside are important for visibility of the aircraft [73].

According to the Visual Flight Rules (VFR), the aircraft has to be equipped with anti-collision lights for during the day and additionally navigation lights for during the night. [73]

The navigation lights consist of three different lights, namely a red light on the left side, a green light on the right side and a white light at the tail of the aircraft. Depending on which lights of the aircraft are visible, other pilots can determine the position and heading of the aircraft.

To reduce the chance of collisions occurring, the aircraft is also equipped with strobes, the so called anti-collision lights. These lights are always turned on to indicate the position of the aircraft, especially in low-visibility conditions. The lights are turned off when flying into a cloud, as the lights may be reflected and could consequently blind the pilot [73]. Also a landing light is installed on the aircraft. This light is always turned on when approaching to increase visibility [74]. This light is very powerful and can be seen from a large distance.

7.9 Lateral stability

In this section, the dynamic lateral stability of the *T-16* is assessed. Two modes of lateral stability are considered, the aperiodic spiral mode and the periodic Dutch Roll. A range of possible sweep angles is selected in Section 5.4.1. Based on these possible sweep angles, the selection is narrowed down.

Depending on the lateral stability of the aircraft, the aircraft may either have an unstable spiral and a stable Dutch Roll stable, a stable spiral and an unstable Dutch Roll or both a stable spiral and stable Dutch Roll. An unstable Dutch Roll is unwanted as it requires a yaw damper to stop this motion. Spiral instability causes the aircraft to side-slip towards the inside of the turn and thereby decreases the turn radius [75]. However, if the spiral mode is too unstable, initiating a roll induces a too high roll angle, which can eventually lead to a roll overshoot.

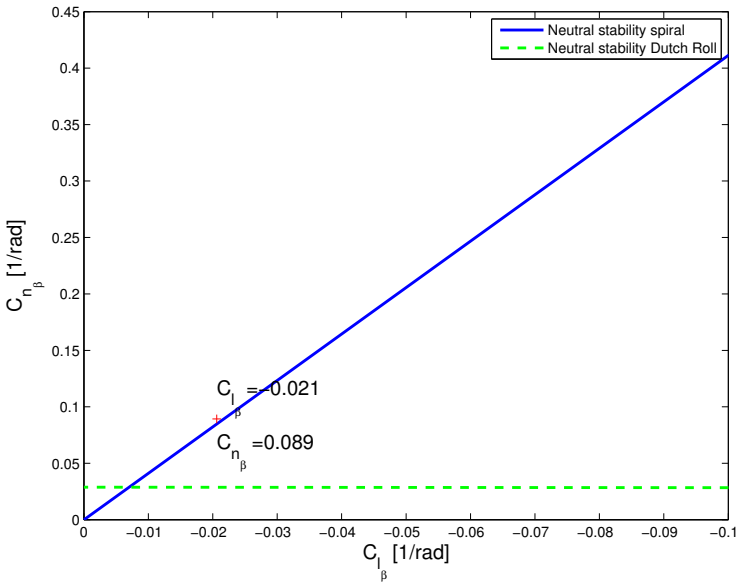

Figure 7.20: Lateral stability plot

For the possible range of quarter chord sweep angles between −10 °-0, the lateral stability is checked. A range of 10% deviation from the neutral stability line is allowed and the selection of sweep angles is narrowed down. The new range of sweep angles corresponds to a range of sweep angles between straight quarter chord and straight leading edge. Since the aircraft needs to be as close to neutral stability as possible, a straight leading edge is chosen, corresponding to a quarter chord sweep angle of $\Lambda_{0.25c} = -2.4°$.

Figure 7.20 shows the spiral neutral stability and Dutch Roll neutral stability lines and the point indicating the stability of the *T-16*. As can be seen in the figure, the aircraft has a slightly unstable spiral mode. However, this is not a problem, since the pilot has sufficient time to recover from a slowly developing spiral, before the aircraft spirals out of control.

7.10 Eigenmotion Analysis

To analyse the eigenmotions of the aircraft a state-space model is used. This model is a linearised, time-invariant system of equations. The state-space model is in the form of $\dot{\vec{x}} = A\vec{x} + B\vec{u}$.

7.10.1 Assumptions

In order to set up a state-space model, several assumptions are made, which are the following:

- Vehicle is a rigid body
- Mass of the vehicle is constant
- Earth is non-rotating
- Earth is flat
- Gravity field is constant
- Aircraft has a plane of symmetry
- Effects of rotating masses are neglected
- The resultant thrust vector lies in the plane of symmetry
- Small disturbances

Additionally, it is assumed that the eigenmotions are decoupled. This means that no aerodynamic coupling exists between the symmetric and asymmetric degrees of freedom [75]. Hence, the asymmetric deviations and disturbances are assumed to have no influence on the symmetric forces X and Z and the symmetric moment M. Also, the symmetric deviations and disturbances are assumed to have no influence on the asymmetric force Y and the asymmetric moments L and N.

7.10.2 Limitations

Due to the extensive list of assumptions, there are some limitations to this method. First of all, higher-order terms are neglected when using linearisation. The disturbances are assumed to be small, thus taking the square of these small disturbances results in very small values. It is therefore justified to discard the higher-order terms.

The aircraft is assumed to be a rigid body with a constant mass (i.e. fuel burn is not taken into account), which makes the stability derivatives independent of the mass. This means the derivatives are constant in time and thus the matrices are constant in time. Furthermore, the moment of inertia is also assumed to be constant.

Since the xz-plane is a plane of symmetry of the aircraft, the moments of inertia I_{xy} and I_{yz} are zero. This simplifies the state-space model.

7.10.3 Symmetric Equations of Motion

The linearised equations of motion (EOM) for symmetric flight are shown in Equation (7.27) [75].

$$\begin{bmatrix} C_{X_u} - 2\mu_c D_c & C_{X_\alpha} & C_{Z_0} & 0 \\ C_{Z_u} & C_{Z_\alpha} + (C_{Z_{\dot{\alpha}}} - 2\mu_c)D_c & -C_{X_0} & C_{Z_q} + 2\mu_c \\ 0 & 0 & -D_c & 1 \\ C_{m_u} & C_{m_\alpha} & 0 & C_{m_q} - 2\mu_c K_Y^2 D_c \end{bmatrix} \begin{bmatrix} \hat{u} \\ \alpha \\ \theta \\ \frac{q\bar{c}}{V} \end{bmatrix} = \begin{bmatrix} -C_{X_{\delta_e}} & -C_{X_{\delta_t}} \\ -C_{Z_{\delta_e}} & -C_{Z_{\delta_t}} \\ 0 & 0 \\ -C_{m_{\delta_e}} & -C_{m_{\delta_t}} \end{bmatrix} \begin{bmatrix} \delta_e \\ \delta_t \end{bmatrix} \tag{7.27}$$

Substituting $\frac{\bar{c}}{V}\frac{d}{dt}$ for D_c allows Equation (7.27) to be written in state-space format. An intermediate step is shown in Equation (7.28), where P, Q and R are the matrices corresponding to the EOM in the form $P\dot{\vec{x}} = Q\vec{x} + R\vec{u}$.

$$
\begin{aligned}
P &= \begin{bmatrix} -2\mu_c \frac{\bar{c}}{V} & 0 & 0 & 0 \\ 0 & (C_{Z_\alpha} - 2\mu_c)\frac{\bar{c}}{V} & 0 & 0 \\ 0 & 0 & -\frac{\bar{c}}{V} & 0 \\ 0 & C_{m_{\dot{\alpha}}}\frac{\bar{c}}{V} & 0 & -2\mu_c K_Y^2 \bar{c} V \end{bmatrix} \\
Q &= \begin{bmatrix} -C_{X_u} & -C_{X_\alpha} & -C_{Z_0} & 0 \\ -C_{Z_u} & -C_{Z_\alpha} & -C_{X_0} & -(C_{Z_q} + 2\mu_c) \\ 0 & 0 & 0 & -1 \\ -C_{m_u} & -C_{m_\alpha} & 0 & C_{m_q} \end{bmatrix} \\
R &= \begin{bmatrix} -C_{X_{\delta_e}} & -C_{X_{\delta_t}} \\ -C_{Z_{\delta_e}} & -C_{Z_{\delta_t}} \\ 0 & 0 \\ -C_{m_{\delta_e}} & -C_{m_{\delta_t}} \end{bmatrix}
\end{aligned} \tag{7.28}
$$

Finally, the symmetric EOM are converted to state-space form using Equation (7.29), where $P^{-1}Q = A$ and $P^{-1}R = B$.

$$
\begin{aligned}
\dot{\vec{x}} &= P^{-1}Q\vec{x} + P^{-1}R\vec{u} \\
&= A\vec{x} + B\vec{u}
\end{aligned} \tag{7.29}
$$

For the obtained state-space model the eigenfrequency, the damping ratio, the period and the time to half amplitude can be determined using Equations (7.30) to (7.33), respectively. These parameters only depend on the eigenvalues $\lambda_c = \eta \pm \xi i$, obtained from system matrix A.

$$\lambda_s = \sqrt{\eta^2 + \xi^2}\frac{V}{\bar{c}} \tag{7.30}$$

$$\zeta_s = \frac{-\eta}{\sqrt{\eta^2 + \xi^2}} \tag{7.31}$$

$$P_s = \frac{2\pi}{\xi}\frac{\bar{c}}{V} \tag{7.32}$$

$$T_{\frac{1}{2}_s} = \frac{\log(0.5)}{\eta}\frac{\bar{c}}{V} \tag{7.33}$$

The numerically obtained eigenvalues from the system matrix are compared to the eigenvalues obtained from the characteristic equation. The characteristic equation is used to check the Routh-Hurwitz Stability Criteria [75]. Given a characteristic equation $A_s\lambda_c^4 + B_s\lambda_c^3 + C_s\lambda_c^2 + D_s\lambda_c + E_s$, all coefficients need to have the same sign, and the Routh's discriminant $R_s = B_sC_sD_s - A_sD_s^2 - B_s^2E_s$ should have the same sign as the coefficients [75]. Equations (7.34) to (7.38) are used to compute the Routh's coefficients.

The eigenvalues of the system of symmetric EOM are plotted in Figure 7.21 and are stated in Table 7.10.3. There are two pairs of complex conjugate eigenvalues. The pair of eigenvalues with the most negative real part and largest imaginary part corresponds to a short period motion. A large absolute magnitude of the imaginary part indicates a high-frequency oscillation and a very negative real part indicates strong damping of the motion. The pair of eigenvalues with the smallest negative real part and the smallest imaginary part correspond to a phugoid motion, which is characterised by low-frequency oscillations and low damping.

$$A_s = 4\mu_c^2 K_Y^2 (C_{Z_{\dot{\alpha}}} - 2\mu_c) \tag{7.34}$$

$$B_s = C_{m_{\dot{\alpha}}} 2\mu_c (C_{Z_q} + 2\mu_c) - C_{m_q} 2\mu_c (C_{Z_{\dot{\alpha}}} - 2\mu_c) - 2\mu_c K_Y^2 \{C_{X_u}(C_{Z_{\dot{\alpha}}} - 2\mu_c) - 2\mu_c C_{Z_\alpha}\} \tag{7.35}$$

$$C_s = C_{m_\alpha} 2\mu_c (C_{Z_q} + 2\mu_c) - C_{m_{\dot{\alpha}}} \{2\mu_c C_{X_0} + C_{X_u}(C_{Z_q} + 2\mu_c)\} + C_{m_q} \{C_{X_u}(C_{Z_{\dot{\alpha}}} - 2\mu_c) - 2\mu_c C_{Z_\alpha}\} + 2\mu_c K_Y^2 (C_{X_\alpha} C_{Z_u} - C_{Z_\alpha} C_{X_u}) \tag{7.36}$$

$$D_s = C_{m_u} \{C_{X_\alpha}(C_{Z_q} + 2\mu_c) - C_{Z_0}(C_{Z_{\dot{\alpha}}} - 2\mu_c)\} - C_{m_\alpha} \{2\mu_c C_{X_0} + C_{X_u}(C_{Z_q} + 2\mu_c)\} + C_{m_{\dot{\alpha}}} (C_{X_0} C_{X_u} - C_{Z_0} C_{Z_u}) + C_{m_q} (C_{X_u} C_{Z_\alpha} - C_{Z_u} C_{X_\alpha}) \tag{7.37}$$

$$E_s = -C_{m_u} (C_{X_0} C_{X_\alpha} + C_{Z_0} C_{Z_\alpha}) + C_{m_\alpha} (C_{X_0} C_{X_u} + C_{Z_0} C_{Z_u}) \tag{7.38}$$

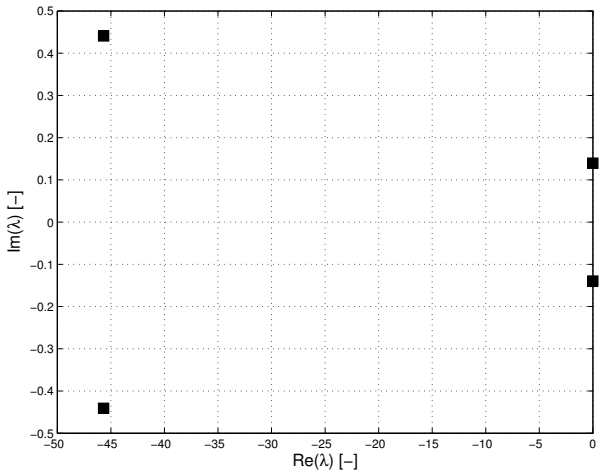

Figure 7.21: Symmetric eigenvalues

Eigenvalue	Value [-]
$\lambda_{1,2}$	$-45.7 \pm 0.44i$
$\lambda_{3,4}$	$-5.10 \pm 0.14i$

Table 7.10: Symmetric eigenvalues

All coefficients and the Routh's discriminant are negative, thus the Routh-Hurwitz Stability Criteria are met. This means the symmetric eigenmotions are stable. The numerically obtained eigenvalues from the system matrix and the eigenvalues obtained from the characteristic equation are found to be exactly the same.

7.10.4 Asymmetric Equations of Motion

The linearised equations of motion for asymmetric flight are shown in Equation (7.39) [75].

$$\begin{bmatrix} C_{Y_\beta} + (C_{Y_{\dot{\beta}}} - 2\mu_b) D_b & C_L & C_{Y_p} & C_{Y_r} - 4\mu_b \\ 0 & -\frac{1}{2} D_b & 1 & 0 \\ C_{l_\beta} & 0 & C_{l_p} - 4\mu_b K_X^2 D_b & C_{l_r} + 4\mu_b K_{XZ} D_b \\ C_{n_\beta} + C_{n_{\dot{\beta}}} D_b & 0 & C_{n_p} + 4\mu_b K_{XZ} D_b & C_{n_r} - 4\mu_b K_Z^2 D_b \end{bmatrix} \begin{bmatrix} \beta \\ \phi \\ \frac{pb}{2V} \\ \frac{rb}{2V} \end{bmatrix} = \begin{bmatrix} -C_{Y_{\delta_a}} & -C_{Y_{\delta_r}} \\ 0 & 0 \\ -C_{l_{\delta_a}} & -C_{l_{\delta_r}} \\ -C_{n_{\delta_a}} & -C_{n_{\delta_r}} \end{bmatrix} \begin{bmatrix} \delta_a \\ \delta_r \end{bmatrix} \tag{7.39}$$

Substituting $\frac{b}{V}\frac{d}{dt}$ for D_b allows Equation (7.39) to be written in state-space form. An intermediate step is shown in Equation (7.40), where P_b, Q_b and R_b are the matrices corresponding to the EOM in the form $P_b \dot{\vec{x}} = Q_b \vec{x} + R_b \vec{u}$.

$$
\begin{aligned}
P_b &= \begin{bmatrix} (C_{Y_{\dot{\beta}}} - 2\mu_b)\frac{b}{V} & 0 & 0 & 0 \\ 0 & -\frac{1}{2}\frac{b}{V} & 0 & 0 \\ 0 & 0 & -4\mu_b K_X^2 \frac{b}{V} & 4\mu_b K_{XZ}\frac{b}{V} \\ C_{n_{\dot{\beta}}}\frac{b}{V} & 0 & 4\mu_b K_{XZ}\frac{b}{V} & -4\mu_b K_Z^2 \frac{b}{V} \end{bmatrix} \\
Q_b &= \begin{bmatrix} -C_{Y_\beta} & -C_L & -C_{Y_p} & -(C_{Y_r} - 4\mu_b) \\ 0 & 0 & -1 & 0 \\ -C_{l_\beta} & 0 & -C_{l_p} & -C_{l_r} \\ -C_{n_\beta} & 0 & -C_{n_p} & -C_{n_r} \end{bmatrix} \\
R_b &= \begin{bmatrix} -C_{Y_{\delta_a}} & -C_{Y_{\delta_r}} \\ 0 & 0 \\ -C_{l_{\delta_a}} & -C_{l_{\delta_r}} \\ -C_{n_{\delta_a}} & -C_{n_{\delta_r}} \end{bmatrix}
\end{aligned} \tag{7.40}
$$

Finally, the asymmetric EOM are converted to state-space form using Equation (7.41), where $P_b^{-1}Q_b = A$ and $P_b^{-1}R_b = B$.

$$
\begin{aligned}
\dot{\vec{x}} &= P_b^{-1}Q_b\vec{x} + P_b^{-1}R\vec{u} \\
&= A_b\vec{x} + B_b\vec{u}
\end{aligned} \tag{7.41}
$$

For the obtained state-space model again the eigenfrequency, the damping ratio, the period and the time to half amplitude can be determined, now using Equations eq7.42 to (7.45), respectively. These parameters depend on the eigenvalues $\lambda_b = \eta \pm \xi i$.

$$\lambda_b = \sqrt{\eta^2 + \xi^2}\frac{V}{b} \tag{7.42}$$

$$\zeta_b = \frac{-\eta}{\sqrt{\eta^2 + \xi^2}} \tag{7.43}$$

$$P_b = \frac{2\pi}{\xi}\frac{b}{V} \tag{7.44}$$

$$T_{\frac{1}{2}b} = \frac{\log(0.5)}{\eta}\frac{b}{V} \tag{7.45}$$

The characteristic equation for the asymmetric eigenmotions is $A_b\lambda_b^4 + B_b\lambda_b^3 + C_b\lambda_b^2 + D_b\lambda_b + E_b$ and the Routh's discriminant is $R_b = B_bC_bD_b - A_bD_b^2 - B_b^2E_b$. Again, all Routh's coefficients and the Routh's discriminant should have the same sign. Equations (7.46) to (7.50) are used to compute the Routh's coefficients.

$$A_b = 16\mu_b^3(K_X^2K_Z^2 - K_{XZ}^2) \tag{7.46}$$

$$B_b = -4\mu_b^2\{2C_{Y_\beta}(K_X^2K_Z^2 - K_{XZ}^2) + C_{n_r}K_X^2 + C_{l_p}K_Z^2 + (C_{l_r} + C_{n_p})K_{XZ}\} \tag{7.47}$$

$$\begin{aligned} C_b = {} & 2\mu_b\left[(C_{Y_\beta}C_{n_r} - C_{Y_r}C_{n_\beta})K_X^2 + (C_{Y_\beta}C_{l_p} - C_{l_\beta}C_{Y_p})K_Z^2\right] \\ & +2\mu_b\left[\{(C_{Y_\beta}C_{n_p} - C_{n_\beta}C_{Y_p}) + (C_{Y_\beta}C_{l_r} - C_{l_\beta}C_{Y_r})\}K_{XZ}\right] \\ & +2\mu_b\left[4\mu_b C_{n_\beta}K_X^2 + 4\mu_b C_{l_\beta}K_{XZ} + \frac{1}{2}(C_{l_p}C_{n_r} - C_{n_p}C_{l_r})\right] \end{aligned} \tag{7.48}$$

$$\begin{aligned} D_b = {} & -4\mu_b C_L(C_{l_\beta}K_Z^2 + C_{n_\beta}K_{XZ}) + 2\mu_b(C_{l_\beta}C_{n_p} - C_{n_\beta}C_{l_p}) \\ & +\frac{1}{2}C_{Y_\beta}(C_{l_r}C_{n_p} - C_{n_r}C_{l_p}) + \frac{1}{2}C_{Y_p}(C_{l_\beta}C_{n_r} - C_{n_\beta}C_{l_r}) \\ & +\frac{1}{2}C_{Y_r}(C_{l_p}C_{n_\beta} - C_{n_p}C_{l_\beta}) \end{aligned} \tag{7.49}$$

$$E_b = C_L(C_{l_\beta}C_{n_r} - C_{n_\beta}C_{l_r}) \tag{7.50}$$

The eigenvalues of the system of asymmetric EOM are plotted in Figure 7.22 and are stated in Table 7.10.4. There are two real eigenvalues and one pair of complex conjugate eigenvalues. The most negative real eigenvalue corresponds to a highly damped roll subsidence motion (i.e. aperiodic roll) [75]. The pair of complex eigenvalues corresponds to a Dutch Roll mode and the slightly positive eigenvalue indicates a slightly unstable spiral mode. In Section 7.9 it is also shown that the spiral mode is slightly unstable. However, this is not a problem, since the pilot will have plenty of time to notice the slowly developing spiral and take corrective actions, before the aircraft spirals out of control.

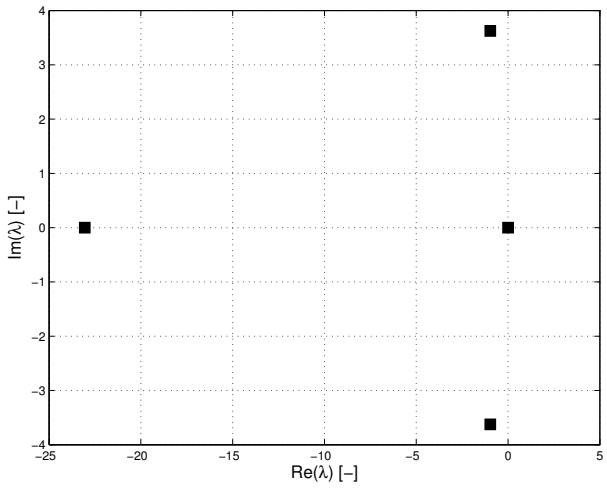

Figure 7.22: Asymmetric eigenvalues

Eigenvalue	**Value [-]**
λ_1	-23.1
$\lambda_{2,3}$	$-0.97 \pm 3.62i$
λ_4	$5.0 \cdot 10^{-4}$

Table 7.11: Assymetric eigenvalues

The signs of the Routh's coefficients are not the same: A_b and E_b have a negative sign, whereas the other coefficients and the Routh's discriminant are positive. Hence, the Routh-Hurwitz Stability Criteria are not met, which means the aircraft has an unstable, asymmetric eigenmotion: the aforementioned spiral mode. Also for the system of asymmetric EOM, the numerically obtained eigenvalues from the system matrix and the eigenvalues obtained from the characteristic equation are found to be exactly the same.

Chapter 8

Landing Gear

Several landing gear options are evaluated in the Mid-Term Report [19]. Based on aspects such as mass, cost, integration into the fuselage and maintainability, the selected concept is a single-leaf spring landing gear. This chapter elaborates on the structural design of the landing gear. First, the loads are estimated, after which the landing gear is designed, starting with the strut shape. Thereafter the strut is sized to cope with the loads. Some attention is then payed to off-the-shelf products that comply with the requirements. Wheels, brakes and wheel fairings are added, after which the connection to the fuselage is discussed. Finally, the exact location of attachment is determined.

8.1 Landing Gear Loading

To design the structure the loads that act on the landing gear need to be computed. Aerobatic racing pilots are known to be very experienced in flying. Therefore, the vertical speed at touchdown can assumed to be really low, in the order of less than 0.5 $m \cdot s^{-1}$. However, a safety margin is added to be able to cope with crosswinds, gusts, a more complicated landing approach with inoperative engine, training sessions or touchdowns with a roll angle that leads to only one wheel absorbing the impact. Therefore, the landing gear is designed to withstand impacts up to a rate of decent of 3.6 $m \cdot s^{-1}$. A vertical speed of 3.6 $m \cdot s^{-1}$ corresponds to letting an object drop from a height of 0.63 m. Slightly overdesigning the structure is more favourable than risking a crash when a hard impact occurs. The challenge is to express the momentum of the aircraft in the form of a force, which can be used to define the required strength of the elastic landing gear leaf spring.

The aircraft, with a mass of 698 kg, touches the runway at a vertical speed of 3.6 m/s, yielding a momentum of:

$$p = 698\ kg \cdot 3.6\ \frac{m}{s} = 2513\ \frac{kg \cdot m}{s} \tag{8.1}$$

This momentum is expressed in terms of a force F the landing gear has to withstand at touchdown. The relation between momentum and force is stated in Equation (8.2),

$$F = \frac{\delta p}{\delta t} \tag{8.2}$$

where δp and δt represent the change in momentum and change in time, respectively. The next step is to define the time δt in which the aircraft decelerates, as well as the vertical displacement $d_{vertical}$ over which this deceleration occurs. Based on a literature study it seems feasible to allow for elastic deformation of a single leaf spring landing gear that results in a vertical displacement of the fuselage of about 25% of the landing gear height. Assuming a height of about 0.6 m yields a deflection of 0.15 m. To comply with the CS-23 regulations, the landing gear of an aerobatic aircraft must withstand a deceleration of at least 4.5g, hence 45 $m \cdot s^{-1}$ [14]. This yields a time of $\delta t = 0.08\ s$, in which the momentum of the aircraft in vertical direction is reduced to zero.

Substituting values for δp and δt into Equation (8.2) yields a required force of $F = 31.4\ kN$ that the landing gear needs to withstand during the determined time period of 0.08 s.

8.2 Shape and Sizing

The structure of the selected landing gear is rather simple. On each side a tube extends from the edge of the fuselage that has an angle θ with respect to the vertical plane. This angle should not be too small or too large. If θ is too small, the landing loads are mainly absorbed by compression of the strut, leading to a rather hard landing. If θ is too big, the strut needs to be designed stronger than necessary to cope with the high bending load. To prevent the propeller from hitting the ground the fuselage needs to be elevated around 0.6 m at the location of the main landing gear.

The first step is to analyse which inputs result in the vertical deflection $d_{vertical}$ of the landing gear:

- Impact force F
- Strut length $L = 0.6/cos(\theta)$
- Young's Modulus E of landing gear material
- Strut angle θ with respect to the vertical plane
- Strut radius r
- Strut thickness t

An expression is obtained for $d_{vertical}$ based on these inputs, see Equation (8.3). A force that is applied under an angle leads to compression and bending deflections.

$$\begin{aligned} d_{vertical} &= \delta_{compression} \cdot \cos(\theta) + \delta_{bending} \cdot \cos(45°) \\ &= \frac{FL}{EA} \cdot \cos(\theta) + \frac{FL^3}{3EI} \cdot \cos(45°) \\ &= \frac{FL}{E\pi(2rt - t^2)} \cdot \cos(\theta) + \frac{FL^3}{3E\frac{\pi[r^4-(r-t)^4]}{4}} \cdot \cos(45°) \end{aligned} \tag{8.3}$$

Setting $d_{vertical} = 0.15$ m yields two unknowns, the radius r and the tube thickness t. Increasing the radius reduces the mass, but also increases the induced drag. Therefore, the tube is designed as small as possible, resulting in a lightweight strut.

Several material, diameter and thickness combinations are evaluated. The selected material for the strut is aluminium. In Table 8.1 the optimal landing gear sizing parameters are listed. Note that the mass only includes both struts. The horizontal top part as well as the corners and supports for the wheel integration are not included.

Table 8.1: Landing gear sizing parameters

Input		Output	
F	31.4 kN	$d_{vertical}$	0.144 m
L	0.7 m	m	7.48 kg
E	69 GPa		
θ	30°		
r	26 mm		
t	7 mm		

It is determined that the landing gear can withstand a load of 31.4 kN using tubular struts, adding up to a weight of 7.5 kg.

8.3 Off-the-Shelf Product

Since validating, testing and certifying structural parts is a time and cost consuming process, one should always keep an eye open for already existing off-the-shelf products that fulfil the requirements while not compromising performance. Since the landing gear for a small aerobatic aircraft is a

rather simple subsystem, it can be assumed that the products available on the market are already very mature.

Therefore, it is decided to use the *Pitts S2S, S2A, S2B* landing gear by *Grove Aircraft Landing Gear Systems Inc.*, since its characteristics comply with the requirements. The design details of the landing gear are stated in Table 8.2. [76]

Table 8.2: Characteristics of "Pitts S2S, S2A, S2B" landing gear by "Grove Aircraft Landing Gear Systems Inc."

Aircraft Gross Weight	749-793 kg
Weight	15.7 kg
Material	7075-T6 Aluminum
Axle Bolt Hole Pattern	Type 1
Posibillity for Gundrill	Yes
Item Number	P/N 1034-3
Price	€1,200.- + €150.- (Gundrilled brake line)
Height	0.648 m
Width (top)	0.686 m
Width (bottom)	1.423 m

Grove Aircraft Landing Gear Inc. offers the option of adding a gundrilled brake line, so that the brake cable is secured in the strut. An axle bolt hole pattern of Type 1 denotes that this type of landing gear is usually combined with 5.00x5.00 wheels. This code represents the wheel size. The first and second number represent the rim diameter and rim width, respectively, both in inches. An illustration of the general landing gear layout as well as an illustration of the gundrilled brake line can be found in Figure 8.1.

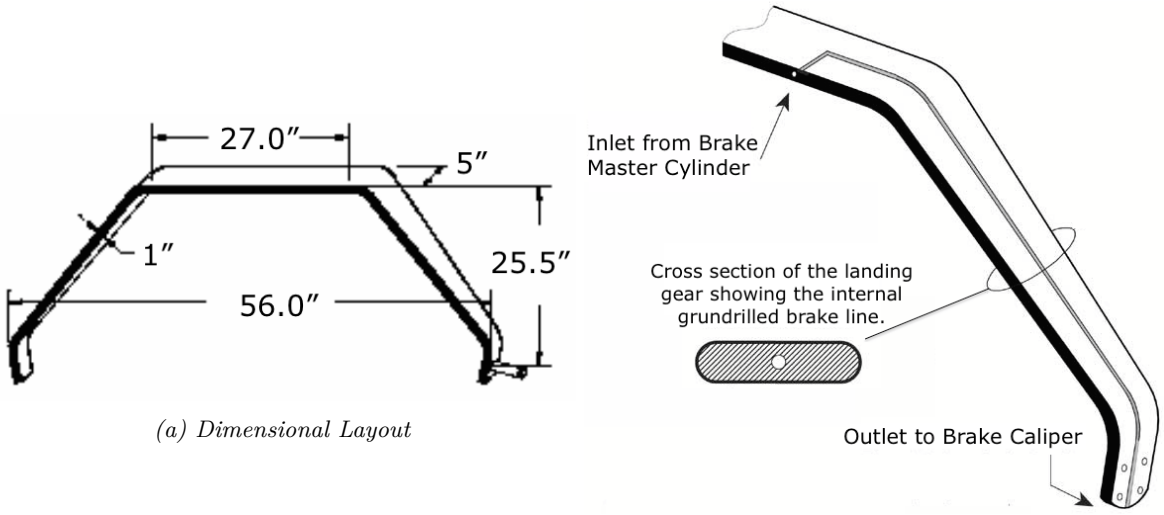

(a) Dimensional Layout

(b) Gundrilled brake line in strut

Figure 8.1: Illustration of "Pitts S2S, S2A, S2B" landing gear by "Grove Aircraft Landing Gear Systems Inc."

8.4 Wheels, Brakes and Fairings

The *Red Bull Air Race* regulations state that wheels need to be at least 5 inches in diameter and shall have a minimum tyre size of 5.00x5.00. Heavy duty brake discs shall be used with a disc thickness of no less than 0.25 inches. Additionally, it is stated that wheels are required to be manufactured by *Grove Aircraft Landing Gear Inc.* These regulations restrict the freedom of choice.

Based on these requirements the optimal wheels are the *55 Series Wheels & Brakes* by *Grove Aircraft Landing Gear Inc.* The wheels are shown in Figure 8.2 [77] and detailed characteristics of the wheels can be found in Table 8.3.

Figure 8.2: The 55-112 Grove Wheels and Brakes

Kit number	55-112
Wheel number	55-1A
Axle Diameter	1.25 [inches]
Static load rating	583 [kg]
Limit load rating	2331 [kg]
Mass	3.45 [kg]
Price	€ 590.-
Brake Pad number	066-111
Axle Pattern Type	1
Disc Thickness	0.25 [inches]

Table 8.3: Characteristics of "55 Series" Wheel and brake by "Grove Aircraft Landing Gear Systems Inc."

To attach the wheel to the strut an axle is required. The *Grove P/N 5013* axle, including two required axle spacers, a standard axle nut and wheel pant axle nut result in an additional weight of 0.9 *kg* and cost about € 143.-.

Finally, the tyres need to be defined. *Red Bull Air Race* requirements state that the minimum tyre size shall be no less than 5.00x5.00. The material shall consist of at least six plies. In addition, the tyres shall be able to withstand regular, non-tarmac landings. A tyre such as the *Michelin Aviator 5.00x5.00 6-ply* would be suitable. The cost budget for tyres and tubes is around € 280.-.

To optimize the aerodynamic design of the aircraft, brake fairings are used. Due to the complexity of designing fairings, it is decided to equip the aircraft with off-the-shelf products. Taking into account the required minimum tyre size of 5.00x5.00, *MF-4* wheel fairings are selected. The fairings are specifically designed for a wheel width of 5 inches and a rim size of 5 inches. The price of these fairings is around €198.50.- each, so the total costs come down to €397.-. [78]

8.5 Connection to Fuselage

Finally, the landing gear design needs to be connect to the fuselage. It is important to realise that the landing gear, being a single-leaf spring, undergoes a deformation at impact. This deformation could induce a torsion onto the fuselage truss, if connected wrongly. Therefore, *Grove Radius Blocks* are used, which act as mounting brackets and are widely used for aluminium spring landing gears. The inside faces have a specific radius that eliminates the torsional force on the fuselage as the landing gear deflects. Two blocks are required for each side, one on the top and one on the bottom of the horizontal part of the landing gear. Four *Grove Radius Blocks* cost about € 185. Figure 8.3a illustrates the way the *Grove Radius Blocks* are mounted and how the structure deforms during a hard landing. [79]

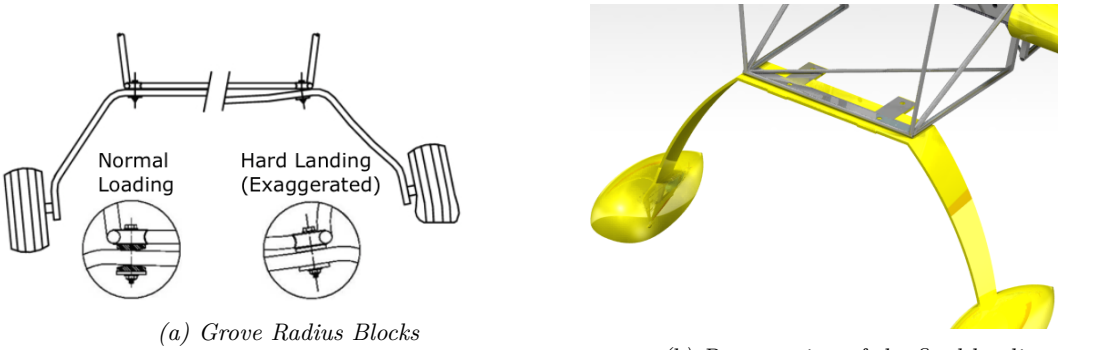

(a) Grove Radius Blocks

(b) Presentation of the final landing gear

Figure 8.3: Illustrations of final landing gear with connection

8.6 Main Landing Gear and Placement

The following summarises the landing gear design by giving a clear overview of what parts are required. Also, cost and mass of the subsystem are stated. Finally, the exact location of the landing gear is determined.

Table 8.4 lists all required components for the landing gear subsystem, indicating the mass and cost of each.

Table 8.4: Components of landing gear subsystem, indicating mass and cost

Component	**Mass** *[kg]*	**Cost** *[€]*
Grove Pitts S2S,S2A,S2B	15.7	1,350.-
Grove 55Series Wheels & Brakes	3.5	590.-
Grove P/N5013 axle	0.9	143.-
Michelin Aviator 500x5 6-Ply + tube	~ 2	280.-
Grove Radius Blocks	~ 0.5	185.-
Total	**22.6**	**2548.-**

In Section 2.3 the centre of gravity of the aircraft is computed and found to be located at $1.597\,m$ from the propeller tip. This c.g. location is now used to position the landing gear. The tail wheel is placed at the very end of the fuselage, connected to the rudder to allow steering on the ground. Literature suggests that the tail wheel should carry about 8% of the weight [14]. Based on this criterion Equation (8.4) can be used to calculate the location of the main landing gear, where $l_{fuselage}$ is the length of the entire aircraft, $l_{c.g.}$ is the centre of gravity location of the aircraft and F_{tail} is the percentage of the weight that shall be carried by the tail wheel (i.e. $F_{tail} = 8\%$).

$$\begin{aligned} l_{LG} &= \frac{(l_{c.g.} - l_{fuselage}) \cdot F_{tail}}{1 - F_{tail}} + l_{c.g.} \\ &= \frac{(1.597 - 6) \cdot 0.08}{1 - 0.08} + 1.597 = 1.214\ m \end{aligned} \tag{8.4}$$

Chapter 9

Final Design

This chapter gives an overview of the final preliminary design of the *T-16*, designed by *Torero*. All subsystems described in the detailed design are integrated into one aircraft and the characteristics of all subsystems are summarised in terms of mass, power and cost budgets. Furthermore, an update is given of the mass, cost and power budgets established in the Mid-Term Report of *Torero* [19]. A list of all detailed aircraft parameters, such as dimensions and performance characteristics, can be found in Appendix B.

9.1 Subsystem Integration

In this section visual representations are provided of the integration of all subsystems of the *T-16*. Renderings and drawings of the aircraft are made using *CATIA* and can be found in Figure 9.1.

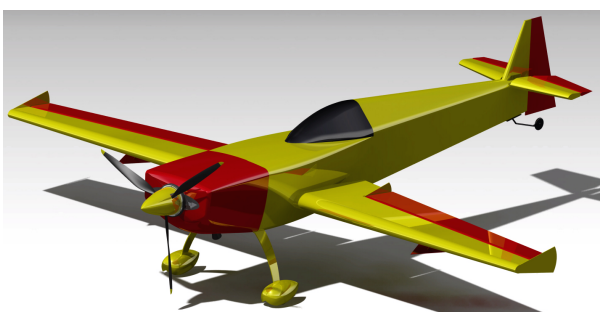

(a) Exterior rendering

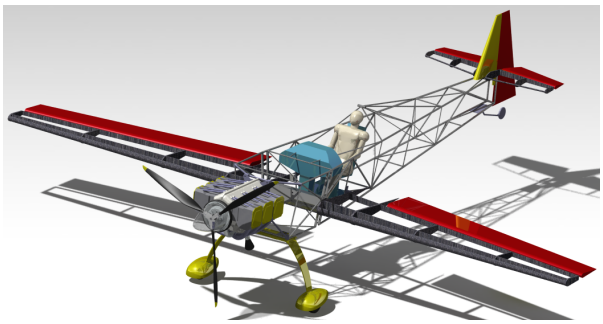

(b) Interior rendering

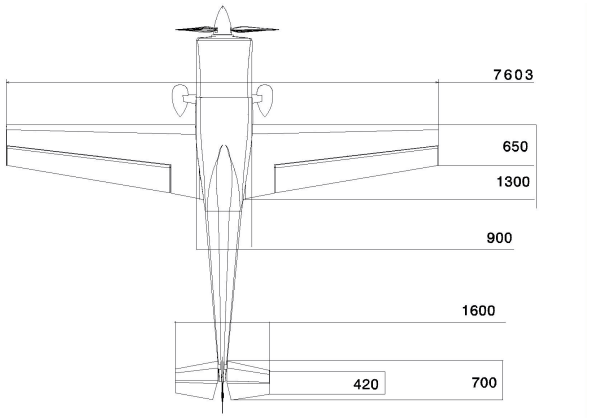

(c) Topview drawing, dimensions in [mm]

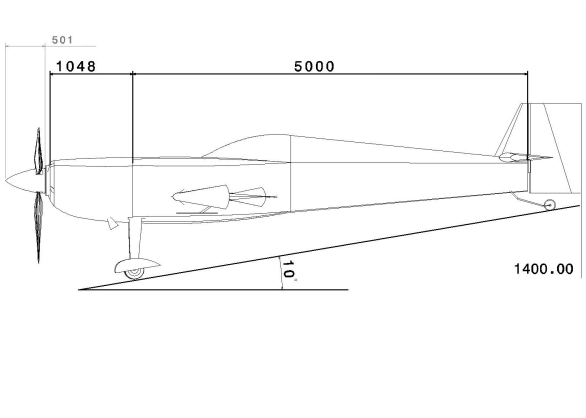

(d) Sideview drawing, dimensions in [mm]

Figure 9.1: Renderings and drawings of the T-16

9.2 Mass Budget

In this section the aircraft weights are shown, see Table 9.1, which result from the final iterations of the *T-16*.

Table 9.1: Mass budget of T-16

Component	**Value** *[kg]*
Wing weight	95
Empennage weight	20
Fuselage weight	97
Engine weight	235
Landing gear weight	24
Control surfaces weight	14
Instruments weight	4
Zero Ballast Empty weight	*489*
Pilot	82
Telemetry	15.3
Cameras and camera control system / EFIS	1.5
G-Race Suit of G-Race-Suit Penalty Weight	6.5
Helmet and parachute	15.7
Payload weight	*122*
Ballast weight	51
Empty Weight, including ballast	540
Fuel weight	36
Maximum Take-Off Weight	**698**

9.3 Cost Budget

This section gives an overview of the estimated cost for the production of the *T-16*, designed by *Torero*. The costs are listed in Table 9.2. *Torero* is given a budget of €275,000.- to design and develop an aerobatic racing aircraft. In Table 9.2 it can be seen that the total production cost of the *T-16* is estimated at €115,900.- which means that the remaining €159,100.- is used to cover development costs and suits as payment for the design team of the *T-16*.

Table 9.2: Cost budget of T-16

Component	**Value** *[€]*
Structure	30,000
Engine	41,000
Propeller	0
Mechanical Controls	750
Power Supply	750
Flight Instruments	5600
Seat	300
Production	37,500
Total Cost	115,900.-

9.4 Power Budget

In this section the power budget is shown, see Table 9.3, which results from research done on the electrical subsystems of the *T-16*. The research on the electrical systems can be found in the Mid-Term Report of *Torero* [19]. No significant changes are made to these values since this previous report, because they are considered to be sufficiently refined.

Table 9.3: Power budget of T-16

Component	**Value** *[W]*
Camera Control and Transmission (CCT) Box	20
Cameras	10
Communication System	19
Flight Instruments	15
Electronic Flight Instrumentation System (EFIS)	3
Starter Motor	1500
Total Power	**1567**

Part III

Aircraft Characteristics

Chapter 1

Performance

In this chapter an analysis of the flight performance of the aircraft is presented, based on the detailed design described in Part II. The chapter starts with a description of the reference system and standard equations of motion in Section 1.1, which are necessary for the analysis. After that, general aircraft characteristics are determined and analysed. However, some characteristics, such as endurance and fastest possible sustained turn, are not relevant for the mission life of the *T-16*. The characteristics that are determined are:

- Range and endurance (see Section 1.2)
- Stall speed (see Section 1.3)
- Maximum velocity (see Section 1.4)
- Climb rate and gradient (see Section 1.5)
- Steepest, tightest and fastest turn (see Section 1.8)
- Noise (see Section 1.9)
- Emissions (see Section 1.10)

Many performance analyses are purely theoretical and do not take into account all physical limitations of the aircraft. The limitations of the calculation methods are elaborated on in Section 1.7. Sections 1.9 and 1.10 discuss qualitative analyses performed on the noise and emissions produced by the *T-16*. These sections also include suggested improvements which can be applied to the aircraft to reduce noise and emissions.

1.1 Equations of Motion

To analyse the performance of the aircraft, first a reference frame is defined and the Equations Of Motion (EOM) expressed in this frame are stated. Figure 1.1 represents the forces and accelerations acting on the aircraft, expressed in the body axis reference frame. This figure also includes the angles between the body reference frame (index b), aerodynamic reference frame (index a) and Earth fixed axis reference frame (index e). The forces are expressed in components parallel and perpendicular to the velocity vector. Using Newton's Second Law, the two-dimensional equations of motions for unsteady, curved, symmetric flight can be derived, see Equations (1.1a) and (1.1b). The symbols in these equations represent the lift L, weight W, thrust T, drag D, velocity of aircraft V, gravitational acceleration on Earth $g = 9.81\ m/s^2$, thrust angle α_T, angle of attack α, pitch angle θ, flight path angle γ and derivative with respect to time $\frac{d}{dt}$. [80]

$$T\cos\alpha_T - D - W\sin\gamma = \frac{W}{g}\frac{dV}{dt} \tag{1.1a}$$

$$L - W\cos\gamma + T\sin\alpha_T = \frac{W}{g}V\frac{d\gamma}{dt} \tag{1.1b}$$

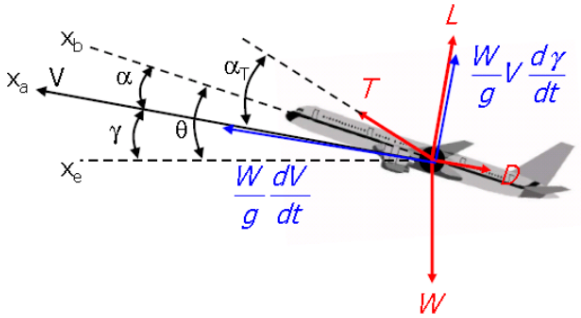

Figure 1.1: Free body and kinetic diagram of a general aircraft, expressed in the body axis reference frame

From these equations the power equations can be derived, which give a relation between the power available P_a, power required P_r, engine power $P_e = 315\,hp = 235\,kW$, propeller efficiency $\eta_p = 0.8$ and rate of climb rc, see Equations (1.2a) and (1.2c). [80]

$$P_r = D \cdot V \tag{1.2a}$$

$$P_a = P_e \cdot \eta_p \tag{1.2b}$$

$$\frac{P_a - P_r}{W} = rc + \frac{V}{g}\frac{dV}{dt} \tag{1.2c}$$

The lift and drag at any point in flight can be computed with Equations (1.3a) to (1.3c), with lift coefficient C_L, drag coefficient C_D, drag coefficient at zero lift C_{D_0}, air density ρ, wing surface area S, aspect ratio A and Oswald efficiency factor e.

$$L = C_L \frac{1}{2}\rho V^2 S \tag{1.3a}$$

$$D = C_D \frac{1}{2}\rho V^2 S \tag{1.3b}$$

$$C_D = C_{D_0} + \frac{{C_L}^2}{\pi A e} \tag{1.3c}$$

The thrust angle is zero $\alpha_T = 0$, since the engine of the *T-16* is positioned directly along the longitudinal body axis X_b. Atmospheric properties are computed with the International Standard Atmosphere (ISA) model. ISA sea-level conditions are: air density $\rho_0 = 1.225\,kg/m^3$, temperature $T_0 = 288.15\,K$ and ambient pressure 101325 Pa. [37]

1.2 Range and Endurance

The range and endurance of an aircraft are important parameters for cruise and loiter flights, because these numbers represent how far and how long the aircraft can fly before running out of fuel. The range R and endurance E is computed with Equations (1.4) and (1.5).

Where:

- η_p is the propeller efficiency
- $g = 9.81\,m/s^2$ is the gravitational acceleration on Earth
- SFC is the specific fuel consumption
- C_L is the lift coefficient
- C_D is the drag coefficient
- W_{start} is the aircraft weight at the start of cruise
- W_{end} is the aircraft weight at the end of cruise
- V is the aircraft velocity

To gain maximum range and endurance it is required to have a maximum lift over drag ratio C_L/C_D. This can be computed using Equation (1.6). [80, 81]

$$R = \left(\frac{\eta_p}{g \cdot SFC}\right)_{cruise} \cdot \left(\frac{C_L}{C_D}\right)_{max} \ln\left(\frac{W_{start}}{W_{end}}\right)_{cruise} \tag{1.4}$$

$$E = \left(\frac{1}{V \cdot g \cdot SFC}\right)_{cruise} \cdot \left(\frac{C_L}{C_D}\right)_{max} \ln\left(\frac{W_{start}}{W_{end}}\right)_{cruise} \tag{1.5}$$

$$C_{L_{opt}} = \sqrt{3 \cdot C_{D_0} \cdot \pi \cdot A \cdot e} \tag{1.6}$$

The parameters W_{start} and W_{end} are computed using Equations (1.7a) and (1.7b), based on the following assumptions, which are based on the fuel weight estimation method described by [81]:

- The fuel weight used for the cruise flight is 80% of the total fuel weight.
- The fuel weight used for starting-up the aircraft, taxi, take-off and climbing to cruise altitude is 7% of the total fuel weight.
- The fuel weight used for landing and shut-down is 3% of the total fuel weight.
- The back-up fuel weight is 10% of the total fuel weight.

$$W_{start} = \text{MTOW} - 0.07 \cdot W_{fuel} \tag{1.7a}$$

$$W_{end} = W_{start} - 0.8 \cdot W_{fuel} \tag{1.7b}$$

The input parameters used for the equations can be found in Appendix B. The results for range and endurance are the following:

- Maximum lift over drag ratio $\frac{C_L}{C_D} = 14$.
- Range, $R = 404\,km$.
- Endurance, $E = 1.4\,hr$.

1.3 Stall Speed

The stall speed that can be achieved only varies with the maximum lift coefficient $C_{L_{max}}$ and the air density ρ, which is directly related to the flight altitude. From the requirements defined by *Red Bull*, the stall speed should be no more than $V_{s_{max}} = 61\,kts = 31.4\,m \cdot s^{-1}$ (see Chapter 3 in Part III) [16]. Equation (1.8) is used to compute the stall speed. [80]

$$V_{stall} = \sqrt{\frac{W}{S}\frac{2}{\rho}\frac{1}{C_{L_{max}}}} \tag{1.8}$$

The stall speed of the *T-16* at sea-level conditions at a maximum lift coefficient of $C_{L_{max}} = 1.8$ is $V_{stall} = 29.2\,m \cdot s^{-1}s = 105\,km \cdot h^{-1}$. Hence, the requirement of having a stall speed of at most $31.4\,m/s$ is met.

1.4 Maximum Velocity

In this section the maximum velocity that can be achieved by the aircraft is determined. The following assumptions for the equations of motions, described in Section 1.1, are made to analyse the performance:

- The aircraft is in steady, symmetric, horizontal flight. So $\frac{dV}{dt} = 0$, $\frac{d\gamma}{dt} = 0$, $\gamma = 0$ and $rc = 0$.
- The aircraft flies at full throttle, thus with maximum available power.
- The maximum velocity is analysed at sea-level conditions.

These assumptions lead to the simplifications for the equations of motion stated in Equations (1.9a) to (1.9c).

$$L = W \tag{1.9a}$$

$$T = D \tag{1.9b}$$

$$P_a = P_r \tag{1.9c}$$

Then, by rewriting Equation (1.3a) to Equation (1.10b) and substituting this together with Equations (1.3b) and (1.3c) into Equation (1.2a), a direct relation can be obtained between the

power available, power required, maximum velocity and lift coefficient, see Equation (1.10a). Solving this equation yields the maximum velocity of the aircraft at a given available power.

$$P_r = \left(C_{D_0} + \frac{{C_L}^2}{\pi A e} \right) \frac{1}{2} \rho {V_{max}}^3 S \tag{1.10a}$$

$$C_L = \frac{W}{\frac{1}{2}\rho {V_{max}}^2 S} \tag{1.10b}$$

$$P_a = \left(C_{D_0} + \frac{\left(\frac{W}{\frac{1}{2}\rho {V_{max}}^2 S} \right)^2}{\pi A e} \right) \frac{1}{2} \rho {V_{max}}^3 S \tag{1.10c}$$

The power diagram, from which the maximum velocity is obtained based on the power available and power required, can be found in Figure 1.2. Equation (1.10c) gives two solutions for the velocity where $P_a = P_r$, where the highest value corresponds to V_{max}. The power diagram in Figure 1.2 is based on sea-level conditions and an aircraft weight equal to $W = \text{MTOW} \cdot g$. The values for C_{D_0}, S, A and e can be found in Appendix B.

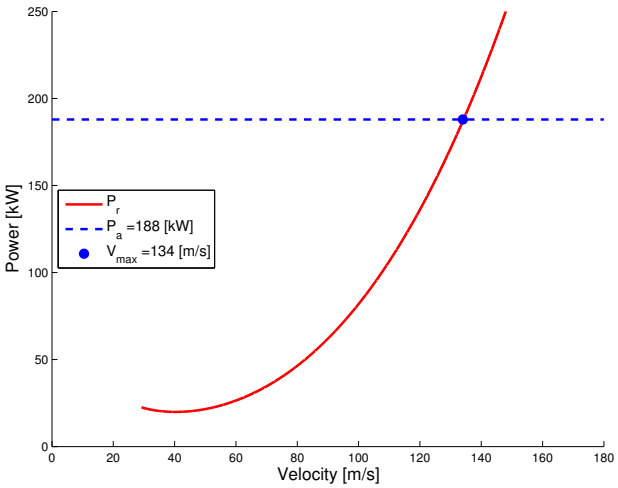

Figure 1.2: Power diagram to compute the maximum velocity, at sea-level conditions.

From Figure 1.2 it can be seen that the maximum velocity at sea-level conditions is $V_{max} = 134\, m \cdot s^{-1} = 482\, km \cdot h^{-1}$. However, this computed value for the maximum aircraft velocity is a theoretical value, based on the wing planform and aircraft weight. During flight, the aircraft cannot reach such high velocities, because the airframe is not be able to withstand the forces and vibrations asociated with these high velocities. Moreover, at a certain velocity the propeller loses efficiency [82]. It is recommended that during a next design phase a more detailed airframe and propeller analysis is performed to verify what the physical maximum velocity is, also called the Never Exceed speed V_{ne}, and how much it differs from the theoretical maximum velocity. The limitations of the equations used to compute the maximum velocity are elaborated on in Section 1.7.

1.5 Climbing Performance

In this section the climb performance of the *T-16* is analysed. As defined by requirement FARA-Sys-Afs-04, see Chapter 3 in Part III, the *T-16* should have a minimum climb rate of $rc = 18\, m/s$. According to the CS-23 regulations, the aircraft shall have a minimum climb gradient of $\gamma = 8.3\%$ [14]. There are two types of climb rates: steady and unsteady. Unsteady climb means that the pilot flies at constant Indicated Airspeed (IAS). However, as the aircraft climbs, the air density decreases, which results in an increasing True Airspeed (TAS), while still flying at constant IAS. Therefore, climbing at constant IAS is an unsteady climb. In the steady climb the pilot climbs at constant TAS. [80]

In this section the steady rate of climb is analysed at sea-level conditions, since sea-level performance is the most relevant for the *Red Bull Air Race*. The following assumptions for the equations of motions, described in Section 1.1, are made to analyse the performance:

- The aircraft flies in a steady, symmetric climb: $\frac{dV}{dt} = 0$ and $\frac{d\gamma}{dt} = 0$.
- The climb is performed at sea-level conditions.

With these assumptions, Equation (1.2c) is simplified to Equation (1.11a). For this equation the only unknown is the required power, which is computed in a similar way as described in Section 1.4, see Equation (1.11b).

$$rc = \frac{P_a - P_r}{W} \tag{1.11a}$$

$$P_r = \left(C_{D_0} + \frac{\left(\frac{W}{\frac{1}{2}\rho V^2 S} \right)^2}{\pi A e} \right) \frac{1}{2}\rho V^3 S \tag{1.11b}$$

1.5.1 Rate of Climb

The rate of climb is plotted versus the TAS in Figure 1.3. The values for C_{D_0}, S, A and e can be found in Appendix B and the aircraft weight is equal to $W = \text{MTOW} \cdot g$.

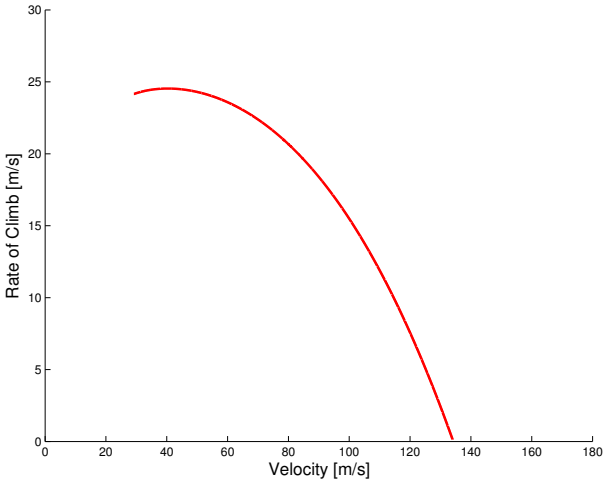

Figure 1.3: Rate of climb diagram, at sea-level conditions

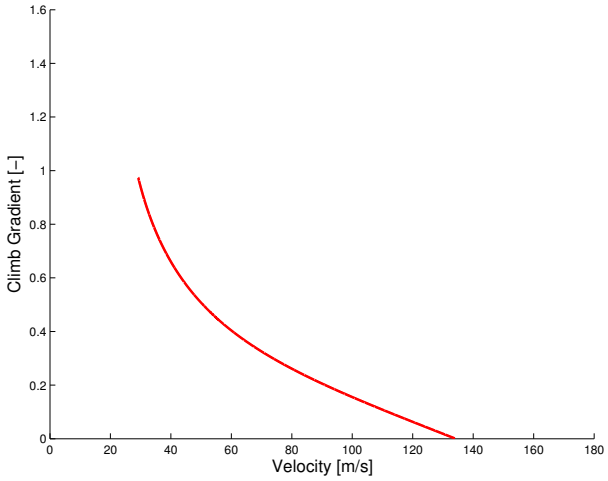

Figure 1.4: Climb gradient diagram, at sea-level conditions

The rate of climb diagram is related to the power diagram, see Figure 1.2, because they are based on the same equation to compute the required power during flight. It can be seen that at the maximum velocity, the rate of climb is equal to $rc = 0$. This is valid, since the rate of climb depends on the difference between the power available and power required, and at the maximum velocity $P_a = P_r$, thus $rc = 0$, see Equation (1.11a).

As can be seen in Figure 1.3 the maximum steady rate of climb at sea-level is $rc_{st} = 24.5\, m \cdot s^{-1}$. The corresponding velocity is $V_{rc_{max}} = 40\, m \cdot s^{-1} = 145\, km \cdot h^{-1}$ and the corresponding power required is $P_{r_{min}} = 19.9\, kW$. Comparing this minimum power required with Figure 1.2 it can be seen that this value is also the minimum in the graph.

1.5.2 Climb Gradient

$$\sin\gamma = \frac{rc}{V} \tag{1.12}$$

The climb gradient can be computed with Equation (1.12) [80] and is plotted versus velocity in Figure 1.4. The maximum climb gradient of the *T-16* is $\gamma = 0.97 = 62\%$, which corresponds to a flight path angle of $\gamma = 56\,^{\circ}$. It should be noted that the flight path angle and the climb gradient are essentially the same, only one is expressed in degrees and the other is dimensionless. Therefore, the same symbol is used for the flight path angle and the climb gradient.

With these results, i.e. $rc_{st} = 24.5\,m/s$ and $\gamma = 62\%$, requirement FARA-Sys-Afs-04, which requires a rate of climb of $18\,m/s$ and requirement FARA-Sys-Afs-05, which requires a climb gradient of 8.3%, are both met, see Chapter 3 in Part III.

1.6 Service Ceiling

The service ceiling which is required by *FlashCo.* is $5000\,m$, see requirement FARA-Stk-12 in Section 3.1. The service ceiling of the *T-16* is computed in a similar way as the rate of climb, see Section 1.5. The rate of climb is defined as the difference between the power available P_a and power required P_r divided by the aircraft weight W, see Equation (1.11a). From Equation (1.11b) it can be seen that the main variables are the airspeed V and the air density ρ. The air density is related to the temperature, which is related to the altitude, see Equations (1.13a) and (1.13b). The air density and temperature T depend on the altitude h, lapse rate $a = -0.0065\,K/m$, gravitational acceleration on Earth $g = 9.81\,m/s^2$, gas constant of air $R_{air} = 287.05\,J/(kg \cdot K)$ and atmospheric conditions at sea level. [37]

The service ceiling is defined as the altitude where the rate of climb is equal to zero, so where $P_a = P_r$.

$$\frac{\rho}{\rho_0} = \left(\frac{T}{T_0}\right)^{\left(-\frac{g}{a \cdot R_{air}} - 1\right)} \tag{1.13a}$$

$$T = T_0 + a(h - h_0) \tag{1.13b}$$

The power available is also dependent on the air density and therefore the altitude, see Equation (1.14) [80]. This equation is verified with the engine data, provided by *Lycoming* [83].

$$P_a = P_{a_0}\left(\frac{\rho}{\rho_0}\right)^{0.75} \tag{1.14}$$

By increasing the altitude of the power diagram shown in Figure 1.2, which is used to compute the maximum velocity at sea-level, the power lines shift until the minimum P_r is equal to P_a. The resulting power diagram is depicted in Figure 1.5a. Although it can be seen that the minimum power required is equal to the power available, and the power lines shifted, the resulting service ceiling is almost $15\,km$. This result is considered invalid because of the fact that above an altitude of $11,000\,m$ the atmospheric model changes from the troposphere to tropopause. Since the lapse rate of the Tropopause is $a = 0\,K/m$, the equations used to construct the power diagrams are invalid at altitudes above $11\,km$. [37]

Furthermore, any aircraft which flies above an altitude of $3000\,m$ should be equipped with an oxygen system, because the air does not contain enough oxygen for the pilot to breathe [84]. This means that requirement FARA-Stk-12 can not be complied with, unless an oxygen system is implemented. However, this is not required for flying in the *Red Bull Air Race*, since it is held at sea-level conditions, and would only add weight.

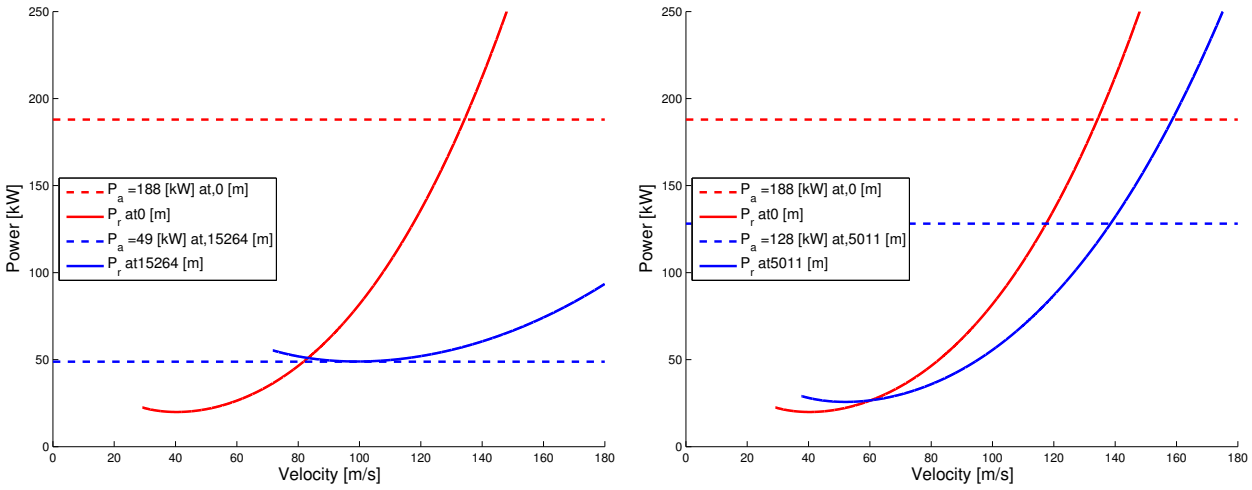

(a) Power diagram for service ceiling

(b) Power diagram at an altitude of $5000\,m$

Figure 1.5: Power diagrams to compute the service ceiling

Simulations are run to analyse the performance of the *T-16* flying at an altitude of $5000\,m$, because the power equations are still valid for this altitude. The resulting performance diagram can be found in Figure 1.5b. It can be seen that at an altitude of $5000\,m$, the aircraft can achieve a rate of climb of $rc = 15\,m/s$ and a maximum velocity of $V_{max} = 138\,m \cdot s^{-1} = 497\,km \cdot h^{-1}$. Still these results seem overestimated, since the reference aircraft of the *Red Bull Air Race* are not able to achieve these performance characteristics [6].

A possible cause for the overestimated power diagrams is the fact that the equations used to construct the power diagrams do not take into account the physical limitations of the propulsion system. The limitations of the service ceiling analysis are elaborated on in Section 1.7.

1.7 Limitations of Performance Diagrams

In the previous sections an analysis of the flight performance of the *T-16* is presented. However, it is noted that the results obtained from the simulations seem to be invalid. Most results seem overestimated compared to the performance of the reference aircraft.

The following determined performance characteristics are considered unreliable:

- Maximum velocity at sea-level equals $482\,km/h$
- Maximum rate of climb equals $24.5\,m/s$
- Service ceiling equals $15\,km$

Compared to the reference aircraft in Appendix A, the expected maximum velocity is around $420\,km/h$, the rate of climb around $18\,m/s$ and the service ceiling between $3000\,m$ and $5000\,m$.

The cause of these overestimated values potentially lies in the power calculations. Since all these performance characteristics are calculated with the power available P_a and power required P_r, it is most likely that there are factors in these equations which play a role in the overestimated performance results. The corresponding equations are Equations (1.15a) and (1.15b), with $P_{a_0} = 188\,kW$. It is identified that these equations are variable with altitude, since the air density ρ varies with altitude [37].

$$P_a = P_e \cdot \eta_p \cdot \left(\frac{\rho}{\rho_0}\right)^{0.75} \tag{1.15a}$$

$$P_r = \left(C_{D_0} + \frac{\left(\frac{W}{\frac{1}{2}\rho V^2 S} \right)^2}{\pi A e} \right) \frac{1}{2} \rho V^3 S \tag{1.15b}$$

However, based on more detailed analyses of the propeller and engine efficiency it is concluded that Equation (1.15a) may be invalid. It is still correct that the available power depends on the altitude, but the factor of 0.75 may not be entirely correct as firstly assumed based on literature research [80]. It is found that the propeller efficiency also depends on the velocity and propeller pitch angle θ_p. Therefore, the power available can be written as Equation (1.16). [82]

$$P_a(h) = P_e(h) \cdot \eta_p(h, V, \theta_p) \tag{1.16}$$

The equations used for the performance analyses are purely theoretical and do not take these specific altitude limitations into account. For instance, the propeller efficiency depends on the altitude and the airspeed. At high altitudes, the air density is lower and therefore the propeller generates a lower mass flow of air at a certain rpm than compared to sea-level conditions. Furthermore, if the propeller pitch is high, the propeller blades stall earlier, at high airspeeds, than at a lower pitch angle. These two aspects decrease the propeller efficiency at high altitudes. Another physical limitation of the propulsion system is related to the combustion process of the engine. The engine of the *T-16* is air breathing, which means that the available power depends on the mass flow of air at the intake of the engine. At higher altitudes, the air density is lower which result in a lower mass flow of air at the intake, which decreases the propulsion efficiency. [82]

These aspects are currently not included in the calculations, which is a possible cause of the overestimated performance values. It is recommended to perform a more detailed analysis on the propulsion system to improve the performance analysis of the *T-16*.

1.8 Turning

This section analyses the turning performance of the *T-16*. To analyse the turns, first the free body diagrams and kinetic diagrams have to be redefined, since the diagram of Figure 1.1 can not be used to analyse turns. It is assumed that the turns are sustained, by making a turn the aircraft produces sufficient lift to compensate the aircraft weight. When the aircraft rolls to make a turn, the vertical component of the lift vector decreases. To increase the vertical component of the lift vector to compensate the weight, the pilot needs to pull the stick to increase the angle of attack and therefore the lift. The free body and kinetic diagram, which indicate all forces and accelerations acting on the aircraft in a turn, is depicted in Figure 1.6. [80]

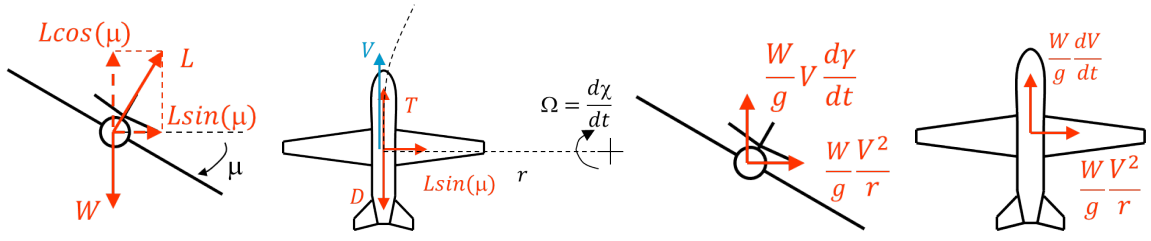

(a) Free Body Diagrams *(b) Kinetic Diagrams*

Figure 1.6: Free body and kinetic diagrams during sustained turn

The additional symbols represent the bank angle μ, turn radius r, heading angle χ and rotational velocity Ω. An overview of all assumptions made for the turn performance is given:

- The turn is sustained, which means that the vertical component of the lift vector is equal to the aircraft weight: $L\cos\mu = W$.
- The turn is steady and horizontal: $\frac{dV}{dt} = 0$ and $\frac{d\gamma}{dt} = 0$.
- The turns are analysed at sea-level conditions.

This leads to a new set of equations of motion, see Equations (1.17a) to (1.17d). Furthermore, the power available equation, which depends on the load factor n, is derived by combing Equation (1.10c) and Equation (1.19a) into Equation (1.18b).

$$T = D \tag{1.17a}$$
$$P_a = P_r \tag{1.17b}$$
$$\frac{W}{g}\frac{V^2}{r} = L\sin\mu \tag{1.17c}$$
$$L\cos\mu = W \tag{1.17d}$$

$$D = \left(C_{D_0} + \frac{\left(\frac{W}{\frac{1}{2}\rho V^2 S}\right)^2}{\pi A e}\right)\frac{1}{2}\rho V^2 S \tag{1.18a}$$
$$P_a = \left(C_{D_0} + \frac{\left(\frac{nW}{\frac{1}{2}\rho V^2 S}\right)^2}{\pi A e}\right)\frac{1}{2}\rho V^3 S \tag{1.18b}$$
$$n = \frac{L}{W} \tag{1.19a}$$
$$n = \frac{1}{\cos\mu} \tag{1.19b}$$

The (n, V)-plot which is made with these equations exist of two parts. The first part is limited by the $C_{L_{max}}$ of the aircraft, the second part is limited by the P_a. To find n_{max} in the first part, Equation (1.18a) is used, where the value for $C_{L_{max}}$ is substituted to find the maximum drag at a certain airspeed. Now n can be varied in Equation (1.18b) to find the drag at a certain load factor. At the value of n for which the two drag values are equal, n_{max} is found. Subsequently for part B, n_{max} is found at the point where drag equals available thrust. The result is the variation of n_{max} with airspeed V . [80].

$$n = \frac{C_{L_{max}}}{\frac{W}{S}\frac{2}{\rho}\frac{1}{V^2}} \tag{1.20a}$$
$$n = \frac{T}{W}\frac{C_L}{C_D} = \frac{P_a V}{W}\frac{C_L}{C_D} \tag{1.20b}$$
$$V = \sqrt{\frac{nW}{S}\frac{2}{\rho}\frac{1}{C_L}} \tag{1.20c}$$

These equations are used to analyse three types of turns:

- Steepest turn: turning with maximum load factor $n_{max} = 10$
- Tightest turn: turning with minimum turn radius r_{min}
- Fastest turn: turning wight minimum time to turn 360 °

1.8.1 Steepest Turn

The steepest turn is flown at maximum lift-over-drag ratio (C_L/C_D). Therefore, the optimal lift coefficient ($C_{L_{opt}}$) and corresponding drag coefficient are required, see Equations (1.6) and (1.3c). The velocity at the maximum turning load factor is computed using Equation (1.21). The (n, V)-diagram is shown in Figure 1.7, which also includes the maximum manoeuvre load factor $n_{max} = 10$ as defined by *Red Bull* [16]. It can be seen that the theoretical steepest turn can be performed at $V = 100\,m/s$ for $n_{max} = 25$. However the *Red Bull* regulations only allow a turn of $n_{max} = 10$ at a bank angle of $\mu_{n_{max}} = 84\,°$, which can be achieved at a wider range of velocities. Furthermore, the structure is designed for a maximum load factor of $n_{max} = 15$, so the aircraft is physically not able to fly at a maximum load factor of 25.

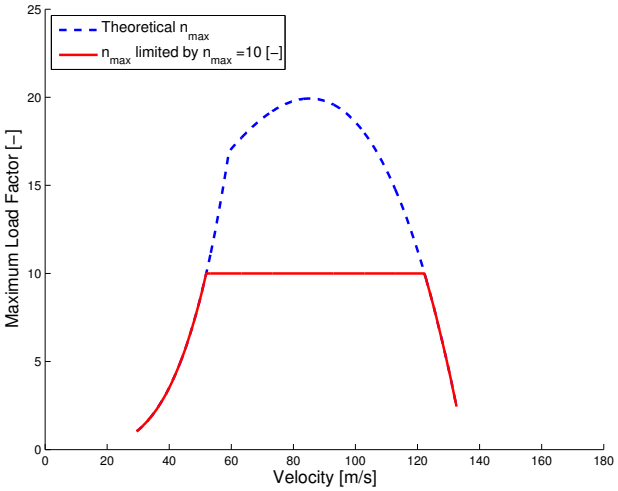

Figure 1.7: n,V-diagram to indicate the maximum theoretical turn load factor, including limitation of 10g defined by the Red Bull regulations.

$$V_{n_{max}} = \sqrt{\frac{n_{max} W}{S} \frac{2}{\rho} \frac{1}{C_{L_{opt}}}} \tag{1.21}$$

1.8.2 Tightest Turn

The turn radius R is computed using Equation (1.22). The resulting R, V-diagram is shown in Figure 1.8, which also includes the limitation of $n_{max} = 10$ as defined by *Red Bull* [16]. It can be seen that the tightest allowed turn has a turn radius of $R_{min} = 28\,m$ at a velocity of $V = 52.0\,m/s = 187\,km/h$.

$$R = \frac{V^2}{g \cdot \sqrt{{n_{max}}^2 - 1}} \tag{1.22}$$

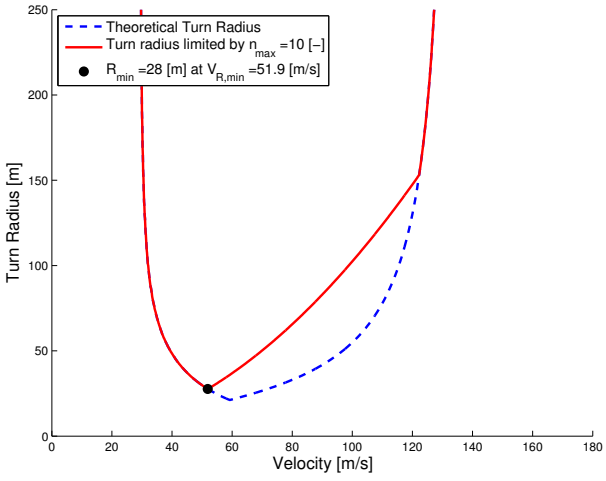

Figure 1.8: R,V-diagram to indicate the minimum theoretical turn radius, including limitation of 10g defined by the Red Bull regulations.

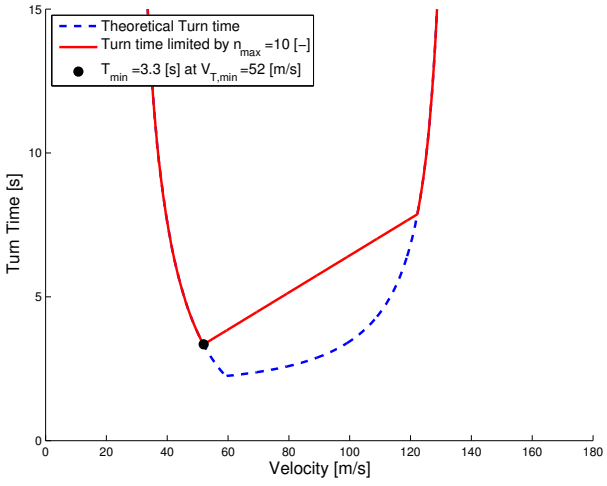

Figure 1.9: T,V-diagram to indicate the minimum theoretical turn time, including limitation of 10g defined by the Red Bull regulations.

1.8.3 Fastest Turn

The time to turn 360 ° is computed using Equation (1.23). This time is obtained by substituting the values of R from Figure 1.8 in the equation. The resulting T, V-diagram can be found in

Figure 1.9. It can be seen that the fastest allowed turn has a turn time of $T_{min} = 3.3\,s$ at a velocity of $V = 52.0\,m/s = 187\,km/h$.

$$T = \frac{2\pi R}{V} \tag{1.23}$$

From these results it is concluded that for the *T-16* the fastest and tightest turn are performed at the same V with the same R at sea-level conditions, thus they coincide. If the *T-16* would fly at its maximum theoretical load factor, see Figure 1.7, the tightest and fastest turn would not be the same.

1.9 Noise Characteristics

Another important performance characteristic of the aircraft is the noise production. To be certified to fly, the *T-16* must undergo noise tests to prove compliance with EASA noise certification limits [14]. If compliance is proven, a noise type certificate for light, propeller driven aircraft can be obtained. Noise levels for the *Extra 300L* powered by the *Lycoming AEIO-540* engine, are 82.5 dBA at take-off and 72.7 dBA for a fly-over. These noise levels can be assumed to be the same for the *T-16*, as it classifies in the same aircraft category and the same engine is used under the same conditions. [85]

Red Bull has not stated any regulations regarding noise levels applying to participating aircraft. However, besides the CS-23 regulations that should be taken into account, also the sustainability of the design can be increased by reducing aircraft noise. To reduce aircraft noise, first it must be established what the main sources of noise are. For piston-engine aircraft, the four main sources of noise that are discussed in this section are:

- Engine intake
- Engine exhaust
- Propeller blade
- Propeller tip

1.9.1 Engine Intake

In this part of the engine, a turbulent intake airflow causes noise. One solution for noise reduction is locating a large diffuser volume downstream of the engine intake to facilitate noise attenuation [86]. Before this modification can be applied, it must be stated in the engine logbook to demonstrate supplier approval and then it must be approved by the *Red Bull Race Committee*.

1.9.2 Engine Exhaust

Considering the exhaust system, most noise is produced by combustion and turbulence. Energetic exhaust products leaving the engine cylinders meet the ambient air, causing pulsation. The energy level of these products can be reduced by placing a muffler after the exhaust to reduce the backpressure and increase the engine efficiency. As a rule of thumb, the intake diffuser volume should be at least half the volume of the exhaust muffler. [86]

1.9.3 Propeller Blade

Blade noise is caused by tip vortices. The noise due to tip vortices can be reduced by increasing the propeller diameter, such that the propeller rpm can be reduced. Also, an extra blade can be added, such that the diameter can be decreased, resulting in a lower tip velocity for the same rpm. This, however, increases propeller weight and cost. [86]

1.9.4 Propeller Tip

A solution for noise generated at the propeller tip, is implementing bended propeller tips. Another option is ducting the propeller. This is claimed to reduce the propeller noise levels by 80%. However, using ducts for tractor propeller aircraft is not widely applied. It demands complete design modifications, which makes it not easily applicable for the post-mission phase. [86]

Concluding the noise characteristics analysis, multiple options are available to reduce the aircraft noise. Most of these options require additional structure to be added which increases the weight. In case engine modifications are implemented for the post-mission phase, a trade-off between noise reduction and weight increase must be made. Implementing these modifications for the race is not considered, because this is not allowed by the *Red Bull* regulations. [16]

1.10 Emissions Analysis

As stated in Section 3.1 in Part II, the fuel supplied at the *Red Bull Air Race* is *Aviation Gasoline 100LL* in accordance with ASTM D 910 [16]. *Avgas 100LL* is a low lead version of the *Avgas 100* containing $0.56\, g \cdot L^{-1}$ of tetraethyl lead [87]. This lead content is used to prevent knocking of the engine, i.e. ignition outside the normal combustion process. Also ethylene bromide is added to clear the engine components from lead oxide remains. Modifications to the *100LL Avgas* by means of other additives cannot be implemented by the racing teams, since it is not allowed by the *Red Bull* regulations [16]. This means that the fuel used is fixed and non-negotiable during the race.

Emission factors of *Avgas* are CO_2 $(2.19 \cdot 10^3\ g \cdot L^{-1})$, CH_4 $(9.50 \cdot 10^{-2}\ g \cdot L^{-1})$ and NO_2 $(1.85 \cdot 10^{-2}\ g \cdot L^{-1})$ [88]. Alternative fuels are considered in Section 2.1.

Chapter 2

Approach Sustainable Design

A key factor in the design of the *T-16* is sustainability, which *Torero* defines as:

> Sustainability is one main focus in designing the *T-16* aircraft such that the aircraft is designed as efficient as possible to achieve maximum performance during the *Red Bull Air Race*, with the use of an acceptable amount of resources (e.g. cost, time, labour and energy), without compromising the environment more than necessary and still being able to find a practical use for the aircraft after the *Red Bull Air Race World Championship*.

A distinction is made between designing for the mission, i.e. the *Red Bull Air Race*, and designing for possible post-mission applications. The applied materials and production processes should be as sustainable as possible for both the mission and the post-mission phase, while still satisfying all requirements. The main difference between these two life phases, in terms of sustainability, is that for the post-mission phase the aircraft mainly needs to have a practical purpose, since the aircraft retires from competition after three seasons, while for the mission-phase the focus is on the use of sustainable materials and production processes. The challenge for *Torero* is to come up with a successful design that is sustainable in both phases.

In this chapter unique design features of the *T-16* related to sustainability are presented. *Torero* integrates biodegradable composite materials in the fuselage skin, not only to decrease the carbon footprint of the aircraft structure, but also to make a mark in the aerospace industry and at the same time promote *FlashCo.*. This feature and other sustainable design aspects are presented in Section 2.1. Furthermore, the post-mission options are increased by realising a modular aircraft design. Its corresponding plug-and-fly principle is the revolutionary idea that *Torero* invented to increase the post-mission purpose of the *T-16* after the *Red Bull Air Race*. This is explained in Section 2.2. For another post-mission application research is done to decrease emissions by switching to an electrical power system. The elaboration and recommendations on this electrical propulsion system can be found in Section 2.3.

2.1 Sustainable Design Aspects

The increase in sustainability of the *T-16* aircraft, of which most likely only a single one or at most a few are manufactured, does not lead to a great decrease in emissions in global aviation. However, because the aircraft participates in the *Red Bull Air Race*, an event that is followed by millions of people all over the world, the attention is drawn to the importance of sustainability and the difference that can be made in that regard. Examples that illustrate the approach *Torero* takes to a sustainable design are summarised in the following sections.

2.1.1 Recyclable Materials

The fuselage structure is a major component providing sufficient room for sustainable design aspects. The tubular frame material, the ASTM A514 steel alloy, is discussed in Section 4.1 in Part II, has the great advantage of being recyclable after the aircraft reaches its end-of-life. In Section 4.2 in

Part II the fully biodegradable jute reinforced Biopol composite material is selected to cover part of the fuselage. This composite material can be ground and composted at disposal of the aircraft. The second material of the fuselage skin is very durable synthetic fabric that does not need replacement even long after the mission.

2.1.2 Engine Modifications

Because the propulsion system used during the race is largely fixed by *Red Bull Air Race* regulations, engine modifications to increase efficiency are very limited. Section 3.2 in Part II describes the options that are available during the post-mission phase to increase engine efficiency which contributes to sustainability. One of those options is to decrease the fuel consumption of the aircraft by changing to an engine with less power. Performance calculations with less powerful engines concluded that the *T-16* can well operate with an engine which produces around 80 hp, which is considered as a regular engine for small propeller aicraft and therefore more suitable for commercial banner towing flightsts. An example of this type of engine is the *Continental 200 series*, which has an engine power of 95 hp and weighs 80 kg [89]. The dimensions of this engine are smaller, so provided that the engine mount is compatible with this series and certification can be achieved, this engine can be installed.

2.1.3 Alternative fuels

The last aspect of the sustainable approach to be discussed in this section is the fuel used by the *T-16*. Besides the emission factors presented in Section 1.10, emission products after combustion of *100LL Avgas* include lead dibromide, which pollutes the atmosphere by increasing the lead content. This emission product is the result of the fuel's lead mixture that prevents engine knocking. To minimise environmental pollution, unleaded fuels are being tested, but only few of them meet ASTM specifications. High-octane unleaded UL102 developed by *Swift Enterprises* was used as alternative fuel for a *Lycoming* IO540-K engine during a 150-hour endurance test. As a result, this fuel type met all ASTM D 910 specifications for 100LL Avgas. Still the fuel needs more testing on this type of engines to show full material compatibility and to receive full certification. After that it can be used during the post-mission phase. [90]

2.2 Modular Design

The *T-16*, which is designed to compete in the *Red Bull Air Race* is a high performing aerobatic racing aircraft, which is able to withstand exceptionally high manoeuvre load factors up to $10g$. However, this high performance is not required during the post-mission phase, when the aircraft does not continue racing. For regular conventional flight it is not necessary to make fast turns with high load factors. Therefore it is concluded that the *T-16* is structurally and in terms of propulsion over designed for any commercial post-mission purpose. This over design leads to a limited range and endurance due to the small internal fuel tanks and a high fuel consumption.

To solve these post-mission complications, *Torero* develops a plug-and-fly modular design for the *T-16*. This modular design enables the owner of the aircraft to easily change subsystems of the aircraft to adapt for a different purpose. The fuselage of the *T-16* suits as a fixed base of the aircraft, but the owner is free to replace the engine, wing, landing gear and empennage. For instance, if the owner prefers to increase the fuel efficiency of the engine, the engine can be replaced by a low-performing but more fuel-efficient engine, such as the *Continental 200 Series*. Another interesting changeable subsystem is the wing. Since the wing used for the *Red Bull Air Race* is designed to withstand high loadings, it is over designed for any non-aerobatic-racing purposes. Furthermore the wings cannot carry fuel, preventing the possibility to make long flights. This can be solved by using a slender wing, which increases range and endurance of the aircraft. [80].

The main objective of the modular design of the *T-16* is to improve its practical purposes for post-mission commercial flights, by staying airborn for a longer period. This comes in useful when doing promotional flights, such as towing banners for *FlashCo.*, or generally being present during large events. How these design solutions are implemented, is explained in Sections 2.2.1 and 2.2.2.

2.2.1 Engine

As already explained in Section 3.2 in Part II, the engine used for the *Red Bull Air Race* is overpowered for conventional flights and hence requires a higher fuel flow. Therefore it is beneficial to apply modifications to the engine, or to even replace it by a less but sufficiently well performing engine that is more fuel efficient. Interchanging engines is fairly simple, since only the engine mounting needs to be exchanged to connect it to the structure. This connection is further discussed in Section 3.3 in Part II.

During the post-mission phase, the fuel to be used while racing in the *Red Bull Air Race* can be exchanged for a more sustainable fuel, resulting in less harmful emissions. This is discussed in Section 2.1.

2.2.2 Cruise Wings

Another aspect of the plug-and-fly principle of the modular design of the *T-16* is to switch to a different wing, which can be used to increase the endurance and range. The current wings are optimised for aerobatic air racing, but not for conventional flights such as promotional banner towing flights. By implementing a modular wing design, the *T-16* can be equipped with either high-performing race wings or high-enduring cruise wings, to increase the post-mission purposes.

To increase the endurance and range of the aircraft, slender wings are beneficial. To make wings more slender, the aspect ratio is increased. As a result, the induced drag is decreased, see Section 5.4 in Part II [80]. To increase the aspect ratio, the wing span is increased to $b = 9.5\,m$. For the non aerobatic post-mission flights the maximum allowed load factor and required rate of climb are reduced to $n_{max} = 3$ and $rc = 5\ m/s$, respectively. These parameters affect the wing and power loading diagram, which determine the wing surface area, see Chapter 2 Part II. Fuel tanks are integrated into the wings to further increase range and endurance. The cruise wings also have larger winglets, since this is beneficial for the induced drag without compromising flying capabilities, see Section 5.5 in Part II. Since the implementation of the cruise wings affects the total aircraft, iterations are performed to verify design feasibility.

Performance Analysis

The mathematical approach to compute the range and endurance of the *T-16* for race and cruise configuration is done with Equations (1.4) and (1.5), see Section 1.2. To be able to compare the difference in performance of the two different sets of wings, it is assumed that the same propulsion system is used. Therefore the specific fuel consumption is considered the same. Furthermore race and cruise wings are assumed to have the same Oswald factor. Since for the post-mission phase the requirement of using symmetrical wings does not longer hold, the airfoil of the cruise wings is cambered, decreasing the zero lift drag coefficient [47]. However, a larger wingspan increases the zero lift drag coefficient, because the frontal area of the wing increases. Therefore, these effects are assumed to cancel each other out, yielding the same value of C_{D_0} for both wing designs.

The parameters and results of the comparison between the race and cruise wings can be found in Table 2.1. It can be seen that by only increasing the wingspan and therefore the aspect ratio, the maximum lift over drag ratio increases by 25%. This 25% increase goes too for range and endurance, see Equations (1.4) and (1.5). The reason for the increase in range and endurance for

the cruise wing configuration beyond those 25%, is due to the additional fuel carried in the cruise wings.

Table 2.1: Comparison Race and Cruise Wings

Parameter	**Race Wings**	**Cruise Wings**
Wing surface area, S $[m^2]$	7.3	6.8
Wing span, b $[m]$	7.6	9.5
Aspect ratio, A $[-]$	7.9	13.2
Spanwise location of MAC, y_{MAC} $[m]$	1.7	2.1
Wing weight $[kg]$	95	90
Empennage weight $[kg]$	20	7
Fuselage weight $[kg]$	97	97
Engine weight $[kg]$	235	235
Landing gear weight $[kg]$	24	24
Surface controls weight $[kg]$	14	13
Zero Ballast Empty Weight $[kg]$	488	470
Payload weight $[kg]$	122	122
Fuel weight $[kg]$	36	70
Ballast weight $[kg]$	52	0
Maximum Take-Off Weight $[kg]$	698	663
Fuel weight from start-up to cruise $[kg]$	2.5	4.9
Fuel weight from cruise to shut-down $[kg]$	1.1	2.1
Back-up fuel weight $[kg]$	3.6	7
Cruise fuel weight $[kg]$	28.8	56
Propeller efficiency, η_p $[-]$	0.8	0.8
Specific fuel consumption, SFC $[kg/J]$	$12 \cdot 10^{-6}$	$12 \cdot 10^{-6}$
Cruise speed, V_{cruise} $[km/h]$	350	350
Maximum manoeuvre load factor, n_{max} $[-]$	10	3
Maximum Lift coefficient $C_{L_{max}}$ $[-]$	1.8	1.8
Zero lift drag coefficient, C_{D_0} $[-]$	0.017	0.017
Oswald factor, e $[-]$	0.7	0.7
Maximum lift over drag ratio, $\frac{C_L}{C_D}$ $[-]$	14	18
Maximum range, R [km]	**404**	**1097**
Maximum endurance, E [hr]	**1.4**	**3.9**

Structural Analysis

Based on the performance, it is beneficial to implement slender cruise wings for commercial post-mission flights. Even though the maximum lift force does not increase by exchanging the wing, due to its increased length the bending moment might change. To ensure that the fuselage can handle the change in lift and bending moment, the maximum bending moment at the root is computed with Equations (2.1a) to (2.1c). The maximum lift force acts at the MAC, and depends on the aircraft weight and maximum manoeuvre load factor.
By using the values of Table 2.1 the following maximum bending moments at the root are computed:

$$L_{max} = n_{max} \cdot W \tag{2.1a}$$

$$M = l \cdot L_{max} \tag{2.1b}$$

$$M_{max} = y_{MAC} \cdot n_{max} \cdot \text{MTOW} \cdot g \tag{2.1c}$$

- $M_{max_{race\ wings}} = 11.6 \cdot 10^4\ Nm$
- $M_{max_{cruise\ wings}} = 4.1 \cdot 10^4\ Nm$

The fuselage is designed to withstand the root bending moment of the race wings at maximum load factor. This bending moment is almost three times higher than the maximum bending moment at the root of the cruise wings, therefore it can be concluded that the fuselage does not require any structural enforcements when the cruise wings are installed on the *T-16*.

Based on the data presented in Table 2.1 it can be concluded that the slender cruise wing design has a significant improvement on the range and endurance of almost 270%. Since the fuselage structure is designed to enable quick (dis-)assembly of the wings, see Section 4.1 in Part II, it is feasible to easily interchange the two sets of wings. The fuselage is designed to withstand manoeuvre load factors of $10g$. The cruise wing configuration is designed for a maximum manoeuvre load factor of $n_{max} = 3$. Therefore the fuselage does not have to be adapted to deal with the loads. However, the empennage shall be redesigned to deal with the new aerodynamic moment.

2.3 Electrical Design

Nowadays electric cars are a considerable part of the automotive industry and are gaining more and more popularity amongst consumers and researchers. The reason for this increasing demand is the modern and innovative design of the cars, while the aspect of 'zero emissions' also appeals to the customers [91]. For similar reasons *Torero* considers the post-mission conversion of the *T-16* aircraft from piston powered to electrically powered flight.

Advertising an aircraft that is the flagship in terms of sustainable electric propulsion could tremendously add to the chances of success in the marketing campaign of the *Flash energy drink*. This section discusses the feasibility of such an electrical design.

One of the main advantages of the electrical propulsion system over a piston engine is the higher overall efficiency. With the same amount of energy stored in batteries as strored in fuel, the aircraft can fly further and longer. However, up until now batteries require a huge weight and size when compared to conventional fuel, which are two aspects that prevent break-through of fully electrically powered aircraft in the aviation industry. On top of that, the cost increases exponentially with increasing energy density within the battery. The most suitable battery type would be a lithium ion battery because of its high specific energy at reasonable cost relative to other battery types. Still this technology needs more development to achieve the level of performance that can be reached by piston engines.

The following explains an example of the change in weight. As is mentioned in Section 2.1 the *T-16* aircraft needs an engine power of around 80 hp for banner towing applications. A lithium ion battery that can provide 80 hp for one hour weighs approximately 415 kg, while current engines that provide 80 hp such as the *Continental 200 Series* weigh about 80 kg [89]. The current battery packs are simply too heavy to be successfully installed in the aircraft to power the *T-16* electrically. However, it should be noted the *T-16* aircraft is the ideal candidate for this type of propulsion, being extremely lightweight and not having the objective to carry payload. Additionally, there is no strict limit on neither range nor endurance, which mitigates fast discharge rate of the battery pack. [92]

Although complications arise when considering electricity as a main power source, research and technological advancements have lead to fully electric aircraft. One example is the *SkySpark* prototype built by the *Polytechnic University of Turin* that set the world record for electrically powered hybrid aircraft of a top speed of 250 km/h in June 2009 [93]. High cost and the lack of heavy payload carrying capabilities have prevented the prototype to gain success, but the prototype has certainly proven the capabilities of this young type of propulsion in aviation. It can be concluded that a lot of resources are required to successfully design an electrical power system for the *T-16* that is capable of providing the minimum power for basic flight including taking-off, flying and landing. As a rough estimate, the technology could be ready ten years after the aircraft start its post-mission phase. The budgets not only consider the allocation of the motor, electronics, batteries, liquid hydrogen cell and liquid hydrogen reservoir for the *SkySpark*, but also the technology itself. Whether this conversion of power system is chosen or not solely depends

on the market strategy *FlashCo.* is deciding to take and their objective. The technology is not developed yet, but in the near future the chance exists to make a huge mark by investing into this technology and demonstrating feasibility of the system.

Chapter 3

Requirements Verification

To verify whether the aircraft design complies with all the requirements, a requirements compliance list is made, accompanied by a feasibility analysis.
The stakeholder, system and subsystem requirements compliance is listed in Section 3.1, 3.2 and 3.3 , respectively. A check mark (✓) in front of a requirement indicates that the requirement is met, a cross (X) means that the requirement has not been met, while a bullet (•) indicates that the requirement cannot be verified in the current design phase. Comments on an individual requirement are given in italics.

The requirements are indicated with the following code: <project code> − <type of requirement> − < # >. The project code is defined as FlashCo. Aerobatic Racing Aircraft (FARA), the stakeholder requirements are coded with (Stk), the system requirements with (Sys) and the subsystem requirements with (Ssys).

3.1 Stakeholder Requirements

The stakeholder requirements are top-level requirements, which need to be fulfilled to make the mission successful. These requirements are already stated in the Project Plan [94], Baseline Report [56] and Mid-Term Report [19].

- • FARA-Stk-01: The aircraft shall comply with all *Red Bull Air Race World Championship* rules and regulations [16]. *Rules too elaborate - requires more detailed design.*
- ✓ FARA-Stk-02: The aircraft shall only require a crew of one pilot.
- ✓ FARA-Stk-03: The unit cost shall be below €275,000.- (including development costs and return of investment). *Total production cost is € 115,882.- as stated in Section 9.3 in Part II.*
- ✓ FARA-Stk-04: The aircraft shall be ready to compete in the *Red Bull Air Race World Championship* in 2017. *See Section 4 in Part I.*
- ✓ FARA-Stk-05: It shall be possible to transport the aircraft to the race site without flying it to the location. *See Section 4.1.3 in Part II.*
- • FARA-Stk-06: The aircraft shall comply with the CS-23 certification specifications [14]. *Rules too elaborate - requires more detailed design and testing.*
- • FARA-Stk-07: It shall be possible for the pilot to abandon the aircraft within 10 seconds at speeds between stall speed and design diving speed. *Requires more detailed design and demonstration.*
- • FARA-Stk-08: The aircraft shall provide the capability to beat the current record times of the champions in the *Red Bull Air Race World Championship. Requires a validated aircraft model and full-scale testing.*
- ✓ FARA-Stk-09: The aircraft shall be able to withstand a maximum load factor of 12g. *See Sections 4.1 and 5.6 in Part II.*
- ✓ FARA-Stk-10: The aircraft shall have a minimum empty mass of 540 kg. *Empty weight is 489 kg, which means that the aircraft would require* 51 *kg of ballast, as stated in Section 9.2 in Part II*

- ✓ FARA-Stk-11: The race mass of the aircraft shall not be less than 698 kg. *MTOW is 698 kg, see Section 9.2 in Part II.*
- ✓ FARA-Stk-12: The aircraft shall have a service ceiling of 5000 m. *The theoretical service ceiling is 15 kilometres. The validity of this value is discussed in Section 1.7 in Part III.*

As can be seen from this list, some requirements have not been met yet, but no requirements have definitively not been met. The regulation requirements FARA-Stk-01 and FARA-Stk-06 could not yet be fulfilled because both are very detailed - too detailed for the design that is presented in this report. Requirement FARA-Stk-07 is too detailed for consideration in this design phase, but is addressed in a future design phase - the requirement can potentially be fulfilled by modifying the canopy to allow quick opening. FARA-Stk-08 can only be verified once an aircraft model is developed and once a test aircraft is produced. This requirement is identified as a key requirement, which means that the aircraft model shall be developed in the next design phase.

3.2 System Requirements

The system requirements follow from the system description given in Section 1 in Part I and are furthermore based on the stakeholder requirements, CS-23 regulations [14] and the *Red Bull Air Race World Championship* regulations [16]. The coding of the system requirements is slightly adapted, since the subsystems are also indicated in the codes. The coding is done as follows: <project code> − <type of requirement> − <type of subsystem> − < # >. The subsystems are coded as:

- Airframe structure (Afs)
- Controls (Con)
- Data handling (Dat)
- Power (Pow)
- Propulsion (Pro)
- Smoke (Smo)

The system requirements are:

- ✓ FARA-Sys-Afs-01: The airframe shall be a 'conventional' configuration, as specified by the *Red Bull Air Race* regulations: "Propeller at the front end of the Race Aircraft followed by a fixed symmetrical aerofoil wing and a horizontal and vertical tail." [16]
- ✓ FARA-Sys-Afs-02: The airframe structure shall be able to withstand all loads encountered during flight, including aerobatic loads and landing forces.
- ✓ FARA-Sys-Afs-03: The aircraft shall be equipped with a fixed landing gear.
- ✓ FARA-Sys-Afs-04: The aircraft shall have a rate of climb of at least 18 m/s. *Rate of climb equals* 24.5 m/s, *see Section 1.5.2 in Part III.*
- ✓ FARa-Sys-Afs-05: The aircraft shall have a climb gradient of at least 8.3%. *Climb gradient equals 62%, see Section 1.5.2 in Part III.*
- ✓ FARA-Sys-Con-01: The aircraft shall be safely controllable and manoeuvrable during all flight phases.
- ✓ FARA-Sys-Con-02: The aircraft's pitch, yaw and roll rate shall be high enough to fly the *Red Bull Air Race* course. *The pitch rate is 55.2* $°/s$, *the spin recovery yaw acceleration is 80* $°/s^2$ *and the roll rate is 475* $°/s$.
- ✓ FARA-Sys-Con-03: The primary flight control system shall be mechanically operated.

- ✓ FARA-Sys-Con-04: The aircraft shall not contain auto pilots of any kind.
- ✓ FARA-Sys-Con-05: The aircraft shall be able to perform ground manoeuvres, including taxiing, take-off and landing.
- ✓ FARA-Sys-Dat-01: The aircraft shall be equipped with a radio, a Mode S capable transponder, an EFIS and a g-meter.
- FARA-Sys-Dat-02: The aircraft shall be able to accommodate two cockpit and two outboard cameras with fairings. *The fairings for the cameras are not designed yet - requires more detailed design.*
- ✓ FARA-Sys-Pow-01: The aircraft shall have a system that is able to supply power to all electrical systems.
- ✓ FARA-Sys-Pro-01: The engine shall be the *Lycoming Thunderbolt AEIO-540-D.*
- ✓ FARA-Sys-Pro-02: The propeller shall be the *Hartzell 3-bladed 7690.*
- ✓ FARA-Sys-Pro-03: The oil system shall be the *Christen inverted oil lubrication system.*
- ✓ FARA-Sys-Pro-04: The exhaust system shall be the *Sky Dynamics 6 to 1 standard exhaust system.*
- ✓ FARA-Sys-Pro-05: The fuel used shall be *Aviation Gasoline 100LL according to ASTM D 910.*
- FARA-Sys-Smo-01: The aircraft shall be be equipped with a smoke system that achieves a flow rate of not less than 2.0 litres per minute. *Requires more detailed design.*

As can be seen above, the vast majority of system requirements is fulfilled. No thought is yet given to the outboard cameras and their fairings, since it is very detailed and is likely not to have a big influence on the characteristics and performance of the aircraft. Similarly, the smoke system has not been designed yet. Both are considered during the next design phase.

3.3 Subsystem Requirements

- ✓ FARA-Ssys-Afs-01: The wing shall have a span between 7.0 and 7.6 metres. *The wingspan is 7.6 metres.*
- ✓ FARA-Ssys-Afs-02: The airframe shall include an additional roll-over structure.
- ✓ FARA-Ssys-Afs-03: The stall speed of the aircraft may not exceed 61 knots. *The stall speed is 57 knots.*
- FARA-Ssys-Afs-04: Any materials that may disintegrate, resulting in splintering in the case of an incident, shall be avoided inside the cockpit area. *Not all materials for the cockpit have been selected yet - requires more detailed design.*
- FARA-Ssys-Afs-05: The pilot seat shall be designed in a way that the pilot is sitting in the cockpit in an upright position in order to provide sufficient outside front view and side view for the pilot. *Seat is not designed yet, but the canopy provides sufficient view for the pilot - requires more detailed design and demonstration.*
- ✓ FARA-Ssys-Afs-06: The airframe shall provide fuel storage for at least 50 L.
- FARA-Ssys-Con-01: The aileron shall not fail due to pylon impact. *Requires testing and demonstration.*
- FARA-Ssys-Pow-01: The aircraft shall be able to generate electric power. *Requires more detailed design.*
- FARA-Ssys-Pow-02: The aircraft shall be able to regulate electric power. *Power budget is made, but the system requires more detailed design.*

- FARA-Ssys-Pro-01: The aircraft shall be equipped with an inverted fuel and oil system capable of sustaining inverted flight for a minimum of 30 seconds at full power. *Requires more detailed design and demonstration.*
- ✓ FARA-Ssys-Smo-01: The pilot shall be able to turn the smoke system on and off from the inside of the cockpit during flight.

For the subsystem requirements, many requirements have not been met yet, as many are too detailed for the current design phase. For instance, the pilot position is determined, but the seat itself is not yet designed. The aileron's dimensions are determined, but the mechanical system is not designed yet. FARA-Ssys-Afs-04, FARA-Ssys-Afs-05, FARA-Ssys-Con-01 and FARA-Ssys-Pro-01 are considered during the next design phase.

For FARA-Ssys-Pow-01 and FARA-Ssys-Pow-02, a power budget is presented in Section 9.4 in Part II, but this is not worked out in detail. The power generation is most likely be produced by an alternator connected to the engine. Again, this system is not yet worked out in detail, which is done in an upcoming design phase.

In general, one can conclude that all requirements are either met or an effort is made to meet them in a future design phase. There are no requirements that are not met, which would require a design revisit.

Chapter 4

Risk Assessment

It is important to identify the technical risks that may occur during system development. Events that may induce risk are identified and for each of these events, its probability of occurrence as well as its consequence are estimated. The product of these two characteristics is defined as the risk, meaning that the highest risk is associated to an event that is most likely to happen and has a relatively big impact.

The events are derived from the aircraft systems as defined in the Functional Breakdown Structure, see Section 1.3.2 in Part II. The events are selected based on the criterion that it may lead to the aircraft being damaged, loss of the aircraft, pilot injury or disqualification from the *Red Bull Air Race*. For each subsystem, the events that are determined to impose high risk on the system are listed below.

1. Power system failure
2. Short circuit in power system
3. Pilot-aircraft interface
4. Control system mechanical actuation system failure
5. Aileron/elevator/rudder stuck in maximum deflection
6. Aileron failure due to pylon impact
7. Control system hinge failure
8. Engine failure
9. Propeller failure
10. Throttle stuck
11. Fuel system failure
12. Smoke system failure, or "insufficient smoke"
13. Data not transmitted in real time
14. Data not recorded
15. Structure deforms
16. Structure fails under flight loads
17. Landing gear failure
18. Subsystem failure during aircraft transport

For each of the stated events, the consequence and probability of occurrence is estimated, based on engineering sense. The results are summarised in the risk map shown in Table 4.1, which in vertical direction shows the probability of occurrence and in horizontal direction the consequence.

Table 4.1: Risk map for the mission

Frequent		6		
Probable	13, 18	1	3	8, 14, 16
Improbable		2, 12, 15	7, 10, 17	4, 5, 9, 11
Impossible				
	Negligible	**Marginal**	**Critical**	**Catastrophic**

Note that the events having the highest risk are in the top right corner in Table 4.1. The events with the highest estimated risk are numbers 3, 8, 14 and 16. in the following, each of these events is discussed.

The pilot-aircraft interface imposes a moderate risk on the system. This interface could potentially fail in two ways: the pilot does not understand the flight instruments, or the flight instruments have a systematic offset. In either case, the likelihood is estimated to be probable and its impact could be critical.

Engine failure is one of the most important failure modes the aircraft has, especially since part of the mission is flown very close to the ground. Therefore, the engine system should be designed and optimised in such a way that the chances of engine failure would be minimised.

It is mandatory for participating in the *Red Bull Air Race* to store data from subsystems like the EFIS and the g-meter. When this data is not being recorded, this might result in sanctions according to the *Red Bull Air Race* Regulation Part A "Sporting Regulations" [16]. This will influence the aircraft's race classification and hence the risk of data recording failure is high.

The airframe structure is designed to withstand the loads expected during the mission. However, since the airframe structure is a complicated system and the loads acting on the aircraft cannot be modelled perfectly, system, subsystem or component failure might occur. Because the failure of these may lead to the aircraft being damaged — or worse, the aircraft going down and endangering the pilot — this event is labelled as catastrophic.

Chapter 5

RAMS Characteristics

The Reliability, Availability, Maintainability and Safety (RAMS) characteristics of the system are described and explained in both the Baseline Report and the Mid-term report [56]. In this chapter all four characteristics are being refined for the actual design. The expected reliability and availability is updated, the maintenance schedule is revisited and finally safety critical functions are addressed.

5.1 Reliability

> "The probability that a system will perform in a satisfactory manner for a given period of time under specified conditions" [18]

It is favourable to have a reliability as high as possible, because failure in high speed low altitude flight might have catastrophic consequences. Therefore influencing factors such as wear, oxidation and loading conditions need to be controlled carefully. Wear and oxidation can be managed by having periodical maintenance checks, this is addressed in Section 5.3. A safety factor of 1.5 is used in designing the fuselage truss, which means that the fuselage is designed for a load factor of 15g. The maximum allowable load during the race is $10g$, so the risk of the truss failing during operation is minimised. The landing gear also has an incorporated safety margin. Although pilots are able to land the aircraft with a vertical speed of $0.5\,m/s$ just before touchdown, the landing gear can still cope with a vertical speed of $3.6\,m/s$. Since these safety margins are incorporated in the loading conditions the reliability of the system is improved. Furthermore, inspections and checklists make sure that aircraft systems are in optimal state which minimises the probability of failure. As an example of inspection activities, the 'life item and inspection' sheet can be considered, giving the period after which components need to be checked or changed . Furthermore the 'pre-race inspection sheet' consists of 32 inspection steps that need to be evaluated before each race. The last method is redundancy of subsystems. However, this design philosophy is avoided in aerobatic racing aircraft since aircraft weight is minimised. A future recommendation to improve the reliability of the aircraft is to have a better understanding of the fatigue characteristics of the materials that are used. This can be done by executing fatigue tests on materials, resulting in S-N curves, which give time to failure as function of stress applied. [16]

5.2 Availability

> "The degree, percent, or probability that a system will be ready or available when required for use" [18]

The objective is to make the first test flight in 2017. Therefore existing materials are mostly used, since there is no time to develop and certify a new material that is both able to support high loads, while being very sustainable. Because the fuselage skin material biodegradable jute

reinforced Biopol composite is not carrying major structural loads, this material is categorised under a different class of composites according to CS-23. This class does need to be evaluated for damage tolerance and environmental degrading, but certification procedures are expected not to counteract availability. For the truss, steel is used which is a material that is produced in large quantities. The wing structure consists of carbon reinforced polymers, which is a more expensive material than steel. The production of these polymers consists of a lay up process that is labour intensive [95]. Therefore delivery times are possibly higher than for steel. Since the first flight takes place in three years all material delivery times are still acceptable. Regarding aircraft avionics and instruments, it is necessary to use off-the-shelf products, since developing such products takes too much time which increases the risk of exceeding the availability objective. To further improve the availability of the aircraft, off-the-shelf products are used to assemble the undercarriage of the aircraft. So the landing gear and wheel fairings are all ordered products and are not specifically designed. These products have short delivery times [78]. It can be concluded that room for innovation is little, but alternative sustainable materials are considered if availability constrains allow. The aircraft is likely to be available on time using existing technologies. The schedule for having the aircraft ready in three years, is elaborated on in Section 4.1.

5.3 Maintenance

> "The ease, accuracy, safety and economy in the performance of maintenance actions" [18]

If the aircraft maintenance status is deemed not airworthy, the team is excluded from the race. Besides, maintainability of the system directly influences the safety of the pilot and bystanders on the ground.

The maintenance activities for the product at hand are based on reference aircraft like the *Extra 330 LX*, where maintenance activities are subdivided in scheduled- and non-scheduled maintenance checks. Maintenance activities are in accordance with FAR-23 regulations. The scheduled different maintenance checks take place at 25, 50, 100, 200, 300, 400, 500 and 1000 hour flight time intervals [33]. On top of that an annual maintenance check equal to a 100 hour check needs to take place. Maintenance involves all areas of the aircraft, such as: airframe systems, structures, propeller, and power plant checks. The engine lubrication maintenance is scheduled every 25 or 50 hours and other engine operational checks are performed every 50 or 100 hours. The same is true for fuselage, landing gear and fuel system. Important aspects of this maintenance is the inspection of materials and attachments. For example the area where the landing gear is attached to the fuselage is extensively checked for cracks. Significant item inspection must be performed every 1000 hours in addition to the previously stated inspections. This holds for the wing, flight controls, flight instruments and hardware. Ailerons are removed from the main wing and the wing is checked for dents, cracks and delaminations. The controls are checked, among other checklist items, for possible corrosion of the metal rods.

Besides these scheduled checks, unscheduled checks follow after abnormal events. Events such as violent stopping of the engine or in the event of an engine fire, the engine and propeller components need profound maintenance. A 'hard landing', requires checks on the landing gear, control surfaces and the engine mount. A complete aircraft inspection is required after a 'lightning strike'. Other abnormal events must be considered after the first flight of the aircraft, to provide adequate maintenance instructions.

5.4 Safety

> "The freedom of hazards to human or equipment" [18]

Three main safety critical functions should be addressed to perform the mission: the aircraft should provide an emergency exit, fire resistance and protection from impact. These safety issues are regulated by the *Red Bull Air Race* regulations and CS-23. A short description of these regulations is given below. A mechanism for opening the cockpit should be developed such that the race pilot can easily and quickly leave the aircraft, even when crashed on water when the aircraft is fully submerged. The pilot should be able to leave the aircraft within 10 seconds [16]. A clear release marking of the canopy should be on the outside too, such that the aircraft is accessible from the outside. These requirements should be taken into account when designing the cockpit layout during the next design phase. After manufacturing the cockpit, compliance should be demonstrated. The aircraft should also be equipped with a fire extinguisher that is installed within reach of the pilot.

A titanium plate with a thickness of $0.41mm$ is used as firewall. According to CS-23 this material is suitable as fire protection. The firewall cannot ignite when subjected to a flame of $1093°C$ for at least 15 minutes [14]. Self-extinguishing materials should also be used within different parts of the aircraft, for example structural flooring, seat cushions and more. Special attention needs to be taken when refuelling the aircraft, since this is a safety critical procedure. Following specific guidelines, such as de-energising electrical systems while refuelling, should prevent accidents. Furthermore, the engine should be equipped with an auxiliary electrical fuel pump in case of failure of the engine driven pump. Different parts of the aircraft should be bird strike proof. The aircraft must be impact proof for pylon hits or for collision with objects up until a certain size. The carbon fibre reinforced composite leading edge of the wings needs to be tested to demonstrate compliance with this requirement. The use of low impact resistant fabric materials is justified because the material is only integrated into fuselage sections not subject to impact. Lastly, all race aircraft need to be fitted with a special air intake screen to supply the engine with air, even when the main air intake is closed [16].

Last but not least, during the race the race pilot wears a helmet, g-suit and parachute when flying the aircraft. These measures are enforced by *Red Bull Air Race* regulations to increase pilot safety.

Conclusion and Recommendations

This report describes the final preliminary design of the *T-16* aerobatic racing aircraft for the *Red Bull Air Race* and informs *FlashCo.* about the design progress. The major design parameters are fixed, but the majority of systems and subsystems are not fully worked out yet into detail. The design meets all relevant requirements: the more detailed requirements shall be accounted for in a future design phase. *Torero* is confident the aircraft is able to be competitive in the *Red Bull Air Race*.

Multiple features on the aircraft make the *T-16* stand out from other aircraft currently competing in the *Red Bull Air Race*: first of all, the aileron control system is non-linear, which reduces drag as the ailerons are deflected. Secondly, wingtip devices are used to increase aileron effectiveness. Also special attention is paid to sustainability, resulting in the use of biodegradable composites for the fuselage skin.

The aircraft zero ballast weight is 489 kg, which is 51 kg lighter than the 540 kg required to compete in the *Red Bull Air Race* and thus ballast weight is required. Its maximum take-off weight including ballast is 698 kg, which is equal to the minimum race weight defined by *Red Bull*. The total production cost of the *T-16* is €115,900.- which means that the remainder of the €275,000.- provided by *FlashCo.* can be used for development costs.

The reliability of the aircraft is ensured by using a safety factor of 1.5 for all structural subsystem designs, and by doing inspections and using checklists. The aircraft will go into maintenance in accordance with the Certification Specifications. The aircraft is designed to provide an emergency exit, fire resistance and impact protection. To ensure availability, already certified materials are mostly used for the aircraft, while off-the-shelf products are used for subsystems like the avionics and landing gear. This decreases the innovative aspects to be implemented in the design.

Still *Torero* has put effort in improving the aircraft's practical purposes such as performing post-mission commercial flights. As a result, a revolutionary modular plug-and-fly design is developed. The high performance racing engine can be replaced by a more fuel efficient engine, while the race wings can be replaced by cruise wings, optimised for range and endurance. This enables the aircraft to fly promotional banner flights for *FlashCo.*, without significantly changing the structural elements of the fuselage. To increase the recyclability of the aircraft, the truss structure is designed as a tubular steel truss structure and part of the fuselage skin is made from a fully biodegradable natural composite.

With the current technology it is not possible to convert the aircraft from piston powered to electrically powered. Therefore this is not suitable to implement in the *T-16* now, but it is an interesting design option for the aircraft's post-mission purposes.

The main risks during the mission phase are identified. The pilot could potentially misinterpret the flight instruments or the flight instruments could have a systematic offset. Engine failure is a significant risk, as is structural failure. Finally, to avoid sanctions in the *Red Bull Air Race*, the aircraft must record flight data.

For next design phases, a number of recommendations are made. To further analyse the aircraft's aerodynamic performance, Computational Fluid Dynamics (CFD) analyses are recommended. The main goal of this is to analyse the effect of the propeller wake on aerodynamic performance, which cannot be modelled accurately without an advanced CFD program such as *Fluent*. Furthermore,

wind tunnel test for both small scale and full scale are recommended, for instance to study airfoil hysteresis effects.

Furthermore, instead of the the current linear, time-independent state-space model, a non-linear, time-dependent state-space model should be developed, to analyse the aircraft's dynamic behaviour more accurately. It is recommended to also build a simulator, to evaluate the aircraft's handling. Finally, the influence of the propeller on the tail control surfaces should be investigated. To improve the performance analyses, it is recommended to perform detailed analyses on the variation of efficiency with altitude of the engine and propeller. By improving the accuracy of the available power provided by the propulsion system, the resulting performances become more realistic.

For the structural analysis, the current models include many simplifications. It is advised to develop more detailed models. Furthermore, an investigation into fatigue is recommended to be initiated.

Bibliography

[1] About Red Bull Air Race. http://www.redbullairrace.com/en_AE/article/about-red-bull-air-race. [Online; accessed 08-05-2014].

[2] 4 New Pilots In Red Bull Air Race 2009. https://airlineworld.wordpress.com/2008/11/23/4-new-pilots-in-red-bull-air-race-2009/. [Online; accessed 08-05-2014].

[3] Air Racing History: The History of Air Racing and Record Breaking. http://www.air-racing-history.com/index.htm. [Online; accessed 30-04-2014].

[4] Red Bull Air Race: Official Site. www.redbullairrace.com. [Online; accessed 30-04-2014].

[5] Smoke On! Webzine; Aircraft Flown 2003-2010 at RBAR. http://redbullairracefan.wordpress.com/aircraft/. [Online; accessed 30-04-2014].

[6] Red Bull Air Race: Planes. http://www.redbullairrace.com/en_US/article/planes. [Online; accessed 01-05-2014].

[7] IHS Jane's. http://www.ihs.com/products/janes/defence/det-products/worlds-aircraft-development.aspx. [Online; accessed 12-05-2014].

[8] Red Bull Air Race: Challenger Class. http://www.redbullairrace.com/en_US/article/new-challenger-cup-ready-take-2014. [Online; accessed 01-05-2014].

[9] Red Bull Air Race: Pilots. http://www.redbullairrace.com/en_US/pilots. [Online; accessed 01-05-2014].

[10] About.com: Low Priced Carbon Fibers Will Open New Markets to Composites. http://composite.about.com/blmattech1.htm. [Online; accessed 01-05-2014].

[11] My Purchasing Center: Carbon Fiber Prices More Competetive. http://www.mypurchasingcenter.com/commodities/commodities-articles/carbon-fiber-prices-more-competitive/. [Online; accessed 01-05-2014].

[12] F. Monfort-Windels. Part 4: Carbon Fiber Reinforced Composites. Technical report, 2013.

[13] M. Mizui K. Ogi, T. Shinoda. Strength in concrete reinforced with recycled CFRP pieces. Technical report, January 2005.

[14] Joint Aviation Authorities Comm. *Certification Specifications for Normal, Utility, Aerobatic, and Commuter Category Aeroplanes*. European Aviation Safety Agency, March 2010.

[15] Red Bull Air Race Rises to Logistics Challenge. http://www.redbull.com/cs/Satellite/en_air/Article/Red-Bull-Air-Race-Rises-To-Logistics-Challenge-021242745716250. [Online; accessed 16-05-2014].

[16] Race Committee. *Red Bull Air Race World Championships Regulations*. Red Bull Air Race GmbH, March 2010.

[17] R.J. Hamann and M.J.L. van Tooren. Systems Engineering and Technical Management Techniques Survival Kit. University Lecture Slides, 2014.

[18] E. Gill, G. LaRocca, and R. Curran. AE3211-I Systems Engineering and Aerospace Design, Lecture Slides . University Lecture Slides, 2014.

[19] DSE Group 16. Midterm Report Torero T-16. Technical report, May 2014.

[20] E. Torenbeek. *Synthesis of Subsonic Airplane Design*. Kluwer Academic Publishers, 1982.

[21] Hartzell. *Application Guide*. Hartzell Propeller Inc., February 2014.

[22] SA-100 SERIES 3.5 GALLON KITSl. http://www.warteraviation.com/extreme-smoke/. [Online; accessed 20-06-2014].

[23] Precision Pistons. http://dsportmag.com/browse/tech/precision-pistons. [Online; accessed 23-05-2014].

[24] Improve aircraft performance with more power. https://www.aopa.org/News-and-Video/All-News/2013/November/04/Improve-aircraft-performance-with-more-power-part-5.aspx. [Online; accessed 23-05-2014].

[25] Fuel Injection. http://www.enginehistory.org/Accessories/HxFuelSys/FuelSysHx10.shtml. [Online; accessed 23-05-2014].

[26] Power and Torque. http://www.epi-eng.com/piston_engine_technology/power_and_torque.htm. [Online; accessed 01-06-2014].

[27] Matrix Frame Software. http://www.matrix-software.com/. [Online; accessed 24-06-2014].

[28] M. van Woudenwerg. Systems- & Certification Verification Engineer at Extra Aircraft. Personal correspondence. 02-06-2014.

[29] Aircraft Fabric Covering. http://www.faa.gov/regulations_policies/handbooks_manuals/aircraft/amt_airframe_handbook/media/ama_Ch03.pdf. [Online; accessed 19-06-2014].

[30] J Gassan A.K Bledzki. Composites reinforced with cellulose based fibres. *Elsevier, Prog. Polym. Sci.*, 24:270, 1999.

[31] et al. M. K. Hossain. Physical, mechanical, and degradability properties of chemically treated jute fiber reinforced biodegradable nanocomposites. *Journal of Engineering Materials and Technology*, 133:041003–6, 2011.

[32] M. K. Cox. Recycling biopol-composting and material recycling. *Journal of Macromolecular Science*, 133:608, 2006.

[33] Extra 330LX. *Maintenance Manual Extra 330LX*. Extra Flugzeugproduktions- und Vertriebs-GMBH, September 2013.

[34] M.S. Selig. Modeling Propeller Aerodynamics and Slipstream Effects on Small UAVs in Realtime. *University of Illinois*, 2010.

[35] L.L.M. Veldhuis. Propeller Wing Aerodynamic Interference. *TU Delft*, 2005.

[36] ANSYS Inc. *Known Issues and Limitations*, November 2011.

[37] J.D. Anderson. *Introduction to Flight (7th Edition)*. McGraw-Hill Higher Education, 2011.

[38] H. Multhopp. Aerodynamics of the fuselage. *NACA Report*, 1036, 1942.

[39] J.B. Delano R.G. Robinson. An investigation of the drag of windshields in the 8-foot high-speed wind tunnel. *NACA Report*, 730:65–77, 1942.

[40] S.F. Hoerner. *Fluid-dynamic drag*. Mrs. A. Liselotte Hoerner, 1985.

[41] *XFLR5 Analysis of foils and wings operating at low Reynolds numbers*, July 2008.

[42] M. Drela and H. Youngren. *XFOIL 6.9 User Guide*. MIT, January 2001.

[43] L.L.M. Boermans. Assistant Professor at Faculty of Aerospace Engineering at TU Delft. Personal correspondence. 12-06-2014.

[44] L. Boermans. Aerodynamic Design Lectures. University Lecture Material.

[45] H.J. van Overvest. Aerobatics Pilot, Red Bull Air Race Judge (Rotterdam). Personal correspondence. 07-06-2014.

[46] L.S. Stivers Jr. I.H. Abbott, A.E. von Dönhoff. *Summary of Airfoil Data*. National Advisory Committee for Aeronautics, 1945.

[47] S.F. Hoerner. *Fluid-dynamic lift*. Mrs. A. Liselotte Hoerner, 1985.

[48] Airfoil tools, airfoil database. http://airfoiltools.com/airfoil/. [Online; accessed 13-05-2014].

[49] Veldhuis en van Oudheusden. Incompressible flow over finite wings. University Lecture Slides, 2012.

[50] XFLR5 routines. http://aircraftdesign.nuaa.edu.cn/aca/2008/09-vortex%20lattice%20methods(software).pdf. [Online; accessed 15-06-2014].

[51] Dr. R. Vos. Assistant Professor at Faculty of Aerospace Engineering at TU Delft. Personal correspondence. 21-05-2014.

[52] Nigel Lamb on Winglets. http://www.redbullairrace.com/m/en_US/article/nigel-lamb-winglets. [Online; accessed 10-06-2014].

[53] Mark D. Maughmer. About Winglets. http://ultraligero.net/Cursos/varios/todo_sobre_los_winglets.pdf. [Online; accessed 10-06-2014].

[54] Peter Masak. Winglet Design for Sailplanes. http://www.soaridaho.com/Schreder/Technical/Winglets/Masak.htm. [Online; accessed 10-06-2014].

[55] Dr.ir.C.Kassapoglou. *Design and Analysis of Composite Structures*. Wiley, 2013.

[56] DSE Group 16. Baseline Report Torero T-16. Technical report, May 2014.

[57] Airfoil database. http://www.airfoildb.com/. [Online; accessed 09-06-2014].

[58] XFLR5 theory. http://www.xflr5.com/docs/Point_Out_Of_Flight_Envelope.pdf. [Online; accessed 24-06-2014].

[59] M.H. Sadraey. *Aircraft Design – A Systems Engineering Approach*. John Wiley & Sons, Ltd, 2013.

[60] Take-off in a taildragger. http://www.taildraggers.com/Documentation.aspx?page=Takeoff. [Online; accessed 11-06-2014].

[61] J. Kay, W.H. Mason, W. Durham, F. Lutze and A. Benoliel. Control Authority Issues in Aircraft Conceptual Design: Critical Conditions, Estimation Methodology, Spreadsheet Assessment, Trim and Bibliography. Technical report, November 1993.

[62] Extra Flugzeugproductions und Vertriebs gmbh. *Maintenance manual Extra 330LX*, March 2011.

[63] D. Stinton. *The Design of the Aeroplane*. BSP Professional Books, 1983.

[64] FAR-23 Airworthiness Standards: Normal, Utility, Acrobatic and Commuter Category Airplanes. http://www.ecfr.gov/cgi-bin/text-idx?SID=51078d8cdfa7b75cf2f1175bc0cad578&node=14:1.0.1.3.10.2.66.42&rgn=div8. [Online; accessed 12-06-2014].

[65] B.P. Niehaus. The USAF Stability and Control Digital DATCOM. Technical report, April 1979.

[66] W.J. Baars, R.O. Stearman, C.E. Tinney. Wind Tunnel Studies Employing higher Order Statistics to Detect Icing Induced Upsets. Technical report, 2009.

[67] How Thing Work: Flying Upside Down. http://www.airspacemag.com/flight-today/how-things-work-flying-upside-down-27746739/?no-ist. [Online; accessed 17-06-2014].

[68] Flying Giants. http://www.flyinggiants.com/forums/attachment.php?attachmentid=39141&d=1172011776. [Online; accessed 19-06-2014].

[69] Aircraft Primary Flight Controls. http://www.pilotfriend.com/training/flight_training/fxd_wing/primary.htm. [Online; accessed 17-06-2014].

[70] J. Roskam. *Airplane Design — Part VI: Preliminary Calculation of Aerodynamic, Thrust and Power Characteristics*. Roskam Aviation and Engineering Corporation, 1987.

[71] H. Benedictus,aerospace engineer and pilot working at TU Delft. Aerospace Engineer and Pilot, working at the TU Delft. Personal correspondence. 18-06-2014.

[72] Federal Aviation Administration. *Pilot's Handbook of Aeronautical Knowledge*. U.S. Department of Transportation, January 2008.

[73] Explaining Airplane External Lighting. http://www.brighthub.com/science/aviation/articles/81415.aspx. [Online; accessed 17-06-2014].

[74] Piper PA28-161 Warrior Normal Checklists. http://www.shorelineflyingclub.com/aircraft/doc/49Bchecklist.pdf. [Online; accessed 17-06-2014].

[75] J.C. van der Vaart E. de Weerdt C.C. de Visser A.C. in 't Veld E. Mooij J.A. Mulder, W.H.J.J. van Staveren. *Flight Dynamics — AE3202 Lecture Notes*. Delft University of Technology, March 2013.

[76] Landing Gear Products Grove Aircraft Landing Gear Inc. http://www.groveaircraft.com/landing_gear.html. [Online; accessed 11-06-2014].

[77] Wheels Grove Aircraft Landing Gear Inc. http://www.groveaircraft.com/5series.html. [Online; accessed 11-06-2014].

[78] Wheel Fairings Aircraft Spruce. http://www.aircraftspruce.com/catalog/appages/mf4.php?clickkey=6937. [Online; accessed 16-06-2014].

[79] Grove Radius Block Description. http://www.groveaircraft.com/radiusplates.html. [Online; accessed 13-06-2014].

[80] M. Voskuijl. AE2104 Flight and Orbital Mechanics. University Lecture Slides, 2012.

[81] R. Vos and B.T.C. Zandbergen. AE1201 Aerospace Design and Systems Engineering Elements I, Lecture Slides . University Lecture Slides, 2014.

[82] Propeller Efficiency - Rule of Thumb. http://www.nar-associates.com/technical-flying/propeller/cruise_propeller_efficiency_screen.pdf. [Online; accessed 19-06-2014].

[83] Lycoming. *Operator's Manual for Lycoming O-540 and IO-540 series*. Lycoming, October 1999.

[84] Cabin Decompression and Hypoxia . http://www.theairlinepilots.com/medical/decompressionandhypoxia.htm. [Online; accessed 19-06-2014].

[85] Noise type certificates. https://easa.europa.eu/document-library/noise-type-certificates-approved-noise-levels. [Online; accessed 15-05-2014].

[86] Darrol Stinton. *The design of the aeroplane*. BSP Professional Books, 1983.

[87] Avgas grades and specifications. http://www.shell.com/global/products-services/solutions-for-businesses/aviation/shell-aviation-fuels/fuels/types/avgas.html. [Online; accessed 16-05-2014].

[88] Emission Factors for Greenhouse Gas Inventories. http://www.epa.gov/climateleadership/documents/emission-factors.pdf. [Online; accessed 16-05-2014].

[89] Continental Motors, 200 series engine specifications. http://www.continentalmotors.aero/uploadedFiles/Content/xHome/Billboards/200series_032012-web.pdf. [Online; accessed 18-06-2014].

[90] Full-Scale Engine Endurance Test of Swift Enterprises UL102 Fuel. http://www.experimentalaircraft.info/homebuilt-aircraft/aviation-biofuel-swift.php. [Online; accessed 23-06-2014].

[91] Electric Drive Transport Association. http://electricdrive.org/index.php?ht=d/sp/i/27103/TPL/LandingPageTechIss/pid/27103. [Online; accessed 19-06-2014].

[92] Electric powered light aircraft - Design and Feasibility. http://www.ptrivedi.com/projects/Electric_light_aircraft.pdf. [Online; accessed 18-06-2014].

[93] SkySpark technical characteristics. http://www.skyspark.eu/web/eng/caratteristiche.php. [Online; accessed 18-06-2014].

[94] DSE Group 16. Project Plan Torero T-16. Technical report, April 2014.

[95] Jos Sinke. *Process for thermoplastic and thermoset composites*. Delft University of Technology, 2014.

[96] Red Bull Air Race Planes. http://www.redbullairrace.com/en_INT/article/planes. [Online; accessed 08-05-2014].

[97] Extra 300LX Technical Data. http://extraaircraft.com/330LX.php. [Online; accessed 02-05-2014].

[98] Introduction to Buckling. http://aeweb.tamu.edu/haisler/aero405/Lecture_Notes/A11_Introduction_to_Buckling_by_Pollock.PDF. [Online; accessed 15-06-2014].

Appendix A

Reference Aircraft

This appendix contains the most relevant data of the reference aircraft used in the *Red Bull Air Race*. [96, 97].

Table A.1: Relevant parameters of reference aircraft.

	Extra 300LX	**Zivko Edge 540**	**Corvus Racer 540**	**MXS-R**
Length $[m]$	6.96	6.30	6.57	6.51
Height $[m]$	2.62	2.36	2.50	1.83
Wingspan $[m]$	8.00	7.44	7.40	7.32
Wing surface $[m^2]$	10.7	9.1	9.0	9.5
Wing aspect ratio [-]	6.0	6.1	6.1	5.6
Wing taper ratio [-]	0.48	0.47	0.43	0.53
Horizontal tailplane span $[m]$	3.2	2.46	2.50	2.62
Horizontal tailplane area $[m^2]$	3.2	2.46	2.50	2.62
Vertical tail area $[m^2]$		1.6	1.6	1.5
Vertical tail length $[m]$		3.4	3.5	3.2
Vertical tail volume [%]		8.0	8.4	6.9
Aileron area $[m^2]$	1.71		1.76	2.15
Elevator area $[m^2]$	0.77		0.8	
Rudder area $[m^2]$	0.51		0.23	
Empty weight $[kg]$	682	531	545	572
MTOW $[kg]$	952	816	685	835
Wing loading $[kg/m^2]$		77.2	77.8	76.6
Power loading $[kg/kW]$		3.22	2.72	
Top speed $[m/s]$	88	118	123	118
Never exceed speed $[m/s]$	113	118	125	118
Manoeuvre speed $[m/s]$	81	88	93	93
Climb rate $[m/s]$	16.3	18.7	21.8	17.8
Service ceiling $[m]$	4875		3050	
Roll rate $[°/s]$	400	420	440	420
Maximum g-load $[-]$	+/-10	+/-10	+12/-10	+/-12

(a) Extra 300LX *(b) Zivko Edge 540* *(c) Corvus Racer 540* *(d) MXS-R*

Figure A.1: Reference aircraft images

Appendix B

Detailed Design

Table B.1: Preliminary empennage parameters

Parameter	Symbol	Value
Horizontal tail span $[m]$	b_h	1.6
Horizontal tail surface area $[m^2]$	S_h	0.9
Horizontal tail aspect ratio $[-]$	A_h	3.0
Horizontal tail taper ratio $[-]$	λ_h	0.6
Horizontal tail root chord $[m]$	c_{r_h}	0.7
Horizontal tail tip chord $[m]$	c_{t_h}	0.4
Horizontal tail moment arm $[m]$	l_h	4.0
Horizontal tail volume $[-]$	V_h	0.5
Horizontal tail Leading Edge sweep angle $[deg]$	Λ_{LE_h}	9.4
Horizontal tail half chord sweep angle $[deg]$	$\Lambda_{0.5c_h}$	0
Horizontal tail quarter chord sweep angle $[deg]$	$\Lambda_{0.25c_h}$	4.7
Vertical tail span $[m]$	b_v	1.4
Vertical tail surface area $[m^2]$	S_v	1.1
Vertical tail aspect ratio $[-]$	A_v	1.9
Vertical tail taper ratio $[-]$	λ_v	0.3
Vertical tail root chord $[m]$	c_{r_v}	1.2
Vertical tail tip chord $[m]$	c_{t_v}	0.3
Vertical tail moment arm $[m]$	l_v	4.0
Vertical tail volume $[-]$	V_v	0.6
Vertical tail Leading Edge sweep angle $[deg]$	Λ_{LE_v}	35

Table B.2: Preliminary wing parameters

Parameter	Symbol	Value
Wing span $[m]$	b	7.6
Wing surface area $[m^2]$	S	7.3
Wing aspect ratio $[-]$	A	7.9
Wing taper ratio $[-]$	λ	0.5
Wing root chord $[m]$	c_r	1.3
Wing tip chord $[m]$	c_t	0.6
Wing Mean Aerodynamic Chord $[m]$	MAC	1.0
Wing Leading Edge sweep angle $[^\circ]$	Λ_{LE}	0.0
Wing half chord sweep angle $[^\circ]$	$\Lambda_{0.5c}$	-4.8
Wing quarter chord sweep angle $[^\circ]$	$\Lambda_{0.25c}$	-2.4

Table B.3: Preliminary fuselage parameters

Parameter	Symbol	Value
Fuselage length $[m]$	l_f	6.0
Fuselage width $[m]$	b_f	0.9
Fuselage height $[m]$	h_f	0.7

Table B.4: Preliminary weight parameters

Parameter	Symbol	Value
Wing weight $[kg]$	W_w	95
Empennage weight $[kg]$	$W_{empennage}]$	20
Fuselage weight $[kg]$	W_f	97
Total Engine Weight $[kg]$	W_e	235
Landing gear weight $[kg]$	W_{lg}	24
Control surfaces weight $[kg]$	W_{cs}	14
Instruments weight $[kg]$	W_{ins}	4
Zero Ballast Empty weight $[kg]$	EW_0	489
Ballast weight	$W_{ballast}$	51
Empty Weight $[kg]$	EW	540
Payload weight $[kg]$	W_{pl}	122
Fuel weight $[kg]$	W_{fuel}	36
Maximum Take-Off Weight $[kg]$	$MTOW$	698

Table B.5: Preliminary propulsion parameters

Parameter	Symbol	Value
Engine power $[hp]$	P_e	315
Propeller efficiency $[-]$	η_p	0.8
Available power $[kW]$	P_a	188

Table B.6: Preliminary performance parameters

Parameter	Symbol	Value
Design cruise speed $[m/s]$	V_{cruise}	97
Maximum stall speed $[m/s]$	$V_{s_{max}}$	29.2
Maximum theoretical speed $[m/s]$	V_{max}	134
Maximum maneuver load factor $[-]$	n_{max}	10
Maximum structural load factor $[-]$	n_{struc}	15
Rate of climb $[m/s]$	rc	24.5
Oswald efficiency factor $[-]$	e	0.7
Maximum lift coefficient $[-]$	$C_{L_{max}}$	1.8
Parasite drag coefficient $[-]$	C_{D_0}	0.017
Maximum lift over drag ratio $[-]$	$\left(\frac{L}{D}\right)_{max}$	14
Maximum range $[km]$	R	404
Maximum endurance $[h]$	E	1.4

Appendix C

Control force methodology

The methodology of the control force coefficients is explained in this appendix. Three coefficients need to be determined: hinge moment with respect to angle of attack C_{h_α} Section C.1, hinge moment with respect to control surface deflection C_{h_δ} Section C.2 and hinge moment with respect to tab deflection $C_{h_{\delta_t}}$ Section C.3. To calculate these hinge moment coefficients, a method described by Roskam is used [70].

C.1 Control surface hinge moment with respect to angle of attack

The first derivative that is calculated is the control surface hinge moment derivative with respect to angle of attack C_{h_α}. The 2D coefficient is determined using Equation (C.1). The subscript 'theory' refers to the situation where the lift-curve slope is equal to the theoretical value $C_{l_\alpha} = 2\pi$.

$$c'_{h_\alpha} = \left(\frac{c'_{h_\alpha}}{c_{h_\alpha}}\right)_{theory} (c_{h_\alpha})_{theory} \tag{C.1}$$

Both parameters can be determined from Figures C.1a [70] and C.1b [70], respectively.

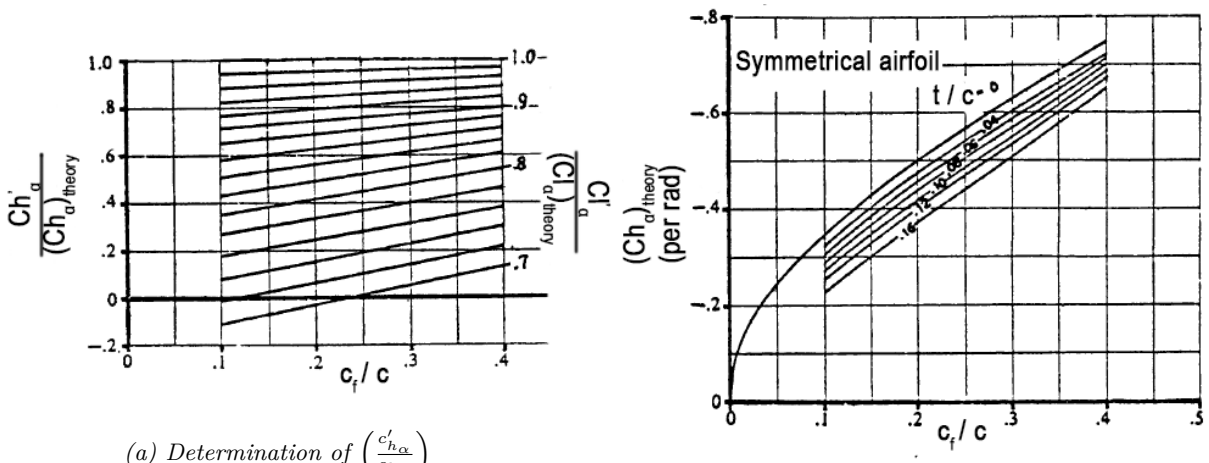

(a) Determination of $\left(\frac{c'_{h_\alpha}}{c_{h_\alpha}}\right)_{theory}$

(b) Determination of $(c_{h_\alpha})_{theory}$

Figure C.1: Determination of c'_{h_α}

Based on the 2D coefficient, it is possible to calculate the 3D derivative. The 3D coefficient is obtained using Equation (C.2),

$$C_{h_\alpha} = \frac{A\cos(\Lambda_{0.25c})}{A + 2\cos(\Lambda_{0.25c})}(c'_{h_\alpha}) + \Delta C_{h_\alpha} \tag{C.2}$$

where ΔC_{h_α} is calculated according to Equation (C.3).

$$\Delta C_{h_\alpha} = \frac{\Delta C_{h_\alpha}}{c_{l_\alpha} B_2 K_\alpha \cos(\Lambda_{0.25c})} \left(c_{l_\alpha} B_2 K_\alpha \cos(\Lambda_{0.25c})\right) \tag{C.3}$$

The contribution ΔC_{h_α} is determined using Figure C.2 [70].

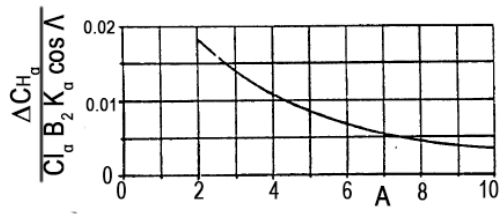

Figure C.2: Determination of fraction $\frac{\Delta C_{h_\alpha}}{c_{l_\alpha} B_2 K_\alpha \cos(\Lambda_{0.25c})}$

In the expression for ΔC_{h_α}, c_{l_α} is the airfoil lift-curve slope and B_2 accounts for the chord ratio of the control surface and balancing surface. B_2 is obtained from Figure C.3a. K_α accounts for the effect of the control surface span: $K_\alpha = \frac{(K_\alpha)_{\eta_i}(1-\eta_i)-(K_\alpha)_{\eta_o}(1-\eta_o)}{\eta_o-\eta_i}$. $(K_\alpha)_{\eta_i}$ and $(K_\alpha)_{\eta_o}$ can be found from Figure C.3b [70].

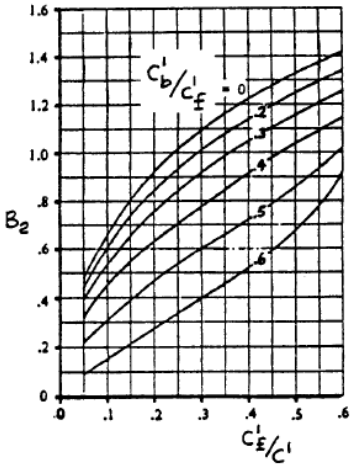

(a) Determination of B_2

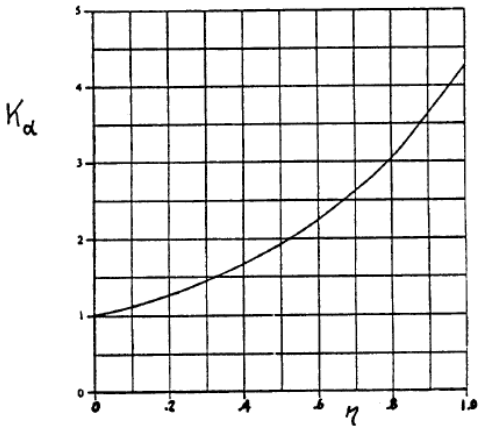

(b) Determination of $(K_\alpha)_\eta$

Figure C.3: Determination of two parameters for 3D C_{h_α}

C.2 Control surface hinge moment due to control surface deflection

The second coefficient that is explained is the hinge moment due to the control surface deflection C_{h_δ}. The 2D coefficient of the hinge moment due to control surface deflection is determined according to Equation (C.4).

$$c'_{h_\delta} = \frac{c'_{h_\delta}}{(c_{h_\delta})_{theory}} (c_{h_\delta})_{theory} \tag{C.4}$$

Both parameters can be found using Figure C.4a [70] and C.4b [70].

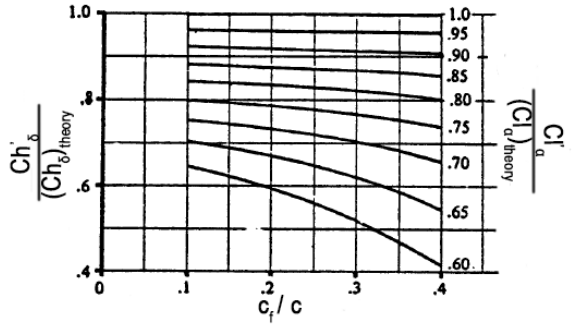

(a) Determination of $\frac{c'_{h_\delta}}{(c_{h_\delta})_{theory}}$

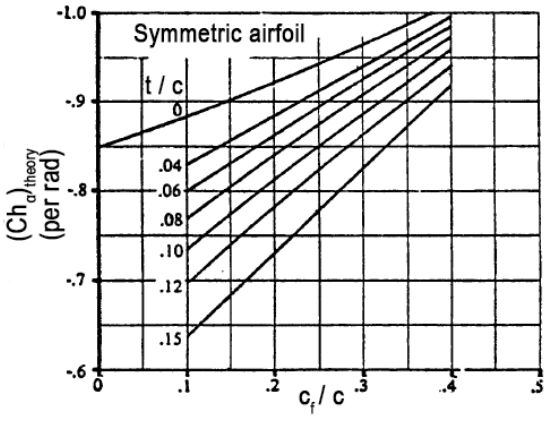

(b) Determination of $(c_{h_\delta})_{theory}$

Figure C.4: Determination of two parameters for 2D c'_{h_δ}

Equation (C.5) shows the calculation of the 3D control derivative,

$$C_{h_\delta} = \cos(\Lambda_{0.25c})\cos(\Lambda_{hl})\left(c'_{h_\delta} + \alpha_d c'_{h_\delta}\left[\frac{2\cos(\Lambda_{0.25c})}{A + 2\cos(\Lambda_{0.25c}}\right]\right) + \Delta C_{h_\delta} \tag{C.5}$$

where ΔC_{h_δ} is calculated in Equation (C.6).

$$\Delta C_{h_\delta} = \left(\frac{\Delta C_{h_\delta}}{c_{l_\delta} B_2 K_\delta \cos(\Lambda_{0.25c})\cos(\Lambda_{hl})}\right)(c_{l_\delta} B_2 K_\delta \cos(\Lambda_{0.25c})\cos(\Lambda_{hl})) \tag{C.6}$$

Figure C.5 [70] shows how to find α_d based on the maximum deflection and chord ratio.

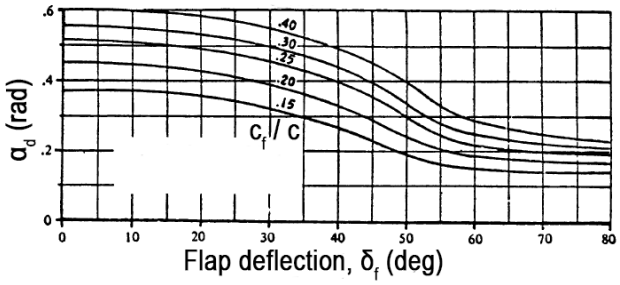

Figure C.5: Determination of α_d

A correction factor K_δ for the control surface deflection is used and can be calculated using: $K_\delta = \frac{(K_\delta)_{\eta_i}(1-\eta_i)-(K_\delta)_{\eta_o}(1-\eta_o)}{\eta_o-\eta_i}$. In this equation, $(K_\delta)_{eta}$ is determined from Figure C.6b [70]. Figure C.6a [70] shows how to obtain $\frac{\Delta C_{h_\delta}}{c_{l_\delta} B_2 K_\delta \cos(\Lambda_{0.25c})\cos(\Lambda_{hl})}$.

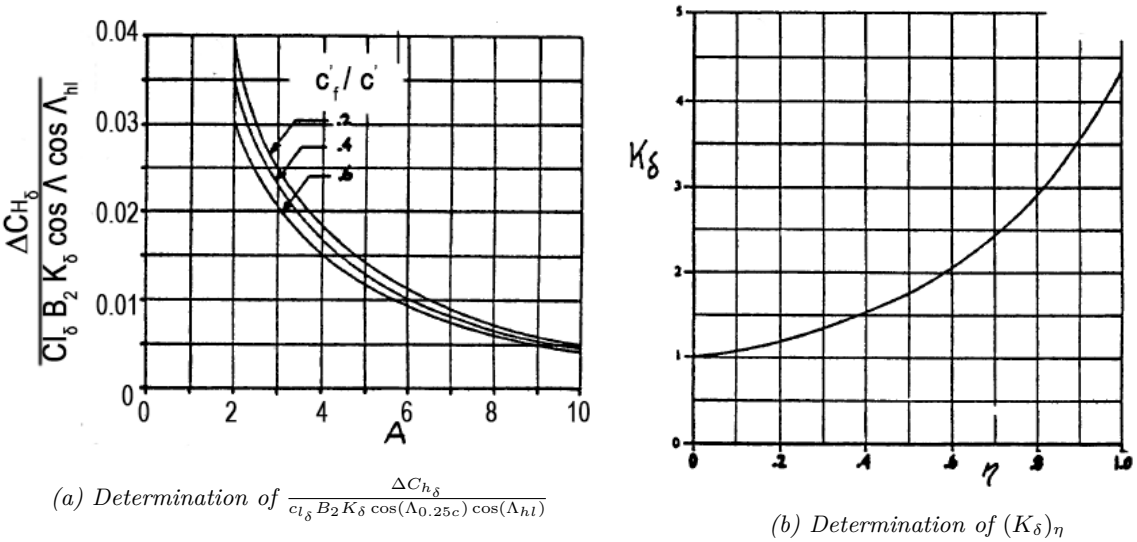

(a) Determination of $\frac{\Delta C_{h_\delta}}{c_{l_\delta} B_2 K_\delta \cos(\Lambda_{0.25c}) \cos(\Lambda_{hl})}$

(b) Determination of $(K_\delta)_\eta$

Figure C.6: Determination of two parameters for 3D C_{h_δ}

C.3 Control surface hinge moment due to tab deflection

The third coefficient that is required is the hinge moment due to the trim tab deflection $C_{h_{\delta_t}}$. The 2D coefficient can be calculated using Equation (C.7).

$$c_{h_{\delta_t}} = (c_{h_{\delta_t}})_{cl} - (c_{h_{c_l}})_{\delta_t} (c_{l_\alpha})_{\delta_t} (\alpha_{\delta_t})_{c_l} \tag{C.7}$$

$(c_{l_\alpha})_{\delta_t}$ is the lift-curve slope of the main surface where the trim tab is attached to. Figure C.7 [70] shows how to determine the change of angle of attack due to a change in trim tab deflection.

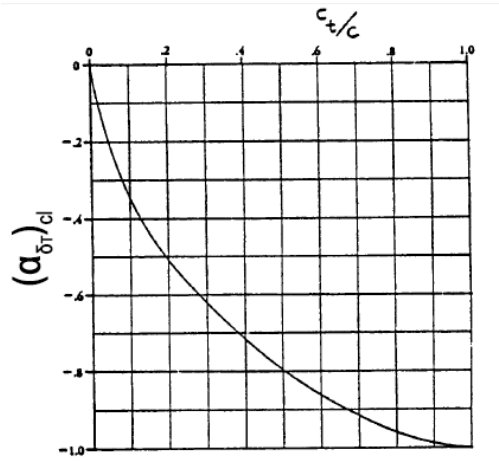

Figure C.7: Determination of $(\alpha_{\delta_t})_{c_l}$.

The two last parameters required to determine the 2D value of $c_{h_{\delta_t}}$ are $(c_{h_{c_l}})_{\delta_t}$ and $(c_{h_{\delta_t}})_{cl}$. These can be obtained from Figures C.8a [70] and C.8b [70], respectively.

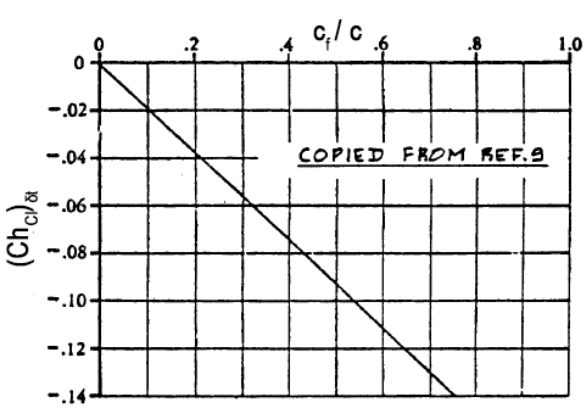

(a) Determination of $(c_{h_{c_l}})_{\delta_t}$.

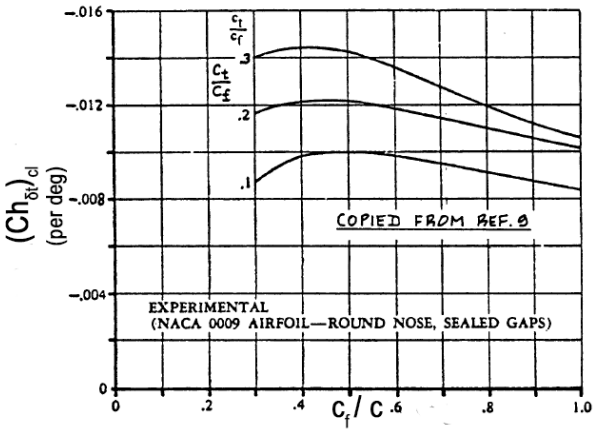

(b) Determination of $(c_{h_{\delta_t}})_{c_l}$.

Figure C.8: Determination of the 2D hinge moment parameters $(c_{h_{c_l}})_{\delta_t}$ and $(c_{h_{\delta_t}})_{c_l}$, required to obtain the 2D hinge moment due to trim tab deflection $c_{h_{\delta_t}}$.

Equation (C.8) shows the calculation of the 3D control derivative,

$$C_{h_{\delta_t}} = \cos(\Lambda_{0.25c})\cos(\Lambda_{hl})\left(c_{h_{\delta_t}} + \alpha_d c'_{h_{\delta_t}}\left[\frac{2\cos(\Lambda_{0.25c})}{A + 2\cos(\Lambda_{0.25c}}\right]\right) + \Delta C_{h_{\delta_t}} \tag{C.8}$$

where all coefficients can be calculated using the same method as stated in the section of the control surface hinge moment due to control surface deflection.

Appendix D

Buckling Coefficients

In Section 5.6 of Part II, the critical buckling stress for plates in either compression or shear is determined using coefficients k_c and k_s. Figure D.1a [98] gives the critical compressive buckling coefficient k_c as a function of the plate aspect ratio. Figure D.1b [98] gives the critical shear buckling coefficient k_s as a function of the plate aspect ratio.

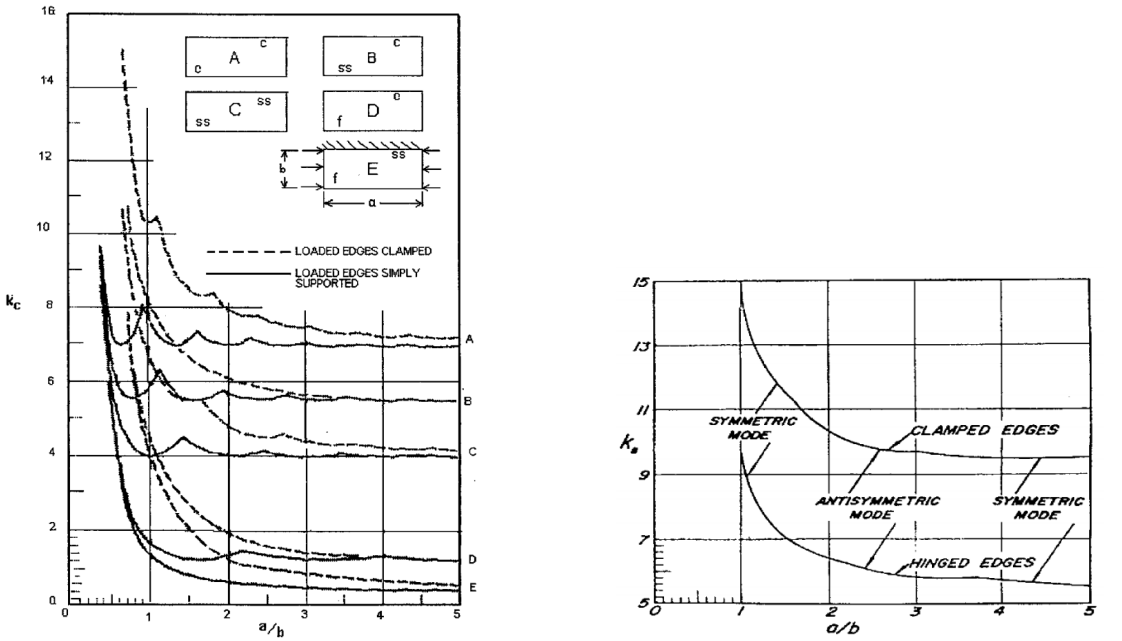

(a) Critical compression buckling coefficient *(b) Critical shear buckling coefficient*

Figure D.1: Buckling coefficients